NASA-CR-164003
19810010458

The Telecommunications and Data Acquisition Progress Report 42-61

November and December 1980

N. A. Renzetti
Editor

February 15, 1981

National Aeronautics and
Space Administration

Jet Propulsion Laboratory
California Institute of Technology
Pasadena, California

The Telecommunications and Data Acquisition Progress Report 42-61

November and December 1980

N. A. Renzetti
Editor

February 15, 1981

National Aeronautics and
Space Administration

Jet Propulsion Laboratory
California Institute of Technology
Pasadena, California

The research described in this publication was carried out by the Jet Propulsion Laboratory, California Institute of Technology, under NASA Contract No. NAS7-100.

Preface

This publication was formerly entitled *The Deep Space Network Progress Report*. Although the practice of reporting progress in the development and operations of the Deep Space Network continues, the report has been expanded to include developments in Earth-based radio technology as applied to other research programs. These programs are:

(1) Geodynamics: For several years, the laboratory has been developing radio interferometry at microwave frequencies for application to geodetic measurements. This branch of telecommunications technology is now being applied to the study of geodynamics.

(2) Astrophysics: The deep space stations, individually and in pairs as an interferometer, have been used by radio astronomers for astrophysics research by direct observations of radio sources.

(3) An activity closely related to radio astronomy's use of the deep space stations is NASA's continuing program of radio search for extraterrestrial intelligence in the microwave region of the electromagnetic spectrum.

Each succeeding issue of this report will present material in some, but not all, of the following categories:

Radio Astronomy
Search for Extraterrestrial Intelligence
Radio Interferometry at Microwave Frequencies

- Geodetic Techniques Development
- Spacecraft Navigation
- Orbiting Very Long Baseline Interferometry

Deep Space Network

- Description
- Program Planning
- Planetary and Interplanetary Mission Support
- Advanced Systems
- Network and Facility Engineering and Implementation
- Operations
- Spacecraft Radio Science
- Planetary Radar
- Energy

In each issue, there will be a report on the current configuration of one of the seven DSN systems (Tracking, Telemetry, Command, Monitor and Control, Test Support, Radio Science, and Very Long Baseline Interferometry).

The work described in this report series is either performed or managed by the Telecommunications and Data Acquisition organization of JPL.

Contents

Ground Communications

Deep Space Stations

ENERGY

Atmospheric Media Effects on ARIES Baseline Determination

S. C. Wu
Tracking Systems and Applications Section

Large-scale atmospheric media increase apparent baseline length in ARIES baseline determination. Relying on the "self-calibration" of ionosphere in S-band observations may result in a baseline length error as large as 30 cm over a 200-km baseline. Up to 90 percent of such error can be removed through calibration by a crude ionospheric model.

I. Introduction

It is well known that for VLBI observations over a short baseline (~300 km or shorter) a large part of the media errors is common between the two ray paths and cancels upon differencing. Such "self-calibration" becomes more complete as the baseline length reduces. It has been a general practice in ARIES baseline determination to rely on such self-calibration of ionospheric effects. It is also "well known" that media effects degrade baseline solutions mainly in the vertical component. However, it is found through covariance analyses that the component most sensitive to media depends heavily upon the correlation, between the two stations, of the media effects. It is also found that relying on the cancellation of ionospheric delays between the two ray paths of VLBI observations at S-band results in a large error in baseline length determination.

This article provides a comparison among different types of media effects on ARIES baseline determination. The effectiveness of simple ionospheric calibration models are studied. To perform the covariance analysis, an ARIES observation sequence needs to be assumed. For the current purposes, the observation sequence is selected to be that of experiment 80D over the JPL/Goldstone baseline (~180 km). This experiment consisted of 96 observations over a period of ~25 hours on March 25 to 26, 1980.

II. Atmospheric Media Error Models

We shall study the following five error models of atmospheric media corrupting ARIES baseline determination. Although these models are simple and idealized, their effects approach the average effects on actual ARIES observations.

A. Homogeneous Troposphere

For a constant zenith delay of A_z, the differenced delay between the two ray paths is

$$\Delta\tau = A_z(1/\sin\gamma_1 - 1/\sin\gamma_2) \quad (1)$$

where γ_1 and γ_2 are the elevation angles. Such model applies to an uncalibrated average troposphere with A_z = 230 cm.

B. Locally Homogeneous Troposphere

This model assumes homogeneity of the troposphere with independent zenith delay at each station. Such a model accounts for the systematic delay error after a gross homogeneous effect on each site is independently calibrated. For a residual zenith *differenced* delay of A_z, the effect over the baseline is scaled by the average elevation factor to give

$$\Delta\tau = A_z \frac{1/\sin\gamma_1 + 1/\sin\gamma_2}{2} \quad (2)$$

An A_z of a few cm may exist. A_z = 3 cm will be assumed for this study.

C. Random Troposphere

This model accounts for random deviation of the troposphere from a homogeneous calibration model. Even though the effect is still elevation-angle dependent, it behaves as random noise from observation to observation and should be treated as such. The magnitude of this effect is

$$\Delta\tau = \left(\frac{A_{z,1}^2}{\sin^2\gamma_1} + \frac{A_{z,2}^2}{\sin^2\gamma_2}\right)^{1/2} \quad (3)$$

where A_z is the zenith deviation on each site. $A_{z,1} = A_{z,2} = A_z$ = 2 cm will be assumed.

D. Global Ionosphere

This model assumes that a single model applies to both stations but scaled by factors according to the solar-zenith angle and the elevation angle at each station. Let $f(X)$ be the solar-zenith angle factor and $g(\gamma)$ the elevation angle factor, then

$$\Delta\tau = A_z[f(X_1)\,g(\gamma_1) - f(X_2)\,g(\gamma_2)] \quad (4)$$

where A_z is the zenith delay through the ionospheric peak and

$$f(X) = \begin{cases} 0.2 + 0.8\cos^{2/3} X & X < 90 \text{ deg} \\ 0.2 & X > 90 \text{ deg} \end{cases} \quad (5)$$

$$g(\gamma) = 27[(1.071^2 - \cos^2\gamma)^{1/2} - (1.034^2 - \cos^2\gamma)^{1/2}] \quad (6)$$

During the period of experiment 80D, an independent Faraday rotation measurement indicated an ionospheric peak of ~8 meters at S-band. A_z = 800 cm will be assumed.

E. Random Ionosphere

A random deviation from a global ionospheric model will result in a differenced delay between the two stations. The magnitude of the random delay error is

$$\Delta\tau = A_z \frac{f(X_1)g(\gamma_1) + f(X_2)g(\gamma_2)}{2} \quad (7)$$

where A_z is the rms differenced delay; f and g are as defined in Eqs. (5) and (6), respectively. It is estimated that the differenced delay may amount to 10 percent of the uncalibrated absolute effect for every 1000 km of baseline. Hence, across the 180-km JPL/Goldstone baseline of experiment 80D, A_z = 14 cm.

III. Baseline Determination Errors

To estimate the effects of the media error models outlined in Section II, covariance analyses following Ref. 1 were performed. The solved-for parameters include three baseline components, epoch offset, and frequency offset. The effects of models A, B, and D are treated as systematic errors; those of models C and E are treated as random errors. All the 96 observations are included in a single estimation process. Table 1 summarizes the estimated baseline component errors from the above five types of media errors. It is observed that the "well-known" belief that the baseline *vertical* is most sensitive to media errors is valid only when the errors are uncorrelated (or negatively correlated) between the two stations. When the errors are correlated, as in the cases of homogeneous troposphere and global ionosphere without calibrations, it is the baseline *length* that is most affected. In other words, a media model that is common to both stations and that tends to cancel upon differencing will give rise to an error mainly in baseline length.

The above unexpected results can be visualized, at least in the case of homogeneous troposphere, by the following reasoning. The information of baseline length is extracted mainly from delay observations nearly parallel to the baseline. The delay due to a homogeneous troposphere is always longer for the lagging station due to lower elevation angle as a result of the spherical earth surface. Hence the apparent baseline is always longer than its true value. For the other two components, the information is extracted mainly from delay observations nearly perpendicular to the baseline. The elevation angles and thus the delays due to a homogeneous troposphere are nearly the same for the two stations. Hence baseline components perpendicular to the length are hardly affected.

It should be pointed out that the effects of a homogeneous troposphere can be easily calibrated. This is routinely done in ARIES data processing. It is included in the above study simply for comparison and completeness.

An uncalibrated ionospheric effect appears to be a significant error source (at S-band) in the determination of baseline

length. To examine the modeling effects of the global ionosphere, two smooth models

$$f(X) = 0.2 + 0.8 \cos^4 (X/2) \quad (8)$$

and

$$f(X) = 0.2 + 0.8 \cos^2 (X/2) \quad (9)$$

are also studied in place of Eq. (5). These three models are shown in Fig. 1. The resulting baseline errors due to a global ionospheric error following these three models are summarized in Table 2. The errors in baseline length do not show appreciable differences from one model to another. Hence ionospheric modeling cannot be condemned for the large error in baseline length. The above global ionospheric effect on baseline length was estimated for a 180-km baseline between JPL and Goldstone. This error increases with baseline length: For the 336-km baseline between JPL and OVRO, the baseline length error becomes 49.5 cm. Hence ionospheric calibration for ARIES S-band observations is deemed essential.

IV. Calibration of Ionospheric Effects

Since most ARIES experiments have been carried out at S-band only, S-X calibration is out of the question. An alternative is to make use of Faraday rotation data from Goldstone viewing one of the geostationary satellites. Daily records of these data have been, and continue to be, collected by the Tracking System Analytic Calibration (TSAC) Team. However, since the Faraday rotation measurements are taken at a single station by viewing a fixed ray path (with respect to the station), mappings need to be done before the data can be applied to other stations and ray paths. At present, such mappings are routinely performed by the TSAC Team on ray paths that view deep-space probes near the ecliptic plane. On the other hand, ARIES experiments include observing sources at high declination angles, the mappings to which are out of the current TSAC mapping limit.

Other handy information recorded by the TSAC Team is the zenith total electron content (TEC) plots. The peak value and the night-time value of the TEC on each day can easily be read out from these plots. A simple mapping scheme can be used to generate point-by-point calibration from the peak and the night-time TEC during any particular day when ARIES is taking observations.

To examine how an imperfect mapping will degrade the calibration, simulation analyses are performed. A "true" TEC as a function of solar-zenith angle X is assumed to be

$$E(X) = \begin{cases} E_{min} + (E_{max} - E_{min}) \cos^{2/3} X & X < 90 \text{ deg} \\ E_{min} & X > 90 \text{ deg} \end{cases} \quad (10)$$

The following four imperfectly mapped calibrations are examined:

(1) $E(X) = E_{min} + (E_{max} - E_{min}) \cos^4 (X/2)$

(2) $E(X) = E_{min} + (E_{max} - E_{min}) \cos^2 (X/2)$

(3) Same as (1) with the peak shifted by 30 deg to the east from the sub-Sun point ($X = 0$).

(4) Same as (1) with the peak shifted by 15 deg to the north from the sub-Sun point ($X = 0$).

The assumed "true" ionospheric TEC as a function of X is shown in Fig. 1 as a solid line for $E_{max} = 1$ and $E_{min} = 0.2$. The calibrations of (1) and (2) above are shown in the same figure as a dotted line and a dash-dotted line, respectively. Table 3 summarizes the residual baseline errors due to imperfectly mapped calibrations. Here, E_{max} and E_{min} have been chosen to be equivalent to the 800-cm and 160-cm delays, which occurred on March 25 to 26, 1980 (Experiment 80D of ARIES). For comparison, the baseline errors without calibration are also shown. These results indicate that, except for model (2), all calibration models remove 90 percent of the baseline length error or better. In other words, to remove 90 percent of the ionospheric effects, the "shape" of the mapping function is allowed to be moderately imperfect, and the peak to be shifted by 30 deg in longitude or by 15 deg in latitude. Even the badly "out-of-shape" mapping of model (2) removes 70 percent of the baseline length error. Such high-degree removal of the global ionospheric effect is the result of decorrelating the effects between the two stations; the systematic effect is thus somewhat randomized and less corrupting on baseline length.

V. Conclusion

In baseline determination by the VLBI technique, the sensitivities of baseline components to atmospheric media effects depend heavily upon the correlation between the two ends of the baseline. The global-type media tends to affect mainly the baseline length. The effects are such as to lengthen the estimated baseline. High-degree removal of such ionospheric effects is possible even with a crude model, providing correct diurnal peak and minimum ionospheric levels are input. Uncalibrated ionospheric effects may result in an error of tens of centimeters at S-band over a baseline of 100 km or longer.

Acknowledgment

The information for Faraday rotation measurement is provided by H. N. Royden and T. E. Litwin of TSAC Team.

Reference

1. Wu, S. C., "Error Estimation for ORION Baseline Vector Determination", *TDA Progress Report 42-57*, Jet Propulsion Laboratory, Pasadena, Calif., June 15, 1980, pp. 16-31.

Table 1. Media effects on JPL/Goldstone baseline determination

Media error model	Value of A_z, cm	Baseline component errors, cm		
		Length	Lateral	Vertical
Homogeneous troposphere	230	28.0	2.9	2.4
Locally homogeneous troposphere	3	0.1	0.5	8.9
Random troposphere	2	1.0	1.1	2.4
Global ionosphere	800	26.5	3.4	1.3
Random ionosphere	14	1.3	1.3	2.8

Table 2. Global ionospheric effects on JPL/Goldstone baseline determination

Medial model	Value of A_z, cm	Baseline component errors, cm		
		Length	Lateral	Vertical
Eq. (5)	800	26.5	3.4	1.3
Eq. (8)	800	25.8	1.1	2.5
Eq. (9)	800	33.7	1.2	0.4

Table 3. Residual ionospheric effects on JPL/Goldstone baseline determination

Calibration model	Baseline component errors, cm		
	Length	Lateral	Vertical
No Calibration	26.5	3.4	1.3
Model (1)	0.7	2.3	1.3
Model (2)	7.2	4.6	0.9
Model (3)	1.0	5.1	3.1
Model (4)	2.9	1.3	1.3

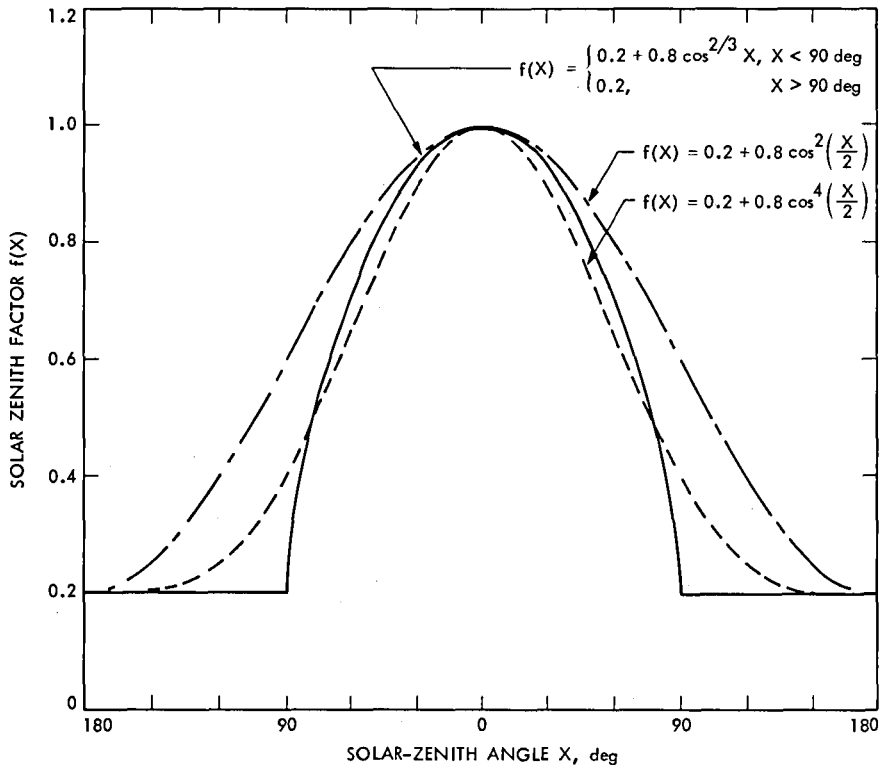

Fig. 1. Solar-zenith angle factors of global ionospheric models

Historical Data on Characteristics of Radio Systems Used for United States Deep-Space Communications

N. F. de Groot and H. R. Bahadori
Telecommunications Systems Section

Historical data on selected communication parameters are presented in tables and charts for 14 deep-space missions. Some observations are made about trends in communication capability.

I. Introduction

The DSN is engaged in examining past trends and future requirements to assure the timely development and implementation of systems to support deep-space radio communications. In connection with this effort, historical data on selected characteristics of past and present spacecraft communication systems has been gathered and is presented in this article.

II. Selected System Characteristics

The characteristics selected as indications of communication capability are:

(1) Maximum and minimum telemetry rate.

(2) Command rate.

(3) Command word length.

(4) Data storage capacity.

(5) Spacecraft antenna size.

(6) Spacecraft transmitter power.

Values for these parameters are tabulated and plotted for 14 missions. The 17 spacecraft included in these missions are listed in Table 1 along with their launch dates. Subsequent Tables 2 through 4 list the parameter values associated with each mission, not each spacecraft.

Parameter values are plotted in Figs. 1 through 9 as a function of time to make trends visible. In some cases, the arithmetic values listed in the tables have been converted to logarithmic (dB) values in the corresponding figures. For example, the 16.2-k bits/s maximum telemetry rate for Mariner-Mars 69 has been plotted as 42 dB (bits/s). This plotting method was used because it is often convenient to think of relationships between communication parameters in terms of logarithmic values expressed in the form of decibels.

III. Performance Ratios and Figure of Merit

In an attempt to shed additional light on the changing capability of deep-space communications, ratios of some parameters have been taken. These ratios are expressed logarithmically and are:

$$\beta_1 = 10 \log \frac{\text{maximum telemetry rate}}{\text{minimum telemetry rate}}$$

$$\beta_2 = 10 \log \frac{\text{maximum telemetry rate}}{\text{command rate}}$$

The reader is invited to consider the meaning and implications of these ratios shown in Figs. 10 and 11. For example, the decrease in ratio of telemetry rate to command rate since 1973 seems to illustrate the increasingly complex control that is demanded by spacecraft designed to be largely autonomous in executing desired sequences of events during critical periods such as planetary encounter.

A telemetry figure of merit has also been derived as shown in Fig. 12. It is a logarithmic expression that includes the maximum telemetry rate and the square of the communication distance at planet encounter. The telemetry rate is related to the sum of all the spacecraft and ground performance parameters, including antenna size, transmitter power, receiver noise temperature, and coding gain. The communication distance is squared to account for the inverse square law of free-space propagation.

The unchanged value of the telemetry figure of merit since 1977 is indicative of economic constraints on the development of increased communication capability.

For missions beyond Jupiter, the current figure of merit dictates that the data rate must be correspondingly reduced below 115 kbits/s. No change to ground equipment is needed to accommodate these lower rates. In contrast, the current figure of merit yields a data rate capability of 1 Mbit/s for the proposed VOIR mission to Venus. In this case, changes are required to ground equipment if the radio communication capability is to be fully utilized. This is because existing telemetry demodulation and detection equipment will not handle a rate as high as 1 Mbit/s. (The figure of merit presented here does not include the enhancement of ground antenna arraying).

IV. Further Work

An important element of deep-space communication is the navigation and scientific data obtained from radio metric measurements. The accuracy of these has improved with time, and it would be interesting to trace this development. There are, however, numerous parameters involved and it is not yet clear that the needed historical data is available, or how a meaningful presentation could be accomplished. It is expected that further study will be undertaken.

V. Information Sources

Data collected for this article was found in an extensive set of project reports, handbooks, requirements documents, support plans, and NASA histories. The authors may be contacted for information about these sources.

Table 1. Mission launch date

Mission	Launch date
Mariner-Mars 64 (Mariner 4)	November 28, 1964
Pioneer 6	December 5, 1965
Pioneer 7	August 17, 1966
Mariner-Venus 67 (Mariner 5)	June 14, 1967
Pioneer 8	December 13, 1967
Pioneer 9	November 8, 1968
Mariner-Mars 69 (Mariner 6)	February 25, 1969
Mariner-Mars 69 (Mariner 7)	March 27, 1969
Mariner-Mars 71 (Mariner 9)	May 30, 1971
Pioneer 10	March 3, 1972
Pioneer 11	April 6, 1973
Mariner-Venus-Mercury 73 (Mariner 10)	November 3, 1973
Viking 75 (Viking 1)	August 20, 1975
Viking 75 (Viking 2)	September 9, 1975
Voyager 1	August 20, 1977
Voyager 2	September 5, 1977
Galileo	February 1984

Table 2. Telemetry rate

Mission	Minimum telemetry rate S-band, bits/s	Maximum telemetry rate S-band, bits/s	Minimum telemetry rate X-band, bits/s	Maximum telemetry rate X-band, bits/s
Mariner-Mars 64	8-1/3	33-1/3	(see footnote a)	
Pioneer 6	8	512		
Pioneer 7	8	512		
Mariner-Venus 67	8-1/3	33-1/3		
Pioneer 8	8	512		
Pioneer 9	8	512		
Mariner-Mars 69	8-1/3	16.2 K		
Mariner-Mars 71	8-1/3	16.2 K		
Pioneer 10	16	2048		
Pioneer 11	16	2048		
Mariner-Venus-Mercury 73	8-1/3	117.6 K		
Viking 75	8-1/3	16.2 K		
Voyager	10	115.2 K	10	115.2 K
Galileo	40	115.2 K	40	115.2 K

[a]Blank entries indicate that spacecraft did not have X-band telemetry capability.

Table 3. Spacecraft characteristics

Mission	Diameter or size, m	Antenna gain S-band, dBi	Antenna gain X-band, dBi	Spacecraft transmitter power S-band, W
Mariner-Mars 64	Elliptic reflector 1.17 × 0.54	23.3		20
Pioneer 6	Colinear broadside array	11.2		8
Pioneer 7	Colinear broadside array	11.2		8
Mariner-Venus 67	1	25.8		20
Pioneer 8	Colinear broadside array	11.2		8
Pioneer 9	Colinear broadside array	11.2		8
Mariner-Mars 69	1	25.8		20
Mariner-Mars 71	1	25.8		20
Pioneer 10	2.75	32.6		8
Pioneer 11	2.75	32.6		8
Mariner-Venus-Mercury 73	1.4	28.0	38.8	20[a]
Viking 75	1.5	28.1	39.5	20[a]
Voyager	3.7	35.3	48.2	20 (S and X)
Galileo	4.8	38.5	50.3	20 (S and X)

[a]Mariner-Venus-Mercury 73 and Viking 75 carried 250-mW experimental X-band transmitters.

Table 4. Command rate, bits per command word, and spacecraft data storage capacity

Mission	Command rate, bits/s	No. of bits per command word	Data storage capability, bits
Mariner-Mars 64	1	26	5.24×10^6
Pioneer 6	1	23	15232
Pioneer 7	1	23	15232
Mariner-Venus 67	1	26	10^6
Pioneer 8	1	23	15232
Pioneer 9	1	23	15232
Mariner-Mars 69	1	26	1.8×10^8
Mariner-Mars 71	1	26	1.8×10^8
Pioneer 10	1	22	49152
Pioneer 11	1	22	49152
Mariner-Venus-Mercury 73	1	26	1.8×10^8
Viking	4	67	11.2×10^8
Voyager	16	87	538×10^6
Galileo	32	48	269×10^6

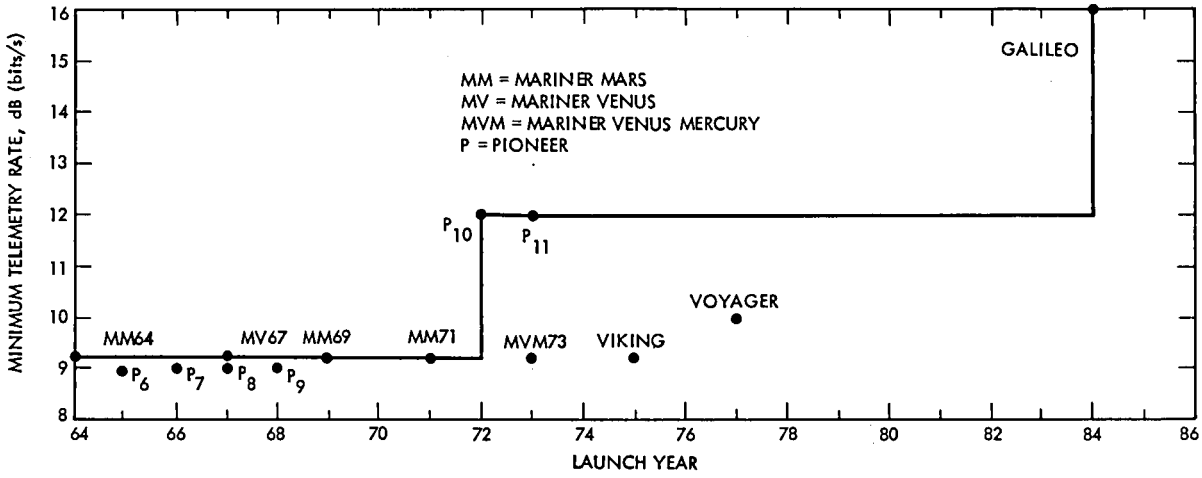

Fig. 1. Minimum telemetry rate vs launch year

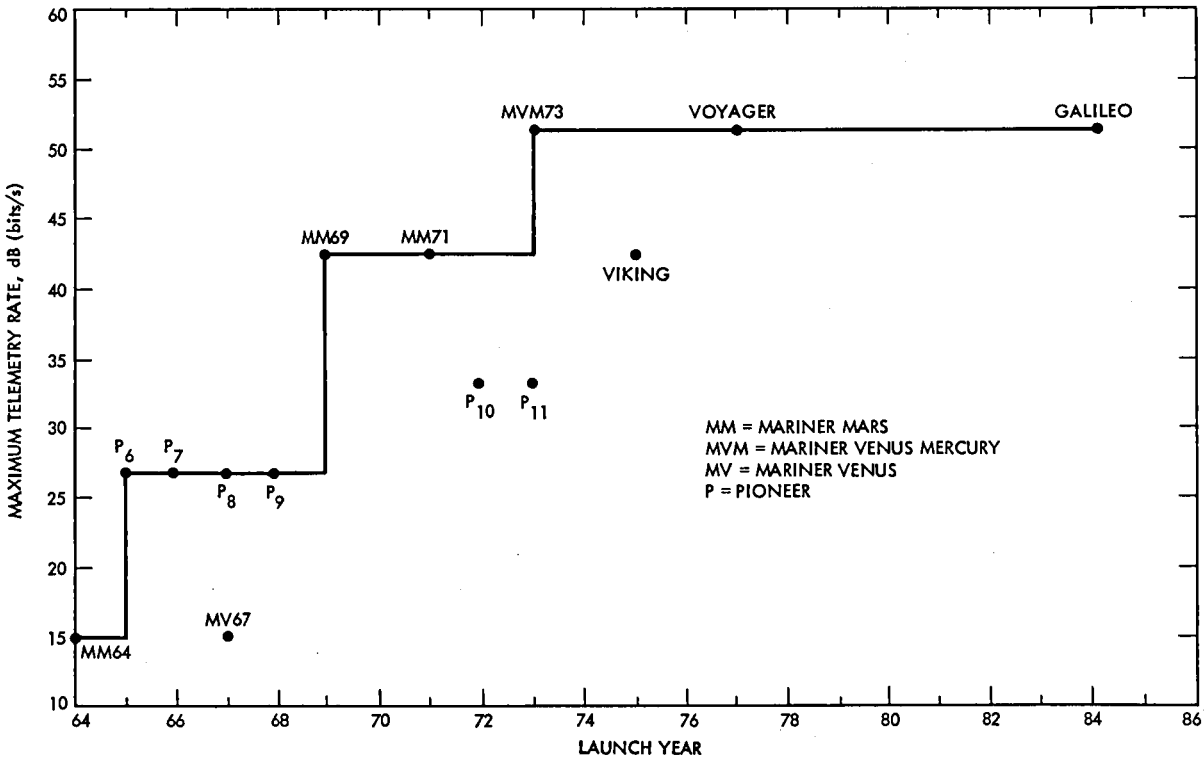

Fig. 2. Maximum telemetry rate vs launch year

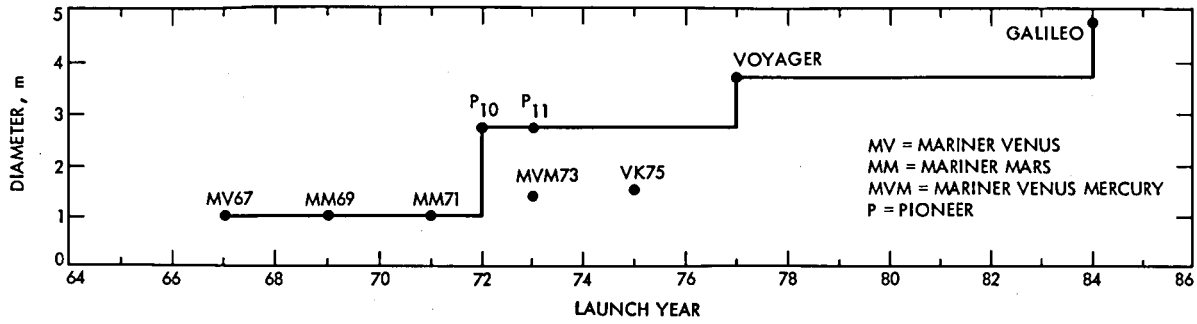

MM64 HAD 1.17 X 0.54 ELLIPTIC REFLECTOR
P6-9 HAD COLINEAR BROADSIDE ARRAY

Fig. 3. Spacecraft antenna diameter vs launch year

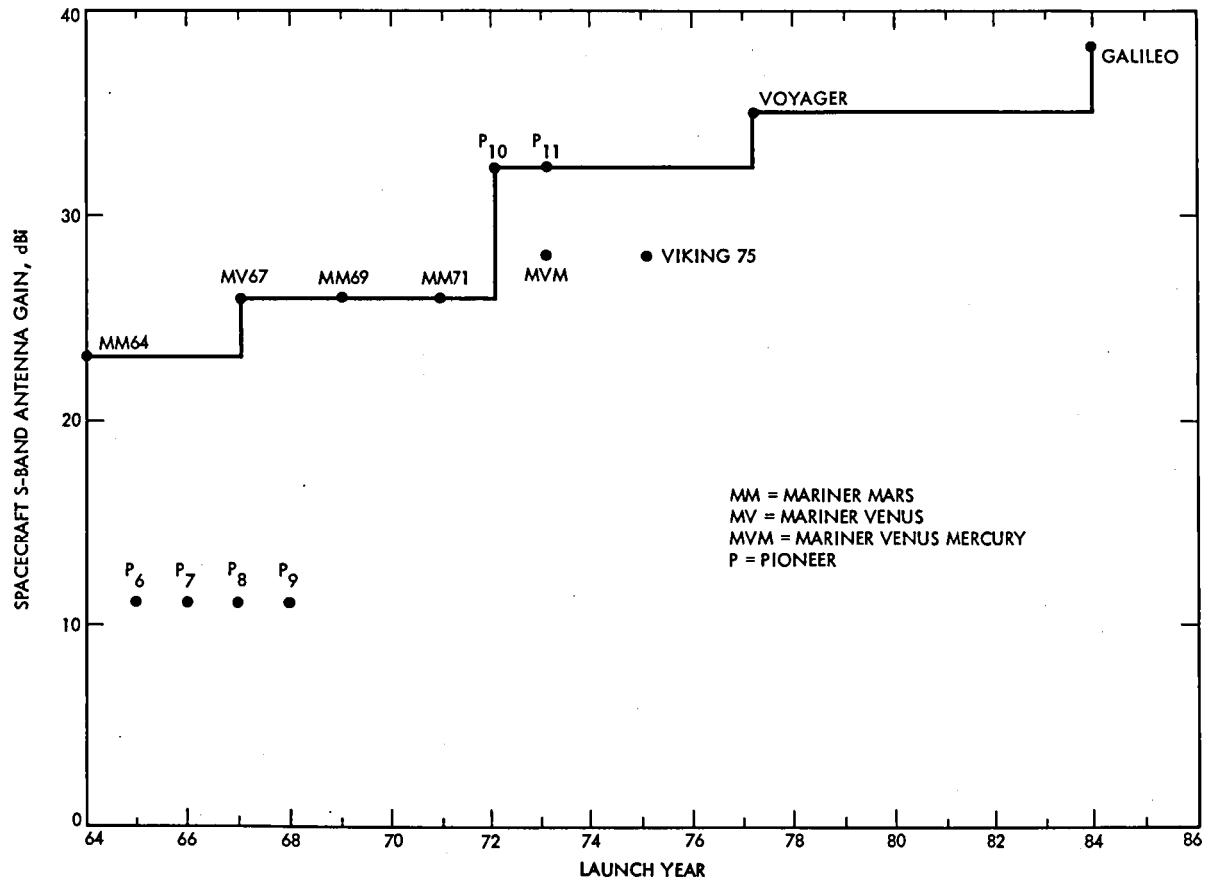

Fig. 4. Spacecraft S-band antenna gain vs launch year

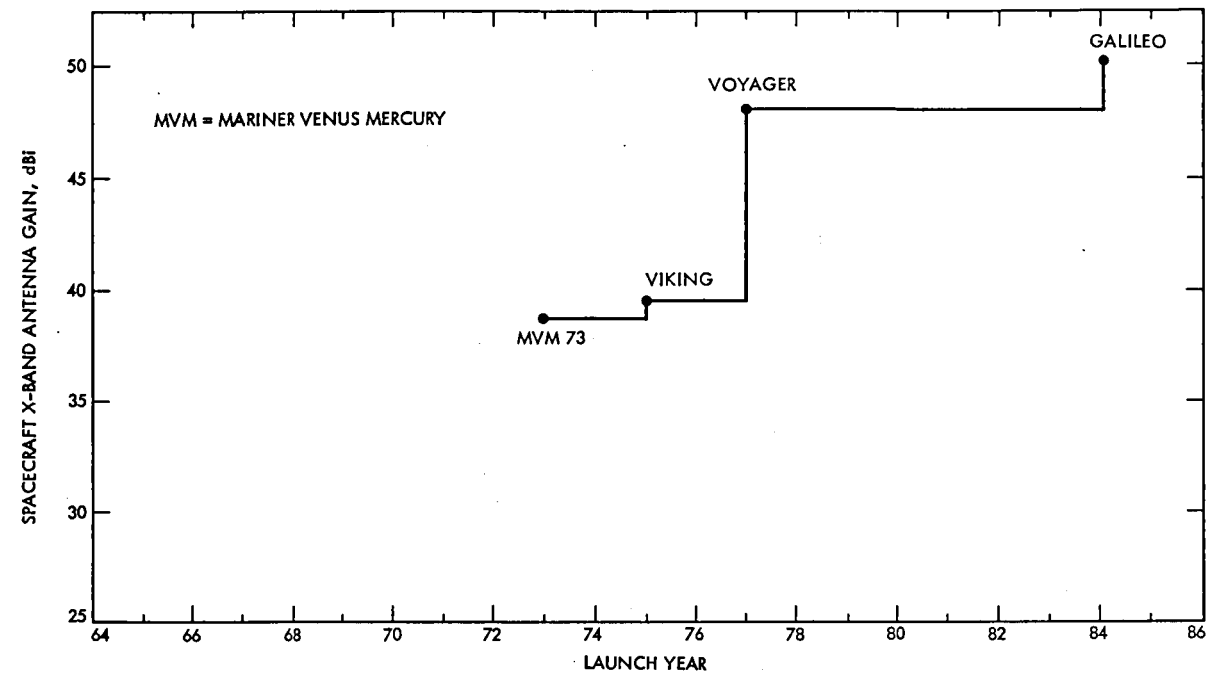

Fig. 5. Spacecraft X-band antenna gain vs launch year

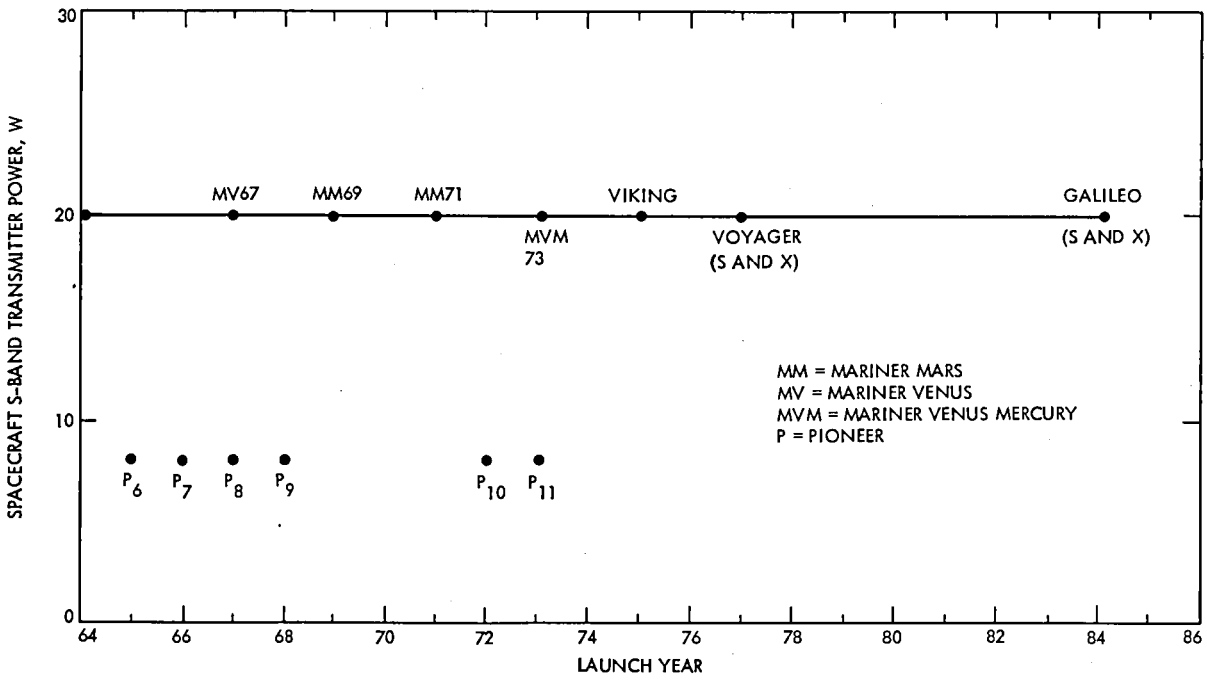

Fig. 6. Spacecraft transmitter power vs launch year

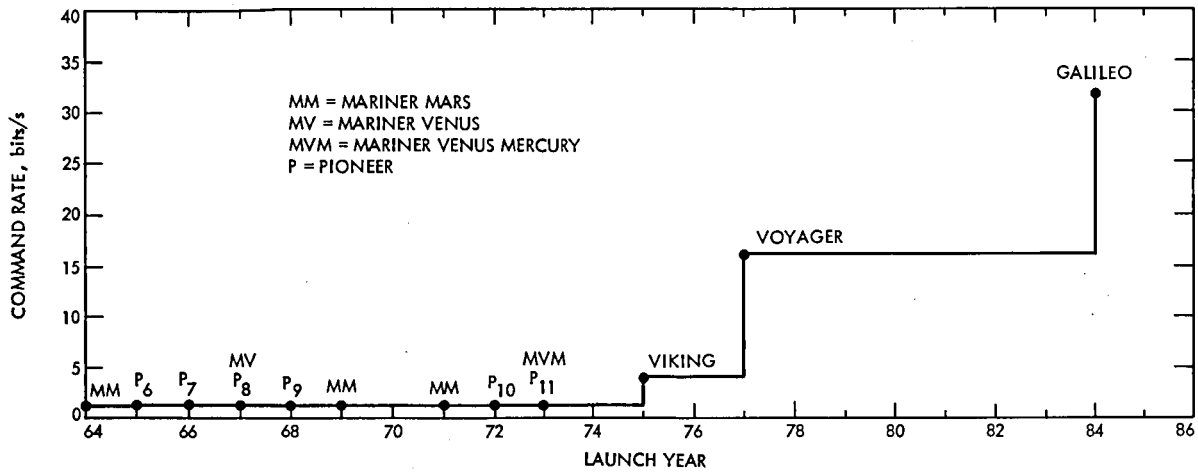

Fig. 7. Command rate vs launch year

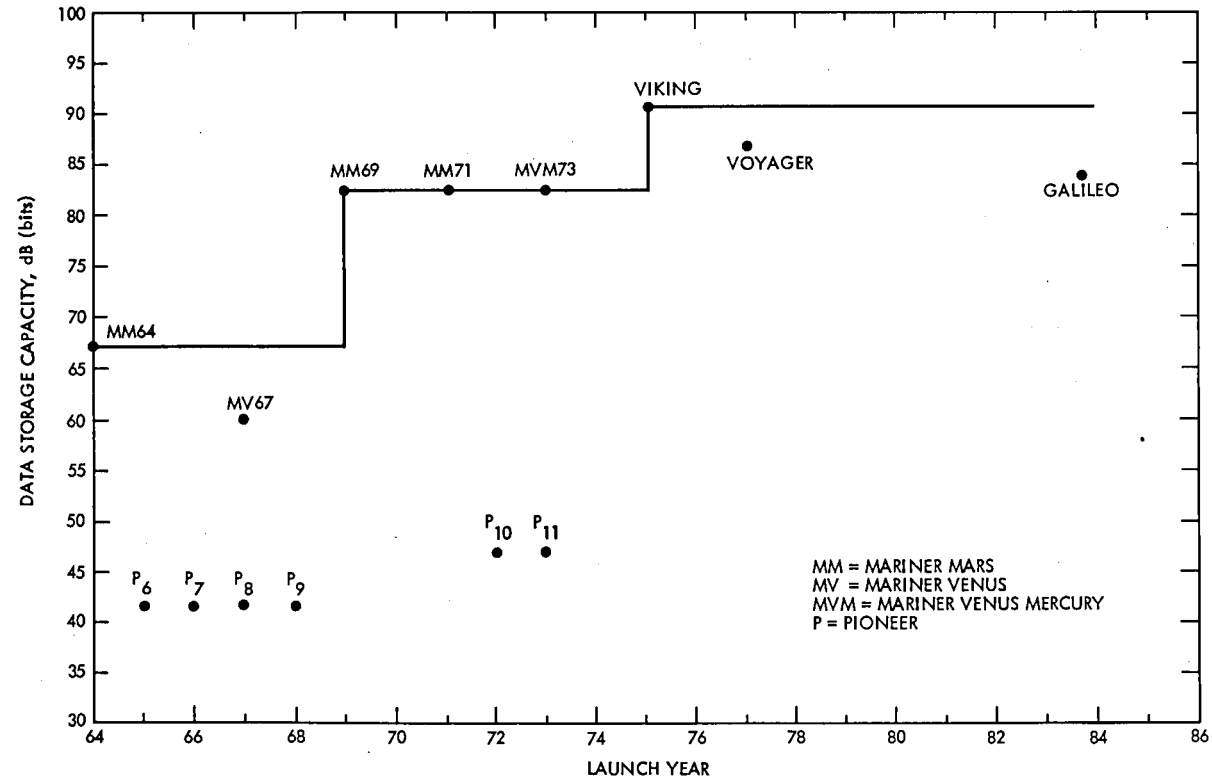

Fig. 8. Spacecraft data storage capacity vs launch year

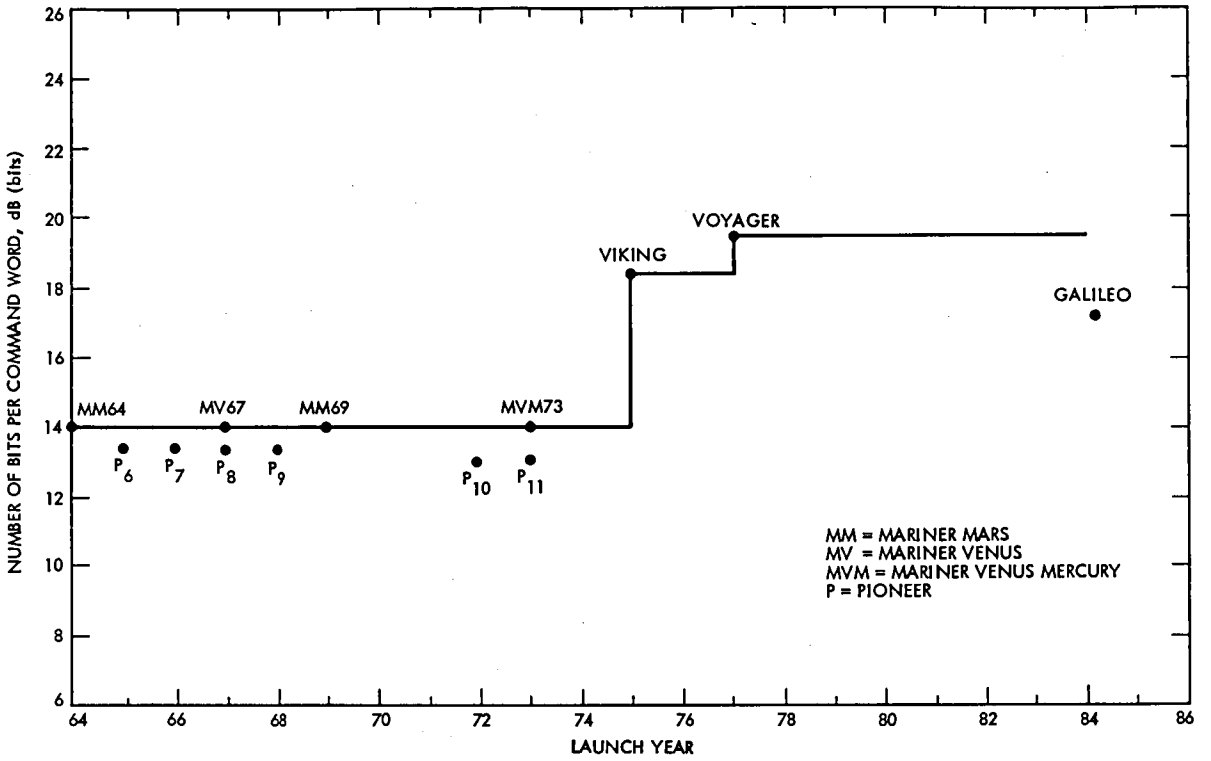

Fig. 9. Number of bits per command word vs launch year

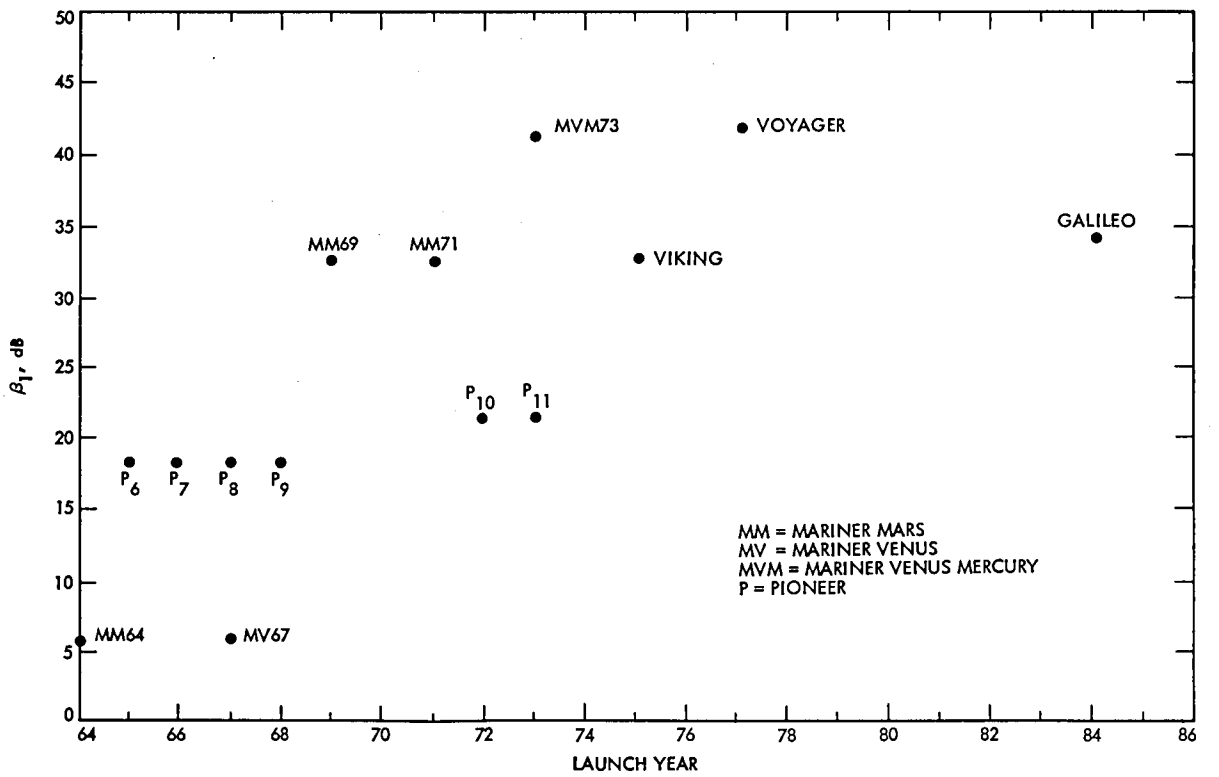

Fig. 10. Ratio β_1 vs launch year

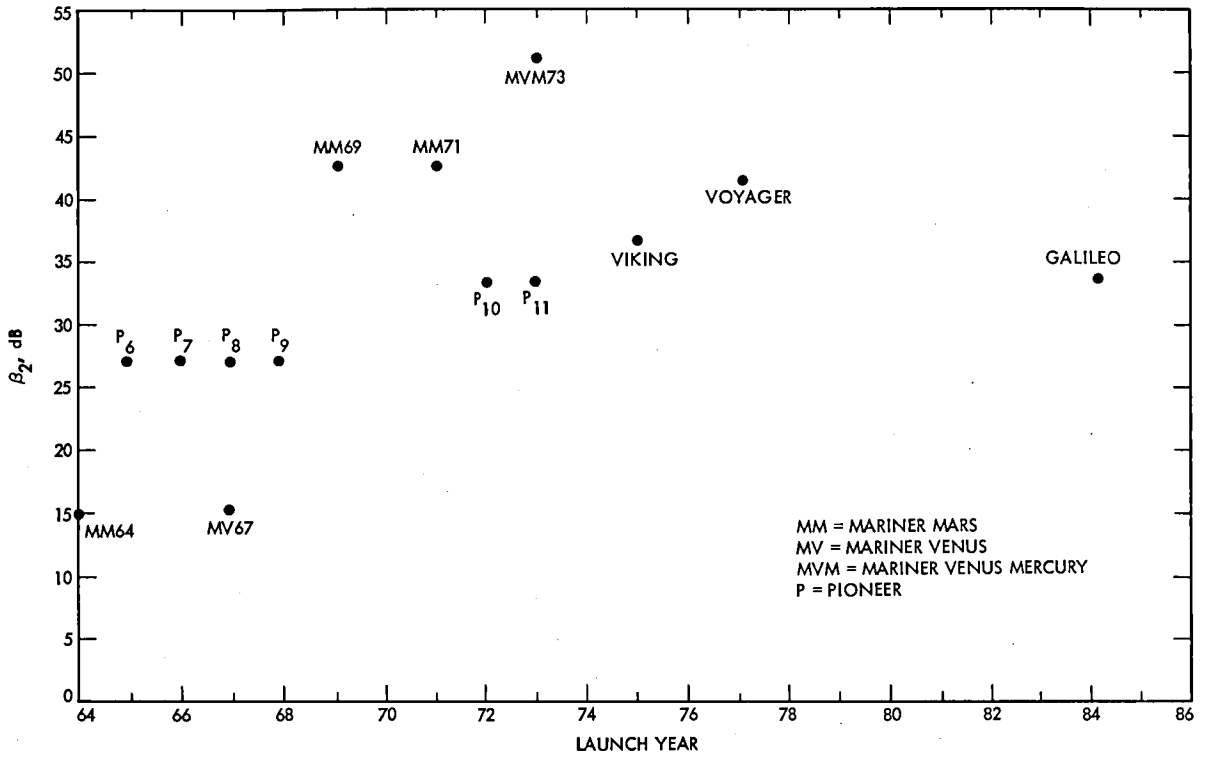

Fig. 11. Ratio β_2 vs launch year

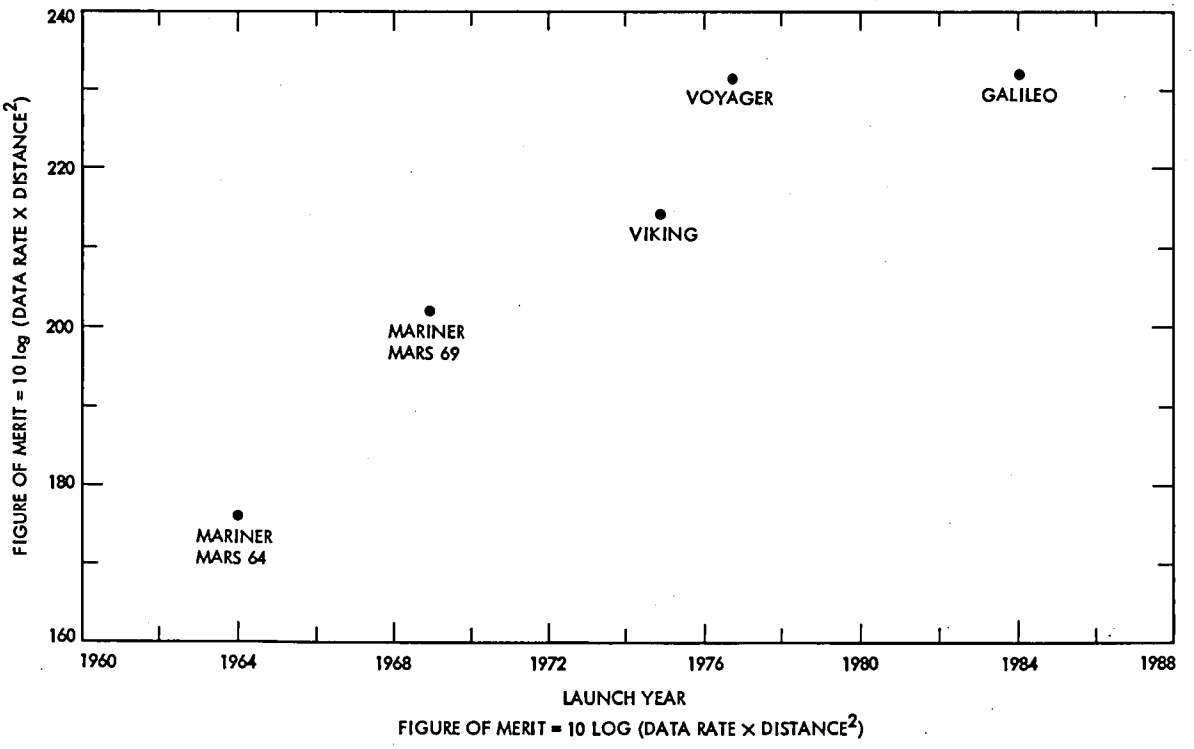

Fig. 12. Telemetering figure of merit vs launch year

Pioneer 10 and 11 Mission Support

R. E. Nevarez
Control Center Operations Section

The current estimate of the Deep Space Network (DSN) performance capability in tracking the Pioneer 10 and Pioneer 11 spacecrafts to the end of their projected life expectancy is given.

I. Introduction

Performance estimates based on measured performance indicate that a 64-meter station, using the existing 18.5-kelvin low-noise S-band cone, will be able to support the Pioneer 10 spacecraft through 1989. This is about 13 AU and 4 years further than previous estimates (Ref. 1) due to reduction of deletion rate requirements by Project.

The above 64-meter station configuration will support the Pioneer 11 spacecraft well beyond its predicted life expectancy.

II. Projected Spacecraft Life

Both Pioneers 10 and 11 are expected to have sufficient attitude control propellant (necessary for antenna pointing) out to 1990. The projected life expectancy is based upon when the Radioisotope Thermoelectric Generators (RTG) output has degraded to the minimum power for spacecraft operations of 76 watts. This degradation is expected to occur by 1990 for both spacecraft.

III. Telecommunications Limits for Pioneer 10 and Pioneer 11

The telecommunications limits as predicted in the downlink performance graphs (Figs. 1, 2, and 3) for each spacecraft indicate that the 64-meter station capability will exceed the life expectancy of the radioisotope thermoelectric generators.

Two cautions are in order with regard to estimating the end of both Pioneer 10 and 11 missions. The first is that the RTG life is only an estimate. Although the RTG performance has been following the updated prediction of its degradation for the past two years, it is possible for the rate of degradation to change. The second is to notice the leverage that a small uncertainty in dB has in both range and time for the telecommunications limit.

Acknowledgment

The downlink performance estimates were provided by Ursula Mayer of the Telemetry Performance Analysis Group.

Reference

1. Miller, R. B., "Pioneer 10 and 11 Mission Support," in *The Deep Space Network Progress Report 42-47*, pp. 21-25. Jet Propulsion Laboratory, Pasadena, Calif.

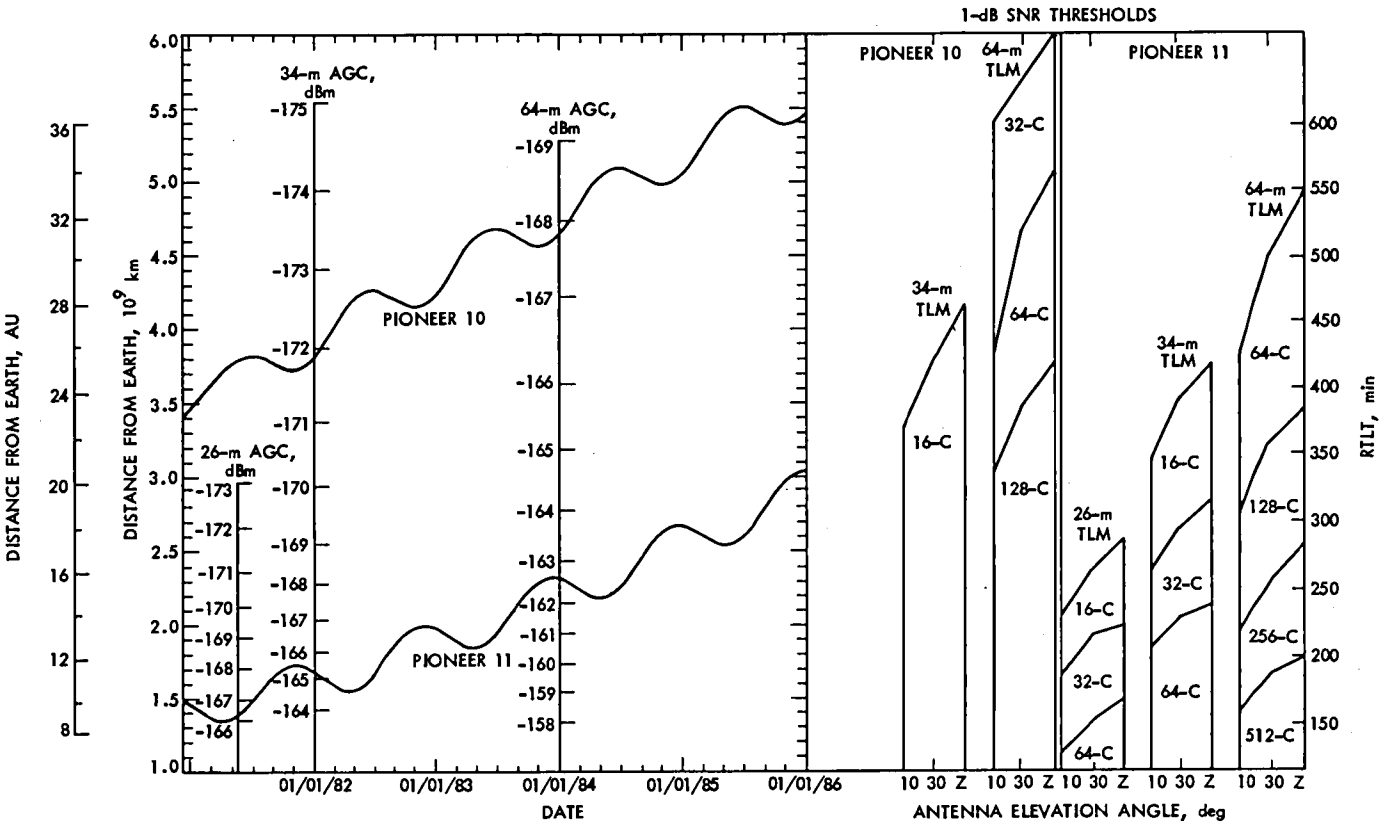

Fig. 1. Downlink performance estimates for 1982 through 1986

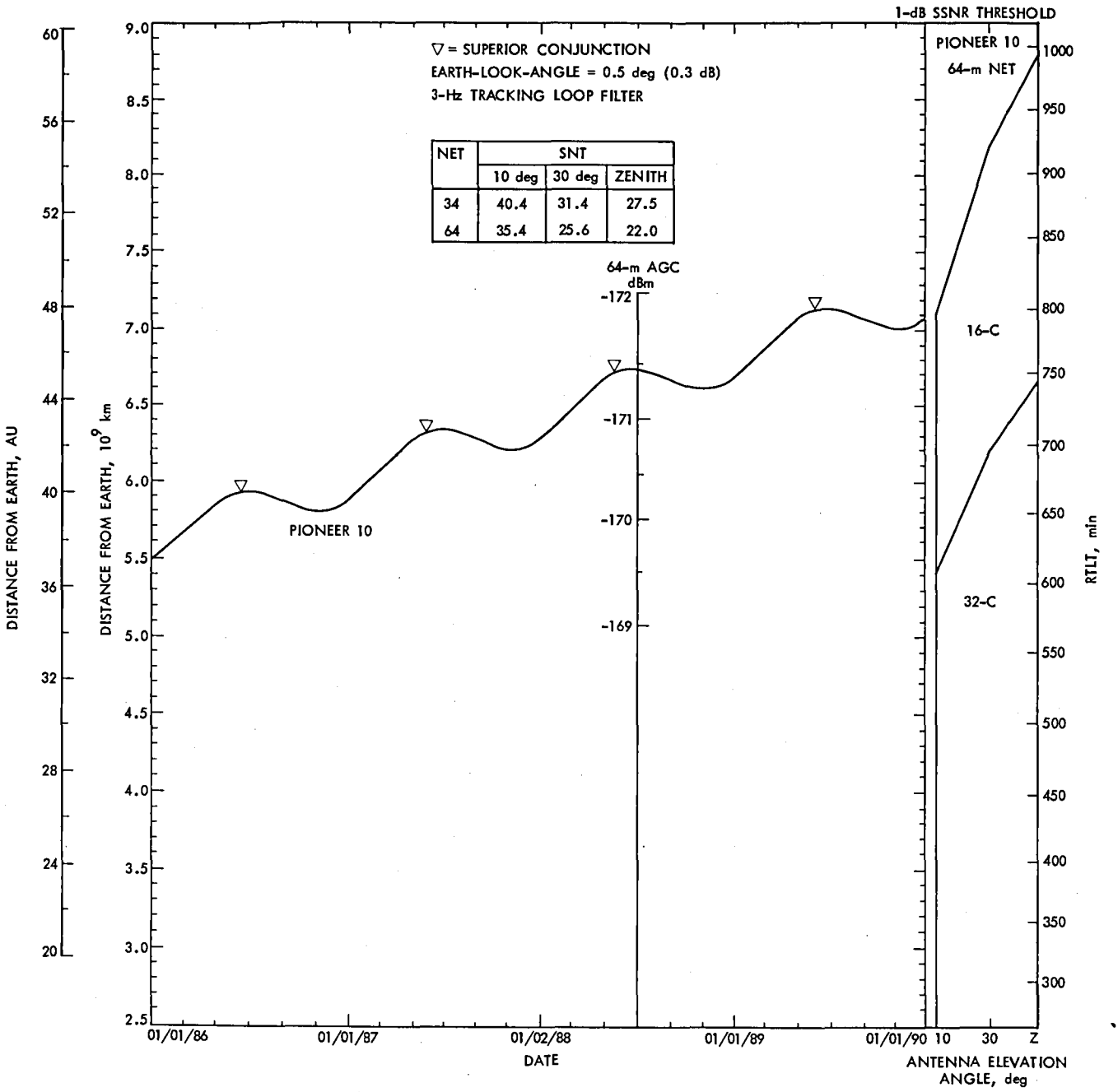

Fig. 2. Downlink performance estimates for Pioneer 10 for 1986 to 1990

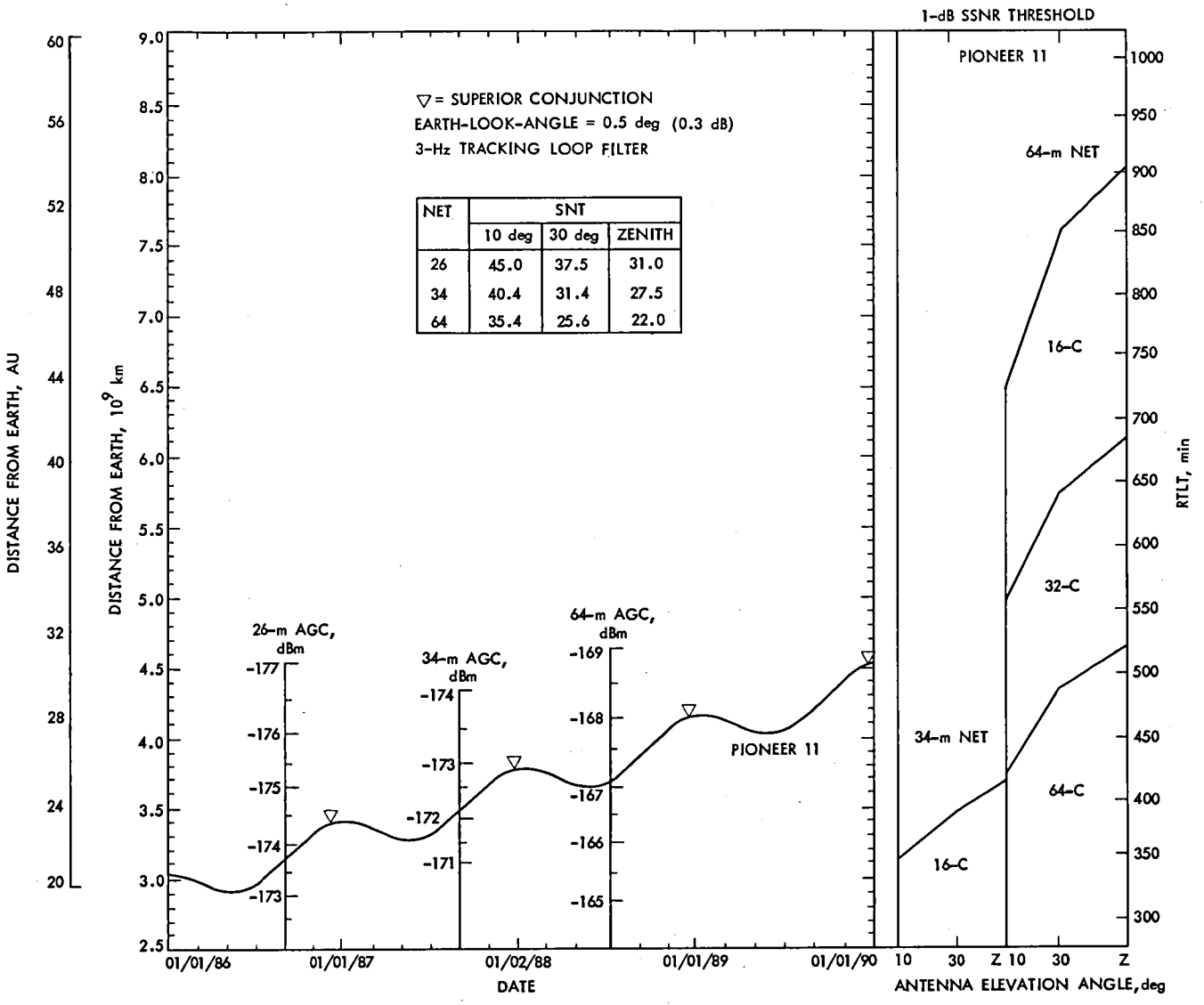

Fig. 3. Downlink performance estimates for Pioneer 11 for 1986 to 1990

Voyager Mission Support

N. Fanelli and H. Nance
Control Center Operations

This is a continuation of the Deep Space Network report on Tracking and Data Acquisition for Project Voyager. This article covers the period of November 1980.

I. Introduction

Voyager 1 completed the Far Encounter 2, Saturn Near Encounter and started the Post Encounter phase of its mission operation.

Voyager 2 continued in the Jupiter-Saturn Cruise Phase of its mission operations.

II. DSN Support

By both DSN and Voyager Project standards, the Deep Space Stations and Network Operations Control Team provided excellent professional support for the Voyager 1 encounter period.

A. Navigation Cycle

The Voyager 1 Far Encounter began with a dual Navigation Cycle. During a dual Navigation Cycle, each 64 meter station tracks the spacecraft at least twice with DSS 43 accomplishing three passes as this station starts and ends the cycle. This Navigation Cycle had the primary function of providing precise orbital determination data in preparation for a final trajectory correction prior to closest approach to Titan. During this Navigation cycle, all 34/64 meter stations tracked in an array configuration to improve telemetry data return of critical Optical Navigation and Imaging information while obtaining the radio metric data.

Near Simultaneous Ranging (NSR) was accomplished by DSS 63/43 during their common view period. A unique geometry, zero declination, existed at Saturn Encounter for Voyager. This geometry made it impossible to solve for the spacecraft declination by fitting doppler data as it is normally done in the orbit determination process. The alternate technique for deriving the declination is to use range data taken almost simultaneously from stations at widely separated latitudes and triangulating to solve for the declination angle. This dependence upon range data required that highly accurate range measurements and range delay calibration information be provided by the stations to the Navigators and Radio Scientists. To accomplish this, the stations were required to make numerous uplink transfers to provide data redundance for data confidence. The standard DSN transfer cannot be used for these NSR uplink transfers, since the normal tuning pattern changes the phase relationship of ground reference and received range codes, causing loss of range data from the transferring station for the round-trip light time (RTLT).

To avoid the loss of the NSR data, an alternative transfer tuning procedure is used. This procedure, upon completion of all required tuning, restores both the frequency and code

phase relationships required for good ranging through the RTLT following an uplink transfer. This procedure takes advantage of the programming and precision tuning capabilities of the synthesizer controllers available at the 34- and 64-meter stations. The procedure calls for both incoming and outgoing DSSs to execute precision symmetrical tuning patterns between specified limits, at fixed rates, and at specified times. Figure 1 depicts an NSR transfer and related events. It can be seen that the transfer requires four ramps to achieve the desired symmetrical tuning pattern. All ramps are done at the same rate, the initial direction of the first ramp being dependent upon whether the estimate of the spacecraft best-lock frequency corrected for doppler (XA) is above or below the Tracking Synthesizer Frequency (TSF). Since the XA is a doppler dependent frequency, it constantly changes; therefore, the frequency for any given transfer time is different. The total time to execute the entire transfer and tuning pattern is approximately five minutes.

B. Radio Science OVTs

On 3 and 4 November, the last Radio Science Operational Verification Tests (OVTs) were conducted with DSS 43 and 63, one station on each day. These OVTs included the changes in countdown procedures, calibration parameters, and configuration requirements as revealed by the previous OVTs. The OVTs also included a voice interface capability between the Radio Science (RS) Team at JPL and the DSN Radio Science representative at DSS 43 and 63. It was deemed advisable to have a representative from JPL at the stations during the critical RS activity to assist the station personnel and to interface with the RS Team to discuss problems and requirements in real-time. This interface was limited to six areas of operation:

(1) Selection of ODA predict sets.

(2) Selection of ODA time offsets.

(3) Selection of ODA frequency offsets.

(4) Selection of SSI display channels.

(5) Initiating, extending, and restarting ODA run/idle modes.

(6) Selection of PPM Noise diode and integration times.

On 5 November, the RS ORT #5 was conducted with both DSS 43/63. This ORT simulated the Saturn Encounter Operation within the station overlap period. The ORT required the configuration as specified for the upcoming encounter and the data requirement applicable for the actual period. The ORT was a success and the stations declared ready for the occultation experiments.

C. TCM-A9

On 6 November, a Trajectory Correction Maneuver (TCM-A9) was performed to provide the necessary adjustment to the spacecraft flight path to ensure the closest approach to Titan without danger of impacting the satellite. The maneuver required the spacecraft to rotate off earth point, resulting in a loss of the downlink while the TCM "burn" was being accomplished. After the trajectory change, the spacecraft returned to earth point. DSS 63 had prepared their high-power transmitter for emergency support. The high-power transmitter would provide an added probability of commanding the spacecraft to the proper orientation if required. However, DSS 63 reacquired the downlink at the appropriate time, and data evaluation confirmed the maneuver was a success.

D. Post-TCM Navigation Cycle

On 7-10 November, a post-TCM dual navigation cycle was supported to provide the new trajectory information for orbit determination. During this Navigation Cycle NSR were conducted by DSS 14/43 and DSS 14/63 during each common view period for the more precise zero declination information. Arraying by the 34/64 meter stations was likewise accomplished during their tracking periods. Optical navigation pictures to provide additional refinement were periodically received during the period.

E. Cyclic Phase

On 10 November, the spacecraft data mode entered the encounter cyclic phase during which the telemetry formats and bit rates changed frequently. This mode allowed the several different imaging formats, playback of recorded data and various general science formats to be transmitted in bit rates from 19.2 through 44.8 kbps in rapid succession. This mode required the stations to be alert to the sequence and reinitialize the TPAs for the bit rate changes to insure that the telemetry strings were locked up and good data was processed without undue delay. This mode of operation continued throughout the closest encounter period.

F. Contingency Operation

On 11 November (DOY 316) at 1125Z, with the acquisition of Voyager 1 by DSS 14, the requirement was imposed on the 64-meter network to countdown the high power transmitter (100 kW) and have it on standby for contingency operation. Under these circumstances, the 64-meter stations performed their normal uplink functions with the normal transmitter, using 10 kW uplink power from the 20 kW transmitter, with the option at the request of the Project to

switch to the backup high power transmitter to support contingency plans. This requirement continued until 14 November (DOY 319) at 2115Z with the conclusion of the DSS 14 tracking period. No problems were encountered that required the implementation of contingency plans.

G. Titan Encounter

On 11 November, preparations began for the closest approach of Titan. One of the first actions was to reorient the spacecraft tracker from Canopus to Miaplacidus to avoid obscuration of Titan. This reorientation was accomplished by a roll turn while completing a Fields and Particles Measurement. This maneuver required DSS 14/12/43/42 to track the downlink carefully in case the spacecraft did not complete the proper reference and the downlink became lost. Although the signal fluctuated, the stations maintained lock and the maneuver was completed successfully.

The Radio Science Experiment with the Titan occultation was diametric so as to allow the deepest possible atmospheric penetration of the ray path to Earth. The duration of the occultation was only 12 minutes. The objectives were:

(1) Measure atmospheric temperature and pressure as a function of height and contribute to the determination of atmospheric constituents.

(2) Investigate the microwave absorbing properties of the atmosphere.

(3) Determine ionospheric profiles and plasma densities at the entrance and exit location on Titan.

(4) Measure the radius of the solid surface and help determine the mean density of Titan.

The ground events for the occultation occurred primarily at DSS 63. However, DSS 62 provided S-band, closed-loop occultation backup coverage and DSS 61 performed dual-frequency, closed-loop tracking of Voyager 2 in order to obtain independent measurements of the solar plasma for calibration of the occultation data. DSS 63 tracked Voyager 1 with CONSCAN OFF and a fixed subreflector focus position so as to remove station-induced signal variations. The downlink was recorded on the mediumband, open-loop receiver system in the two-channel configuration. Ionospheric data was obtained from the closed-loop receiver system. A signal profile was provided by the Project and during the operation it was found to be fairly accurate.

H. Saturn Encounter

On 13 November, the closest approach to Saturn was made. Again, the major activity was concerned with radio science occultation data. The occultation began approximately 100 minutes after Saturn's closest approach and lasted for about 90 minutes. The spacecraft performed a limb-tracking maneuver for the majority of the occultation, with the spacecraft orientation not being changed for a 35 minute period for the benefit of the UVS Sun occultation exit measurement. The limb-tracking maneuver was designed to keep the high-gain antenna pointed at the virtual image of the Earth, as that image moves around the limb of Saturn. (The virtual image of the Earth is that point where, at a given time, the radio raypath can be refracted around Saturn and back to Earth.)

The objectives of the Saturn occultation experiment were to:

(1) Measure atmospheric temperature and pressure as a function of height and help determine the hydrogen-to-helium ratio.

(2) Investigate the microwave-absorbing properties of the atmosphere and determine the ammonia abundance.

(3) Determine the structure and characteristics of Saturn's ionosphere.

(4) Measure the oblateness of Saturn.

(5) Investigate turbulence and waves in the neutral atmosphere.

(6) Investigate ionospheric irregularities.

(7) Interpret the measured dynamics for indications of large-scale motion and energy flow in the atmosphere and ionosphere.

The ground events for the Saturn occultation occurred primarily at DSS 43 for the entrance measurement and at DSS 63 for the exit measurement. Due to general mission planning considerations and science trade-offs, which were made during the trajectory-selection process, DSS 43 set time was about one minute before occultation exit and DSS 63 rise was about halfway through the occultation. This geometry necessitated the special low elevation tracking procedure designed to maintain accurate pointing during the period of extreme signal dynamics. DSS 43 continued to track after the antenna pre-limit was reached and DSS 63 was on point at antenna pre-limit prior to exit occultation. DSS 44 and DSS 62 provided S-band, closed-loop receiver occultation backup coverage and DSS 42 and DSS 61 performed dual-frequency, closed-loop receiver tracking of Voyager 2 to obtain independent measurements of the solar plasma for calibration of the occultation data. DSS 43 and DSS 63 tracked Voyager 1 with CONSCAN OFF and a fixed subreflector focus position so as to remove station-induced signal variations from the data. The occultation downlink was recorded on the medium-band, open-loop receiver system at DSS 63. Ionospheric data was

obtained from the closed-loop system. The signal profile provided by the Project for the occultation did not prove to be as accurate during operations as did the one for Titan.

I. Ring Occultation

Immediately following the Saturn occultation exit was the ring occultation. The ring occultation lasted from the atmosphere of Saturn until exit from "F" ring (outermost visible ring) occultation. The duration of the ring occultation measurements was approximately 27 minutes.

The objectives of the ring occultation experiment were to:

(1) Map the optical depth of the rings at two radio wavelengths versus radial distance with high (less than 100 km) radial resolution.

(2) Determine the predominant particle size.

(3) Determine the number of particles per unit area and thus the mass of the rings.

The spacecraft high-gain antenna remained pointed at Earth for the duration of the ring occultation and the downlink configuration was a continuation of the Saturn occultation exit; X-band high power, S-band lower power, ranging channels OFF, telemetry drivers OFF, and TWNC ON. The primary ground events were supported by DSS 63 while DSS 62 provided S-band, closed-loop backup coverage and DSS 61 tracked Voyager 2 for the solar plasma calibration. Open-loop receiver recording was performed by DSS 63; however, a different configuration was used. Since polarization information was a primary data source, both RCP and LCP channels for S/X-band downlink were recorded. Also, these signals were recorded on the medium bandwidth system because large frequency dispersions were encountered. Closed-loop receiver system lock-up was not possible during the ring occultation.

J. Ring Scattering Experiment

A ring-scattering experiment was conducted during a period of approximately 100 minutes after completion of the ring occultation measurements. The spacecraft was maneuvered so as to track the center of the "A" ring with the HGA boresight.

The objective of this experiment was to:

(1) Determine ring particle size and size dispersion in the decimeter to meter size range.

(2) Determine the vertical structure of the rings.

During the ring-tracking maneuver the HGA was 12 DEG off-Earth point and required precise tracking operation. After return to Earth point a mini-ASCAL was supported by the tracking station. All the ground events were supported by DSS 63 in the configuration as used for the ring occultation measurements.

K. UVS Maneuver

On 22-23 November, an ultraviolet vertical scan maneuver was performed. The purpose of this maneuver was to align the long axis of the UVS instrument parallel to the ring plane. This was accomplished by performing yaw turns. The objective was to determine if a gas torus existed around Titan, and if so, to measure its extent.

During this maneuver the spacecraft was again off Earth point and downlink telemetry was lost. The maneuver took approximately 20 hours, during which a no data condition existed. DSS 14 supported the loss of data by tracking the signal with the SSI and supported the reacquisition of the downlink again making an early search with the SSI. The maneuver was successful and DSS 14 acquired the signal slightly after predicted time. DSS 61 and DSS 12 were backup to DSS 14 and acquired the downlink at the predicted time.

L. Post Encounter

Activities of 23-30 November settled into a routine of IRIS composition measurements, radio emission studies, plasma wave instability measurements, celestial mechanics studies, removal of residual measurements, coverage of Saturn's illuminated crescent, system scans, intensity of emission from Titan's orbit, and six-level system scan covering Titan's entire orbit. These data were received by the stations in either the real-time or playback modes during the normal scheduled tracking periods.

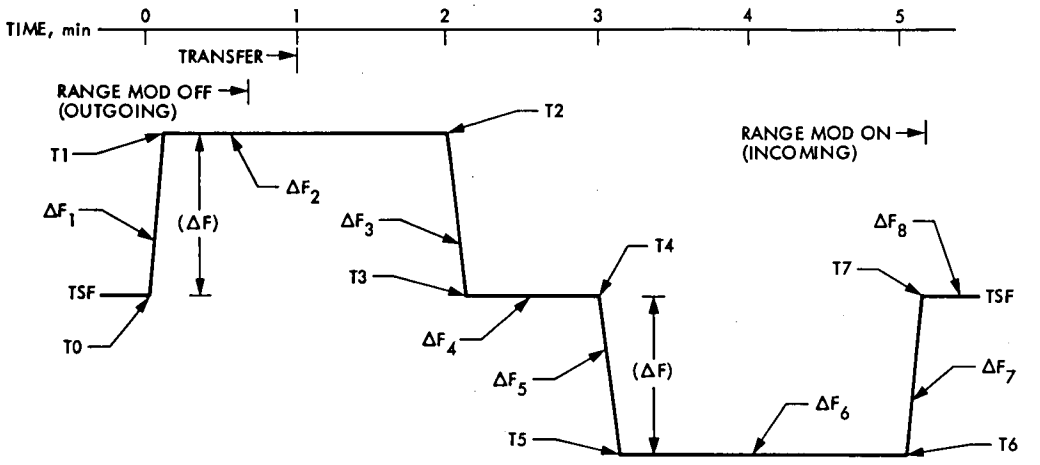

ΔF_1 = XA (OF TRANSFER) - TSF, COMPUTED TO ONE TENTH Hz
ALL TUNING RATES ARE 5 Hz/DC sec
T0 = TIME OF TRANSFER - 1 min
T2 = TIME OF TRANSFER + 1 min
T4 = TIME OF TRANSFER + 2 min
T6 = TIME OF TRANSFER + 4 min
PRA MUST NOT BE INTERRUPTED REGARDLESS OF TRANSMITTER OR RANGE MOD STATUS
DOPPLER SAMPLE INTERVAL = 10 sec
RECEIVER BANDWIDTHS SET 30 Hz-WIDE, NO TUNING AT TRANSFER REQUIRED
TRANSFERS TO OCCUR ON 35 min CENTERS

Fig. 1. An NSR transfer and its related events

A Binary Coherent Optical Receiver for the Free-Space Channel

V. A. Vilnrotter
Telecommunications Systems Section

The free-space channel is an ideal medium for communicating by means of spatially and temporally coherent optical fields. Here we derive the structure of a maximum a-posteriori optical homodyne receiver for binary antipodal signals. The effects of background radiation and phase referencing errors on receiver performance are also examined. It is shown that this receiver structure is relatively insensitive to random phase errors, while moderate background radiation has virtually no effect on receiver performance.

I. Introduction

The structure of a binary optical receiver for processing spatially and temporally coherent optical fields is derived, based on the maximum a-posteriori (MAP) decoding criterion. The effects of background radiation and phase error on receiver performance are also examined. The receiver structure is shown in block diagram form in Fig. 1. The received field $f_r(t)$ is assumed to be in the form of a coherent plane wave. The optical antenna consists of a lens (or properly shaped mirror) of total collecting area $(A_r + A_e)$, which focuses the captured field towards the active surface of the photodetector. A fraction of the captured field is diverted to the phase-estimator subsystem by the beam splitter B_1, with power transmission factor $T_1 = A_r/(A_r + A_e)$, while only a negligible fraction of the received field is lost in propagating through the beam splitter B_2 (power transmission factor $T_2 \leqslant 1$), which is used to spatially combine the received and local fields. The total signal power reaching the detector therefore appears to have been collected by an effective collecting area A_r. The output of the phase estimator subsystem is a continuous estimate of the received phase, $\hat{\phi}_r(t)$, which is used to control the phase of the local laser. The local optical field combines with the received field on the surface of B_2 and the sum field, composed of the reflected portion of the local field and the transmitted part of the received field, propagates to the active surface of the photodetector. Even though only a small fraction of the local field is reflected by B_2, this is usually of little concern since generally ample local power is available. It is further assumed that the local field is processed so that the spatial distribution of the local and received fields over the detector surface are identical.

It is well known that if the amplitude of the local field is sufficiently great, then the effects of thermal noise generated within the receiver are suppressed, and shot-noise limited operation is achieved (Ref. 1). Assuming arbitrarily large detector bandwidth, the detector output can therefore be modelled as a point process with average rate determined entirely by the optical power of the detected local and received fields. An optical filter (with bandwidth $\Delta\nu$ Hz), a polarizer, and a spatial filter are also employed to reduce the intensity of the background radiation reaching the photodetector. To minimize the average bit-error probability, the output of the photodetector is processed by a MAP decoder. The decoder structure derived here is the MAP decoder only for the

case of negligible phase error and background radiation. However, the performance of this receiver in the presence of random phase errors and background fields will also be examined.

II. MAP Receiver Structure

The received optical field is assumed to be in the form of a linearly polarized plane wave, normally incident on the receiver aperture. Therefore it can be represented entirely in terms of its temporal characteristics as

$$f_r(t) = a_r\, p(t) \exp\,[j(\omega t + \phi_r(t))] \tag{1}$$

where $p(t) = (-1)^{i+1}$, $i = 0, 1$ over the interval $(0, \tau)$, a_r is the real received field amplitude, ω is the radian frequency of the optical field, and $\phi_r(t)$ is a random phase process due to phase instabilities within the transmitter laser. The local field can be referred back to the receiver aperture and represented as

$$f_L(t) = a_L \exp\,[j(\omega t + \phi_L(t))] \tag{2}$$

where again a_L is the (real) local field amplitude and $\phi_L(t)$ is a random phase process due to phase variations within the local laser.

The photodetector responds to the total optical power collected over its active surface. The count intensity at the output of the photodetector is due to the total power generated by the sum of the received and (equivalent) local fields over the receiver aperture (with effective collecting area A_r), and can be represented as

$$n(t) = \alpha A_r |f_r(t) + f_L(t)|^2 = \alpha A_r \left\{a_L^2 + a_r^2 + 2a_L a_r p(t) \cos \phi_e(t)\right\} \tag{3}$$

where $\alpha = \eta/h\nu$ (η is the detector quantum efficiency, h is Planck's constant, and $\nu = \omega/2\pi$ is the optical frequency) and $\phi_e(t) = \phi_r(t) - \phi_L(t)$ is defined as the phase-error process. If a sufficiently small phase-error can be maintained, then we can let $\cos \phi_e(t) \cong 1$. Since $p(t)$ takes on the values ± 1 (depending on the binary hypothesis), the count-intensity is seen to be the sum of a constant count-rate due to the local and received fields, and a hypothesis-dependent rate that is either added to or subtracted from the constant level. If background radiation can be ignored, then the total count over each synchronous τ-second signaling interval can be modeled as a Poisson random variable, with average count

$$K_i = \alpha A_r \int_0^\tau n(t|H_i)\, dt = \alpha A_r \tau \left\{a_L^2 + a_r^2 + 2(-1)^{i+1} a_L a_r\right\}; \quad i = 0, 1 \tag{4}$$

where H_i denotes the i-th hypothesis.

It is well known that the bit-error probability is minimized if a maximum a-posteriori (or MAP) decoding strategy is employed. For equilikely hypotheses, the MAP decoder decides on the basis of the log-likelihood test

$$\ell n[P(k|H_0)] \underset{H_1}{\overset{H_0}{\gtrless}} \ell n[P(k|H_1)] \tag{5}$$

where k is the observed count, with probability density

$$P(k|H_i) = \frac{K_i^k}{k!} e^{-K_i} \tag{6}$$

and the average counts K_i are defined by Eq. (4). Substituting Eqs. (4) and (6) into Eq. (5) yields the test

$$k \ln K_0 - K_0 \underset{H_1}{\overset{H_0}{\gtrless}} k \ln K_1 - K_1 \tag{7}$$

or, equivalently

$$k \underset{H_0}{\overset{H_1}{\gtrless}} \frac{K_1 - K_0}{(\ln K_1 - \ln K_0)} \triangleq T_h \tag{8}$$

Equation (8) is seen to be a simple threshold test. The MAP decoder therefore observes the total count at the end of each τ-second interval, and selects on the basis of a threshold comparison. Note that for $a_r << a_L$ (which is generally the case) we can write

$$\ln K_1 - \ln K_0 = \ln \left(1 + \frac{2a_r}{a_L}\right) - \ln \left(1 - \frac{2a_r}{a_L}\right) \approx \frac{4a_r}{a_L} \tag{9}$$

from which it follows that

$$T_h = \alpha A_r a_L^2 \tau \tag{10}$$

Therefore, the threshold is the average count due to the local field over the counting interval.

The performance of the binary homodyne MAP receiver can be obtained by summing the count random-variables above and below threshold. Assuming that T_h is not integer-valued, and defining ε as the greatest integer contained in T_h, the average bit-error probability becomes

$$P(E) = \frac{1}{2}\left[\sum_{k=\varepsilon+1}^{\infty} \frac{K_0^k}{k!} e^{-k_0} + \sum_{k=0}^{\varepsilon} \frac{K_1^k}{k!} e^{-K_1}\right] = \frac{1}{2}\left[\frac{\Gamma(1+\varepsilon, K_1)}{\varepsilon!} + \frac{\gamma(1+\varepsilon, K_0)}{\varepsilon!}\right] \tag{11}$$

where

$$\Gamma(a, x) = \int_x^{\infty} e^{-t_t(a-1)}\, dt$$

and

$$\gamma(a,x) = \int_0^x e^{-t_t(a-1)}\,dt$$

This expression does not yield to further simplification by analytic means. However, we can invoke the Central Limit Theorem, and argue that since the average counts K_i are large, each observed count can be considered the sum of a large number of independent Poisson random variables, and therefore we can approximate the discrete sums in Eq. (11) by integrals of the normal density (with mean and variance K_i). Defining the random variables y_i as

$$y_i = \frac{x_i - K_i}{\sqrt{K_i}}; \quad i = 0, 1 \tag{12}$$

we obtain

$$P(E) = \frac{1}{2}\left[\sum_{i=0}^{1} \int_{T_{hi}}^{\infty} \frac{e^{-y_i^2/2}}{\sqrt{2\pi}}\,dy_i\right] \tag{13}$$

$$T_{hi} = (-1)^i \frac{T_h - K_i}{\sqrt{K_i}} \simeq \sqrt{4K_S} \tag{14}$$

where we again assumed that $a_r/a_L \ll 1$ and $K_S = \alpha A_r a_r^2 \tau$ is the average count due to the signal field. This expression can be written in terms of the function $Q(u)$, where

$$Q(u) = \frac{1}{\sqrt{2\pi}} \int_u^{\infty} e^{-\beta^2/2}\,d\beta \tag{15}$$

Substituting Eq. (15) into Eq. (13) yields

$$P(E) \simeq Q\left(\sqrt{4K_S}\right) \tag{16}$$

It is clear, therefore, that when background radiation and phase estimation errors can be neglected, the performance of the homodyne receiver depends exponentially on the sum of the count-energies in the binary signals, $2K_s$. This can be seen from the asymptotic upper bound

$$Q(u) \leqslant (2\pi u^2)^{-1/2} e^{-u^2/2} \tag{17a}$$

or

$$Q\left(\sqrt{4K_s}\right) \leqslant (8\pi K_s)^{-1/2} e^{-2K_s} \tag{17b}$$

Receiver performance for the ideal case discussed here is shown in Fig. 2. Next we examine the effects of background fields on receiver performance.

III. The Effects of Background Fields on Receiver Performance

To assess the effects of background radiation on receiver performance, we shall represent the background radiation in complex form as (Ref. 2):

$$b(t) = [B_c(t) - jB_s(t)]\, e^{j\omega t} \tag{18}$$

where $B_c(t)$ and $B_s(t)$ are uncorrelated, zero mean, narrowband Gaussian noise envelopes with two-sided spectral level N_0. If the optical detector is preceded by a narrowband optical filter of bandwidth $\Delta\nu$ Hz, then the first and second moments of the noise field become

$$E[b(t)] = 0 \tag{19a}$$

$$E[|b(t)|^2] = E[B_c^2(t)] + E[B_s^2(t)] = 2N_0\Delta\nu \tag{19b}$$

For homodyne detection, the detector responds to the total optical power generated by the sum of the local, received, and background fields. Assuming that phase-errors can be neglected, and that the amplitude of the local field is much greater than either the amplitude of the received field or the standard deviation of the noise field (collected in a single spatial mode) the count-intensity at the detector's output can be represented as

$$n(t) = \alpha A_r |a_L + a_r p(t) + B_c(t) - jB_s(t)|^2 \simeq \alpha A_r\, [a_L^2 + 2a_L\, (a_r p(t) + B_c(t))] \tag{20}$$

The use of a narrowband optical filter generally ensures the validity of this approximation. It is apparent therefore that with negligible phase-error, the detector responds to the local field, the signal field, and the in-phase component of the noise envelope. The average count at the end of each τ-second signaling interval is the time-integral of the count-intensity process

$$K_i = \alpha A_r a_L^2 \tau + (-1)^{i+1}\, 2a_L a_r \tau \alpha A_r + y \tag{21}$$

where we define the (Gaussian) random variable y as the integral of the background-induced noise process

$$y = 2\alpha a_L A_r \int_0^\tau B_c(t)\, dt \tag{22}$$

Clearly, $E[y] = 0$. The variance can be evaluated by writing y^2 as a product of integrals, and taking the expectation over the integrand:

$$E[y^2] = 4\alpha^2 a_L^2 A_r^2 \int_0^\tau d\zeta_1 \int_0^\tau d\zeta_2 E\,[B_c(\zeta_1)\, B_c(\zeta_2)] = 4\alpha^2 a_L^2 A_r^2 \int_0^\tau d\zeta_1 \int_0^\tau d\zeta_2 R_c(\zeta_1 - \zeta_2) \tag{23}$$

where we define the autocorrelation function $R_c(\zeta)$ as

$$R_c(\zeta) = N_0 \int_{-\Delta\nu/2}^{\Delta\nu/2} e^{j2\pi f\zeta}\, df = N_0 \Delta\nu \left[\frac{\sin(\pi\Delta\nu\zeta)}{\pi\Delta\nu\zeta}\right] \tag{24}$$

Letting $\zeta = \zeta_1 - \zeta_2$, Eq. (23) can be rewritten as

$$E[y^2] = 4\alpha^2 a_L^2 A_r^2 \tau \int_{-\tau}^{\tau} \left(1 - \frac{|\zeta|}{\tau}\right) R_c(\zeta)\, d\zeta \simeq 4\alpha^2 a_L^2 A_r^2 \tau \int_{-\infty}^{\infty} R_c(\zeta)\, d\zeta = 4\alpha^2 a_L^2 A_r^2 \tau N_0 \triangleq \sigma_y^2 \tag{25}$$

In evaluating the first integral of Eq. (25), we made use of the fact that the coherence-time of the noise envelope is much smaller than the signaling interval, τ.

The performance of the homodyne receiver can be evaluated by again invoking the Central Limit Theorem, approximating the sum of the Poisson density (conditioned on y) by a properly defined integral of the normal density, and averaging over the density of y. Since y is Gaussian with zero mean and variance σ_y^2, the average bit error-probability becomes

$$P(E) = \frac{1}{2} \int_{-\infty}^{\infty} dy\, \frac{e^{-y^2/2\sigma_y^2}}{\sqrt{2\pi\sigma_y^2}} \left\{ \int_{T_{h1}}^{\infty} \frac{e^{-(x_1 - (T_h - m + y))^2/2(T_h - m + y)}}{\sqrt{2\pi(T_h - m + y)}}\, dx_1 \right.$$

$$\left. + \int_{-\infty}^{T_{h2}} \frac{e^{-(x_2 - (T_h + m + y))^2/2(T_h + m + y)}}{\sqrt{2\pi(T_h + m + y)}}\, dx_2 \right\} \tag{26}$$

where

$$m = 2\alpha A_r \tau a_L a_r$$

$$T_{h1} = (m - y)/\sqrt{T_h - m + y}$$

$$T_{h2} = (-m - y)/\sqrt{T_h + m + y}$$

If we make the change of variables

$$z_1 = \frac{x_1 - (T_h - m + y)}{\sqrt{T_h - m + y}} \tag{27a}$$

$$z_2 = \frac{x_2 - (T_h + m + y)}{\sqrt{T_h + m + y}} \tag{27b}$$

then Eq. (26) can be written as

$$P(E) = \frac{1}{2}\int_{-\infty}^{\infty} dy \frac{e^{-y^2/2\sigma_y^2}}{\sqrt{2\pi\sigma_y^2}} \left\{ Q\left(\frac{m-y}{\sqrt{T_h}\left(1+\frac{m+y}{T_h}\right)^{1/2}}\right) + Q\left(\frac{m+y}{\sqrt{T_h}\left(1-\frac{m-y}{T_h}\right)^{1/2}}\right)\right\} \tag{28}$$

where $Q(\cdot)$ is defined in Eq. (15).

The $Q(\cdot)$ functions can be expanded as

$$Q_1 \triangleq Q\left(\frac{m-y}{\sqrt{T_h}\left(1-\frac{m-y}{T_h}\right)^{1/2}}\right) = Q\left(\frac{m-y}{\sqrt{T_h}}\left[1+\frac{m-y}{2T_h}+\cdots\right]\right) \tag{29a}$$

$$Q_2 \triangleq Q\left(\frac{m+y}{\sqrt{T_h}\left(1+\frac{m+y}{T_h}\right)^{1/2}}\right) = Q\left(\frac{m+y}{\sqrt{T_h}}\left[1-\frac{m+y}{2T_h}+-\cdots\right]\right) \tag{29b}$$

Note that $(m \pm y)/\sqrt{T_h}$ is a function of a_r, but not of (a_r/a_L), while $(m \pm y)/T_h$ is a function of (a_r/a_L). If we hold a_r fixed, then as $(a_r/a_L) \to 0$, $(m \pm y)/T_h \to 0$ as well, whereas $(m \pm y)/\sqrt{T_h}$ remains constant. Therefore, as $(a_r/a_L) \to 0$, the bracketed term on the right-hand side approaches one, i.e.,

$$\left[1 \pm \frac{m \mp y}{2T_h} + \cdots\right] \to 1 \tag{30}$$

and the approximations

$$Q_1 \simeq Q\left(\frac{m-y}{\sqrt{T_h}}\right) \tag{31a}$$

$$Q_2 \simeq Q\left(\frac{m+y}{\sqrt{T_h}}\right) \tag{31b}$$

become valid. Note that these are exactly the results we would have obtained if the inner integrals in Eq. (26) were integrals of Gaussian random variables with mean $(T_h \pm m + y)$, and variance T_h. Substituting Eq. (31) into (28), averaging over y, and making use of Eqs. (10) and (25) yields the limiting form

$$P(E) \simeq Q\left(\sqrt{\frac{m^2}{T_h\left(1+\frac{\sigma_y^2}{T_h}\right)}}\right) = Q\left(\sqrt{\frac{4K_s}{1+4\alpha A_r N_0}}\right) \tag{32}$$

in the limit as $(a_r/a_L) \to 0$.

It is perhaps more meaningful to relate receiver performance to the noise-field parameter $K_b = 2\alpha A_r N_0 \Delta\nu\tau$, which is defined as the average number of counts generated by a multimode noise field at the output of a direct-detection receiver with effective collecting area A_r. When expressed in terms of K_b, the error probability of the homodyne receiver becomes

$$P(E) \simeq Q\left(\sqrt{\frac{4K_s}{1+\delta}}\right) \tag{33}$$

$$\delta = \frac{2K_b}{\Delta\nu\tau} = 4\alpha A_r N_0$$

Note that the use of very narrowband optical filters for background suppression is not required, since δ is not a function of $\Delta\nu$. The optical filter bandwidth must be narrow enough only to guarantee that Eq. (20) remains valid.

The ability of the homodyne receiver to suppress background radiation is evident from Eq. (33), since in typical applications the product of the optical bandwidth $\Delta\nu$ and the bit duration τ is a very large number ($\Delta\nu\tau >> 1$). This implies that the performance of the homodyne receiver remains unaffected by background radiation, even when operating in relatively high-background environments corresponding to $K_b \gg 1$. In contrast, the performance of receiver structures that direct detect the noise field deteriorate significantly when background fields of comparable intensity are present (Ref. 1).

The effect of background radiation on receiver performance is shown in Fig. 3, as a function of the noise parameter δ. Note that over the range of error-probabilities considered, $P(E)$ remains essentially unaffected by background radiation until the noise intensity becomes so great that δ exceeds ~0.1. In typical applications, $\Delta\nu \gtrsim 3 \times 10^{11}$ Hz (corresponding to an optical bandwidth of $\Delta\lambda \gtrsim 10$ Å at a wavelength of $\lambda = 1\mu$), while the bit-duration is generally greater than 10^{-9} seconds; this implies that the background field must be intense enough to generate a large number of equivalent direct-detected counts ($K_b \gtrsim 15$) over the bit interval. In well designed receivers, background fields of this intensity are encountered only if the Sun, or other bright interference, is directly included in the receiver's field of view (Ref. 3).

IV. The Effects of Phase-Error on Receiver Performance

When the received field is corrupted by background radiation, and the effects of phase error also have to be taken into account, the count-intensity becomes

$$n(t) = \alpha A_r \left[a_L^2 + 2a_L a_r p(t)\cos\phi_e(t) + 2a_L(B_c(t)\cos\phi_e(t) + B_s(t)\sin\phi_e(t)\right] \tag{34}$$

The count intensity is therefore influenced both by random phase-error, and by random background noise. If we assume that the phase error is narrowband compared to both the modulation and the noise envelope, then the phase error can be considered constant over the signaling interval, and treated as a random variable. The noise term now contains in-phase and quadrature components weighted by sinusoidal functions of the phase error. Conditioned on a given phase error, the count intensity becomes

$$K_i(\phi_e) = \alpha A_r a_L^2 \tau + 2(-1)^{i+1} a_L a_r \tau \alpha A_r \cos\phi_e + y$$

$$y = 2\alpha A_r a_L \left(\cos\phi_e \int_0^\tau B_c(t)\,dt + \sin\phi_e \int_0^\tau B_s(t)\,dt\right) \tag{35}$$

Clearly, y is a zero-mean Gaussian random variable, with variance $\sigma_y^2 = 4\alpha^2 a_L^2 A_r^2 N_0 \tau$, exactly as before. The conditional error probability, $P(E|\phi_e)$, is therefore given by an expression similar to Eq. (33), but with $\sqrt{4K_s}$ replaced by $\sqrt{4K_s}\cos\phi_e$:

$$P(E \mid \phi_e) = Q\left(\sqrt{\frac{4K_s}{1+\delta}}\cos\phi_e\right) \tag{36}$$

The bit-error probability is the average of the conditional error-probability over the density of the random phase error:

$$P(E) = \overline{Q\left(\sqrt{\frac{4K_s}{1+\delta}}\cos\phi_e\right)}^{\phi_e} \tag{37}$$

The probability density of the phase-error can often be modelled in terms of the parameterized Tikhonov density (Ref. 4):

$$p(\phi_e) = \frac{e^{\sigma_e^{-2}\cos\phi_e}}{2\pi I_0(\sigma_e^{-2})}\ ;\quad |\phi_e| \leq \pi \tag{38}$$

where $I_0(\sigma_e^{-2})$ is the modified Bessel function of zero order, argument σ_e^{-2}, and where σ_e^2 is roughly the variance of the phase error for $\sigma_e^2 \ll 1$. Numerical integration was employed to evaluate Eq. (37), using the phase error density of Eq. (38). Receiver performance in the presence of phase error, but with negligible background interference, is shown in Fig. 4a. It is apparent that phase error effects do not become significant until the rms phase error exceeds 0.14 radians (corresponding to $\sigma_e^2 \gtrsim 0.02$) in the range of error probabilities considered: therefore, we can conclude that the performance of the homodyne receiver is not very sensitive to phase error effects.

The effects of background radiation and random phase errors are shown in Fig. 4b, corresponding to $\delta = 0.1$, or $K_b = 0.2\,\Delta\nu\tau$. We emphasize that since $\Delta\nu\tau$ is generally a large number, $\delta = 0.1$ implies very intense background radiation. However, since the background radiation enters the error-probability expression only as $\sqrt{1+\delta}$ in Eq. (33), even relatively high-intensity radiation has little effect on the average bit-error probability, as can be seen by comparing the performance curves of Figs. 4a and 4b.

V. Summary and Conclusions

The structure of a coherent binary optical MAP receiver has been derived, and the effects of background radiation and phase estimation errors on receiver performance were evaluated. It was found that random phase errors do not affect the performance of the coherent receiver significantly, as long as the standard deviation of the phase error remains less than roughly 0.14 radians (or 8 degrees). It was also shown that background radiation is effectively suppressed by the optical homodyne receiver: Significant deterioration in receiver performance is observed only in the presence of extremely intense background fields. The most notable characteristic of the binary optical homodyne receiver therefore appears to be its ability to achieve quantum-limited performance in high-background environments, provided that sufficiently accurate estimates of the received phase can be obtained.

References

1. Gagliardi, R. M., and Karp, S., *Optical Communications*, John Wiley, 1976, pg. 180.
2. Yariv, A., *Introduction to Optical Electronics*, Holt, Rinehard, and Winston, 1971, pg. 248.
3. Pratt, W. K., *Laser Communications Systems*, J. Wiley, New York, 1969, p. 120.
4. Van Trees, H. L., *Detection, Estimation, and Modulation Theory: Part I*, J. Wiley, New York, 1968, p. 338.

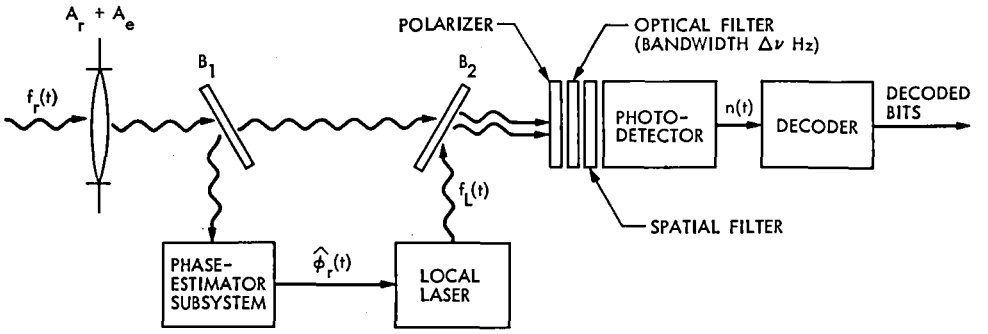

Fig. 1. Coherent optical receiver block diagram

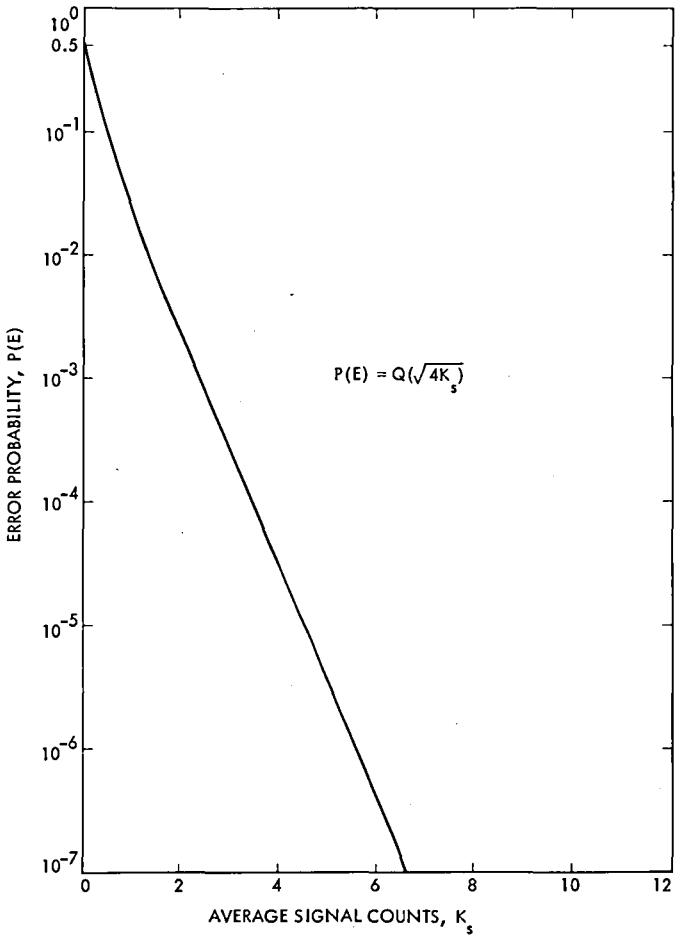

Fig. 2. Receiver performance under ideal conditions: negligible background radiation and phase error

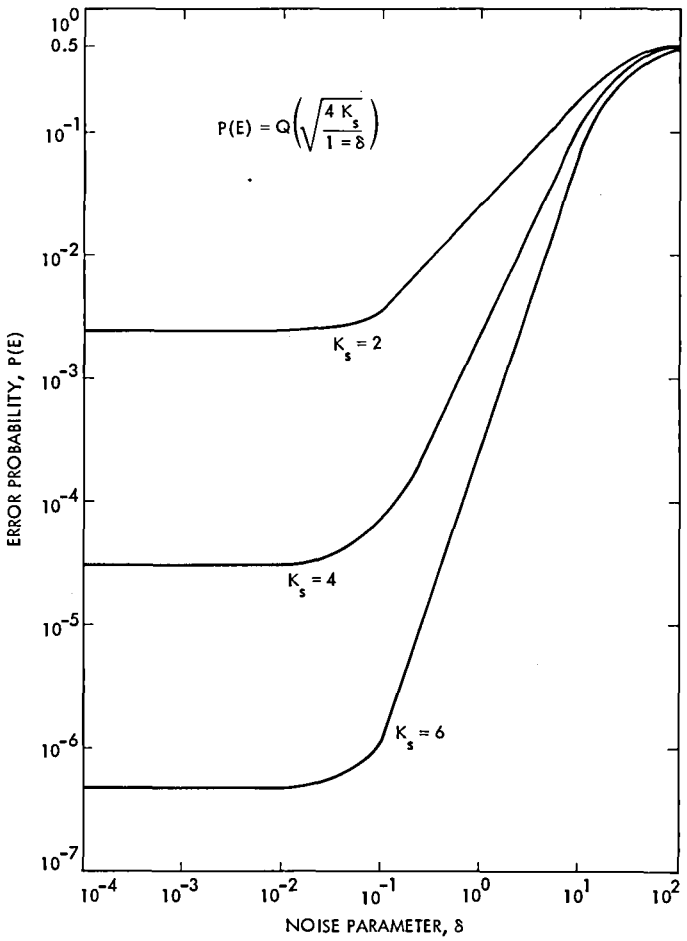

Fig. 3. Receiver performance in the presence of background radiation; negligible phase error

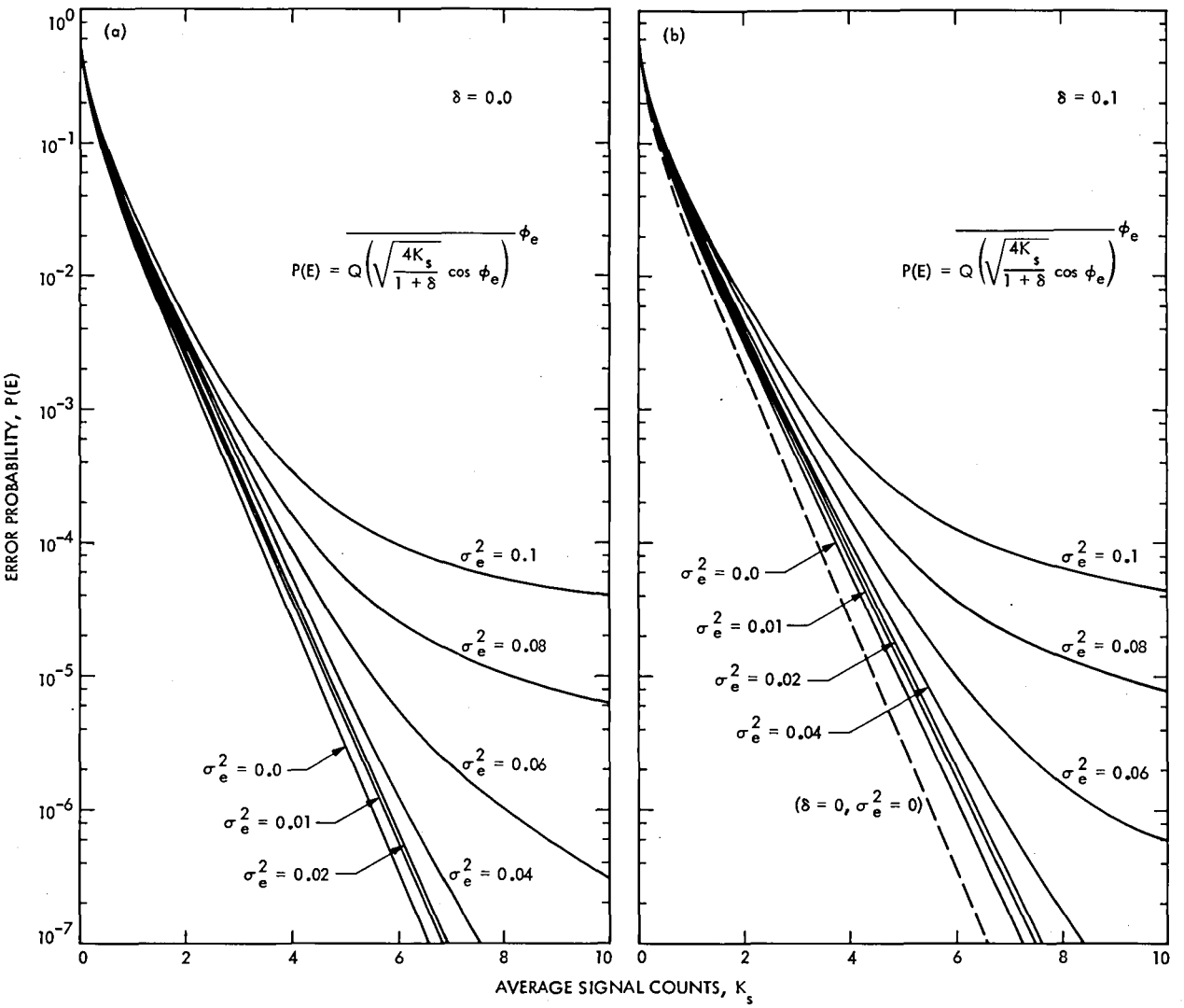

Fig. 4. Receiver performance in the presence of phase error: (a) negligible background; (b) high-intensity background

Deep Space Network Software Cost Estimation Model

R. C. Tausworthe
DSN Data Systems Section

This article presents a parametric software cost estimation model prepared for JPL Deep Space Network (DSN) Data Systems implementation tasks. The resource estimation model incorporates principles and data from a number of existing models, such as those of the General Research Corp., Doty Associates, IBM (Walston-Felix), Rome Air Force Development Center, University of Maryland, and Rayleigh-Norden-Putnam. The model calibrates task magnitude and difficulty, development environment, and software technology effects through prompted responses to a set of approximately 50 questions. Parameters in the model are adjusted to fit JPL software life-cycle statistics. The estimation model output scales a standard DSN Work Breakdown Structure skeleton, which is then input into a PERT/CPM system, producing a detailed schedule and resource budget for the project being planned.

I. Introduction

The early-on estimation of required resources and schedule for the development and maintenance of software has been one of the least precise aspects of the software life cycle and, yet, an orderly and rational attempt is necessary to plan and organize an implementation effort. Such an approach implies the need for a resource and schedule model that accepts as input the technical requirements to be achieved; the enormity of the task; the physical, environmental, human, and management constraints assumed or known to be in effect; the history base of similar and dissimilar experience; the means, alternatives, and technology available to the task; and a theory which is capable of correlating these parameters with measured results.

The least precise of such models is one which relies entirely on experience, intuition, and luck. It is sometimes referred to as a "WAG," or "Wildly Aspiring Guess." (More often, the acronym is somewhat differently derived, but with the same general connotation.) When a more formalized, mathematical model with some statistical verification can be formulated, the model appelation is upgraded to "Scientific WAG," or "SWAG."

The prediction of human programming behavior is a problem in estimating a series of events in a stochastic process governed by an unknown probability function. The goal of a SWAG model is therefore to predict the events in such a way as to produce minimum variance (or risk). The optimum SWAG model can predict only to the limit imposed by the statistical distribution actually characterizing the human activity.

The optimal SWAG model would require the precise quantification of all technical, environmental, management, and human behavioristic parameters, and would combine these

into a mathematical formula producing maximum likelihood or least mean-square error results. Lacking this precise quantification, the best that one may hope for in a SWAG model is that it accommodate the principal factors affecting the estimate variance (or risk) in a way that reduces the variance (or risk) from what it would be, had that factor not been included.

There are a number of SWAGs in existence. Fourteen software cost estimation models are summarized in Ref. 1, and nine were evaluated for use by the Jet Propulsion Laboratory in Ref. 2. None on these, by itself, seemed to the author to contain sufficient range of application and adaptability to the diverse kinds of software being produced at the Jet Propulsion Laboratory as to quantify the relevant cost factors and risks with sufficient accuracy to be useful. Taken all together, however, these models seemed to possess, in their union, the potential for as good a SWAG as could be obtained at the current state of the art.

An IBM study (Ref. 3) reported the analysis of 50 software projects with respect to 68 variables believed to influence productivity. Of these, 29 showed a significant, high correlation with productivity and were included in their estimation model.

A number of other models (General Research Corp., Doty Associates, TRW, Air Force Electronic Systems Division, Tecolote, Aerospace Corp., et al., reported in Ref. 1, and the University of Maryland, Ref. 4) provide productivity data with best-fit curves using many fewer parameters.

Still other models, notably the Rayleigh-Norden-Putnam model (Refs. 5 and 6) presuppose a few-parameter, specific mathematical model, which is then calibrated using available industry data to provide trade-offs among effort, duration, and risk.

Several models (Ref. 7) proceed to detail resource expenditures into the various phases of activity. This TRW model additionally compensates for task difficulty and some environmental factors.

Some of the models are fully automated, such as PRICE-S (Ref. 8), SLIM (Ref. 9), and SLICE (Ref. 10). The others appear to be calculative, or perhaps small programs, to be used by project planning staffs.

The software cost model described in this article is fully automated; it borrows and extends features from many of the models above. It utilizes 7 factors from the GRC model, 29 factors from, or similar to, the Walston-Felix model, and incorporates an inherited (or existing) code model due to the author. It utilizes the PERT estimation technique to estimate the expected size and variance of the software elements to be produced. It utilizes a modification of the Rayleigh-Norden-Putnam model to check on the confidence factors associated with the resultant resource estimates. It applies the estimated effort, staff, and duration to a standard Work Breakdown Structure (WBS) developed for JPL Deep Space Network (DSN) software tasks, and automatically produces a task budget and schedule to be used at either the initial system/subsystem planning, software implementation planning, or software maintenance planning stages of a project.

There are about 70 parameters within the model which relate to productivity, duration, staffing level, documentation, and computer resources. Another 70 parameters divide the total estimated effort among WBS subtasks; an additional 70 relate total duration to subtask durations. Subtask precedences are preset (but adjustable) and drive a PERT/Critical-Path-Method scheduling algorithm.

The outputs of the model include estimates and variance values for program size, staff productivity, effort, duration, staffing, documentation, and computer resources, together with confidence level checking, a complete scheduling early/late start/finish and float-time budget, and a Gantt chart (schedule bar chart) of the planned activities.

All parameters in the automated model are easily altered by a simple text editing process, without recompilation of the programs. For all its seeming complexity, the model itself is simple to use. Only a series of questions relating to size and environment need to be answered.

The ensuing sections of this article describe the model in more detail. The values of parameters used currently are subject to modification and refinement as further calibration and usage of the model proceeds.

Concerning accuracy: at this writing, insufficient data have been collected from DSN projects to optimize the parameters of the model to fit DSN productivity, duration, etc. Therefore, the model accuracy is unknown as pertaining to DSN prediction. However, the model does fit industry statistics (or can be made to fit any of the cited source models) by proper parameter selection. For this reason, it is felt that the few JPL data points that have been factored in will yield accuracy figures as good as, or perhaps better than, the other models in their stated environments.

The model is currently being used to estimate and plan all new programming activities involving DSN Data Systems implementations.

II. Model Description

The Software Cost and Resource Estimation Model (the acronum SCAREM is *not* used!) overview appears in Fig. 1 in data-flow-diagram format. Program size and staff productivity factors are separately estimated and then combined to estimate effort, staffing, duration, documentation, and computer resources. The model produces uninflated dollar costs for documentation and computer resources. Both estimated mean and variance values for all resources are output.

Estimated values are presented in the automated model to the user as advice. The user is admonished to use these figures, adding sufficient margin to ensure project completion within a desired confidence value.

The model then accepts any two of the three parameters: effort, average staff, and duration. These entries are checked against a model akin to the Rayleigh-Norden-Putnam model, but altered to conform with power-law fits to measured data. A confidence factor is computed to the resources entered. The user may alter the input estimates, if desired, for another check.

Once acceptable resources and duration have been decided, the model proceeds to produce a standard DSN software implementation work breakdown structure and schedule without further input from the user.

A. Estimation of Program Size

The size of the software task is measured in "equivalent" Kilo-Source-Lines of Executable Code (KSLEC). A source line of executable code is defined basically as a source language statement occupying one physical line in the source medium that results in generation of object code, reservation of storage, or definition of data type. Comments are excluded, as are statements merely defining labels and equivalences of identifiers. If several basic statements may appear on one physical source line, each such statement should be added separately into the KSLEC count.

Source lines of new code are weighted differently than lines of reused code, in proportion to the relative amount of effort required to adapt the inherited code to the current task. Even deleted lines of code contribute to the programming effort and therefore increase the "equivalent" KSLEC count.

The programming tasks involved with the generation of new code and reuse of existing code are depicted in Fig. 2. The efforts to specify, produce, document, and test a new line of code are normalized to unity; the lines of code added, changed, deleted, and retested-only contribute to the equivalent line count according to relative effort. The extent of existing-module modification is measured by the number of lines added in, the number changed, and the number deleted. The equivalent lines of code produced is then defined to be a weighted linear sum of the lines of code in each category.

The assumptions with respect to each component are the following:

(1) New code is subjected to the entire standard implementation process.

(2) The recognition of the reuse of existing code is made in the preliminary design phase, so code added, changed or deleted from modules goes only through subsequent phases.

(3) Added code takes the same effort as new code in corresponding phases where activity takes place.

(4) Changed code requires the same design and testing effort as new code, but less documentation and coding effort.

(5) Deleted lines from existing modules require reduced design, coding, and documentation effort, and no testing of the deleted lines.

(6) Any module changed is completely retested and requalified.

(7) Deleted modules require reduced architectural, interface, and detailed design considerations than new code; only that coding effort required to remove the unwanted code contributes to the coding time; no testing of the deleted code is possible; and documentation effort involves removal of entire sections of existing material and minor clean up. Retesting is covered in modules which interfaced with the deleted module.

(8) Retested unmodified code requires revalidation of the interface design and retesting efforts only.

Each of the size parameters is estimated by the PERT technique (Ref. 11) which produces a maximum likelihood value and variance.

The estimated value for the "equivalent lines of code" is composed of the weighted sum of the maximum likelihood estimate for each parameter, and its standard deviation is the weighted root-sum-square of the individual deviations. The weights are determined as the relative effort required for each category of code.

B. Estimation of Productivity

In this model, the productivity P is defined as total equivalent KSLEC (here denoted L) produced divided by the total staff work effort (here denoted W):

$$P = \frac{L}{W}, \frac{\text{KSLEC}}{\text{staff-month}}$$

A number of data bases (Refs. 3, 12, and 13) have shown that L and W are well correlated through a power-law relationship:

$$W = \frac{L^a}{P_1}$$

where P_1 is the average 1-KSLEC productivity rate.

The value of P_1 is primarily set by technology and environment. In fact, industry studies show that P_1 may vary by as much as 50:1 (or more!) as a function of such factors. The value of a, however, in each environment where data is available, shows a relative constancy at a value near unity.

It seems intuitive, all other things being equal, that productivity cannot increase as the program size rises; however, the least-square-power-law fits to data bases yield a-values of 0.91 (IBM), 0.991 (Doty), 0.986 (University of Maryland), and 0.975 (RADC). The consistency of these figures therefore seems to indicate that utilization of tools and technology takes place on larger projects (where it counts) more than on smaller projects.

The value for a currently being used is unity. Thus, the model may tend to be somewhat conservative.

Several models have contributed to the formula by which P_1 is calculated, principally those of GRC (Ref. 14) and IBM (Ref. 3). The form of P_1 is

$$P_1 = P_0 A$$

where P_0 is a constant factor and A is a technology and environmental adjustment factor. The value of A is computed from factors judged to be significant,

$$A = A_1 A_2 \cdots A_n$$

where each factor A_i ranges between a maximum value and a minimum value for that factor, depending on the extent to which the factor is present in the software task. The ratio of A_{max} to A_{min} is currently adjusted to span a 50:1 ratio of productivity.

C. Estimation of Implementation Task Duration

The IBM, University of Maryland, and RADC statistics suggest that the average duration T required for L KSLEC and W staff-months effort is approximated by

$$T = T_1 W^b$$

where T_1 is the 1-KSLEC average duration, and b is a time-factor exponent found from industry statistics. The value used in the DNS model, $T_1 = 4.8$, was adjusted to fit limited available DSN data, and $b = 0.356$ was the average power-law for the more extensive IBM, RADC, and GRC data.

D. Average Staff

The average staff, in persons, results from manipulation of the duration equation

$$S = \frac{W}{T} = \left(\frac{1}{T_1}\right) W^{1-b}$$

The staffing exponent, $1 - b = 0.644$, implied in the DSN model compares with measured values averaging 0.629 across industry.

E. Documentation Sizing and Cost

IBM statistics showed a nearly linear relationship between pages of documentation and lines of code, whereas the University of Maryland measured almost a square-root relationship. DSN experience over six Mark-III Data System programs revealed an exponent about midway in between (0.83). A study of maintenance user needs (Ref. 15) recommended that documentation be about 40 to 50 pages per KSLEC for programs in the 30 KSLEC vicinity. The formula used in the model for the number of pages of documentation is

$$D = D_1 L^d$$

The model currently uses $D_1 = 90$ and $d = 0.83$ to match the DSN experience and guidelines.

The documentation cost is found by a straight dollar-per-page rate; a figure of $30 per page is used in the current model.

F. Computer Resources

IBM and TRW give statistical figures for computer time costs as functions of lines of code and total effort, and also as a fraction of total cost. The DSN, however, mostly has dedicated minicomputers for which operational costs are not assessed to the implementation task on a usage basis. TRW does, however, also estimate a linear relationship between CPU time required per machine code instruction of about 25.2 CPU hours per thousand instructions.

The DSN model computer CPU resources as

$$C = C_1 L^c$$

The exponent value $c = 0.96$, given by Walston and Felix (who give dollar costs, rather than CPU time), is adopted to account for the general trend of CPU time with program size.

If CPU dollar cost is relevant, the model computes this at a straight dollar-per-CPU-hour figure (zero in the DSN model, but a parameter is available for other applications).

G. Confidence Level Computation

The values predicted by the SWAG model are average values based on statistics taken over many projects. The estimated values represent but one set of resources that, on the average, produce the intended success. However, effort and time can be traded (to some extent) to produce other equally valid project scenarios.

The Rayleigh-Norden-Putnam model has a time-effort relationship for checking the reasonability of resource values other than the average values produced by the SWAG. However, in order to use this model, several adaptations were felt to be indicated.

First, the basic differential equation was modified to accommodate a nonlinear "pace" factor (or learning curve). The model assumes the work equation to be of the form

$$w' = \alpha t^r (K - w)$$

in which $w = w(t)$ is the cumulative work effort up to time t, K is the total life-cycle effort, and r is the "pace-of-work" exponent.

Second, the model assumes the following parametric form of the software equation:

$$L = c_p w^p t^q$$

The factor $f = q/p$ sets the time-effort trade-off law. Putnam uses $p = 1/3$, $q = 4/3$ ($f = 4$), and such a value may well be valid for large projects in his data base. However, for the smaller projects typifying the DSN, an f factor which would require only 1.5 times the effort (three times the staff) to reduce schedule by a factor of 2 seems to be more within the DSN experience (more data is needed here).

Based on these modifications, it is possible to solve for p, q, and r, and c_p in terms of the parameters of observed average power-law relationships between L, w, and t.

$$f = 0.585$$

$$p = 0.828$$

$$q = 0.484$$

$$r = 1.81$$

$$c_p = \frac{0.0621}{A}$$

This model is used to compute confidence for any values of L, W, and T proposed for the project. The software equation is used to estimate the margin over or under the average project figures. By assuming that the statistics are log-normal (verified by the RADC data base), the confidence factor in producing L KSLEC in W staff-months effort and T months duration is

$$\text{Conf} = P\{L_{act} \leqslant L, w \leqslant W, t \leqslant T\}$$

Computation of the confidence level involves finding the optimum operating point on the software-equation curve for margin calculation, and then numeric integration of the normal probability function.

One interesting revelation to the author was that the probability of success in not expending more than W staff-months of effort *and* not requiring more than T months' duration, for the *average* SWAG estimate case, is only about 25 percent. Moreover, a significant amount of bias in W and T is required to raise the confidence to 50 percent.

Management should not despair, however. What the confidence limit indicates for average projects is that one out of four will go okay; the others will require some form of management intervention, in the form of schedule or resource extension.

III. Typical Operation of the Model

Blank forms and/or CRT prompted inputs are used to specify the parameters needed by the cost model program. Outputs can be selected and include a WBS task file, PERT plan, and schedule. The WBS task file can be edited to modify task titles, precedences, allocated resources, or durations; in addition, new tasks may be entered and actual completion or need dates may be affixed, so that the PERT and schedule portions of the program form a project detailed planning and control tool. Typical inputs and outputs are shown in Appendix A.

IV. Summary and Conclusion

The Software Cost Model reported here is the first of a series of planned refinements. As the model is used and as performance data are collected, no doubt changes will be made: adjustments of parameters, alteration of formulas, modifications of formats, new input data types, and additional kinds of outputs. Extensions currently envisioned are the automated transfer of the WBS data base generated by the model into the project control system currently being used in DSN Data Systems implementation projects, and the refinement of the model to include nonlinear scaling of overall effort and duration into individual task requirements.

If the model, even now, seems complex, then it is justly so, for the factors which affect human performance are generally complex and unpredictable, except in statistical terms. One sample function chosen from a stochastic ensemble is hardly ever "average" or "typical." One must expect variations between actual behavior and predictions made by any model.

The directions for the future are to refine the model for greater accuracy (within human performance estimation capacity limits), to extend the utility of the model throughout the entire life cycle, and to provide the basis for indicating where, and in what form, new software technology is needed.

References

1. *Quantitive Software Models,* Report SRR-1, Data and Analysis Center for Software, RADC, Griffiss Air Force Base, New York, March 1979.
2. Galorath, D. D., and Reifer, D. J., *Analysis of the State-of-the-Art of Parametric Software Cost Modeling,* Report SMC-7R-006, Software Management Consultants, Torrance, Calif. August 1980.
3. Walston, C. E., and Felix, C. P., "A Method of Programming Measurement and Estimation," *IBM System Journal*, Vol. 16, No. 1, 1977.
4. Freburger, K., and Basili, V. R., *The Software Engineering Laboratory: Relationship Equations*, Technical Report TR-764, SEL-3, NSG-5123, University of Maryland, Computer Science Center, College Park, Md., May 1979.
5. Norden, P. V., "Project Life Cycle Modeling," *Software Life-Cycle Management Workshop*, United States Army Computer Systems Command, pp. 217-306, August 1977.
6. Putnam, L. H., "Influence of the Time-Difficulty Factor in Large-Scale Software Development," *Software Life-Cycle Management Workshop,* United States Army Computer Systems Command, pp. 307-312, August 1977.
7. Wolverton, R. W., "The Cost of Developing Large Scale Software," *IEEE Transactions on Computers*, Vol. C-23, No. 6, June 1974.
8. Freiman, F. R., *PRICE Software Model,* RCA PRICE Systems Publication, Morestown, N.J., November 1977.
9. *Software Life-Cycle Management (SLIM) Estimating Model,* Quantitative Software Management, Inc., McLean, Va., 1978.
10. Kustanowitz, A. L., "System Life Cycle Estimation (SLICE)", *IEEE First International Computer Software and Applications Conference*, Chicago, Ill.
11. The author is unable to trace the definitive reference for this work. The usage cited is exposed in Putnam, L. H., "Example of an Early Sizing, Cost and Schedule Estimate for an Application Software System," *COMPSAC '78*, November 13-16, 1978.

12. Graver, C. A., et al., *Cost Reporting Elements and Activity Cost Tradeoffs for Defense System Software*, CR-1-72/1, General Research Corp., Santa Barbara, Calif., May 1977.

13. Nelson, R., *Software Data Collection and Analysis, Partial Report*, Rome Air Force Development Center, Data and Analysis Center for Software, Griffiss Air Force Base, New York, Sept. 1978.

14. Carriere, N. M., and Thibodeau, R., *Development of a Logistics Software Cost Estimating Technique for Foreign Military Sales*, General Research Corp., CR-3-839, Santa Barbara, Calif., June 1979.

15. Tausworthe, R. C., *Preparation Guide for Class B Software Specification Documents*, External Publication 79-56, Jet Propulsion Laboratory, Pasadena, Calif., October 1, 1979.

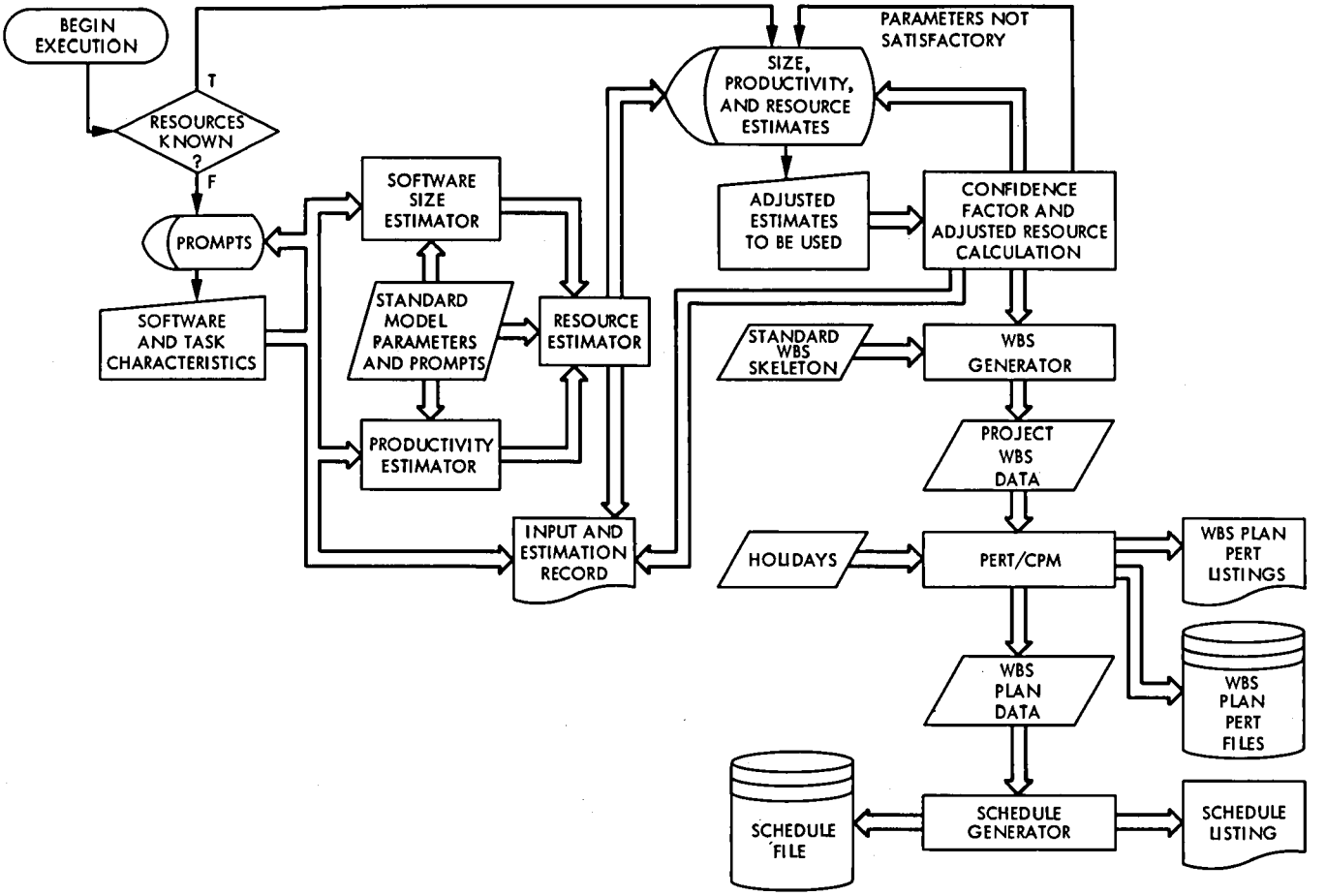

Fig. 1. DSN Software cost estimation model data flow diagram

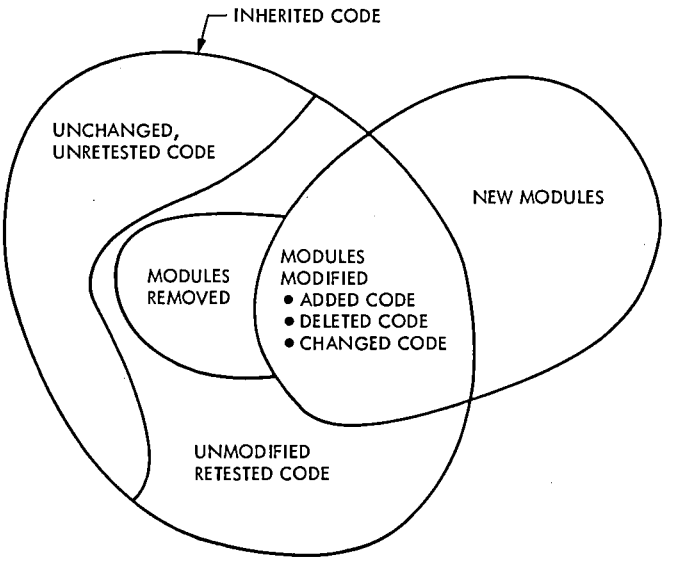

Fig. 2. Software implementation tasks related to new and inherited code activities

Appendix
Example of Operation

This Appendix contains a sample of the sequence of inputs and outputs from the Deep Space Network Software Cost Estimation Model.

```
TITLE:  VERSION CONTROL EDITOR          CDE:  Angus Day
ECR/ECO:  e80.176                       PROG. ID.:  HUP-D2-OP-D.2
SUBSYS:  X21.6                          Date Estimated: 14NOV80
                                        Model Data Version 1.3    31OCT80
-------------------------------------------------------------------------------
Answer the following items to the best of your estimation.

1.  How much new code is to be produced (completely new modules)?
    Maximum value, kilo-lines executable source(99% confidence level)?      3.5
    Expected value, kilo-lines executable source?                           3.3
    Minimum value, kilo-lines executable source(99% confidence level)?      3.1

2.  How much code exists in modules requiring modification?
    Maximum value, kilo-lines executable source(99% confidence level)?      6.9
    Expected value, kilo-lines executable source?                           6.6
    Minimum value, kilo-lines executable source(99% confidence level)?      6.3

3.  How much code will be deleted from these existing modules?
    Maximum value, kilo-lines executable source(99% confidence level)?       .4
    Expected value, kilo-lines executable source?                            .3
    Minimum value, kilo-lines executable source(99% confidence level)?       .2

4.  How much code will be added to these existing modules?
    Maximum value, kilo-lines executable source(99% confidence level)?       .7
    Expected value, kilo-lines executable source?                            .6
    Minimum value, kilo-lines executable source(99% confidence level)?       .4

5.  How much code will be changed in other ways in these modules?
    Maximum value, kilo-lines executable source(99% confidence level)?      1.2
    Expected value, kilo-lines executable source?                            .9
    Minimum value, kilo-lines executable source(99% confidence level)?       .7

6.  How much code will be deleted as entire modules from existing code?
    Maximum value, kilo-lines executable source(99% confidence level)?      1.4
    Expected value, kilo-lines executable source?                           1.3
    Minimum value, kilo-lines executable source(99% confidence level)?      1.1

7.  How much of the remaining existing code must be retested?
    Maximum value, kilo-lines executable source(99% confidence level)?      2.1
    Expected value, kilo-lines executable source?                           1.9
    Minimum value, kilo-lines executable source(99% confidence level)?      1.5

8.  Expected percentage of code to be developed actually delivered
    (0-90, 91-99, 100)?                                                   91-99

9.  How many different kinds of input/output data items per 1000 lines of
    new or modified code(>80, 16-80, 0-15)?                               16-80

10. Overall complexity of program and data base architecture
    (high, medium, low)?                                                  MEDIUM

11. Complexity of code logical design(high, medium, low)?                   LOW

12. What percent of the programming task is in Assembly language?             9

13. What percent of the new or modified code must be storage-optimized?       9
```

Fig. A-1. Hard copy format input parameter record

14. What percent of the new or modified code must be timing-optimized?	9
15. What percent of the total programming task is 'easy'?	20
16. What percent of the total programming task is 'hard'?	30
17. When is work to start, on the(FRD/FDD, SRD, SDD)?	FRD/FDD
18. What percent of the total program requirments will be established and stable before design, and will not be altered before delivery?	80
19. What percent of the requirements are likely to change slightly before delivery, but will do so under baseline change control?	10
20. What percent of the requirements are likely to change more drastically before delivery, but will do so under baseline control?	5
21. Complexity of program functional requirements(high, medium, low)?	LOW
22. Expected user involvement in requirements definition (much, some, none)?	MUCH
23. Customer experience in application area(much, none, some)?	SOME
24. Customer/implementor organizational interface complexity (high, normal, low)?	NORMAL
25. Interfaces with other SW development projects or organizations (many, few, none)?	FEW
26. Efficiency of implementing organization(poor, ok, good)?	GOOD
27. Overall implementation personnel qualifications and motivation (low, average, high)?	HIGH
28. Percentage of programmers doing functional design who will also be doing development(<25, 25-50, >50)?	25-50
29. Previous programmer experience with application of similar or greater size and complexity(minimal, average, extensive)?	AVERAGE
30. What is the average staff experience, in years, obtained from work similar to that required in the task being estimated?	6
31. Previous experience with operational computer to be used (minimal, average, extensive)?	MINIMAL
32. Previous experience with programming language(s) to be used (minimal, average, extensive)?	MINIMAL
33. Use of top-down methodology(low, medium, high)?	HIGH
34. Use of structured programmer team concepts(low, medium, high)?	HIGH
35. Use of Structured Programming(low, medium, high)?	HIGH

Fig. A-1 (contd)

36. Use of design and code inspections(low, QA, peer)?	QA
37. Classified security environment for computer(yes, , no)?	NO
38. Hardware under concurrent development(much, some, none)?	NONE
39. Percent of work done at primary development site (<70, 70-90, >90)?	70-90
40. Development computer access mode(remote, scheduled, demand)?	DEMAND
41. Percent of development computer access availability(<30, 30-60, >60)?	30-60
42. Quality of SW development tools and environment(poor, ok, good)?	OK
43. Maturity of system and support software(buggy, ok, good)?	OK
44. Overall adverse constraints on program design (severe, average, minimal)?	MINIMAL
45. Is the program real-time, multi-task(chiefly, some, no)?	NO
46. SW to be adaptable to multiple computer configurations or environments (yes, , no)?	NO
47. Adaptation required to change from development to operational environment(much, some, minimal)?	MINIMAL

Fig. A-1 (contd)

```
Estimated Overall Parameters:
                                                =average value
                                        +1-sigma                -1-sigma
Adjusted Lines of code= 6182 SLEC
 6280           6085
Effort= 26.5 person-months
 45.8            15.3
Staff productivity= 233 SLEC/staff-month
 404            135
Duration= 15.7 months
 19.0            12.9
Avg. Staff=  1.7
  2.9             1.0
Documentation=  537 pages     $16.1K
  645             448            $19.4K            $13.4K
Computer CPU time=  319 hours      $0.0K
  478             212             $0.0K             $0.0K

Use these figures to arrive at Effort, Duration, and Staffing
requirements. Include factors to provide acceptible risk
and confidence levels.


Values specified are:
   Kilo-lines of code=                                                  6.18
   Effort (person-months):                                             32.0
   Duration (months):                                                  16.0
   Average staff (persons):                                             2.0

    For the numbers you have entered, a reasonableness check indicates that
the average project would produce 7303 lines of code, using 32 staff-months
of resources and 16 months of duration, with an average staff of 2 persons,
for a productivity of 228 SLEC/staff-month.

The level of confidence in delivering 6182 lines of code,
on-time and within resources= 33 %.

Is output to be saved in a file?                                          Y

Name of output file to be created:                                   VCEDIT

Schedule start date:                                                 17NOV80


Select desired outputs and output media, or enter RETURN only for
defaults. Defaults are 1A, 2A, and 3A. Choices are:

                  1=Gantt Chart                 A=file
                  2=PERT data, 132 width        B=line printer
                  3=PERT data, 80 width

Choice(s):                                                        1B,2B,3A
```

Fig. A-2. Output of cost model using the parameters from the previous figure

PAGE 1

TITLE: VERSION CONTROL EDITOR — CDE: Angus Day
ECR/ECO: e80.176 — PROG. ID.: HUP-D2-OP-D.2
SUBSYS: X21.6 — STATUS AS OF: 14NOV80

CODE	TASK	WHO	EFF ORT	START EARLY DAY	START EARLY DATE	START LATE DAY	START LATE DATE	FINISH EARLY DAY	FINISH EARLY DATE	FINISH LATE DAY	FINISH LATE DATE	FLOAT TIME DAYS
*0.	START		0	0	17NOV80	0	17NOV80	0	17NOV80	0	17NOV80	0
*1.	Sys Plans, Reqts, & Design		0	32	9JAN81	32	9JAN81	32	9JAN81	32	9JAN81	0
* 1.1	Define Subsys Reqts		15	0	17NOV80	0	17NOV80	10	3DEC80	10	3DEC80	0
* 1.2	FRD		0	13	8DEC80	13	8DEC80	13	8DEC80	13	8DEC80	0
| 1.2.1	Write all sections		4	0	17NOV80	9	2DEC80	3	20NOV80	12	5DEC80	9
* 1.2.2	Edit and release FRD		2	12	5DEC80	12	5DEC80	13	8DEC80	13	8DEC80	0
* 1.3	Level B Review		3	13	8DEC80	13	8DEC80	15	10DEC80	15	10DEC80	0
* 1.4	Define Sys Architecture		18	15	10DEC80	15	10DEC80	27	31DEC80	27	31DEC80	0
* 1.5	FDD		0	30	7JAN81	30	7JAN81	30	7JAN81	30	7JAN81	0
| 1.5.1	Write all sections		4	15	10DEC80	27	31DEC80	17	12DEC80	29	6JAN81	12
* 1.5.2	Edit and release		2	29	6JAN81	29	6JAN81	30	7JAN81	30	7JAN81	0
* 1.6	Level C Review		3	30	7JAN81	30	7JAN81	32	9JAN81	32	9JAN81	0
*2.	SW Planning and Reqts		0	58	16FEB81	58	16FEB81	58	16FEB81	58	16FEB81	0
* 2.1	Define Software Reqts		25	32	9JAN81	32	9JAN81	50	4FEB81	50	4FEB81	0
* 2.2	SRD		0	56	12FEB81	56	12FEB81	56	12FEB81	56	12FEB81	0
| 2.2.1	Write all sections		4	32	9JAN81	53	9FEB81	34	13JAN81	55	11FEB81	21
* 2.2.2	Edit and release		2	55	11FEB81	55	11FEB81	56	12FEB81	56	12FEB81	0
* 2.3	Level D Review		2	56	12FEB81	56	12FEB81	58	16FEB81	58	16FEB81	0
*3.	SW Architecture and Design		0	93	6APR81	93	6APR81	93	6APR81	93	6APR81	0
* 3.1	Define SW architecture		31	58	16FEB81	58	16FEB81	81	19MAR81	81	19MAR81	0
* 3.2	SDD		0	91	2APR81	91	2APR81	91	2APR81	91	2APR81	0
| 3.2.1	Write all sections		4	58	16FEB81	88	30MAR81	60	18FEB81	90	1APR81	30
* 3.2.2	Edit and release		2	90	1APR81	90	1APR81	91	2APR81	91	2APR81	0
| 3.3	System Interface Design		22	58	16FEB81	78	16MAR81	70	4MAR81	90	1APR81	20
* 3.4	Level E Review		2	91	2APR81	91	2APR81	93	6APR81	93	6APR81	0
*4.	SW Detailed Design & Prod		0	273	22DEC81	273	22DEC81	273	22DEC81	273	22DEC81	0
| 4.1	SSD		0	315	23FEB82	327	11MAR82	315	23FEB82	327	11MAR82	12
| 4.1.1	Write Sections 1,2,3		6	93	6APR81	268	15DEC81	96	9APR81	271	18DEC81	175
* 4.1.2	Write Section 4		18	93	6APR81	93	6APR81	107	24APR81	107	24APR81	0
| 4.1.3	Write Section 5		43	107	24APR81	249	16NOV81	129	27MAY81	271	18DEC81	142
| 4.1.4	Write Section 6		4	93	6APR81	269	16DEC81	95	8APR81	271	18DEC81	176
| 4.1.5	Write Section 7		9	93	6APR81	266	11DEC81	98	13APR81	271	18DEC81	173
| 4.1.6	Edit and release		6	312	18FEB82	324	8MAR82	315	23FEB82	327	11MAR82	12
| 4.2	SOM		0	314	22FEB82	327	11MAR82	314	22FEB82	327	11MAR82	13
* 4.2.1	Write preliminary draft		8	107	24APR81	107	24APR81	113	4MAY81	113	4MAY81	0
| 4.2.2	Complete all sections		9	133	2JUN81	266	11DEC81	138	9JUN81	271	18DEC81	133
| 4.2.3	Edit and release		4	312	18FEB82	325	9MAR82	314	22FEB82	327	11MAR82	13
* 4.3	High-level Design Review		2	131	29MAY81	131	29MAY81	133	2JUN81	133	2JUN81	0
* 4.4	Module Production & Integ		0	271	18DEC81	271	18DEC81	271	18DEC81	271	18DEC81	0
* 4.4.1	Executive and control		18	113	4MAY81	113	4MAY81	131	29MAY81	131	29MAY81	0
* 4.4.2	I/O Modules		18	133	2JUN81	133	2JUN81	151	26JUN81	151	26JUN81	0
* 4.4.3	Interface handlers		18	151	26JUN81	151	26JUN81	169	23JUL81	169	23JUL81	0

Fig. A-3. Full form PERT/CPM work breakdown structure and schedule table output of the software cost model

TITLE: VERSION CONTROL EDITOR — CDE: Angus Day
ECR/ECO: e80.176 — PROG. ID.: HUP-D2-OP-D.2
SUBSYS: X21.6 — STATUS AS OF: 14NOV80

CODE	TASK	WHO	EFF ORT	START EARLY DAY	START EARLY DATE	START LATE DAY	START LATE DATE	FINISH EARLY DAY	FINISH EARLY DATE	FINISH LATE DAY	FINISH LATE DATE	FLOAT TIME DAYS
* 4.4.4	Function A		18	169	23JUL81	169	23JUL81	186	17AUG81	186	17AUG81	0
* 4.4.5	Function B		18	186	17AUG81	186	17AUG81	203	11SEP81	203	11SEP81	0
* 4.4.6	Function C		17	203	11SEP81	203	11SEP81	220	6OCT81	220	6OCT81	0
* 4.4.7	Function D		17	220	6OCT81	220	6OCT81	237	29OCT81	237	29OCT81	0
* 4.4.8	Function E		17	237	29OCT81	237	29OCT81	254	23NOV81	254	23NOV81	0
* 4.4.9	Function F		17	254	23NOV81	254	23NOV81	271	18DEC81	271	18DEC81	0
4.5	Special Tasks		0	139	10JUN81	271	18DEC81	139	10JUN81	271	18DEC81	132
4.5.1	Support software		12	133	2JUN81	265	10DEC81	139	10JUN81	271	18DEC81	132
4.5.2	Other		6	133	2JUN81	268	15DEC81	136	5JUN81	271	18DEC81	135
* 4.6	Acceptance Readiness Rvw		2	271	18DEC81	271	18DEC81	273	22DEC81	273	22DEC81	0
*5.	SW Test and Transfer		0	332	18MAR82	332	18MAR82	332	18MAR82	332	18MAR82	0
* 5.1	Verification tests		28	273	22DEC81	273	22DEC81	299	1FEB82	299	1FEB82	0
5.2	Contingency		25	96	9APR81	314	22FEB82	109	28APR81	327	11MAR82	218
5.3	STT		0	313	19FEB82	332	18MAR82	313	19FEB82	332	18MAR82	19
5.3.1	Write all sections		14	133	2JUN81	292	21JAN82	140	11JUN81	299	1FEB82	159
5.3.2	Edit and release		2	312	18FEB82	326	10MAR82	313	19FEB82	327	11MAR82	14
* 5.4	Acceptance tests		20	299	1FEB82	299	1FEB82	312	18FEB82	312	18FEB82	0
* 5.5	Demonstration tests		22	312	18FEB82	312	18FEB82	327	11MAR82	327	11MAR82	0
* 5.6	Transfer, CDE to COE		7	327	11MAR82	327	11MAR82	332	18MAR82	332	18MAR82	0
6.	Mgt Tasks and Milestones		0	19	16DEC80	332	18MAR82	19	16DEC80	332	18MAR82	313
6.1	CDE Activities		37	0	17NOV80	313	19FEB82	19	16DEC80	332	18MAR82	313
* 6.2	Develop prelim budget		3	10	3DEC80	10	3DEC80	12	5DEC80	12	5DEC80	0
* 6.3	Develop Sys Impl Plan		3	27	31DEC80	27	31DEC80	29	6JAN81	29	6JAN81	0
* 6.4	Draft Software Impl Plan		6	50	4FEB81	50	4FEB81	55	11FEB81	55	11FEB81	0
* 6.5	Revise Impl Plan		12	81	19MAR81	81	19MAR81	90	1APR81	90	1APR81	0
6.6	QA Audit		26	312	18FEB82	318	26FEB82	326	10MAR82	332	18MAR82	6
*FINISH			0	332	18MAR82	332	18MAR82	332	18MAR82	332	18MAR82	0

Fig. A-3 (contd)

PAGE 1

TITLE: VERSION CONTROL EDITOR — CDE: Angus Day
ECR/ECO: e80.176 — PROG. ID.: HUP-D2-OP-D.2
SUBSYS: X21.6 — STATUS AS OF: 14NOV80

CODE	TASK	WHO	EFF	E-START	L-FINSH	FLT
*0.	START		0	17NOV80	17NOV80	0
*1.	Sys Plans, Reqts, & Design		0	9JAN81	9JAN81	0
* 1.1	Define Subsys Reqts		15	17NOV80	3DEC80	0
* 1.2	FRD		0	8DEC80	8DEC80	0
| 1.2.1	Write all sections		4	17NOV80	5DEC80	9
* 1.2.2	Edit and release FRD		2	5DEC80	8DEC80	0
* 1.3	Level B Review		3	8DEC80	10DEC80	0
* 1.4	Define Sys Architecture		18	10DEC80	31DEC80	0
* 1.5	FDD		0	7JAN81	7JAN81	0
| 1.5.1	Write all sections		4	10DEC80	6JAN81	12
* 1.5.2	Edit and release		2	6JAN81	7JAN81	0
* 1.6	Level C Review		3	7JAN81	9JAN81	0
*2.	SW Planning and Reqts		0	16FEB81	16FEB81	0
* 2.1	Define Software Reqts		25	9JAN81	4FEB81	0
* 2.2	SRD		0	12FEB81	12FEB81	0
| 2.2.1	Write all sections		4	9JAN81	11FEB81	21
* 2.2.2	Edit and release		2	11FEB81	12FEB81	0
* 2.3	Level D Review		2	12FEB81	16FEB81	0
*3.	SW Architecture and Design		0	6APR81	6APR81	0
* 3.1	Define SW architecture		31	16FEB81	19MAR81	0
* 3.2	SDD		0	2APR81	2APR81	0
| 3.2.1	Write all sections		4	16FEB81	1APR81	30
* 3.2.2	Edit and release		2	1APR81	2APR81	0
| 3.3	System Interface Design		22	16FEB81	1APR81	20
* 3.4	Level E Review		2	2APR81	6APR81	0
*4.	SW Detailed Design & Prod		0	22DEC81	22DEC81	0
| 4.1	SSD		0	23FEB82	11MAR82	12
| 4.1.1	Write Sections 1,2,3		6	6APR81	18DEC81	175
* 4.1.2	Write Section 4		18	6APR81	24APR81	0
| 4.1.3	Write Section 5		43	24APR81	18DEC81	142
| 4.1.4	Write Section 6		4	6APR81	18DEC81	176
| 4.1.5	Write Section 7		9	6APR81	18DEC81	173
| 4.1.6	Edit and release		6	18FEB82	11MAR82	12
| 4.2	SOM		0	22FEB82	11MAR82	13
* 4.2.1	Write preliminary draft		8	24APR81	4MAY81	0
| 4.2.2	Complete all sections		9	2JUN81	18DEC81	133
| 4.2.3	Edit and release		4	18FEB82	11MAR82	13
* 4.3	High-level Design Review		2	29MAY81	2JUN81	0
* 4.4	Module Production & Integ		0	18DEC81	18DEC81	0
* 4.4.1	Executive and control		18	4MAY81	29MAY81	0
* 4.4.2	I/O Modules		18	2JUN81	26JUN81	0
* 4.4.3	Interface handlers		18	26JUN81	23JUL81	0

Fig. A-4. Short form PERT/CPM work breakdown structure schedule data

TITLE: VERSION CONTROL EDITOR — CDE: Angus Day
ECR/ECO: e80.176 — PROG. ID.: HUP-D2-OP-D.2
SUBSYS: X21.6 — STATUS AS OF: 14NOV80

CODE	TASK	WHO	EFF	E-START	L-FINSH	FLT
* 4.4.4	Function A		18	23JUL81	17AUG81	0
* 4.4.5	Function B		18	17AUG81	11SEP81	0
* 4.4.6	Function C		17	11SEP81	6OCT81	0
* 4.4.7	Function D		17	6OCT81	29OCT81	0
* 4.4.8	Function E		17	29OCT81	23NOV81	0
* 4.4.9	Function F		17	23NOV81	18DEC81	0
4.5	Special Tasks		0	10JUN81	18DEC81	132
4.5.1	Support software		12	2JUN81	18DEC81	132
4.5.2	Other		6	2JUN81	18DEC81	135
* 4.6	Acceptance Readiness Rvw		2	18DEC81	22DEC81	0
*5.	SW Test and Transfer		0	18MAR82	18MAR82	0
* 5.1	Verification tests		28	22DEC81	1FEB82	0
5.2	Contingency		25	9APR81	11MAR82	218
5.3	STT		0	19FEB82	18MAR82	19
5.3.1	Write all sections		14	2JUN81	1FEB82	159
5.3.2	Edit and release		2	18FEB82	11MAR82	14
* 5.4	Acceptance tests		20	1FEB82	18FEB82	0
* 5.5	Demonstration tests		22	18FEB82	11MAR82	0
* 5.6	Transfer, CDE to COE		7	11MAR82	18MAR82	0
6.	Mgt Tasks and Milestones		0	16DEC80	18MAR82	313
6.1	CDE Activities		37	17NOV80	18MAR82	313
* 6.2	Develop prelim budget		3	3DEC80	5DEC80	0
* 6.3	Develop Sys Impl Plan		3	31DEC80	6JAN81	0
* 6.4	Draft Software Impl Plan		6	4FEB81	11FEB81	0
* 6.5	Revise Impl Plan		12	19MAR81	1APR81	0
6.6	QA Audit		26	18FEB82	18MAR82	6
*FINISH			0	18MAR82	18MAR82	0

Fig. A-4 (contd)

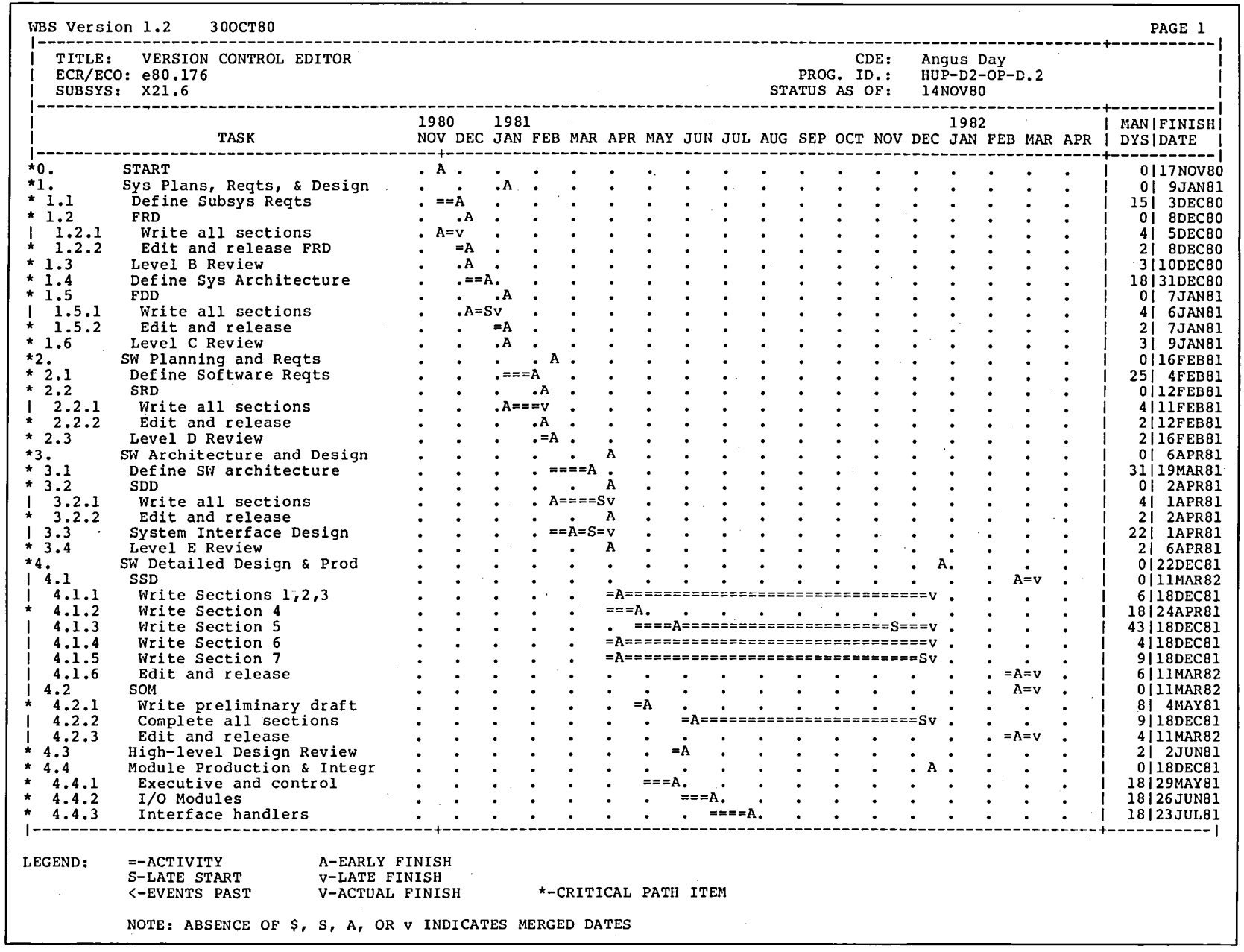

Fig. A-5. Gantt chart output of the software cost model

WBS Version 1.2 30OCT80 PAGE 2

TITLE: VERSION CONTROL EDITOR
ECR/ECO: e80.176
SUBSYS: X21.6
CDE: Angus Day
PROG. ID.: HUP-D2-OP-D.2
STATUS AS OF: 14NOV80

	TASK	1980 NOV	DEC	1981 JAN	FEB	MAR	APR	MAY	JUN	JUL	AUG	SEP	OCT	NOV	DEC	1982 JAN	FEB	MAR	APR	MAN DYS	FINISH DATE
* 4.4.4	Function A	.	.	.	.	.	.	.	.	.	===A	.	.	.	.	.	.	.	.	18	17AUG81
* 4.4.5	Function B	.	.	.	.	.	.	.	.	.	.	===A	.	.	.	.	.	.	.	18	11SEP81
* 4.4.6	Function C	.	.	.	.	.	.	.	.	.	.	.===A	.	.	.	.	.	.	.	17	6OCT81
* 4.4.7	Function D	.	.	.	.	.	.	.	.	.	.	.	===A.	.	.	.	.	.	.	17	29OCT81
* 4.4.8	Function E	.	.	.	.	.	.	.	.	.	.	.	.	====A.	.	.	.	.	.	17	23NOV81
* 4.4.9	Function F	.	.	.	.	.	.	.	.	.	.	.	.	.	===A	.	.	.	.	17	18DEC81
4.5	Special Tasks	.	.	.	.	.	.	.	.A	==========v	.	.	.	.	.	.	.	.	.	0	18DEC81
4.5.1	Support software	.	.	.	.	.	.	.	=A	==========Sv	.	.	.	.	.	.	.	.	.	12	18DEC81
4.5.2	Other	.	.	.	.	.	.	.	A	==========v	.	.	.	.	.	.	.	.	.	6	18DEC81
* 4.6	Acceptance Readiness Rvw	.	.	.	.	.	.	.	.	.	.	.	.	.	=A.	.	.	.	.	2	22DEC81
*5.	SW Test and Transfer	.	.	.	.	.	.	.	.	.	.	.	.	.	.	.	.	.	A	0	18MAR82
* 5.1	Verification tests	.	.	.	.	.	.	.	.	.	.	.	.	.	.	=====A	.	.	.	28	1FEB82
5.2	Contingency	.	.	.	.	.	.	.==A	==========v	.	.	.	.	.	.	.	.	.	.	25	11MAR82
5.3	STT	.	.	.	.	.	.	.	.	.	.	.	.	.	.	.	.	A===v	.	0	18MAR82
5.3.1	Write all sections	.	.	.	.	.	.	.	=A	==========Sv	.	.	.	.	.	.	.	.	.	14	1FEB82
5.3.2	Edit and release	.	.	.	.	.	.	.	.	.	.	.	.	.	.	.	.	A==v	.	2	11MAR82
* 5.4	Acceptance tests	.	.	.	.	.	.	.	.	.	.	.	.	.	.	.	==A	.	.	20	18FEB82
* 5.5	Demonstration tests	.	.	.	.	.	.	.	.	.	.	.	.	.	.	.	.	===A	.	22	11MAR82
* 5.6	Transfer, CDE to COE	.	.	.	.	.	.	.	.	.	.	.	.	.	.	.	.	.=A	.	7	18MAR82
6.	Mgt Tasks and Milestones	.	A	==========v	.	0	18MAR82
6.1	CDE Activities	.	====A	==========S===v	.	37	18MAR82
* 6.2	Develop prelim budget	.	A	.	.	.	.	.	.	.	.	.	.	.	.	.	.	.	.	3	5DEC80
* 6.3	Develop Sys Impl Plan	.	.	=A	.	.	.	.	.	.	.	.	.	.	.	.	.	.	.	3	6JAN81
* 6.4	Draft Software Impl Plan	.	.	.	=A	.	.	.	.	.	.	.	.	.	.	.	.	.	.	6	11FEB81
* 6.5	Revise Impl Plan	.	.	.	.	==A	.	.	.	.	.	.	.	.	.	.	.	.	.	12	1APR81
6.6	QA Audit	.	.	.	.	.	.	.	.	.	.	.	.	.	.	.	.	=S=Av	.	26	18MAR82
*FINISH		.	.	.	.	.	.	.	.	.	.	.	.	.	.	.	.	.	A	0	18MAR82

WBS Version 1.2 30OCT80 PAGE 3

TITLE: VERSION CONTROL EDITOR
ECR/ECO: e80.176
SUBSYS: X21.6
CDE: Angus Day
PROG. ID.: HUP-D2-OP-D.2
STATUS AS OF: 14NOV80

	TASK	1980 NOV	DEC	1981 JAN	FEB	MAR	APR	MAY	JUN	JUL	AUG	SEP	OCT	NOV	DEC	1982 JAN	FEB	MAR	APR	MAN DYS	FINISH DATE
*1.	Sys Plans, Reqts, & Design	.	=======A	.	.	.	.	.	.	.	.	.	.	.	.	.	.	.	.	51	9JAN81
*2.	SW Planning and Reqts	.	.	.=====A	.	.	.	.	.	.	.	.	.	.	.	.	.	.	.	33	16FEB81
*3.	SW Architecture and Design	.	.	.	.	======A	.	.	.	.	.	.	.	.	.	.	.	.	.	61	6APR81
*4.	SW Detailed Design & Prod	.	.	.	.	.	==========	==========A=v	.	287	11MAR82
*5.	SW Test and Transfer	.	.	.	.	.	.==========	==========S==========A	.	118	18MAR82
6.	Mgt Tasks and Milestones	.	==S	==========Av	.	87	18MAR82

LEGEND: =-ACTIVITY A-EARLY FINISH
S-LATE START v-LATE FINISH
<-EVENTS PAST V-ACTUAL FINISH *-CRITICAL PATH ITEM

NOTE: ABSENCE OF $, S, A, OR v INDICATES MERGED DATES

Fig. A-5 (contd)

A Sensitivity Model for Energy Consumption in Buildings Part I. Effect of Exterior Environment

F. L. Lansing
DSN Engineering Section

A simple analytical model is developed for the simulation of seasonal heating and cooling loads of any class of buildings to complement available computerized techniques which make hourly, daily, and monthly calculations. An expression for the annual energy utilization index, which is a common measure of rating buildings, having the same functional utilization, is derived to include about 30 parameters for both building interior and exterior environments. This article, the first of two parts, reports on the sensitivity of a general class building to either controlled or uncontrolled weather parameters. A hypothetical office-type building, located at the Goldstone Space Communication Complex, Goldstone, California, is selected as an example for the numerical sensitivity evaluations. Several expressions of variations in local outside air temperature, pressure, solar radiation and wind velocity are presented. Further study is planned to cover in the ensuing parts the effects of the major parameters of interior building environment.

I. Introduction

Efforts to reduce energy consumption in residential and nonresidential buildings have been addressed quantitatively in enough detail in the literature. Several solutions have been proposed in the form of energy conservation regulations, standard measures, or procedures. Local government offices at city, county, and state levels, together with utility companies, private industries, and other institutions have been updating these regulations to suit the general need. Common modifications such as changing room temperatures in offices down to 18.33°C (65°F) in winter and up to 25.56°C (78°F) in summer, adding or increasing insulation materials to exterior walls, preventing air leakage by weather-stripping, reducing domestic hot water temperatures in boilers down to 40.56°C (105°F), etc., are a few examples to save the building or facility owner some maintenance and operation costs. The impact, however, of implementing these modifications and others on different types of buildings will not be the same since the savings depend on local weather conditions, building size, occupancy density, building activity, lighting levels, internal electrical loads, type of automatic controls, utility cost structure, etc. Taking different weather conditions, for instance, a 1% percentage change in the site heating degree days (HDD) in a selected winter month, around its design or average profile, will cause different percentage changes in the energy consumption for that month if an office building, a central control building, a hospital, a theatre, or a hotel are the buildings under observation.

Other building simulation computer programs have also been developed by various utility companies, architect/engineering offices, consulting engineers and other private profit making and nonprofit organizations. These computer programs are considered valuable tools for the hourly, daily,

monthly and yearly simulations of a given building. The latter could be either in design stage or under a retrofit. To develop a general sensitivity model using these computer programs, many different buildings have to be tested. This proves to be a costly and a cumbersome task, although the technique is advantageous when only a single building is studied. An analytical model of less complexity and use cost thus needs to be established instead.

At the Deep Space Network communication complexes, the above energy conservation measures, in addition to other unique measures, have been studied, designed and implemented as part of a NASA-wide energy conservation program. Also, a computer model for energy analysis has been developed as a tool (Ref. 1) to facilitate the energy computations for over 200 buildings throughout the Network. Although the Network buildings can be grouped into several categories of similar functions, such as control buildings, office buildings, cafeterias, etc., the building size, orientation, energy loads, and environment are different. This will result in different responses to the same energy measures when implemented. Because it is known that these differences are small if the savings are expressed per unit gross floor area, grouping of buildings that have the same function is made to be compared on a uniform basis. Though the computer-aided design tools are more accurate and produce results that are specific to a particular building, general but simpler techniques are also sought for a quick evaluation and screening of measures and the understanding of the physical meaning of both building and equipment behavior under varied operating conditions.

The model should be structured to enable analysts to group analogous buildings which have the same function and occupancy activity but are of different size and floor area for handling on a similar basis when modifications or measures are proposed. The objective of this study is directed toward developing this analytical model for a general-class building. Various simplifying assumptions are made and presented in Section II in order to reduce the complexity of the multivariate problem at hand and to identify the key parameters affecting the total energy consumption and cost. The sensitivity analysis and the parameterization of these key variables are presented next for an example building to give numerically the relative magnitudes and trends of changes. Exterior weather patterns are studied first and presented in this part of the study. The rest of the operating system parameters will be addressed in a following report. While some parts of the present study are described, in some detail, to be viewed by a wide audience spectrum, the study is not intended to review the technical performance at the components level but to cover the whole building treated here as the system for a complete sensitivity analysis.

II. Energy Model and Assumptions

Although buildings operate differently in general, some classifications could still be made according to their function and internal loads. Many differences, however, still exist within same function buildings regarding the size of air-conditioned zones (or spaces); the capacity, and type of fan-coil units, air-handlers, coolers, boilers, furnaces, and heaters; the wattage, and type of lighting equipment; the wattage and type of motors, machines, electrical and electronic equipment; the number and activity of occupying people; the number and type of automatic temperature, pressure, humidity and flow controls; the hours of building operation; the design inside temperatures, etc. Different buildings may look different on the inside and the outside. However, from an energy consumption viewpoint, there are several common features that could be shown. These features are essential in forming the basis for the present model. Figure 1 depicts an interior building envelope with boundaries encompassing the building structure, occupants, and all internal functional equipment such as lighting, machinery, etc., except the heating, ventilation and air conditioning (HVAC) equipment. The HVAC equipment, although physically placed either inside or on the roof of the building, is treated in the model as external equipment to the building envelope. The selected control volume boundary hence encloses the building interior conditioned space, heating and cooling coils, while it leaves in the surroundings the HVAC equipment prime movers (such as boilers, chillers, electric motors for driving fans, motorized dampers, circulating pumps for cold and hot fluids etc.) in addition to the external outdoor equipment (such as external lighting, heated pools, etc.).

In air conditioning practice, a fraction ϵ of the total air flow (which ranges between 0 and 90%) leaves the air-conditioned space as exhaust air, and the balance returns to the fan-coil unit for reutilization in air conditioning. This percentage of the circulated air that is vented to the atmosphere as exhaust air is replaced equally by fresh outside air as a ventilation air. The ventilation process causes an additional burden on the air-conditioning system, depending on the fraction ϵ. The selection of the control surface, as illustrated in Fig. 1 to include this air circulation loop, is more suitable for energy analysis than when the building interior alone, without the air circulation loop, acts as the control volume.

The following assumptions and idealizations are made to simplify the analysis:

(1) A general-class building, with its multiple air-conditioned zones, air handlers, heaters, coolers, mechanical and electrical equipment, is treated as a

single macro-air-conditioned space with two air streams – air supply and air return streams. The average inside design temperature T_i, at any period, is taken as the weighted average of all the air-conditioned zones, with each zone represented by its share of the air flow rate. The volume of the equivalent air-conditioned space Ω is the sum of individual zone volumes, and the equivalent air flow rate V is assumed the sum of individual zone rates.

A general-class building could also be divided into several major sections where heating and cooling requirements are always at odds with each other throughout a given season. This case, however, should be distinguished from different intrinsic zone requirements during a given heating or a given cooling season. To illustrate this point further, consider for instance an industrial building which is divided into an office section and a machinery section. Within the office section, several air-conditioned zones may be present, with each having a minor variation of internal loads. All the zones within the office section may require either cooling or heating energies at a given time period. Also, the machinery section could be divided into several air-conditioned zones, with each generating internally an excessive amount of heat due to the operating machines. Subject to the internal load magnitude, the machinery section may require only cooling energy throughout the year, regardless of the exterior weather conditions. Hence, in the winter season, for instance, the two building sections will be in a different mode of air-conditioning. Therefore, for this type of building, subject to the size and energy requirement and mode of air-conditioning of each internal building section, the analyst should select either the simple approach of averaging the building conditions as one macrozone is appropriate or otherwise divide the building into a number of sections. The study model will proceed assuming the building is represented by a single macrozone composed of several analogous zone energy requirements.

(2) The exterior outside air temperature variations throughout the year are assumed for energy analysis to be categorized into only two seasons: summer and winter. Spring and fall periods will be merged as appropriate such that the summer and winter seasons occur for M_s and M_w months, respectively, which are not necessarily equal, but total 12. Heating energy is commonly consumed in the winter season, and cooling energy is commonly consumed in the summer season, with possible overlapping depending on the type of air handler and the internal load profile. Heating and cooling modes will not necessarily occur in winter and summer, respectively and their energy requirements are allowed in this general model to occur simultaneously, to suit different air-handling mechanisms. Hence, a distinction should be made between summer and winter seasons and cooling and heating modes.

(3) Variations of outside air temperature, throughout a given time period, are generally not predictable and uncontrollable. However, statistical averages obtained from weather bureaus for a particular hour, day, or month, for instance, are found satisfactory for the analysis. The longer the statistical period, the better the expectation of energy consumption will be. Available monthly or yearly data of cooling degree days (CDD) or heating degree days (HDD) for many locations (Refs. 2-6) could be converted, by simple expressions, to give the monthly and seasonal average outside air temperature. In the present model, only two average outside air temperatures are assumed to represent the weather pattern for the two seasons: $T_{o,s}$ for the summer season and $T_{o,w}$ for the winter season. These two temperatures are obtained by averaging the daily or monthly temperatures over the season period. To avoid the transient hourly heat transfer mechanism to and from a building, the minimum period of the system study is taken as 24 hours or one day.

(4) The internal heat gain to (or loss from) a building space Q_i is then taken as the sum of three major quantities. The first, the internal heat generated Q_g, is itemized into the following five categories: (a) due to occupants Q_p, (b) due to lighting Q_l, (c) due to electrical and electronic equipment Q_e, (d) due to mechanical equipment with electrical drives Q_m, and (e) due to internal fuel-fired appliances Q_f, such as ovens, ranges, etc. The second quantity is the heat transmitted to and from the building structure Q_t, which is divided into two categories: (a) a solar heat portion Q_r, due to direct solar radiation incidence upon fenestration areas and to indirect solar radiation falling on exterior walls and roofs (the solar heat is assumed independent of outside air temperature variations, although it takes into consideration reradiation to the sky), and (b) the heat transmission due to varying outside air temperatures on walls, roofs, floors, and glazing areas Q_a. Note that the heat exchanged and transmitted through interior walls or partitions inside the control volume, separating specially controlled zones, which are kept at specific temperature patterns different from their neighbors, is not considered in the model. The reason is shown by the first assumption, which considers a building

section as a single air-conditioned space kept at an equivalent "average" inside temperature, representing the weighted average of the various internal zones.

The third quantity of Q_i is the undesirable heat gain or loss due to infiltration or exfiltration Q_x, which is caused by the repetitive opening and closing of doors and windows, buoyancy losses, and air leakages through various cracks as a result of differences in the pressure between the inside and the outside environments. With only sensible heat calculations made, the energy sum is written as:

$$Q_g = Q_p + Q_l + Q_e + Q_m + Q_f \tag{1}$$

$$Q_t = Q_r + Q_a \tag{2}$$

$$Q_i = Q_g + Q_t + Q_x \tag{3}$$

(5) The latent heat gain to or loss from a space is mainly due to three components: (a) humidity differences associated with moving infiltrated or exfiltrated air, (b) water vapor from the occupants due to their rate of metabolism, and (c) steam generated by internal sources such as food, coffee machines, etc.

In general, the latent heat portion of the total heat to a space is very small although it could be significant in certain building types. The assumption of eliminating the latent heat from direct calculations is made to simplify the analysis but will be incorporated later as the methodology is developed. A detailed itemization of the heat quantities that appear in Eq. (3) is given next.

(6) The heat given off by the building occupants Q_p depends mainly on the number of occupants and the type of occupant activity. The average sensible heat generated per person s_p ranges from 60 W/person (about 205 Btu/hr person) to 150 W/person (about 510 Btu/hr person). Hence,

$$Q_p = s_p N$$

where N is the number of people in the building. For comfortable human spacing, the population density D_p ($=N/A$) is usually designed within certain limits. Therefore, per unit floor area A, the sensible heat gain from people is written as:

$$Q_p'' = s_p D_p \tag{4}$$

(7) For the lighting equipment, electrical energy is converted first into both radiation and convection parts in different proportions depending on the type of light bulb used. The radiation energy part is then converted by multiple reflections and absorptions with the building walls, materials and furnishings, to both convection and conduction parts at a later time. The result of this transient heat transfer is only a reduction of the peak lighting load as "seen" by the air-conditioning system. Note that the illumination part, which is later converted to convection, is still affecting the air-conditioning load even after the lighting equipment is turned off. The heat transfer to the air could be assumed in quasi-steady state if a long period (preferably not less than 24 hours) is considered. In the present model, it is assumed for simplicity, that the heat generated from both incandescent and fluorescent lighting fixtures Q_l is instantaneous and averaged over a given day.

$$Q_l = E_l$$

where E_l is the electrical wattage of all types of light bulbs in the interior air-conditioned space. In practice, illumination engineers use energy intensity limits E_l'' typically between 10-60 W/m^2 (1-6 W/ft^2). Therefore, per unit floor area A, the intensity of lighting heat gain Q_l'' is:

$$Q_l'' = E_l'' \tag{5}$$

(8) The heat gain to the space, as sketched in Fig. 1, from the interior electronic and electrical appliances which have no motor drives (such as computers, TV sets, electric irons, radios, etc.) also is assumed to be instantaneously convected to the air stream. According to the equipment wattage value E_e, the heat gain to the space Q_e, due to electrical and electronic equipment excluding equipment motor drives, is expressed as

$$Q_e = E_e$$

or per unit floor area,

$$Q_e'' = E_e'' \tag{6}$$

(9) For internal electromechanical appliances and machines with motor drives, various configurations arise where both the motor and the driven machine are located either in the same space or one is inside and the other is outside the space. If E_m is the input

wattage of the motor that drives the machine, then the heat generated inside the space Q_m is expressed by any one of the following equations:

$$Q_m = E_m$$

if motor and driven machine are both inside the space, or

$$Q_m = \eta_m E_m$$

if motor is outside the space and the driven machine is inside, or

$$Q_m = (1 - \eta_m) E_m$$

if motor is in the space and the driven machine is outside, where η_m is the average motor efficiency. In general, the above relationships between Q_m and E_m can be written as

$$Q_m = \lambda_m E_m$$

where λ_m is a fraction ranging from $(1 - \eta_m)$ to 1 according to the physical location of motor-driven appliances. With common motor efficiencies ranging from 60% for small-size motors to 90% for large-size motors, the fraction λ_m will range from 0.1 to 1. In addition, if the power density of the electromechanical equipment E_m is specified by the designer, then per unit floor area, the heat rate Q_m is written as

$$Q''_m = \lambda_m E''_m \tag{7}$$

(10) The solar portion of the transient heat transmission to a building Q_r is independent of the outside air temperature variations. It depends on fenestration surface area, orientation, optical transmissivity, emissivity and absorptivity properties; absorptivity and emissivity of exterior opaque walls; and wall orientation and surface area. Under the cyclic variation of ambient air and sky temperatures, a building would have a net heat transmission Q_a out or into its conditioned space according to whether the average daily inside temperature is kept higher than or lower than the average daily outside air temperature, respectively. During a particular day, the calculations of the hourly heat transmission require the solution of a complex transient heat transfer problem involving the building interior thermal mass. The quasi-steady-state approximation, given by Appendix A, on a daily basis, is still, however, a common practice in air-conditioning calculations. The net daily solar heat gain Q_r is treated as a combined building-site characteristic parameter while the net daily ambient heat transmission Q_a is in linear proportionality to the difference between daily average inside and outside temperatures. This building approximation has been used also in several solar collector studies (Ref. 7) which produced good results, since by analogy, a building can be treated as a low-efficiency solar collector. The daily ambient heat transmission Q_a is written as:

$$Q_a = UA\,(T_o - T_i)$$

where U is a building characteristic parameter representing the equivalent coefficient of heat transmission, lost or gained from the building envelope and is given as an area-weighted average of all the individual exterior walls, roof, glazing and floor surface areas A_j. By using Eq. (A-9) in Appendix A,

$$U = \sum_j A_j U_j / A \tag{8}$$

Accordingly, per unit gross floor area, the ambient heat gain to space Q''_a is written in the form

$$Q''_a = U(T_o - T_i) \tag{9}$$

On the other hand, the solar heat transmission part Q_r is written using Eqs. (A-10) and (A-13) in Appendix A as the summation over all the building envelope areas A_j

$$Q_r = AR''$$

where

$$R'' = \frac{1}{A} \sum_j \left[\left(\alpha_j A_j R''_j \frac{U_j}{\theta_{o,j}} \right)_{\substack{opaque \\ exterior \\ walls}} + (\tau_j A_j R_j)_{glazing} \right] \tag{10}$$

where R'' is the daily solar intensity for the building envelope representing the area-weighted average of

net solar heat gain to space due to both absorption by opaque walls and direct transmission by glazing, $\theta_{o,j}$ is the outside heat transfer coefficient as obtained from Eq. (A-4) in Appendix A, and R''_j is the average daily solar radiancy falling on an area A_j at a given orientation. Per unit gross floor area, the solar heat portion Q''_r is written as:

$$Q''_r = R'' \tag{11}$$

(11) The heat gain to a space due to the undesirable infiltration or exfiltration Q_x is determined following the air change method assuming that infiltrated air replaces the air in the space volume by several times each hour. Thus

$$Q_x = \gamma \Omega n_x (T_o - T_i)$$

where n_x is the number of infiltration air changes per hour, Ω is the volume of the building space, and γ is a conversion factor representing the air specific heat times the air density product. For air, γ is calculated at normal temperature and pressure (NTP), [15°C (59°F) temperature and 101 KPa (29.92 in. Hg) pressure] as 0.342 Wh/m^3°C. For a unit gross floor area, the heat gain by infiltration Q''_x is written as

$$Q''_x = \gamma h n_x (T_o - T_i) \tag{12}$$

where h is the average height of the building macrozone. The value of n_x usually ranges from 0.5 hr^{-1} in residential to 3 hr^{-1} in most industrial buildings. Weather stripping is one measure in reducing the effect of infiltration losses.

(12) Ventilation air is allowed in all building designs for hygienic purposes as well as for dust, moisture and odor removal. The amount of ventilation air can be computed by any one of the following four methods: (a) a number of air changes per hour n_v, (b) a specific volume rate supplied per occupant, (c) an air rate required per unit floor area of space or (d) a percentage ϵ of the total circulated air flow to the space. These four computational methods are alternates, and only one method should be selected as appropriate. Because the introduction of outdoor air is an energy-consuming and an expensive process in either winter or summer seasons, the amount of such air should always be kept at a minimum unless it is otherwise specified by health standards. By arbitrarily selecting the first computational method using the number of air changes per hour, n_v, the amount of heat gain associated with the ventilation air, is calculated analogous to Eq. (12) for the infiltration flow. Hence,

$$Q''_v = \gamma h n_v (T_o - T_i) \tag{13}$$

where the temperatures of both return and exhaust air streams in Fig. 1 are taken the same as the average inside space temperature T_i for a given day. Typical values of n_v for instance range from 1-12 in office buildings, 4-20 in restaurants, and 1-5 in apartments.

(13) A simple heat rate balance of the selected control volume in Fig. 1 on a given day and per unit floor area, gives

$$Q''_i + Q''_v = Q''_c - Q''_h \tag{14}$$

or by using Eqs. (1), (2), (3),

$$(Q''_g + Q''_r) + (Q''_a + Q''_x + Q''_v) = Q''_c - Q''_h$$

where Q''_c is the cooling load of the air handler cooling coils (energy extracted from the control volume) and Q''_h is the heating load of the air handler heating coils (energy added to the control volume). Note that simultaneous heating and cooling energies could be expended in a given period, such as the case in some multizone air handling units as described in Appendix B. In the summer season where $T_o > T_i$, the sum $(Q''_i + Q''_v)$ is always positive and it becomes most economical if the proper selection of the cooling setpoint is made to set Q''_h to zero. On the other hand, during the winter season where $T_i > T_o$, the sum $(Q''_i + Q''_v)$ could be, from Eq. (14), a negative, a zero or a positive quantity depending on whether the combined internal heat generation and the solar gain $(Q''_g + Q''_r)$ is less than, equal to, or greater than the combined transmission, infiltration, and ventilation losses $(Q''_a + Q''_x + Q''_v)$, respectively. The sum $(Q''_g + Q''_r)$ is treated from Eqs. (4), (5), (6), (7), and (10) as a positive parameter, independent of the ambient air temperature fluctuations while the sum $(Q''_a + Q''_x + Q''_v)$ depends on the average temperature difference $(T_o - T_i)$ using Eqs. (9), (12), and (13). Therefore, for most economical space conditioning in the heating season, it is essential to minimize or equate to zero the cooling energy expenditure Q''_c. This could be achieved by properly selecting the heating coil setpoint. Note that the relative magnitudes of Q''_c and Q''_h are obtained only by detailed examination of the temperature controls of each air handler as described in Appendix B. In general, for a unit gross floor area,

the gross sensible heat gain $(Q_i'' + Q_v'')$ from Eq. (14) is written using Eqs. (4), (5), (6), (7), (9), (11), (12), and (13) as

$$Q_i'' + Q_v'' = (s_p D_p + E_l'' + E_e'' + \lambda_m E_m'' + Q_f'' + R'') + [U + \gamma h(n_x + n_v)](T_o - T_i) \quad (15)$$

A plot of the relationship between the net sum $(Q_i'' + Q_v'')$ and the temperature difference $(T_i - T_o)$ from Eq. (15) gives, as sketched in Fig. 2, a straight line relationship in the form

$$Q_i'' + Q_v'' = \overline{A} - B(T_i - T_o)$$

where the intercept $\overline{A}$ is given as

$$\overline{A} = s_p D_p + E_l'' + E_e'' + \lambda_m E_m'' + Q_f'' + R'' \quad (16a)$$

The parameter $\overline{A}$ is always a positive quantity which represents the gross heat gain to the building space in the absence of any temperature difference between the inside and outside ambient temperatures. The building parameter $\overline{A}$ represents only the summation of heat gain due to people, lighting equipment, electronic equipment, electrical-powered machines, fuel-fired appliances and the direct solar heat gain through glazing areas and the indirect solar heat absorption by exterior walls. The slope B of the straight line relation in Fig. 2 is obtained also from Eq. (15) as

$$B = U + \gamma h(n_x + n_v) \quad (16b)$$

The parameter B represents the overall heat transfer coefficient due to thermal and fluid convection, conduction, and radiation between the building interior and exterior environments. The larger the slope B the more losses to the ambient the building will have for a given temperature difference $(T_i - T_o)$. A comparison of Eq. (16) and the known Hottel, Whillier and Bliss straight line performance equation for solar collectors (Ref. 7) indicates the resemblance in thermal behavior between solar collectors and buildings. By analogy, any building will act basically like an air solar collector but has two additional features: (a) internal heat generation rate, obtained from Eq. (16a) to equal $(A - R'')$, to augment the absorbed solar heat portion R'', and (b) heat losses due to air leakages, whether controlled or uncontrolled, to or from the ambient air due to infiltration and ventilation. This heat loss is represented by $\gamma h(n_x + n_v)$ in addition to the transmission part U.

The temperature difference at which the sum $(Q_i'' + Q_v'')$ changes its sign from positive (cooling mode) to negative (heating mode) is denoted by the characteristic building temperature difference ΔT^*. This is obtained from Eq. (15) by equating $(Q_i'' + Q_v'')$ to zero.

$$\Delta T^* = \frac{\overline{A}}{B}$$

For a fixed interior temperature T_i, the temperature T_o^* represents the characteristic outside air temperature below which heating the building is required and above which cooling is required. Note that T_o^* is always less than or equal to T_i since

$$T_i - T_o^* = \Delta T^* = \frac{\overline{A}}{B} \quad (17a)$$

Accordingly, in terms of T_o^*, the net heat (or loss) from the control volume is written as

$$Q_i'' + Q_v'' = B(T_o - T_o^*) \quad (17b)$$

Another interpretation of ΔT^* can be made for a given outside air temperature T_o, where the characteristic interior temperature T_i^* is defined as the "equilibrium" temperature at which the building should be, to result in zero heat gain or loss to the ambient. Note that T_i^* is always larger than or equal to T_o since

$$T_i^* - T_o = \Delta T^* = \frac{\overline{A}}{B} \quad (17c)$$

Accordingly, in terms of T_i^*, the net heat gain (or loss) from the control volume is written as:

$$Q_i'' + Q_v'' = B(T_i^* - T_i) \quad (17d)$$

Differentiation between heating and cooling modes or the winter and summer seasons is, therefore, a necessary step once the temperature T_o^* (or T_i^*) is determined. The first two modes represent the times when the outside air temperature T_o differs from T_o^*. If $T_o > T_o^*$, cooling will be the major mode of operation, and if $T_o < T_o^*$ heating will be the major mode of operation instead. Since the summer and winter seasons are taken in this model as the only two representative seasons of the year, the seasons could

be distinguished by whether the daily average temperature T_o differs from an arbitrary selected temperature.[1] When T_o^* differs from T_o, several possibilities can be shown in Fig. 3. In the winter season, both heating or cooling modes can exist, depending on the size of internal heat gain compared to the ambient transmission losses. The situation in summer is the same but with a minor difference. Summer days [with average outside temperature $T_o > 18.33°C$ (65°F)] will require cooling if $T_o > T_o^*$, which is the most common mode of operation. Less frequently is the heating mode in summer which could occur during mild summer days when T_o is higher than 65°F if the temperature T_o^* (which always has to be less than the inside temperature T_i) falls above T_o. In summary, a check of the relative magnitudes of T_i, T_o^* should be made in order to determine the major mode of HVAC equipment operation.

(14) The design of the air circulation rate throughout the building is commonly made based on peak heat gain or peak heat loss as determined by $Q_{i,max}$ or $Q_{i,min}$ during extreme hours. Two-speed fans are sometimes installed to discharge one air rate in summer and another rate, usually lower, in winter. Per unit gross floor area A, the air circulation rate V'' has been found (Ref. 2) to depend on the building function and normally lies within the range: 10-60 $m^3/(m^2 hr)$ [0.5-3 $ft^3/(ft^2\ min)$].

To check on the design value of V'', the following summer and winter flow rates V_s'' and V_w'' should be compared:

$$\left.\begin{aligned} Q_c'' &= (Q_i'' + Q_v'')_s = \gamma V_s''(T_i - T_{cp})_s + Q_{v,s}'' \\ -Q_h'' &= (Q_i'' + Q_v'')_w = \gamma V_w''(T_i - T_{hp})_w + Q_{v,w}'' \end{aligned}\right\} \quad (18)$$

where T_{cp} is the cooling setpoint [which varies from 10°C (50°F) to 15.6°C (60°F)] and T_{hp} is the heating setpoint [which varies from 21.1°C (70°F) to 32.2°C (90°F)]. If only a single air flow rate is used throughout the year, the larger V'' value from Eq. (18) is selected subject to meeting the other ventilation requirements.

(15) The heating, ventilation and air-conditioning equipment is assumed in the model to operate during the year continuously, regardless of the transient behavior of internal load sources. In practice, the HVAC equipment controls will be intermittent in operation with some cycling on and off, depending on the internal loads and the desired inside temperature. Several energy conservation measures call for shutting down HVAC equipment during some predetermined periods such as on weekends, holidays, or during any other periods when the building is unoccupied. These measures claim to reduce the energy consumption and allow the inside space temperature to drift either higher or lower than what is normally set at. This latter temperature drift is not undesirable since the building is unoccupied. However, depending on the magnitude of the heat capacity (or thermal mass) of the building walls, furniture, equipment, etc., and depending on the shutdown duration period, these energy measures may or may not be very effective. The reason is due to the additional energy expenditure either in heating or in cooling needed to bring the building space back to its desired inside temperature after a given shutdown period. This additional energy consumption may or may not offset the energy savings incurred. However, one needs to distinguish between the difference of turning off an air handler during unoccupied periods as mentioned above, and the installation of timers, for instance, to lighting equipment or to any other non-HVAC related equipment for the purpose of energy conservation. The first affects the building energy content while the second is considered part of the internal load fluctuations or transient behavior. Alternating cloudy and sunny days are analogous to the second type of controls by timers which are already accounted for in the model as a reduced daily value of the parameter $\bar{A}$ in Eq. (16).

Since the hourly fluctuations of internal loads will be damped and averaged out if longer periods are studied, the building model assumes the quasi-steady-state case if a minimum of 24-hour modeling period is selected. The fluctuations that could take place due to the building thermal mass are minimized. The model also excludes measures of shutting down HVAC equipment and assumes their operation at all times is uninterrupted. Hence, the heating or cooling loading Q_h or Q_c will represent the equivalent quasi-steady-state loading for the day, month, or season under study.

(16) Regarding the cooling equipment, the type of input energy used could be either in electrical form (e.g., mechanical-driven vapor compression refrigerators) or thermal (e.g., absorption refrigerators driven by fossil fuel combustion, waste heat, solar energy, etc.).

[1] Heating degree days and cooling degree days are based in most weather bureaus on 18.33°C (65°F) reference temperature.

Similarly, the heating equipment could be either electrically powered (e.g., electric-resistance heaters and heat pumps) or thermally powered (e.g., fuel fired heaters or solar heaters, etc.). To simplify the energy accounting, the building space under consideration is assumed to be powered by only two types of energy – electrical and thermal. If more than one fossil fuel is employed in fuel-fired equipment, or if different nonfuel sources of heat are consumed, a unified thermal conversion should be used to unify all thermal energies or fuel rates into one appropriate thermal unit (e.g., kWh(t), therm, Btu, joule). One electrical meter connected to the building would indicate the energy sum of: (a) lighting equipment E_l, (b) internal electronic and electrical equipment which have no motor drives, E_e, (c) mechanical equipment with motor drives E_m, (d) cooling equipment E_c, if electrically driven, (e) heating equipment E_h, if electrically driven, and (f) all electrically powered accessories. The latter accessories are excluded from all internal heat gain calculations although some may have a minor effect. Accessories are divided in the analysis into two groups only as follows:

(a) Accessories that are related to space air conditioning and air circulation such as supply fans, return fans, exhaust fans, boiler circulating pumps, chilled water circulating pumps, condenser fans, cooling tower fans, etc. These accessories consume energy E_{ax1}, proportional to the load of their mother air-handling equipment. The air temperature rise in supply and return fans is assumed negligible with respect to the internal load Q_i. However, the fans' power is still computed as part of the accessories and it is not neglected.

(b) Accessories that are unrelated to HVAC equipment. These are likely to be physically located outside the building control volume, such as the external lights, water pumps for pools, etc. This type of accessory consumes electrical energy E_{ax2} in direct relation only to the building's external activity.

Accordingly, the total electrical meter reading E can be written as the sum:

$$E = E_l + E_e + E_m + E_c + E_h + E_{ax1} + E_{ax2} \tag{19}$$

A similar discussion of a single electrical meter could be made for a single "thermal" meter connected to the building. The thermal meter indicates the sum of all thermal energies consumed in (a) internal fuel-fired appliances G_f, (b) cooling equipment G_c, if heat driven, (c) heating equipment Q_h, if heat driven, and (d) all heat-powered accessories G_{ax}. The thermal accessories are commonly unrelated to HVAC equipment and located outside the building conditioned space such as external heating equipment in swimming pools or in domestic hot water boilers. For the above thermal meter, the total reading G will be

$$G = G_f + G_c + G_h + G_{ax} \tag{20}$$

Note that G_f and G_{ax} are the thermal energies supplied to devices inside the conditioned space and to space-external accessories, respectively, taking into account their conversion efficiency.

(17) To accommodate the simultaneous existence of both types of electrical and thermal-driven coolers or heaters, the fraction of load which is satisfied by each energy type needs to be defined. If β is the fraction of load that is provided by electricity powered devices, then after accounting for the component conversion efficiencies, the cooling equipment consumption will be

$$\left.\begin{aligned} E_c &= \beta_c Q_c/\eta_{ec} \\ G_c &= (1-\beta_c)Q_c/\eta_{fc} \end{aligned}\right\} \tag{21}$$

and for the heating equipment, the consumption will be

$$\left.\begin{aligned} E_h &= \beta_h Q_h/\eta_{eh} \\ G_h &= (1-\beta_h)\,Q_h/\eta_{fh} \end{aligned}\right\} \tag{22}$$

where η_{ec}, η_{fc} are the coefficients of performance of electrical-powered and heat-powered coolers, respectively, and η_{eh}, η_{fh} are the efficiencies of electrical- and heat-powered heaters, respectively.

Once the cooling load Q_c and heating load Q_h are computed, as in Appendix B, subject to the constraints of the temperature-control mechanism of air handlers, Eqs. (19) and (20) are used to give the total electrical and thermal meter readings E and G for the period under investigation.

(18) The energy utilization index is a common measure for rating buildings which have the same functional utilization. The index divides the total energy consumption for the season by the gross floor area of the

building. Since there are two types of energy provided, two energy indices are possible – one for electrical and the other for thermal. A modified representation of the annual energy consumption is to convert the electrical index to an equivalent thermal index by taking into consideration the conversion efficiency at the electrical power plant η_{pp} and add it to the thermal index. Hence, in equivalent thermal units, the energy utilization index representing the energy consumption per unit floor area is written as:

$$I = G'' + E''/\eta_{pp} \tag{23}$$

(19) The operating costs of energy are computed in the analysis based on a simple uniform tariff throughout the year, independent of demand charges, power factors or other seasonal charges. This uniform rate structure could be obtained by dividing the annual cost of energy by the annual energy consumption. If C_e and C_f are the costs of unit electrical and fuel energies, respectively, then the total energy cost per unit floor area C'' is written as:

$$C'' = C_e E'' + C_f G'' \tag{24}$$

The above 19 points constitute the assumptions and idealizations needed for the sensitivity analysis to be developed for any 24-hour period in any season. On a yearly basis, the annual energy index I_y, which is the sum of summer and winter effects, is computed taking into consideration an average of 730 hours per month as

$$I_y = 730(M_s I_s + M_w I_w) \tag{25}$$

where I_s and I_w are the summer and winter season utilization indices, obtained from Eq. (23). For most buildings, the annual energy index I_y ranges from 126 kWh/m^{2}yr (about 40,000 Btu/(ft^{2}yr)) to 1260 kWh/m^{2}yr (400,000 Btu/(ft^{2}yr)) depending on the building usage, size, internal loads, etc.

Before a general expression for modeling air handling equipment could be made, an investigation of various temperature controls was carried out (Appendix B). Different air-handler designs affect to a great extent the determination of the equipment heating and cooling loads. Q_h and Q_c, respectively. A simplified approach to this equipment loading is needed to enable the engineers to make a reasonable assessment of energy conservation measures without being lost in the specific design details.

III. Air Handler Model

Four different types of air handlers are briefly described in Appendix B, to demonstrate their differences in responding to heating and cooling needs. The variation of the quantities Q_c and Q_h takes place according to the type of temperature control, coil setpoints and air flow rate. For a sensitivity analysis to be complete, the specific features of the building air handler(s) dealing with the major loads have to be given. The analysis, in turn, will be narrowly directed toward a specific configuration rather than the general case originally intended. A generalized but simple air handler model is, therefore, sought for the present sensitivity study. While the selected methodology is still applicable to any specific air handler configuration, minor alterations may be necessary. In the simplified air handler configuration, the sum $(Q_i'' + Q_v'')$ is always positive in the cooling mode where only cooling energy is assumed expended upon the proper adjustment of cooling set points. Hence,

$$\left.\begin{aligned} Q_h'' &= 0 \\ Q_c'' &= Q_i'' + Q_v'' \end{aligned}\right\} \tag{26}$$

Similarly, in the heating mode, the net sum $(Q_i'' + Q_v'')$ is always negative where only heating energy is assumed consumed,

$$\left.\begin{aligned} Q_c'' &= 0 \\ -Q_h'' &= Q_i'' + Q_v'' \end{aligned}\right\} \tag{27}$$

Combining Eqs. (26) and (27) with Eqs. (19), (20), and (23), we can write the energy utilization index for cooling and heating modes as

$$I_{cm} = (G_f'' + G_c'' + G_{ax}'')_{cm} + \frac{1}{\eta_{pp}}(E_l'' + E_e'' + E_m'' + E_c'' + E_{ax1}'' + E_{ax2}'')_{cm} \tag{28}$$

$$I_{hm} = (G_f'' + G_h'' + G_{ax}'')_{hm} + \frac{1}{\eta_{pp}}(E_l'' + E_e'' + E_m'' + E_h'' + E_{ax1}'' + E_{ax2}'')_{hm} \tag{29}$$

Furthermore, by using Eqs. (21) and (22) and regrouping of terms, the indices I_{cm} and I_{hm} give the following

At $T_o > T_o^*$ (cooling mode)

$$I_{cm} = (G_f'' + G_{ax}'')_{cm} + \frac{1}{\eta_{pp}}(E_l'' + E_e'' + E_m'' + E_{ax1}'' + E_{ax2}'') + \left(\frac{1-\beta_c}{\eta_{fc}} + \frac{\beta_c}{\eta_{ec}\,\eta_{pp}}\right)(Q_i'' + Q_v'')_{cm} \tag{30a}$$

At $T_o < T_o^*$ (heating mode)

$$I_{hm} = (G_f'' + G_{ax}'')_{hm} + \frac{1}{\eta_{pp}}(E_l'' + E_e'' + E_m'' + E_{ax1}'' + E_{ax2}'') - \left(\frac{1-\beta_h}{\eta_{fh}} + \frac{\beta_h}{\eta_{eh}\,\eta_{pp}}\right)(Q_i'' + Q_v'')_{hm} \tag{30b}$$

where the sum $(Q_i'' + Q_v'')$ at any particular mode is obtained from Eq. (15) as

$$Q_i'' + Q_v'' = (Q_p'' + E_l'' + E_e'' + \lambda_m E_m'' + Q_f'' + R'') + [U + \gamma h (n_x + n_v)]\,(T_o - T_i) \tag{31}$$

Equations (24), (25), (30), and (31) constitute the basic equations of the simplified model needed to obtain the sensitivity relations.

IV. Building Parameters

It is beneficial to the building designer, or owner, to observe, both in magnitude and direction, the effects of small or large changes imposed on the variables and parameters affecting the building energy consumption and operation costs. The sensitivity S, which is the measure of the dependency of a system output Y on variations of a particular input element or parameter X, keeping all other input parameters unchanged, is expressed analytically as:

$$S = \frac{\Delta Y/Y}{\Delta X/X} \quad \text{or} \quad S = \frac{dY}{dX}\cdot\frac{X}{Y} \quad \text{or} \quad S = \frac{d\ln Y}{d\ln X} \tag{32}$$

where Δ represents a differential change in either X or Y, as sketched in Fig. 4. Equation (32) is computed at a reference operating condition of the entire system. A system operating at an optimum value of one of its elements should have zero sensitivity with respect to this element. The concept of sensitivity has been widely used in studying many physical systems, and its present application to energy consumption in buildings is a useful tool in identifying key parameters for optimum energy utilization. The input element, or parameter X, could be any one of the following 30 elements.

Weather parameters

- Outside air temperature T_o
- Outside air pressure p
- Local solar radiation R''
- Wind velocity v_d

Building architecture

- Average height of conditioned space h
- Equivalent heat transmission coefficient U
- Exterior wall absorptivity α
- Glazing transmissivity τ
- Glazing area/floor area ratio
- Opaque wall surface area/floor area ratio

Occupants

- Population density D_p
- Activity or sensible heat generated per person s_p

Internal equipment

- Lighting power density E_l''
- Power density of electronics and electrical equipment without motor drives E_e''
- Power density of electromechanical equipment with motor drives E_m''

Heat rate of fuel-fired equipment Q''_f

Hours of operation of each piece of equipment H

Environment control

Inside space temperature T_i

Total air circulation rate V''

Infiltration air change rate n_x

Ventilation air change rate n_v

Type of air-handler temperature control

Accessories

Power density of electrical accessories E''_{ax}

Heat rate of heat-powered accessories G_{ax}

Equipment performance

Coefficient of performance of coolers η_{ec}, η_{fc}

Efficiency of heaters η_{eh}, η_{fh}

Fraction of electrically powered coolers or heaters β_c, β_h

Electrical power plant efficiency η_{pp}

Costs

Cost of a thermal energy unit C_f

Cost of an electrical energy unit C_e

The building output Y could be any one of the following: (1) the energy utilization index I, (2) the total energy cost C, or (3) any suitable output from the above analysis. Denoting the energy index sensitivity to an input parameter X by S and the total cost sensitivity by $\overline{S}$, the analysis is carried out for the above input parameters using the equations described in Sections II and III. Accordingly, the sensitivity expressions for S and $\overline{S}$ using Eqs. (23), (24), and (32) will be written as:

$$S = \frac{X}{I}\left[\frac{\partial G''}{\partial X} + \frac{\partial (E''/\eta_{pp})}{\partial X}\right] \tag{33}$$

$$\overline{S} = \frac{X}{C''}\left[\frac{\partial (C_e E'')}{\partial X} + \frac{\partial (C_f G'')}{\partial X}\right] \tag{34}$$

Furthermore, if the unit electrical energy cost C_e is directly related to the unit thermal energy cost C_f, through the power efficiency η_{pp} as

$$C_e = \frac{C_f}{\eta_{pp}} \tag{35}$$

then, the sensitivity expressions S and $\overline{S}$ become identical, and in this case, Eqs. (23) and (24) are reduced to

$$C'' = C_f I \tag{36}$$

Since Eq. (35) is considered in practice a good approximation to the unit energy costs, it results that only the sensitivity S needs to be determined for all parameters involved.

The sensitivity expressions are also beneficial in determining the total system variation when more than one input parameter are simultaneously changing. Since the building output Y is a function of all input independent variables, X_1, X_2,. . . (i.e., $Y(X_1, X_2, \ldots)$ it can be proved that

$$\frac{\Delta Y}{Y} = S_1\left(\frac{\Delta X_1}{X_1}\right) + S_2\left(\frac{\Delta X_2}{X_2}\right) + \cdots \tag{37}$$

where S_1, S_2,. . . are sensitivities of the output Y to each of the parameters $X_1, X_2, \ldots$, respectively.

When computing the changes in the annual energy index I_y with respect to an input parameter X due to changes in the summer only, in the winter only, or in both seasons, Eq. (25) gives

$$\Delta I_y = 730\left[M_s\left(\frac{\Delta I}{\Delta X}\right)_s \Delta X_s + M_w\left(\frac{\Delta I}{\Delta X}\right)_w\right]\Delta X_w \tag{38}$$

where I_s, I_w are the energy utilization indices obtained from Eqs. (30) and (31) for the cooling and heating modes of each season, and $\Delta X_s, \Delta X_w$ are the expected summer and winter changes in the input parameter X, respectively.

V. Data of a Hypothetical Office Building

The weather, architectural, internal and external loads data and operating conditions of a hypothetical office building are grouped to form a baseline configuration for the study. Typical office building data and design values are utilized to the maximum extent to represent closely actual conditions except for the artificial inclusion of some energy-consuming equipment that is not necessarily available in all office-type buildings. Hence, the chosen example building represents

neither an existing office building nor an "ideal" configuration from energy conservation viewpoint. The building data are hypothetically constructed this way to illustrate the wide spectrum of energy modification measures and to assist in the numerical evaluation of the sensitivity expressions. The methodology that is followed in analyzing this building, however, could be applied to any other type of office or non-office building. The building site is arbitrarily selected to be at the Deep Space Network Communication Complex, Goldstone, California. Other data are categorized as follows:

Site	
Location	Goldstone, California, USA
Latitude	35° north
Elevation	About 610 m (2000 ft)
Barometric pressure p	93.91 kPa (27.82 in. Hg)
Weather	
Heating degree days, HDD[2]	1549.4°C (2789°F) day
Heating days d_w[2]	212
Heating months M_w[2]	7 (Oct – Apr)
Average outside air temperature during the winter[3] season $T_{o,w}$	51.84°F (11°C)
Sensible-cooling degree days, SCDD[4]	1143.9°C (2059°F) day
Cooling days[4] d_s	153
Cooling months[4] M_s	5 (May – Sept)
Average outside air temperature during the summer season[5] $T_{o,s}$	78.46°F (25.81°C)
Wind velocity v_d	16 km/hr (10 mph)
Building envelope	
Gross floor dimensions[6]	30.5 X 30.5 m (100 X 100 ft)
Space height h	3.1 m (10 ft)
Orientation	Sides are facing compass, E, W, N, and S directions
Occupants	
Gross floor area[7] allocated/person $1/D_p$	10.3 m²/person (111 ft²/person)
Sensible heat dissipation rate[8] s_p	117 W/person (400 Btu/(hr person))
Occupancy duration[9] H_p	2260 hr/yr
Internal lighting	
Design intensity D_l	32.3 W/m² (3.0 W/ft²)
Lighting hours[10] H_l	2760 hr/yr
Internal electrical equipment	
Installed power density D_e[11]	16.1 W/m² (1.5 W/ft²)
Operating hours[12] H_e	1000 hr/yr

[2]The site heating degree days per day is the difference between 18.33°C (65°F) and the daily mean temperature when the latter is less than 65°F. Data are taken from average weather statistics over a 10-year period for the Goldstone Space Communication Complex at Goldstone, California. For major cities or locations, HDD values appear in Ref. 2 or from weather bureaus.

[3]Obtained from the formula

$$T_{o,w} = \left(65 - \frac{\text{HDD}}{d_w}\right), \ °\text{F}$$

[4]The site cooling degree day is defined in Ref. 2 by a complex expression compared to the heating degree day, since the energy consumption for a cooling process is affected not only by the dry bulb temperature, but also by the air relative humidity. Since latent heat calculations are assumed negligible in the present simplified model, an analogous definition to the heating degree day is adopted. The number of sensible cooling degree days per day is the difference between 18.33°C (65°F) and the daily mean temperature when the latter is higher than 65°F. Data are obtained from weather records of the site under investigation.

[5]Obtained from the formula

$$T_{o,s} = \left(65 + \frac{\text{SCDD}}{d_s}\right), \ °\text{F}$$

[6]Building dimensions do not enter into the calculations since all the expressions are evaulated per unit floor area.

[7]Assuming 90 occupants in the building. The occupation density is selected to fit closely densities in office-type buildings.

[8]Assumed the same in both summer and winter seasons

[9]Assuming 9 hr/day (from 8 a.m. to 4 p.m.) for 251 working days per year. This excludes weekends and 10 holidays/year.

[10]Based on 11 hr/day (7 a.m. to 5 p.m.) for 251 working days/year. Evenly distributed over each season.

[11]An assumed figure which is obtained by summing the power of copying machines, TV sets, typewriters, CRT displays, vending machines, water fountains, and other appliances.

[12]Based on an average of 4 hr/day for 250 work days/yr.

Internal fuel-fired equipment	
Installed capacity[13] D_f	15 W/m^2
Operating hours H_f	1000 hr/yr
Internal thermal load Q''_f	1.71 W/m^2

Inside temperatures	
Summer[14] $T_{i,s}$	23.89°C (75°F)
Winter[14] $T_{i,w}$	23.89°C (75°F)

Architecture	
U factors[15]	
Single glass pane	1.13 Btu/(hr ft^2°F) or 6.42 W/m^2°C
Walls	0.3 Btu/(hr ft°F) or 1.70 W/m^2°C
Roof	0.18 Btu/(hr ft°F) or 1.02 W/m^2°C
Floor	Insulated
Area ratios	
Roof/floor	1.0
Gross wall/floor	0.1 for each orientation
Glazing/wall	0.30 for each orientation
Glazing/floor	0.03 for each orientation
Opaque wall/floor	0.07 for each orientation
Optical properties	
Glazing transmissivity, τ	0.80 (all glazing)
Exterior wall absorptivity, α	0.60 (all walls)

Ventilation air	
Ventilation air[16]	25 ft^3/(person min) or 0.71 m^3/(person min)
Number of air changes per hour n_v[17]	1.35

Infiltration air	
Number of air changes per hour n_x	1.2

Primary equipment	
Power plant thermal efficiency n_{pp}	0.33
Coefficient of performance[18] of electrical-driven chillers n_{ec}	2.8
Coefficient of performance[18] of thermal-driven chillers n_{fc} (absorption refrigeration)	0.65
Efficiency of electrical[18] resistance heaters/boilers n_{eh}	0.9
Efficiency of fuel-fired[18] boilers n_{fh}	0.6
Fraction of building cooling load[19] that is provided by electrical powered chillers β_c	1.0
Fraction of building heating load[20] that is provided by electrical resistance heaters β_h	0.0

Accessories	
Supply fan	
Air rate	1 ft^3/(ft^2 min) floor area
Operating hours H_{fan}	8760 hr/yr
Static pressure Δp_{fan}	3 in. water
Electric power per gross floor area[21] E''_{ax1}	5.75 W/m^2 (0.53 W/ft^2)

[13] A mini cafeteria is assumed located in the building providing some snacks for 90 persons. Cooking appliances using natural gas are assumed.

[14] Before the present mandatory energy conservation measures.

[15] Assumed the same in summer and winter seasons.

[16] This will amount to 2250 ft^3/min (63.71 m^3/min) for the building with 90 occupants. The ventilation rate is also equivalent to 0.225 ft^3/(ft^2 min) of gross floor area.

[17] Calculated by dividing 2250 ft^3/min (63.71 m^3/min) of ventilation air rate by the volume of space.

[18] Includes the accessories load such as condenser fans, cooling pumps, boiler pumps, etc.

[19] In this example building, all chillers are assumed electrically powered.

[20] In this example building, all heaters are assumed fuel-fired.

[21] Using the formula: Fan power = $\dot{V}$ cfm × ΔP in. water/ηfan × 8.507, watts, and assuming a 66% fan efficiency.

Domestic hot water heater	
Operating period	250 days/yr
Operating temperature[22]	40.56°C (105°F)
Type of heater	Fuel-fired (natural gas)
Energy consumption[23] G''_{ax}	0.53 W/m^2 (1473 Btu/yr ft^2)
External lighting	
Design intensity D_{ex2}	5.4 W/m^2 (0.5 W/ft^2)
Lighting hours[24] H_{ex2}	4015 hr/yr
Average external lighting power E''_{ax2}	2.48 W/m^2

Energy cost	
Yearly average cost of an electrical unit C_e	0.06 $/kWh(e)
Yearly average cost of a thermal unit C_f	0.02 $/kWh(t)

To manipulate Eq. (15), additional information representing the hypothetical office building at the configuration given is calculated, per unit gross floor area as follows:

People internal load Q''_p[25]	2.92 W/m^2
Internal lights $Q''_l = E''_l$	10.18 W/m^2
Internal electrical and mechanical applicances load[25] $Q''_e = E''_e$	1.84 W/m^2
Daily average solar intensity[26] R''	
For the summer season	20.38 W/m^2
For the winter season	15.05 W/m^2
Specific heat • density product[27] γ	0.318 Wh/m^3°C

[22]Following present energy conservation measures.

[23]Domestic water is assumed heated from 50 to 105°F. The energy consumed in Btu/yr ft^2 is obtained from:

$$\frac{\text{gallon}}{\text{day person}} \times \Delta T^\circ F \times 8.33 \frac{\text{lb}_m}{\text{gallon}} \times \frac{\text{operating days}}{\text{yr}} \times \frac{D_p}{\eta_{boiler}}$$

taking $1/D_p$ as 111 ft^2/person, η_{boiler} as 70%, and 1 gallon/day per person.

[24]Based on 11 hr/day (7 to 5 pm) for full year.

[25]Using Eqs. (4), (5), and (6).

[26]Using Eq. (10) and Table 1.

[27]Obtained from the relation $\gamma = \gamma^* (P/P^*)$, where P^* is the standard atmospheric pressure (29.92 in. Hg or 101 KPa), γ^* is calculated at NTP as 0.342 Wh/m^3°C. See Ref. 4 for the variation of P^* with site elevation.

Overall heat transfer coefficient[28] U	2.269 W/m^2°C (0.4 Btu/hr ft^2°F)
Building intercept parameter[29] $\overline{A}$	
In summer	37.03 W/m^2
In winter	31.70 W/m^2
Building slope parameter B	4.783 W/m^2°C
Characteristic temperature T^*_o	
In summer	16.15°C (61.07°F)
In winter	17.26°C (63.07°F)
Modes of operation during each season	
Since in summer $T_{o,s} > T^*_{o,s}$	All cooling
Since in winter $T_{o,w} < T^*_{o,w}$	All heating
Seasonal energy utilization index	
Summer I_s	113.614 W/m^2
Winter I_w	113.337 W/m^2
Annual EUI I_y	993.8 kWh/m^2 (315,100 Btu/ft^2 yr)

VI. Sensitivity Results

In the previous building example, deliberate inclusion of some energy-consuming equipment was made to show later on the impact of future energy conservation measures. Most parameters used in the sensitivity analysis are expressed in both the metric units (SI) and the common English units. Each parameter is analyzed, for convenience, separately to assess its individual weight on the energy utilization index. This first part of the study is directed toward the understanding of the exterior environment parameters. The rest of the building parameters are examined later in part 2 of this article. Sensitivity derivations are generally avoided for they are self-explanatory from Sections III and IV.

A. Outside Air Temperature

By neglecting the effect of outside air temperature variations on the efficiency of air-conditioning equipment and their associated accessories, the rate of change of I with respect to the average outside temperature T_o is found from:

[28]Using Eq. (8) and Appendix A where

$$\theta_o = \left(1 + \frac{v_d}{3}\right) \text{Btu/hr ft}^2\,^\circ\text{F}$$

where v_d is the wind velocity in mile/hr. For 10 mph, θ_o is about 4.33 Btu/hr ft^2°F (24.59 W/m^2°C).

[29]Using Eq. (16).

$$\left.\begin{aligned} \Delta I_{cm} &= \zeta_c B \Delta T_{o,s} \\ \Delta I_{hm} &= \zeta_h B \Delta T_{o,h} \end{aligned}\right\} \quad (39)$$

where B is the building characteristic thermal loss rate given by Eq. (16b) and ζ_c, ζ_h are the cooling and heating coupling coefficients, respectively, given by

$$\left.\begin{aligned} \zeta_c &= \frac{1-\beta_c}{\eta_{fc}} + \frac{\beta_c}{\eta_{ec}\,\eta_{pp}} \\ \zeta_h &= \frac{1-\beta_h}{\eta_{fh}} + \frac{\beta_h}{\eta_{eh}\,\eta_{pp}} \end{aligned}\right\} \quad (40)$$

Any change in the outside air temperature could take place because of possible yearly variations, due to a different location for the example building, or simply due to an error in measurement. An increase in the yearly average outside temperature will cause an increase in the summer index or a decrease in the winter index. Referring to the numerical example, for instance, a 5°F (2.78°C) increase in the average outside air temperature during the summer will represent an increase of the cooling degree days from 2059 to 2824 for the same number of days, or a 37% increase. This will increase the summer index by 14.38 W/m², which represents a 12.7% increase of the reference summer index. On the other hand, the winter reference index will decrease by 22.15 W/m² if the average outside air temperature in winter increases by 5°F (2.78°C). The latter represents a decrease of the heating degree days (HDD) from 2789 to 1730 for the same number of days, (i.e., a decrease of 38% of HDD). The change in the winter index, thus represents a 19.5% of the reference winter index. The change in the annual index I_y follows from the relation

$$I_y = 730\,(M_s \zeta_c B\, \Delta T_{o,s} - M_w \zeta_h B\, \Delta T_{o,w}) \quad (41)$$

The maximum effect of ambient temperature changes is felt when there is a drift to simultaneous higher temperature in summer and lower temperature in winter, than the reference weather given. If the average daily summer and winter outside temperatures are 83.46°F (28.59°C) and 46.84°F (8.24°C), respectively, (i.e., a change of +5°F during the summer and -5°F during the winter[30] or an amplitude change of 38%). The differential increase in the yearly index I_y becomes +165.7 kWh/(yr m²), i.e., an increase of 16.7 compared to the reference conditions. This gives an EUI sensitivity to outside air temperature variations in the order of 0.44, which could have a significant effect on consumption.

A further examination of Eq. (41), shows that the dominant parameter in ΔI_y is the building characteristic slope B. Building measures which reduce the overall transmission U-factor, infiltration and ventilation rates n_v and n_x will reduce the magnitude of B, thus reducing the role of extreme weather fluctuations on the annual energy consumption.

B. Outside Air Pressure

Variations of the outside air barometric pressure for the example building could take place due to daily weather changes caused by the movement of earth-air boundary layer, or due to designing the building at a different elevation above the sea level, or due to some errors in pressure measurements. The specific heat-density product γ depends mainly on pressure changes (Ref. 4) and is proportional to the pressure P. For instance, if the example building is located at an elevation of 4000 ft instead of 2000 ft above sea level, the barometric pressure P will change to 25.84 in. Hg, i.e., a decrease of 7.1% from the given site pressure. The new value of γ becomes 0.295 Wh/m³°C, and the slope $\Delta I/\Delta\gamma$ is obtained from Eqs. (30) and (31) as:

$$\left.\begin{aligned} (\Delta I/\Delta\gamma)_s &= h\,\zeta_c\,(n_x + n_v)\,(T_o - T_i)_s \\ (\Delta I/\Delta\gamma)_w &= -h\,\zeta_h\,(n_x + n_v)\,(T_o - T_i)_w \end{aligned}\right\} \quad (42)$$

This means that the lower the outside air pressure, the lower the consumption will be in both seasons. The result of the above elevation change is a decrease in the summer index by 0.4 W/m² and a decrease in the winter index by 3.9 W/m², which reduces the annual index by 3.9 W/m², and reduces the annual index, from Eq. (38), by only 21.4 kWh/m². yr. (i.e., -2% of the annual index). Hence, the effect of changing the outside air pressure or having different site elevation is not insignificant, with a sensitivity S in the order of +0.28.

C. Solar Radiation

Given that all other parameters are the same, the seasonal variation of solar radiation falling on a given building site would be affecting directly the building solar characteristic R'' for all wall orientations. Although there is an intrinsic relationship between the solar radiation on a given area and the earth-boundary layer outdoor air temperature, the two are assumed independent of each other. The slope $\Delta I/\Delta R''$ will be obtained from Eqs. (30) and (31) as

[30] The annual average outside air temperature is calculated as 17.2°C (62.93°F) based on 5 summer months at an average of 25.8°C (78.46°F). and 7 winter months at an average of 11°C (51.84°F). The changed annual average outside air temperature becomes 16.7°C (62.1°F).

$$\left.\begin{aligned}(\Delta I/\Delta R'')_x &= \zeta_c \\ (\Delta I/\Delta R'')_w &= -\zeta_h\end{aligned}\right\} \quad (43)$$

which shows the direct correspondence between solar radiation and energy utilization index. For instance, an increase in R'' by 10% in both summer and winter due to either a change in R''_j from Eq. (10), or even an error in computations, will cause an increase in the summer index by 2.21 W/m^2 and a decrease in the winter index by 2.51 W/m^2. This results in a yearly index change of only -0.5%. The percentage change represents a sensitivity S in the order of 0.05, which could be larger if the summer increase of R'' is accompanied by a simultaneous decrease in winter. In this case, an increase of 10% of solar radiation in summer and a decrease of 10% in solar radiation in the winter will cause the index I_y to increase by 2.9%. The solar radiation sensitivity S is, therefore, in the order of 0.3, which is also a significant part of the exterior weather effects.

D. Wind Velocity

Changes in the local wind currents will affect the computations of the following quantities: (a) the building overall heat transmission coefficients U, (b) the infiltration rate n_x, due to air leakage, and (c) the exterior wall heat transfer coefficient θ_0 which appears in the solar parameter R''. An increase in the wind velocity by Δv_d affects each of the above quantities differently, for it will enlarge the coefficients θ_0 and U, but will reduce the parameter R''. The slope $\Delta I/\Delta v_d$ is obtained, by differentiation, as:

$$\left.\begin{aligned}\left(\frac{\Delta I}{\Delta v_d}\right)_s &= \zeta_c\,[\Delta R'' + (T_0 - T_i)(\Delta U + \gamma h\,\Delta n_x)]_s \\ \left(\frac{\Delta I}{\Delta v_d}\right)_w &= -\zeta_h\,[\Delta R'' + (T_o - T_i)(\Delta U + \gamma h\,\Delta n_x)]_w\end{aligned}\right\} \quad (44)$$

Note that the wind velocity builds up a pressure on the windward side of the building and a slight vacuum on the leeward side. The outdoor pressure buildup causes air to infiltrate in the windward side and exfiltrate on the leeward side. Offsetting the infiltration/exfiltration air is usually made, though not completely, by weather stripping and pressurizing the air circulation loop. For the example building, one finds that by increasing the average wind velocity to 20 mph instead of 10 mph (an increase of 100%), and assuming a negligible change Δn_x, then the change in the coefficient U, (using Eq. A-9) will be from 1.13 to 1.275 Btu/(hr ft^2°F) for glazing, from 0.3 to 0.309 Btu/(hr ft^2°F) for opaque walls, and from 0.18 to 0.183 Btu/(hr ft^2°F) for the roof. The new overall heat transfer coefficient will be 0.423 Btu/(hr ft^2°F) or 2.4 W/m^2°C. The solar parameter R'' will also change to 16.79 W/m^2 in the summer and to 12.77 W/m^2 in the winter. The changes in the energy index will be -3.61 W/m^2 in the summer and +6.63 W/m^2 in winter. The yearly index will change, therefore, by +20.7 W/m^2, i.e., increases by 2.1% percentage. The wind velocity effect, as a result, produces a sensitivity S in the order of +0.02. Though the effect of wind speeds in summer is advantageous to air conditioning for the wind acts as a cooling medium, this function in winter becomes undesirable. However, the sensitivity to wind currents is generally of a negligible magnitude.

VII. Summary

A simple analytical model is developed for the simulation of seasonal heating and cooling loads of any class of buildings. The model complements other computerized techniques, previously developed also at the Deep Space Network Engineering Section, to act as a design tool in screening and evaluating energy conservation measures. A general expression for the annual Energy Utilization Index (EUI) is given to include about 30 parameters for both building interior and exterior environments.

The first part of the study is focused on the EUI sensitivity to exterior weather parameters. A hypothetical office type building located at the Goldstone Space Communication Complex, Goldstone, California, is selected for the numerical analysis. The effects of variations in outside air temperature, pressure, and solar radiation are found to be of the same order of magnitude with a sensitivity range from 0.3 to 0.5. Wind currents have shown a negligible effect on consumption. Part 2 of the study, which covers the effects of the interior environment parameters, is being developed and will be presented in a future *TDA Progress Report*.

Acknowledgement

The author would like to acknowledge S. N. Higgins who assisted in the initial phase of the model and who made a number of helpful suggestions in the study preparation.

References

1. Lansing, F. L., et al., *A Computer Model Simulating Heating, Cooling and Energy Loads in Buildings*," Publication 78-76, Jet Propulsion Laboratory, Pasadena, Calif., Sept. 1978.
2. Stamper, E., and Koral, R. L., editors., *Handbook of Air Conditioning, Heating and Ventilating*, Industrial Press. Inc., New York, N.Y., 1979.
3. *Handbook of Fundamentals*, American Society for Heating, Refrigeration and Air Conditioning Engineers (ASHRAE), New York, N.Y., 1972.
4. *Carrier System Design Manual*, Carrier Air Conditioning Co., Syracuse, N.Y., Part 1-12, 1972.
5. Kusuda, T., and Ishii, K., *Hourly Solar Radiation Data for Vertical and Horizontal Surfaces on Average Days in the United States and Canada,* NBS Building Science Series 96 NBS, U.S. Dept. of Commerce, April 1977.
6. Threlkeld, J. L., *Thermal Environmental Engineering*, Prentice Hall, Inc., 1962.
7. Whillier, A., "Design Factors Influencing Solar Collector Performance," *Low Temperature Engineering Application of Solar Energy*, ASHRAE Publication, 1967, Chap. III, pp. 27-40.

Table 1. Solar radiation and outside air temperature of the example building

Month	Wall orientation					Daily average[2] outside air temperature,[b] °C (°F)
	E	W	N	S	H	
	Average daily solar radiation, Btu/ft^2, Ref. 5					
Jan	569	569	253	1249	942	6.4 (43.54)
Feb	778	778	334	1308	1296	11.1 (51.92)
Mar	970	970	415	1221	1703	12.1 (53.79)
Apr	1053	1053	513	911	1907	14.3 (57.67)
May[a]	1112	1112	627	747	2081	19.8 (67.57)
Jun[a]	1180	1180	700	711	2258	26.1 (78.96)
Jul[a]	1257	1257	650	797	2394	29.7 (85.42)
Aug[a]	1162	1162	511	1000	2147	29.1 (84.33)
Sep[a]	1017	1017	410	1294	1809	24.4 (75.96)
Oct	770	770	329	1326	1298	17.4 (63.33)
Nov	574	574	252	1276	953	10.7 (51.33)
Dec	544	544	225	1345	875	5.3 (41.50)
Daily average intensity in 5 summer months, Btu/hr ft^2 (W/m^2)	47.73 (150.5)	47.73 (150.5)	24.15 (76.2)	37.91 (119.6)	89.08 (280.9)	
Daily average intensity in 7 winter months, Btu/hr ft^2 (W/m^2)	31.30 (98.7)	31.30 (98.7)	13.82 (43.6)	51.40 (162.1)	53.42 (168.5)	

[a]Summer months.

[b]For Goldstone, California.

Definition of Symbols

$\overline{A}$ building characteristic thermal gain

A gross floor area of building

B building characteristic heat loss rate

C energy cost

D population or equipment density (per unit floor area)

E electrical power input

e emissivity

G input fuel heat rate

H duration of operation

h average height of building zones

I energy index

k thermal conductivity of walls

M months per season

N number of occupants

n number of air changes

P atmospheric pressure

Q heat rate

R average solar radiation power

S sensitivity

s sensible heat generated

T temperature

U effective heat transfer coefficient for walls

V air flow rate

v wind velocity

X general input parameter

x thickness

Y general output parameter

α absorptivity of exterior walls

β load fraction provided by electric powered heaters or coolers

γ specific heat times density product

Δ change

ϵ ventilation air/total circulation air ratio

η efficiency

θ combined heat transfer coefficient by convection and radiation

λ fraction

τ transmissivity of glazing

σ Stefan-Boltzmann constant

Ω building volume

Suffixes

a transmission by ambient air

ax accessories

c cooling effect

cm cooling mode

conv. convection part

cp cooling setpoint

d wind currents

e electrical device

ec electrical-powered coolers

eh electrical-powered heaters

eq equivalent

f fuel-fired device

fc	heat-powered coolers
fh	heat-powered heaters
g	generated inside a space
h	heating effect
hm	heating mode
hp	hot setpoint
i	inside environment or internal to space
j	index
l	lights
m	mechanical motor-driven machines
o	outside air
p	people
pp	power plant
r	solar radiation effect
rad.	radiation heat transfer part
s	summer season
t	transmitted through walls
v	ventilation
w	winter season
x	infiltration/exfiltration
y	yearly profile

Superscript

"	per unit gross floor area

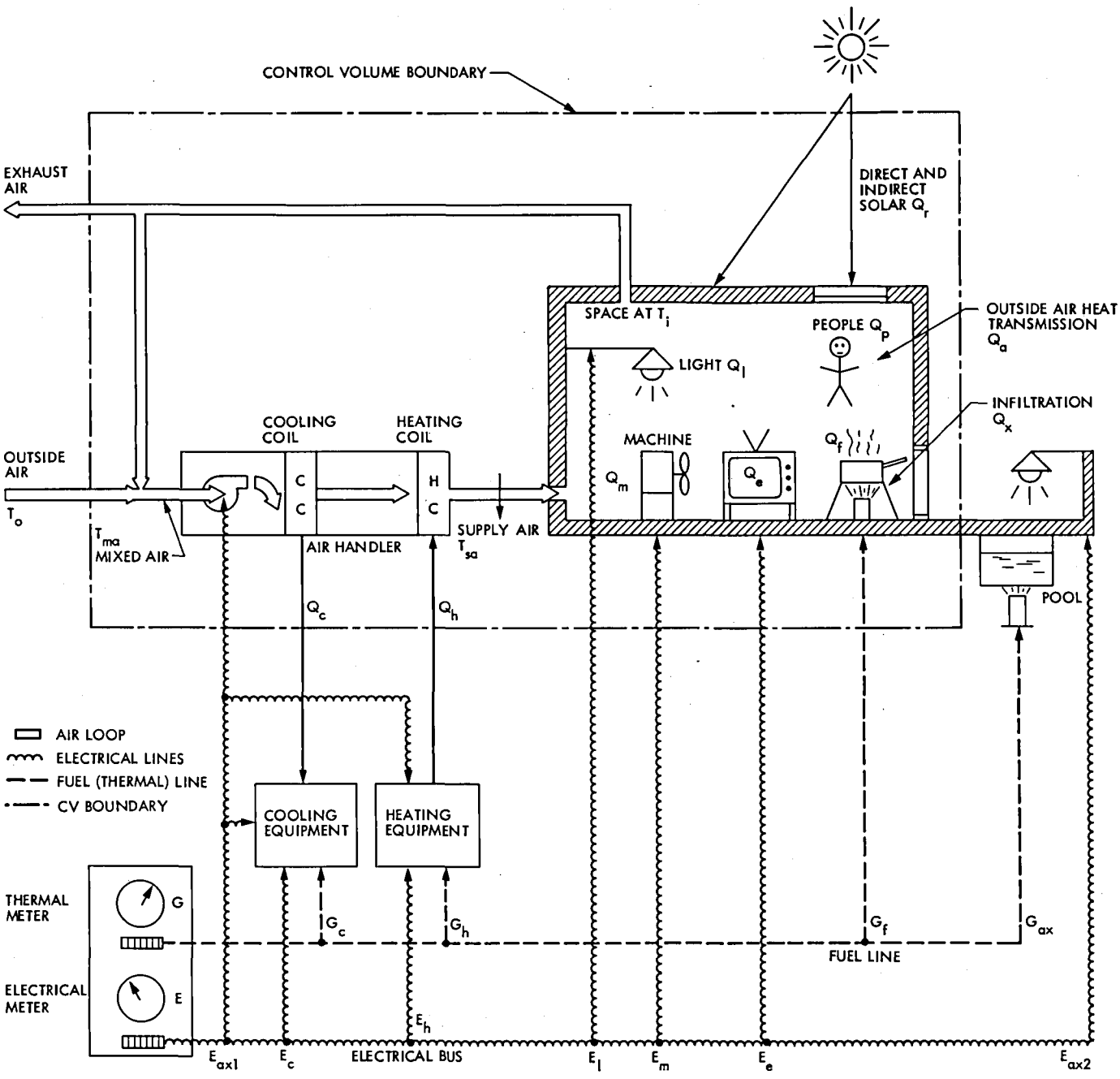

Fig. 1. Energy flows for the building model

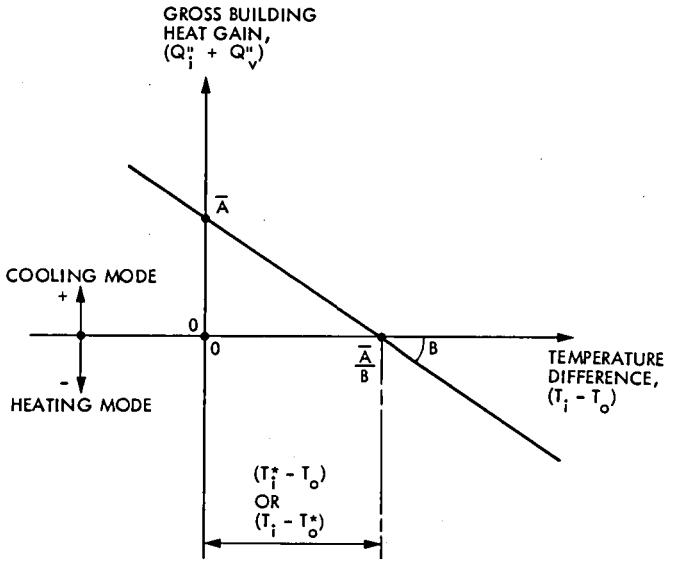

Fig. 2. Building characteristic temperatures T_i^*, T_o^*

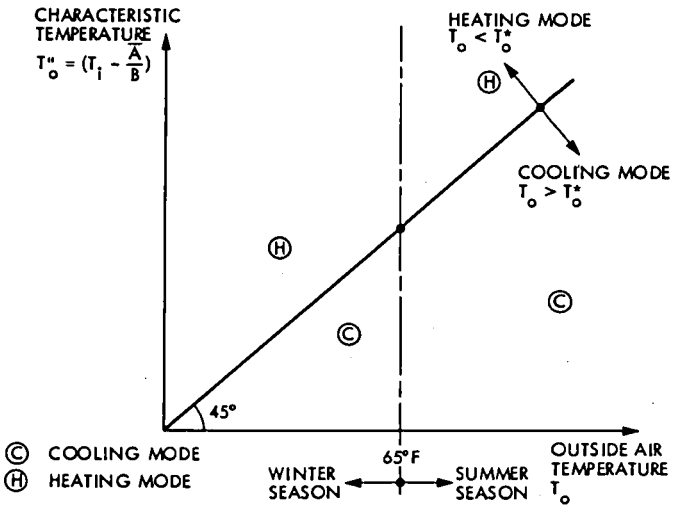

Fig. 3. Heating and cooling modes in different seasons

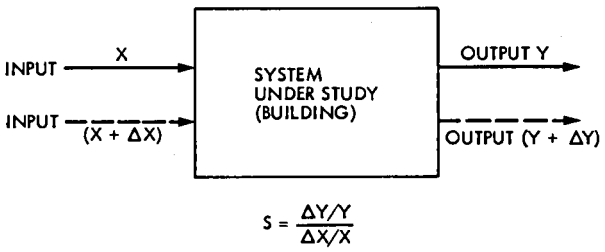

Fig. 4. Sensitivity definition

Appendix A

Heat Transfer Through Solid Walls, Roofs, Floors, and Windows

Because of fluctuating changes in outside air temperature and in incidence of solar radiation, the external thermal environment is constantly changing. Thus steady-state heat transmission seldom occurs in a building structure if short periods (of the order of an hour) are studied. However, the assumption of quasi-steady-state still provides a convenient procedure for some longer periods in the order of 24 hours or more. The following cases are examined assuming quasi-steady-state heat transmission:

I. Heat Transmission Through Walls, Roofs, and Floors

Consider the one-dimensional plane wall shown in Fig. A-1, representing a composite wall, roof, or floor where the wall height or width are large compared to the thickness x. The interior and exterior heat transfer coefficients θ_i and θ_o, respectively, are combining the effects of convection and radiation heat transfer. For the inside wall surface, the heat transfer from the outside Q_t'' through the wall interior at $T_{w,i}$ to the inside environment is written as

$$Q_t'' = \theta_i (T_{w,i} - T_i) \tag{A-1}$$

where

$$\theta_i = \theta_{i,\,conv.} + \frac{\sigma e_i (T_{w,i}^4 - T_{s,i}^4)}{(T_{w,i} - T_i)} \tag{A-2}$$

where σ is Stefan Boltzmann constant (0.1714×10^{-8} Btu/hr ft^2°R^4) and e_i is the emissivity of the interior wall.

On the other hand, the heat transfer through the outside wall layer, at steady-state, is the sum of the absorbed portion of direct solar radiation where the absorptivity is α_0, and the combined convection and sky radiation effects.

$$Q_t'' = \alpha_0 R'' + \theta_o (T_o - T_{w,o}) \tag{A-3}$$

where θ_o is written as

$$\theta_0 = \theta_{o,\,conv.} + \sigma e_o \frac{(T_{s,o}^4 - T_{w,o}^4)}{(T_o - T_{w,o})} \tag{A-4}$$

In Eq. (A-3), R'' represents the total incidence of solar radiation (direct, diffuse and reflected) upon the exterior wall surface, and $T_{s,o}$ represents mostly the sky temperature although it includes the effect of neighboring surfaces. The rate of heat transfer Q_t'' may also be expressed, from Eq. (A-3), as

$$Q_t'' = \theta_o (T_{eq.} - T_{w,o}) \tag{A-5}$$

where T_{eq} is an equivalent outdoor temperature called the sol-air temperature, which combines the effects of solar radiation and outside air temperature T_o. Equations (A-3) and (A-5) give the fictitious temperature T_{eq} as

$$T_{eq} = T_o + \frac{\alpha_o R''}{\theta_o} \tag{A-6}$$

The heat transfer from the outside environment through the composite wall Q_o'' will cause a differential in temperature $(T_{w,o} - T_{w,i})$, where

$$Q_o'' = (T_{w,o} - T_{w,i}) \Big/ \sum_j \frac{X_j}{K_j} \tag{A-7}$$

where K_j and X_j are the thermal conductivity and the thickness, respectively, for the jth layer constituting the composite site.

Combining Equations A-1, A-5, and A-7 at steady-state, an overall heat transfer coefficient U is obtained where the end temperatures T_{eq} and T_i are utilized:

$$Q_o'' = U(T_{eq} - T_i) \tag{A-8}$$

and

$$1/U = \frac{1}{\theta_i} + \frac{1}{\theta_o} + \sum_j \frac{x_j}{K_j} \tag{A-9}$$

the determination of the coefficients, θ_i, θ_o, and U are usually made either by direct calculations from Eqs. (A-2), (A-4), and (A-9) or from the literature such as Refs. 2, 3, 4, and 6 for a

variety of building materials. The coefficient θ_o is particularly dependent on the exterior wind velocity and the outside wall surface emissivity. Substitution of the sol-air temperature expression from Eq. (A-6) into Eq. (A-8) yields for a solid, wall, roof, or floor

$$Q_t'' = U(T_o - T_i) + \frac{\alpha_o R'' U}{\theta_o} \qquad \text{(A-10)}$$

The first term in the right-hand side of Eq. (A-10) represents the quasi-steady-state heat transmission to the space interior Q_a'' due to the ambient air temperature, while the second term $(\alpha_o R'' U/\theta_o)$ represents the solar portion Q_r''. The latter is due to the effect of solar radiation intensity as it falls on the outside surface with the modifier ratio (U/θ_o).

II. Heat Transmission Through Windows

The same discussion presented in Section I applies for the heat transmission through fenestration areas. Equations (A-2), (A-4), and (A-9) are also applied using the glass properties in place of the wall properties. However, the total heat transmission to the interior space will be somewhat different from that given by Eq. (A-10) since it should allow for the directly transmitted solar radiation portion $\tau R''$. Accordingly, the modified expression Q_t'' for the glazing areas (Ref. 6) will be:

$$Q_t'' = U(T_o - T_i) + \left[\frac{\alpha R'' U}{\theta_o} + \tau R''\right] \qquad \text{(A-11)}$$

The first term in the right-hand side in Eq. (A-11) is similar to that in Eq. (A-10), representing the heat transmission portion Q_a'' due to the temperature difference between internal and external environments, while the second bracketed term represents the solar portion Q_r''. For common window glass, the absorptivity is in the order of 3% and the thermal resistance portion in Eq. (A-9), $(\sum_j x_j/K_j)$ could be neglected. Therefore,

$$U_{glass} \cong 1\Big/\left(\frac{1}{\theta_i} + \frac{1}{\theta_o}\right) \qquad \text{(A-12)}$$

The term $\alpha R'' U/\theta_o$ is reduced to $\alpha R''/(1 + \theta_o/\theta_i)$ which could be entirely neglected from Eq. (A-11). Hence, for low absorptivity glass

$$Q_{t,glass}'' = U(T_o - T_i) + \tau R'' \qquad \text{(A-13)}$$

Equations (A-10) and (A-13) constitute the basic equations needed to determine Q_t'', combining all walls, floors, roofs and glazing areas.

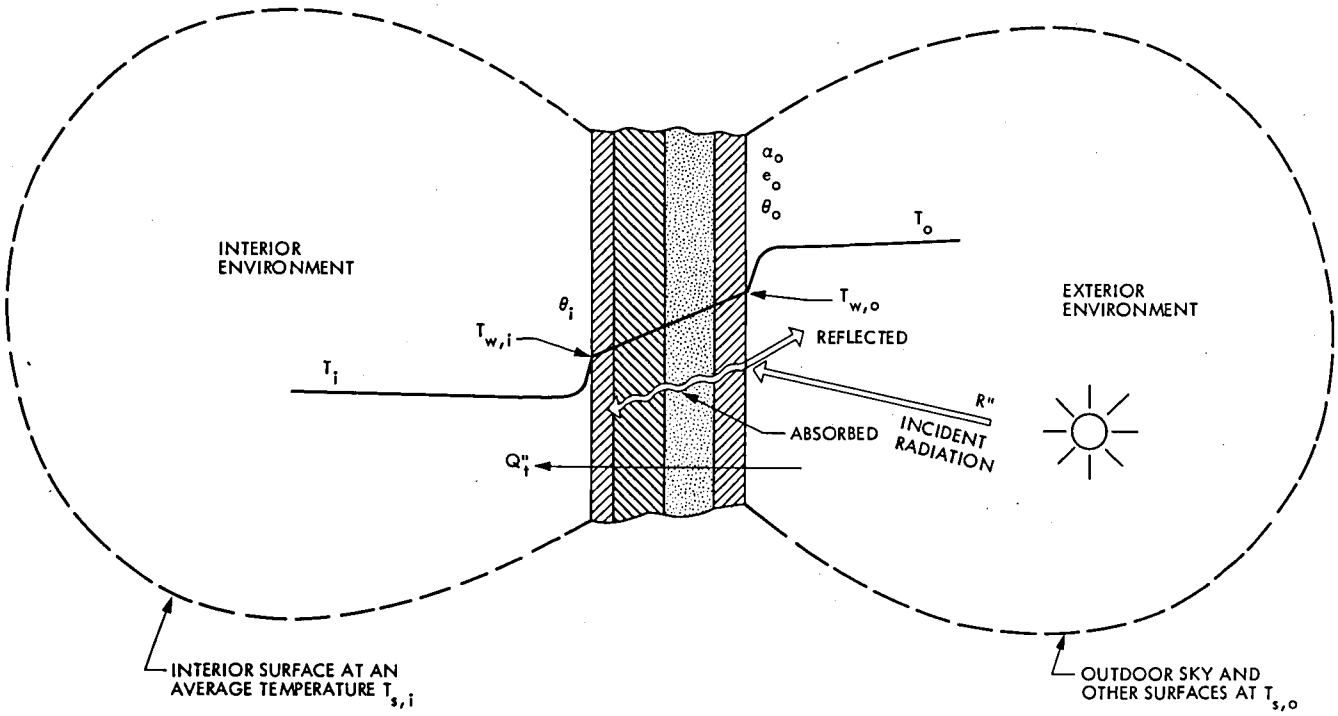

Fig. A-1. Temperature profile across a solid wall separating two environments

Appendix B
Major Air Handling Systems

This appendix is an extension of the building model presented in Section II, where four major types of air-handling systems and their temperature controls are presented. The cooling and heating loads Q_c, and Q_h for each of the four air handlers are analyzed to show their differences.

I. A Dual-Duct System

The dual-duct air handler system is used for multizone applications where two parallel ducts are employed – one carrying cold air, the other warm air. The air flow rate to each zone is constant at all times. In each conditioned zone or space, a mixing box actuated by a room thermostat mixes the warm and cold air in the proper proportions to satisfy the varying space temperature needs. In all seasons, regardless of the net internal heat gain or loss, simultaneous cooling and heating of the air are needed at the air handler. Figure B-1 shows the temperature of air in the various stations. Simple mass and heat balance equations are written for the control volume encompassing the space, which is kept at T_i and has an internal load Q_i together with the mixing box. The mixing box mixes two air streams: the cold stream with a flow rate V_c at temperature T_{cp} and the hot stream with a flow rate V_h at temperature T_{hp}. Hence,

$$V_c + V_h = V$$

$$\gamma V_c T_{cp} + \gamma V_h T_{hp} + Q_i = \gamma V T_i$$

Solving for V_c and V_h gives

$$V_c = [Q_i + \gamma V(T_{hp} - T_i)]/\gamma (T_{hp} - T_{cp}) \quad \text{(B-1)}$$

$$V_h = [\gamma V(T_i - T_{cp}) - Q_i]/\gamma (T_{hp} - T_{cp}) \quad \text{(B-2)}$$

Denoting the mass ratio of ventilation air to total circulation air by ϵ, the mixed air temperature T_{ma} is obtained from a heat balance of the mixing process as:

$$T_{ma} = \epsilon T_o + (1 - \epsilon) T_i$$

or

$$T_{ma} = \epsilon(T_o - T_i) + T_i \quad \text{(B-3)}$$

The cooling load of the cooling coil Q_c will be written as:

$$Q_c = \gamma V_c(T_{ma} - T_{cp})$$

By substituting for V_c and T_{ma} using Eqs. (B-1) and (B-3) and using the definition of the ventilation heat gain Q_v from Eq. (13), then

$$Q_c = [Q_i + \gamma V(T_{hp} - T_i)]\,[Q_v + \gamma V(T_i - T_{cp})]\ /$$

$$[\gamma V(T_{hp} - T_{cp})] \quad \text{(B-4)}$$

Similarly, the heating load of the heating coil Q_h will be expressed as

$$-Q_h = \gamma V_h (T_{ma} - T_{hp})$$

or

$$-Q_h = [\gamma V(T_i - T_{cp}) - Q_i]\,[Q_v - \gamma V(T_{hp} - T_i)]\ /$$

$$[\gamma V(T_{hp} - T_{cp})] \quad \text{(B-5)}$$

If the cold setpoint T_{cp} or the flow rate V are adjusted in the cooling mode such that on the average

$$Q_{i,s} = \gamma V(T_i - T_{cp})$$

then, it follows from Eq. (B-5) that no heating is needed and the average cooling load will be equal to

$$Q_c = Q_i + Q_v \quad \text{(B-6)}$$

On the other hand, if the hot deck temperature T_{hp} or the flow rate V are adjusted in the heating mode such that on the average

$$-Q_i = \gamma V(T_{hp} - T_i)$$

Then, it follows from Eq. (B-4) that the cooling load Q_c will be zero, and the average heating load will be equal to

$$-Q_h = Q_i + Q_v \quad \text{(B-7)}$$

In practice, the temperatures T_{cp} and T_{hp} are about 50°F and 80°F in the cooling season, respectively, and 60 and 100°F in the heating season. Consequently, simultaneous heating and cooling energies are always required to condition the space according to Eqs. (B-4) and (B-5) for Q_c and Q_h computations in any season. However, a heat balance of the control volume encompassing the building and the air handler would still yield at all times:

$$Q_c - Q_h = Q_i + Q_v \tag{B-8}$$

Equation (B-8) can also be verified by summing the equipment loads for the general case, which are represented by Eqs. (B-4) and (B-5), and also for the seasonal average case, as represented by Eqs. (B-6) and (B-7).

II. Face and Bypass Damper System

The second common air-handling system is sketched in Fig. B-2, where either heating energy or cooling energy is expended at one time in a constant air flow. The air temperature modulation is made by using bypassed mixed air dampers to suit the varying space internal loads. Cooling only takes place if the sum $(Q_i + Q_v)$ is positive (or $T_o > T_o^*$), while heating is only taking place if the sum $(Q_i + Q_v)$ is negative (or $T_o < T_o^*$). A simple heat balance of the control volume encompassing both the building and the air-handling system gives for the first case when $(Q_i + Q_v)$ is positive:

$$\left.\begin{aligned} Q_h &= 0 \\ Q_c &= Q_i + Q_v \end{aligned}\right\} \tag{B-9}$$

If $(Q_i + Q_v)$ is negative, then

$$\left.\begin{aligned} Q_c &= 0 \\ -Q_h &= Q_i + Q_v \end{aligned}\right\} \tag{B-10}$$

For this type of air handler, either Eq. (B-9) or Eq. (B-10) is applied to determine the equipment loads at a given hour. The equipment controls operate the heating or cooling coils at one time according to the algebraic sign of the sum $(Q_i + Q_v)$. This type of air handler is found advantageous for buildings, such as theaters, supermarkets, central control buildings, etc., with large positive internal heat gain Q_i which requires a cooling energy expenditure all year around.

III. Variable Air Volume System

In a variable air volume (VAV) system, as sketched in Fig. B-3, the supply air temperature is held constant (either at the cold setpoint or the hot setpoint) while the amount of air flowrate is changed to satisfy the varying space load requirements. The VAV system controls are thus in contrast with the constant volume air handler systems where the air flow rate to a space remains the same while the supply air temperature is varied to suit the varying space loads. Multizone dual ducts with cold and hot air streams and VAV controls are used to supply either cooling or heating energies according to different zone needs. Subject to a zone internal load, either heating or cooling is supplied at one time. Similar to the case of face and bypass damper system, the cooling mode will only take place if the sign of the sum $(Q_i + Q_v)$ is positive and heating will only take place if the sum $(Q_i + Q_v)$ is negative. Accordingly, the above Eqs. (B-9) and (B-10) are also applicable to VAV air-handler systems.

IV. Single Cold Duct and Terminal Reheat System

The temperature control in this type of air-handler system, as sketched in Fig. B-4, is achieved by two different mechanisms. First, in the cooling mode, the mixed air stream is cooled to a fixed cold setpoint temperature T_{cp}, independent of the load variations, but this is followed by a variable-degree heating process up to the desired supply air temperature. Second, for the zone heating mode, the cooling equipment is turned off and only the terminal zone heater is operated to raise the mixed air temperature T_{ma} up to the desired supply air temperature. Cooling or heating modes depend on the sign of the net heat gain $(Q_i + Q_v)$. A simple heat balance of the control volume, including the building space and the heating coil, as sketched in Fig. B-4, yields the following:

(1) When $(Q_i + Q_v)$ is positive, the system is in the cooling mode where,

$$\left.\begin{aligned} -Q_h &= Q_i - \gamma V (T_i - T_{cp}) \\ Q_c &= Q_v + \gamma V (T_i - T_{cp}) \end{aligned}\right\} \tag{B-11}$$

which satisfies the energy balance equation for the building and the air handler:

$$Q_c - Q_h = Q_i + Q_v$$

Note that if T_{cp} is adjusted such that the average conditions of the cooling mode is

$$Q_i = \gamma V (T_i - T_{cp})$$

no heating will be required, and the cooling load Q_c is reduced to

$$Q_c = Q_v + Q_i \tag{B-12}$$

(2) If $(Q_i + Q_v)$ is negative, the system is in heating mode.

$$Q_c = 0$$
$$-Q_h = Q_i + Q_v \tag{B-13}$$

Therefore, if the average building conditions for cooling and heating modes are assumed, it will enable the separation of equipment loads and facilitate the computations of the energy consumption during each season.

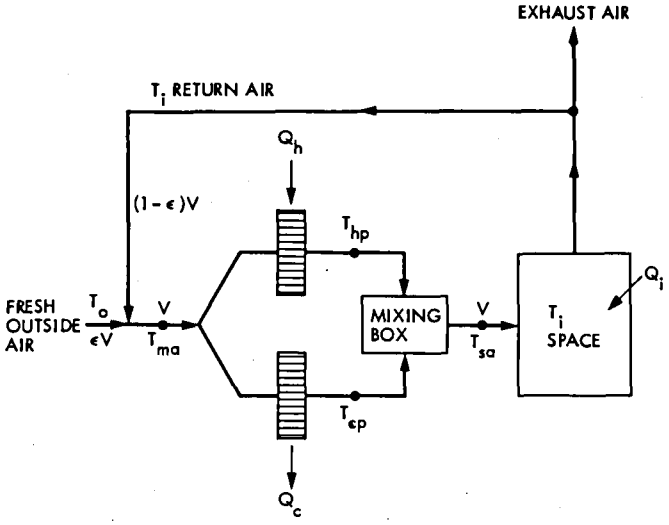

Fig. B-1. Dual duct system

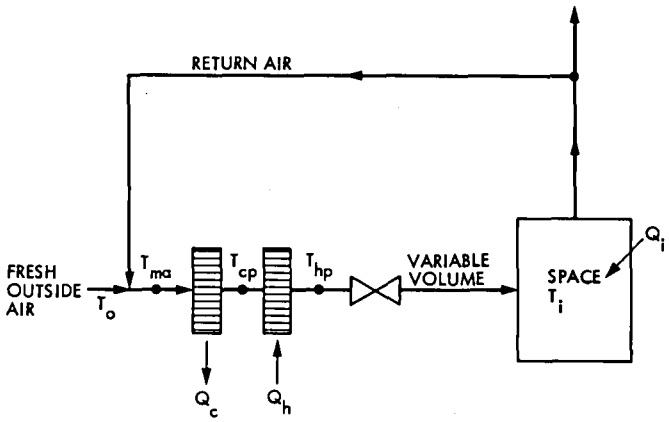

Fig. B-3. Variable volume control system

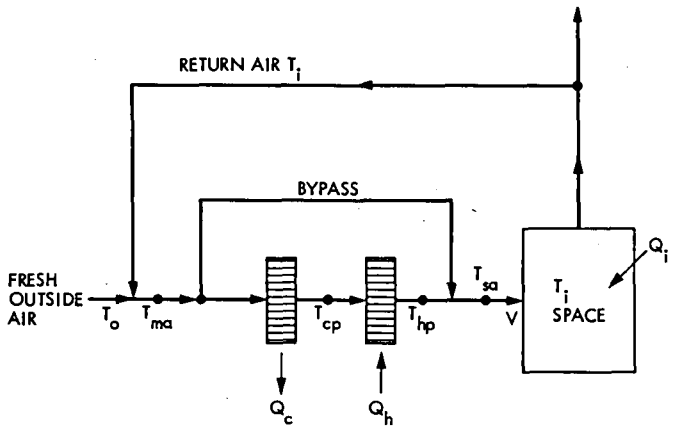

Fig. B-2. Face and bypass damper system

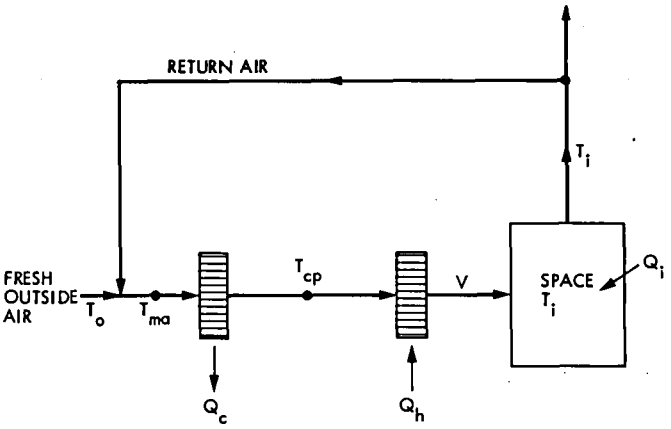

Fig. B-4. Single cold duct and terminal reheat system

The DSN Radio Science System

B. J. Buckles
TDA Engineering Office

The DSN Radio Science System recently supported the Radio Science experiments at Voyager 1 Saturn encounter. These experiments which included two atmospheric occultations, a planetary ring occultation, and ring scattering experiment were supported by Deep Space Stations in Australia (DSS 43) and Spain (DSS 63). This article describes the DSN Radio Science System data flow from receipt of the radio signals at the antenna to delivery of the recorded data to the project.

I. Introduction

Figure 1 is a block diagram representation of the DSN Radio Science System (DRS) recently used to successfully support the Voyager 1 Saturn encounter radio science experiments. The DSN Deep Space Stations (DSS) are the heart of this system. In particular DSS 63 and DSS 43 were the prime supporting stations for the radio science experiments at Voyager 1 Saturn encounter. DSS 63 supported the Titan occultation, the Saturn occultation egress, ring occultation, and ring scattering experiments with four-channel medium band open-loop-receiver recording. DSS 43 supported the Saturn occultation ingress with two channel narrow band open-loop-receiver recording. Both stations provided wide bandwidth open-loop-receiver recording capability as a backup to the prime narrow band and medium band open-loop systems.

In addition to the medium band open-loop recording capability at DSS 63, other new implementation provided to support the Voyager radio science experiments were the Precision Power Monitor, which measures system temperatures, and the Spectral Signal Indicator (SSI) that monitors the open-loop recording system at several points, providing spectral information for the monitored signal.

The following paragraphs describe the DSS subsystems that support the DSN Radio Science System in more detail. In addition, each of the other facilities supporting the DSN Radio Science System, Ground Communications Facility (GCF) and Network Operations Control Center (NOCC), and their support functions are described. The narrative in general will describe the flow of data from receipt at the antenna through the system as indicated on the Radio Science System block diagram (Fig. 1).

II. The Deep Space Stations

The Deep Space Station (DSS) is the Radio Science System instrument. DSS system performance directly determines the degree of success of the experiment and system calibration determines the degree of uncertainty in the results of the experiment. The following paragraphs describe those functions performed by the individual subsystems depicted in Fig. 1. Specific configuration and calibration requirements are

addressed in a separate paragraph after the functional descriptions of the subsystems.

A. The Antenna Mechanical Subsystem

The 64-meter Antenna Mechanical Subsystems function as large aperture collectors which by double reflection focus incoming radio frequency (S- and X-band RCP/LCP) energy into the S- and X-band feedhorns (part of the Antenna Microwave Subsystem).

The large collecting surface of the antenna focuses the incoming RF energy onto the hyperboloid subreflector which is adjustable in both axial and tilt positions to permit optimizing the focusing of energy into the feedhorns. The subreflector is locked into a fixed position for many radio science events. The subreflector then reflects the received energy to the dichroic plate, a device that reflects S-band energy to the S-band feedhorn and transmits X-band energy to the X-band feedhorn.

Transmitted S-band RF energy emanating from the feedhorn is focused by the same reflectors into a narrow cylindrical beam. Since the beam is very narrow, it must be pointed with high accuracy and precision. This is accomplished by a series of drive motors and gear trains which rotate those portions of the structure which support the reflectors, position sensors, and related electronics. Electronic servo amplifiers are used to amplify and condition the axes angle or position error signals, which are received and are provided to the drive-motor controls.

Pointing angles are computed from an ephemeris provided by the project, and the antenna is pointed to these angles. Once the receiver has acquired a signal to provide feedback, a radio source can be tracked by scanning around it (CONSCAN) and computing pointing angles from signal-level information supplied by the receiver. During periods when signal level dynamics are excessive or signal levels received are expected to be low, i.e., during occultations and some other radio science experiments, conscan cannot be used and angle pointing is accomplished by manually inserting offsets to the computed angle predict set.

B. The Antenna Microwave Subsystem

The Antenna Microwave Subsystem accepts the received S- and X-band RCP/LCP signals at the feedhorn from the Antenna Mechanical Subsystem. The received signals are transmitted through the polarizer plates to the orthomode transducer. The polarizer plates are adjusted so that RCP signals are directed to X-band Traveling Wave Maser 2 and S-band Traveling Wave Maser 1 so that LCP signals are directed to X-band Traveling Wave Maser 1 and S-band Traveling Wave Maser 2. After amplification by the masers, the signals are routed to the Receiver-Exciter Subsystem via the Microwave Switching Assembly.

The S-band uplink signal is transmitted via the Diplexer Assembly through the feedhorn to the antenna where it is focused and beamed to the spacecraft.

The noise diode assemblies, under control of the PPM, inject known amounts of noise power into the received signal path so that accurate real-time system temperature measurements may be made.

C. The Transmitter Subsystem

The Transmitter Subsystem accepts the S-band frequency exciter signal from the Receiver-Exciter Subsystem and amplifies it to a transmitted output level of 20 kW. The signal is then routed via the diplexer to the antenna and then focused and beamed to the spacecraft.

D. The Receiver-Exciter Subsystem

The Receiver-Exciter Subsystem receives, amplifies, and frequency down converts spacecraft-radiated S- and X-band RCP/LCP signals. The closed-loop receivers provide doppler and ranging signals to the tracking subsystem. Dedicated open-loop receivers provide baseband signals to the Radio Science Subsystem and fixed-tuned wide bandwidth open-loop receivers provide backup systems to the narrowband and medium band open-loop receivers.

The exciter generates the S-band drive signal provided to the transmitter subsystem that provides the spacecraft uplink signal.

The Spectral Signal Indicator provides local displays of received signal spectrums and routes spectral data to the radio science subsystem. These displays are used to validate radio science system data at the DSS, NOCC, and project areas.

The Precision Power Monitor (PPM) measures system temperatures by injecting known amounts of noise power into the signal path and comparing the total power within a given bandwidth before and during periods of noise injection. System temperature measurements are made for each of the four masers by utilizing the closed-loop receivers as monitoring devices. This use of the receivers imposes a configuration constraint on them when they are used to monitor all four masers. That is, the BLOCK IV receivers must monitor X-band RCP/LCP masers and the BLOCK III receivers are used to monitor S-band RCP/LCP masers.

E. The Tracking Subsystem

The Tracking Subsystem receives the ranging spectrum and doppler signals from the Receiver-Exciter Subsystem. It generates a range code that is routed to the exciter and modulates the S-band uplink carrier. The demodulated range spectrum is compared to a model of the transmitted range code and the round trip signal delay to the spacecraft is computed, formatted and transmitted to the GCF data records subsystem which produces an Intermediate Data Record (IDR) tape upon which the data is delivered to the project. Similarly the doppler phase is counted, formatted, and delivered to the project. This radio metric data supports radio science celestial mechanics and general relativity experiments in addition to providing a partial backup to the open-loop system.

In addition, the Tracking Subsystem computes data residuals and noise estimates, receives and stores predicts, and provides partial status information to the Monitor and Control Subsystem including receiver AGC levels and lock status.

F. The Radio Science Subsystem

The Radio Science Subsystem digitizes, bandwidth reduces, and records (1) very narrow, (2) narrow, and (3) medium bandwidth radio science data and digitizes and records wide bandwidth radio science data. It receives radio science frequency predicts from NOCC, configuration and control data from the Monitor and Control Subsystem, and S- and X-band RCP/LCP signals from the Receiver-Exciter Subsystem. It transmits spectral information from the SSI to NOCC and the project mission support area via the GCF wideband data lines. It controls the narrow and medium band open-loop receiver LO by sending frequency control information to the Receiver-Exciter Subsystem.

G. Monitor and Control Subsystem

The Monitor and Control Subsystem provides control messages to the centrally controlled DSS Subsystems including the Radio Science and Tracking Subsystems. It provides partial status information for these same subsystems. It generates the angle drive tape needed by the Antenna Pointing Subsystem and, in addition, controls the SSI and PPM in the Receiver-Exciter Subsystem. It receives the system temperature information from the PPM and displays it on the data system terminal (DST). It relays the system temperature information to the NOCC Monitor Subsystem for display in NOCC and the project mission support area.

III. The Ground Communications Facility

The Ground Communications Facility (GCF) provides the communication networks required to support the communication requirements of the Radio Science System. These facilities exist at the DSS and JPL and are briefly described in the following paragraphs.

A. GCF High-Speed Data Subsystem

The High-Speed Data Subsystem transmits radio science predictions from the NOCC to the DSS and CTA-21, and Radio Science System performance validation data from the DSS to NOCC.

B. GCF Wideband Subsystem

In real time, the Wideband Subsystem transmits SSI data from the DSS to the NOCC.

C. GCF Data Records Subsystem

The GCF Data Records Subsystem formats and provides radio science data on computer-compatible tape to the flight projects.

IV. Network Operations Control Center

A. NOCC Radio Science Subsystem

The NOCC Radio Science Subsystem generates open and closed-loop radio science DTV graphics displays, and DRS status and configuration displays. In addition, the NRS provides the planetary atmosphere refracted trajectory input to the NOCC Support Subsystem for the purpose of generating radio science predicts.

B. NOCC Monitor Subsystem

The NOCC Monitor Subsystem displays system temperature information and provides the monitor IDR tape upon which system temperature information is delivered to the project.

C. NOCC Support Subsystem

The NOCC Support Subsystem generates DSS frequency and tracking predicts using a polynomial coefficient tape produced by the POEAS software as input. In addition, predicts can be generated using manual inputs.

D. NOCC Display Subsystem

The NOCC Display Subsystem provides the NOCC Radio Science Subsystem generated radio science displays to the Network Operations Control Area and to project radio science support areas, and provides control data to the NOCC Radio Science Subsystem.

E. NOCC Tracking Subsystem

The NOCC Tracking Subsystem generates tracking system status displays and transmits them to the display subsystem to be routed and displayed.

V. Network Radio Science Subsystem

The Network Radio Science Subsystem is located in CTA-21. It bandwidth-reduces wide bandwidth radio science data recorded at the DSS. It receives digital wide bandwidth and medium bandwidth radio science data from the DSS Radio Science Subsystem, generates bandwidth-reduced radio science data, and provides medium and wide bandwidth radio science data on computer-compatible tape to the flight project.

VI. Open-Loop Recording System Prepass Calibration

The recorded open-loop receiver signals were the prime deliverable data type for the Voyager, Titan, and Saturn ring occultations and the ring scattering experiment. For that reason, it was extremely important that the open-loop system be properly set up prior to the recording pass, and that a calibration tape be made. This calibration data serves as a calibration for the data later recorded and establishes the basic uncertainty in the results of the experiment. The following paragraphs describe these calibrations.

A. Purpose of the Calibration

The open-loop recording calibration tapes are made to accomplish the following:

(1) To establish the output of the open-loop receivers at a level that will not saturate the input to the Occultation Data Assembly (ODA) or Digital Recording Assembly (DRA) A/D converters.

(2) To provide data that will establish baseline values for the phase, frequency, and amplitude stability of the open-loop system.

To achieve goal (1) the calibration recording is made using a test signal generated by the exciter-translator that is set to provide the maximum predicted received signal level for the recording period. Then the output level of the receivers is adjusted to the level determined by the equation

$$S = \left[\frac{\text{SNR} + 1}{(2\,\text{SNR} + 2k\sqrt{2\,\text{SNR}} + k^2)}\right]^{1/2} \text{L} \qquad (1)$$

where

S = receiver output levels (volts rms)

SNR = expected received signal-to-noise ratio

k = Number of sigma margin desired for saturation

L = A/D converter saturation level

In order to achieve goal (2) for medium-band recording it is necessary to step the test signal across the bandpass of the receiver filter. This is done in ten 5 kHz (at S-band) steps. Stepping the signal in frequency in this manner allows the necessary phase, frequency, and amplitude calibrations to be made.

Frequency stepping is not necessary for narrow-band recording.

So that an X-band RCP/LCP test signal may be generated, a cap is provided that is placed over the X-band feedhorn from which a linearly polarized signal is injected into the horn. This cap is oriented such that the linearly polarized signal is transmitted equally by the orthomode coupler to its RCP and LCP output ports, thus providing equal RCP/LCP calibration signals.

A consequence of using a cap over the feedhorn in this manner to generate a test signal is that the X-band system temperature has been increased approximately 10 dB. It has, in effect, been terminated into an ambient load. To counter the 10 dB increase in receiver output power due to the presence of the cap it is necessary to insert 10 dB pads into the signal path at appropriate points. These must be removed after the calibration recording is made.

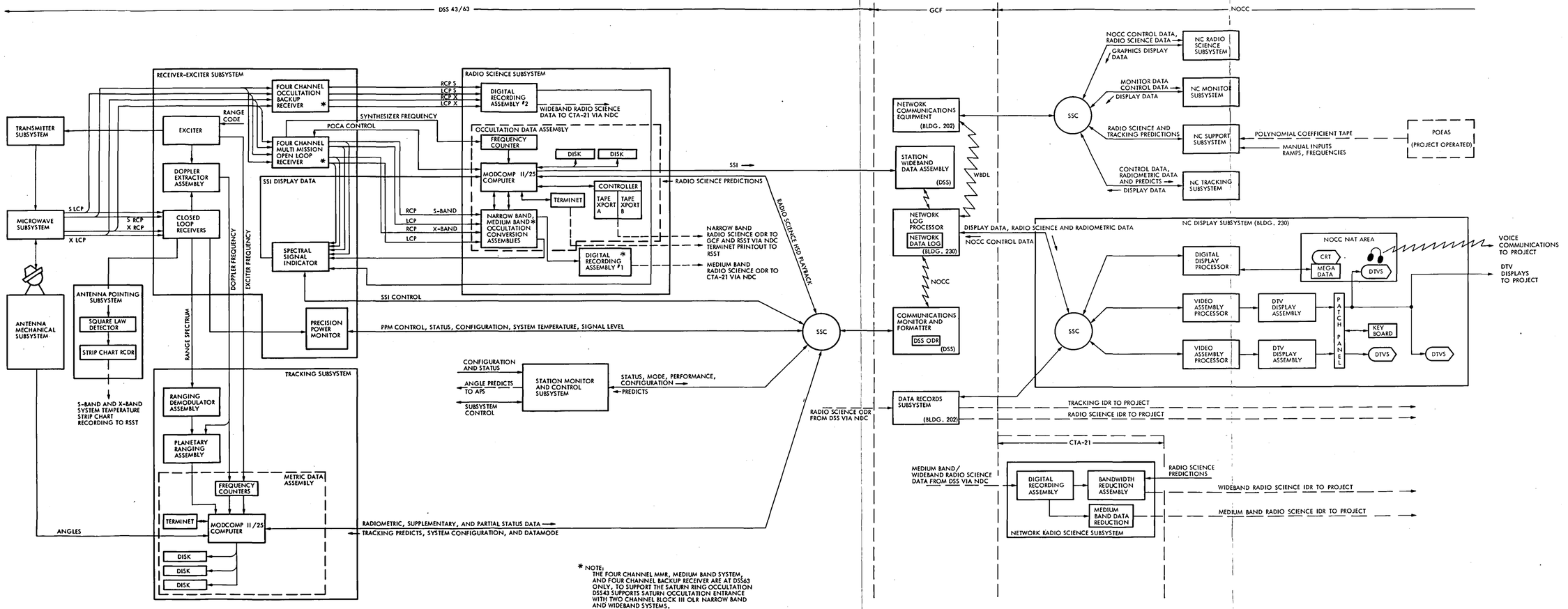

* NOTE:
THE FOUR CHANNEL MMR, MEDIUM BAND SYSTEM, AND FOUR CHANNEL BACKUP RECEIVER ARE AT DSS63 ONLY, TO SUPPORT THE SATURN RING OCCULTATION DSS43 SUPPORTS SATURN OCCULTATION ENTRANCE WITH TWO CHANNEL BLOCK III OLR NARROW BAND AND WIDEBAND SYSTEMS.

Fig. 1. Deep Space Network Radio Science System Block Diagram depicting the Radio Science System as configured to support the Voyager I Saturn encounter.

Conversion of the DSN Teletype Subsystem to the Eight-Level ASCII National Standard

G. J. Brunder
DSN Data System Section

This article provides a functional description of the new eight-level ASCII Teletype Subsystem and its constituent Teletype Assemblies. An overview of the implementation of the Teletype Subsystem is presented together with a discussion of the distinct capabilities of its equipment.

I. Introduction

In 1978, the NASA Communications Network (NASCOM) requested the Deep Space Network (DSN) to convert their Teletype (TTY) Subsystem from a five-level Baudot format to the eight-level ASCII (American Standard Code for Information Exchange) national standard. Other locations served by NASCOM were also being changed to eight-level teletype operation. The conversion was being made to standardize the world-wide NASCOM teletype network. ASCII is a more powerful format than Baudot since it allows additional characters to be printed and provides control functions not available in the Baudot format. In addition, at the time of the conversion, a new Time Division Multiplexor (TDM) was to be provided by NASCOM for installation at the JPL Central Communication Terminal that would make available a total of 50 teletype channels (including five special purpose 300 baud rate channels). The existing TDM System had provision for only 40 channels and did not make provision for 300 baud rate channels.

The DSN implemented the conversion at the Ground Communication Facility (GCF), the Deep Space Stations (DSS's), and the Network Operations Control Center (NOCC). The GCF, DSS's and the NOCC are all elements of the DSN. The conversion work was coordinated with other eight-level conversion work being implemented at NASCOM locations such as the Ames Research Center (ARC), the overseas NASCOM Switching Centers at Canberra, Australia, and Madrid, Spain, and the NASCOM Primary Switching Center at the Goddard Space Flight Center (GSFC) in Greenbelt, Maryland. The GSFC Switching Center consists, in addition to its testing and monitoring capabilities, of a communication processor that automatically switches and routes messages between overseas stations, the JPL communications center, and NASA locations.

The TTY signals are multiplexed and converted into 56 kbps wideband circuits and transmitted via satellite between GSFC, JPL, and overseas locations.

The following paragraphs generally describe the four TTY assemblies that comprise the TTY Subsystem that was converted to eight-level ASCII operation.

A. Central TTY Assembly (CTT)

The CTT consists of all the TTY equipment that is located in the JPL-Pasadena Space Flight Operations Facility (SFOF) Central Communications Terminal. The CTT also consists of

TTY equipment that serves the NASCOM West Coast Switching Center (WCSC). The WCSC is an integral part of the Central Communications Terminal.

B. Area TTY Assembly (ATT)

The ATT consists of the TTY equipment located in the GCF-10 Message Center at Goldstone, California.

C. Station TTY Assembly (STT)

The STT consists of the TTY equipment located at DSS 11, 12, and 14 in Goldstone, California, and at two overseas locations in Spain (DSS 61/63 and 62), and one in Australia (DSS 42/43).

D. External TTY Distribution Assembly (ETD)

The ETD consists of the TTY equipment serving the following facilities, projects, and remote JPL-Pasadena locations:

(1) The GCF-20 Message Center located in the SFOF Bldg. 230, room B31A.

(2) The Network Operations Control Center (NOCC) located on the first floor of the SFOF Bldg. 230.

(3) Locations serving projects such as Voyager and IRAS.

(4) Various remote installations located at JPL-Pasadena and also a remote off-Lab JPL building at Hill Street in Pasadena.

II. Significant Functional Characteristics

The following paragraphs describe the differences between the significant functional characteristics of both the old five-level Baudot format Teletype Subsystem and the new ASCII format Teletype Subsystem.

A. Old Five-Level TTY Subsystem

All transmit and receive TTY circuits in the old TTY Subsystem operated as neutral 130 V dc current mode 60 milliampere loops. Power isolation had to be provided between the common carriers (Pacific Telephone Co. and Western Union Co.) and the CTT. The JPL TTY circuits operated at 100 WPM using five-level Baudot code at a line rate of 74.2 baud. Model 28 Teletype Corp. machines were used extensively throughout the subsystem.

A few circuits operated at 110 baud for use by remote customers served by NASCOM. The subsystem employed a Voice Frequency Telegraph System (VFTG) between JPL and Goldstone as well as between the overseas DSS stations and the NASCOM Switching Centers at Madrid, Spain, and Canberra, Australia. The Databit, Inc., Model 922 TDM System between JPL and GSFC accepted data from a maximum of 40 outbound TTY channels in dc loop current form. The TDM System converted the outbound TTY circuits to a 4.8 kbps aggregate high-speed data (HSD) channel that was multiplexed onto a 56 kbps wideband channel for transmission, via satellite, to GSFC.

B. New Eight-Level TTY Subsystem

1. **Overview.** The new TTY Subsystem uses the standard eight-level ASCII eleven-unit code in an asynchronous mode at a 100 WPM, 110 baud, line rate. The subsystem uses NASCOM-provided Teletype Corp. Model 40/2 Keyboard Display Printers (KDPs) and Receive-Only Printers (ROPs), and Model 4210 Magnetic Tape Terminals.

The interface between the Data Terminal Equipment (DTE) and the Data Communication Equipment (DCE) is specified by the Electronic Industries Associated (EIA) RS-232-C Standard. This specification is applicable to all DTE and DCE equipment employing serial binary data exchange.

The EIA Standard specifies that a signal is considered in the marking condition when the signal is between minus 3 V and minus 25 V, and considered in a spacing condition when the signal is between positive 3 V and positive 25 V.

The subsystem employs a new NASCOM-provided Model T-96 character-interleaved TDM system between JPL and GSFC. It multiplexes up to 50 outbound TTY channels and converts them into one 7.2 kbps HSD aggregate channel. The HSD channel is multiplexed, along with six other HSD channels, onto a 56 kbps wideband channel for transmission, via satellite, to GSFC.

2. **Model 40/2 teletype equipment.** Brief functional descriptions and features of the KDP, ROP, and Magnetic Tape Terminal are provided below:

a. KDP. The Model 40/2 KDP consists of a display monitor (CRT), operator console (keyboard), controller (logic unit), and printer. Characters can be entered and sent on the line directly from the console keyboard or from the display monitor after entry and editing. The display monitor logic can store up to 72 lines (5,760 characters) of data. The KDP can also display received data on its monitor and prepare hard copies on its tractor-feed impact printer. The KDP has a full ASCII printer with an 80-column maximum line length and EIA interface. The KDP console has editing controls for

scrolling, line and character insertion/deletion, cursor tab and movement, segment advance, and control character functions. The KDP and Magnetic Tape Terminal are connected together through a NASCOM-provided EIA switch to permit the interchange of data between the two and permit the KDP to transmit on-line.

b. ROP. The Model 40/2 ROP is an electromechanical line-at-a-time tractor feed impact printer which has the same features as that of the KDP printer. The ROP provides hard copies of the data received from the line. The ROP has a key-and-lamp strip that monitors the paper supply and status of the power supply, permits the interruption of incoming transmission, and signals that an invalid character parity has been detected.

c. Magnetic Tape Terminal. The Magnetic Tape Terminal is a combined send/receive unit arranged for half-duplex operation as an adjunct to the model 40/2 KDP. It is compatible with ASCII code. The data storage medium is 1.27 cm computer grade magnetic tape. The magnetic tape is provided in a cartridge with a 159,000 character capacity. It has a forward/reverse search capability of 400 characters per second and a forward/reverse fast access capability of 4000 characters per second. When accessed directly to the line, it operates at 110 baud. When sending to or receiving from the KDP, it operates at a high-speed rate of 1200 bps. The Magnetic Tape Terminal is arranged to perform the following:

(1) Store outbound TTY traffic for record.

(2) Record incoming traffic during unattended periods.

(3) Recall messages prepared for outbound traffic.

(4) Automatically transmit a large amount of messages, or a multiple-page message, previously stored on its tape.

III. Overview of the Implementation Plan

In 1978, JPL and NASCOM agreed to the following details of the eight-level TTY Subsystem implementation plan.

(1) The definition of the GCF/NASCOM interface, including the electrical signal and mechanical characteristics, and the exact location of the interface for each TTY assembly was established.

(2) NASCOM was to provide the Model 40/2 TTY equipment, VFTG assemblies, TDM System, and the overseas jack modules.

(3) JPL was to provide equipment racks, test sets and test interface equipment, modems, digital bridging equipment, mounting assemblies, and most of the TTY Subsystem cabling.

(4) The configuration of each TTY assembly within the TTY Subsystem was determined, taking into account engineering and operational considerations and budgetary restraints. (The configuration of each assembly is described in Part IV and depicted in Figs. 1 through 4.)

(5) The subsystem cut-over considerations of the new DSN TTY Subsystem would be on a circuit-by-circuit basis with the NASCOM communications processor providing code conversion during the transition period.

A. JPL Equipment Procurement Considerations

Most of the TTY supporting equipment was procured, whenever possible, from commercial sources on an off-the-shelf basis. For cost effectiveness, commercially available EIA cables were procured and used whenever possible. All other cables, test interface panels, and hardware mounting assemblies were designed and fabricated at JPL. Commercially available EIA patch, monitor, and test jack modules were procured for the JPL-Pasadena and Goldstone locations.

B. Installation and Cut-Over of the New TTY Subsystem

The new TTY Subsystem was installed and tested locally at all locations as a separate entity. Noninterference was maintained at all times with the operational capability of the existing TTY Subsystem. The overseas stations were the first to be cut-in to service followed, in August of 1980, by the JPL-Pasadena and Goldstone locations. Close liaison and coordination had to be maintained at all times between JPL and NASCOM to ensure an orderly transition from the old to the new TTY Subsystem.

IV. Functional Description of the Eight-Level TTY Assemblies

Refer to Figs. 1 through 4, which depict the general configurations and interface relationships of the four TTY assemblies.

A. Central TTY Assembly (CTT)

In the CTT there are one KDP and two ROPs. These are considered part of the WCSC. The KDP is used in the full-duplex mode on a TTY orderwire channel between JPL and GSFC. The ROPs are used to monitor, for test purposes, any of the TTY channels that are routed through the CCT. All 50 channels are routed through the jack modules that access each circuit for patching, monitoring, and testing purposes. Each circuit is individually cabled to a TTY TDM where they are converted to a 7.2 kbps aggregate HSD circuit. The HSD circuit is also accessed to a jackfield for patching, monitoring,

and testing purposes. The HSD circuit is then cabled, along with six other 7.2 kbps HSD circuits, to a wideband TDM where they are multiplexed and converted into one 56 kbps wideband circuit. A data service unit converts the wideband signals to baseband bipolar line signals for transmission, via satellite, to GSFC.

All TTY channels to JPL on-Lab and off-Lab locations are either directly cabled or transmitted to their locations via JPL-owned asynchronous modems. The modems convert the TTY RS-232 signals to frequency shift keying (FSK) signals for transmission, over leased or private lines, to their respective locations where they are converted back to RS-232 TTY signals for input to TTY machines.

B. Area TTY Assembly (ATT)

In the ATT there are two TTY channels. One is full-duplex and the other is a receive-only channel. Both are interfaced with the CTT via modems, and the FSK audio signals are transmitted between the CTT and the ATT via Western Union microwave channels. The two channels are accessed to RS-232 jack modules for patching, testing, and monitoring. The receive-only channel is connected, via a digital bridge assembly, to six locations. One location is an ROP at the ATT. The five other locations are remote (see Fig. 2). The RS-232 signals from the digital bridge assembly are converted to FSK by modems and transmitted to those remote locations via intersite facilities. The FSK signals at the remote locations are converted back to RS-232 by modems and interfaced to an ROP at each location. The full-duplex channel is accessed to a prime and backup set of ROPs and Magnetic Tape Terminals via a fallback switch and two EIA RS-232 switches. The fallback switch selects which set is accessed to the line. The RS-232 switches provide for local or on-line modes of operation for each set of KDPs and Magnetic Tape Terminals. Two ROPs are also accessed to the jack modules allowing them to be patched to copy receive traffic.

C. Station TTY Assembly (STT)

TTY signals are exchanged between GSFC and the overseas NASCOM Switching Centers at Canberra, Australia, and Madrid, Spain, by multiplexing them and converting them into 56 kbps wideband signals that are transmitted via satellite. The switching centers convert the multiplexed TTY signals back to RS-232 signals for monitoring and testing. The switching centers interface with the individual stations via NASCOM provided Voice Frequency Telegraph Systems (VFTGs). The VFTGs use frequency division multiplexing techniques to transmit up to four RS-232 channels over one voice frequency line. At the stations the multiplexed signals are again converted to RS-232 channels and connected to jackfields for patching, monitoring, and testing.

Each station has prime and backup sets of KDPs magnetic tape terminals, ROPs, and EIA switches which are utilized as described under "Area TTY Assembly (ATT)."

D. External TTY Distribution Assembly (ETD)

TTY channels are distributed from the CCT to the various JPL on-Lab locations either directly by cable or by JPL-owned modems. Each modem converts the voice frequency line signal between the CTT and ETD back to an RS-232 TTY signal for input to a ROP at each location. The ROP provides hard copy of the TTY message. The TTY channel that serves the GCF-20 message center is full-duplex. The channel is connected to a jackfield and routed through a fallback switch to either a prime or a backup set of KDPs, Magnetic Tape Terminals, ROPs, and EIA switches. The functions of these equipments were described under "Area TTY Assembly (ATT)."

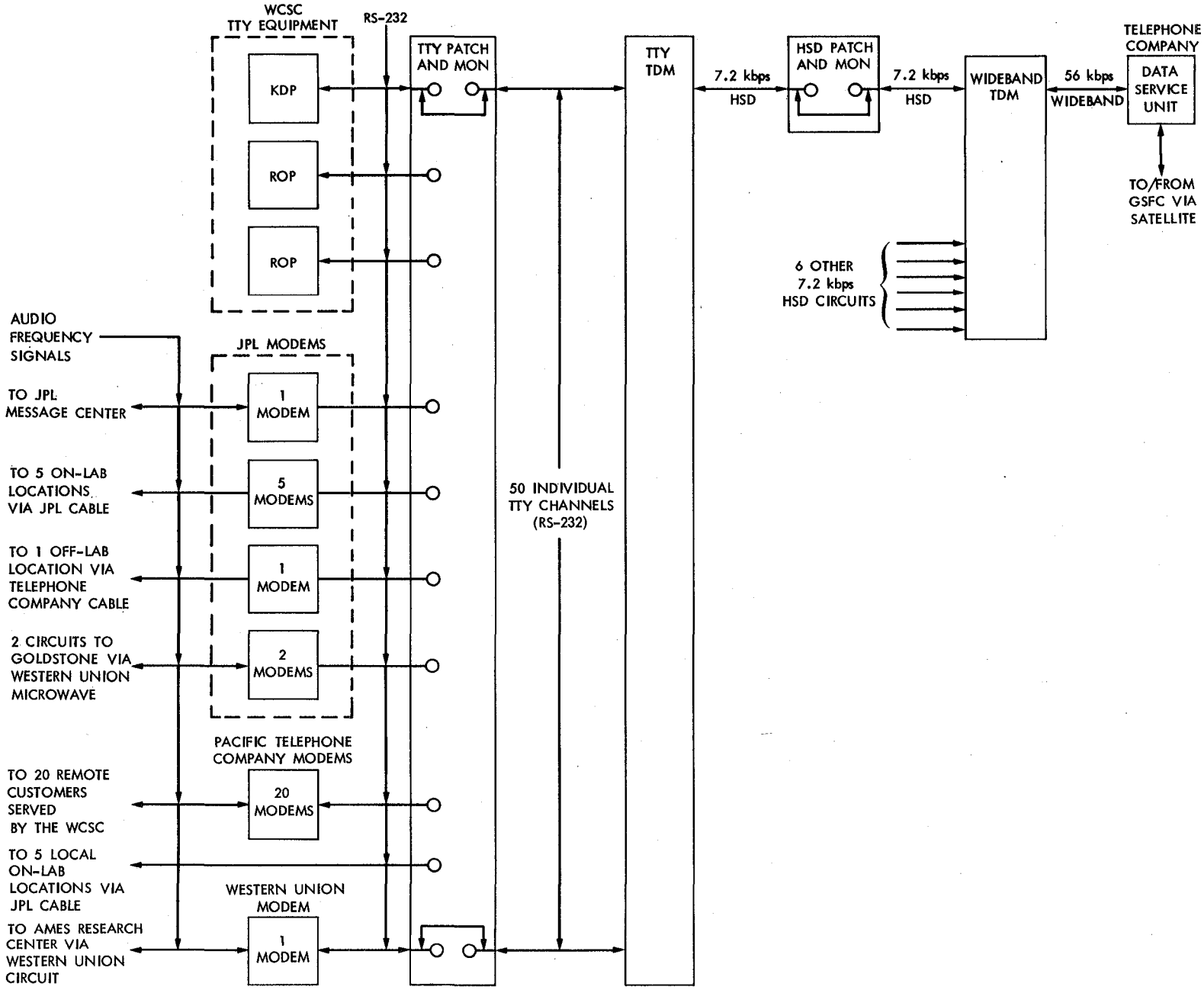

Fig. 1. Central TTY assembly (CTT), eight-level TTY configuration

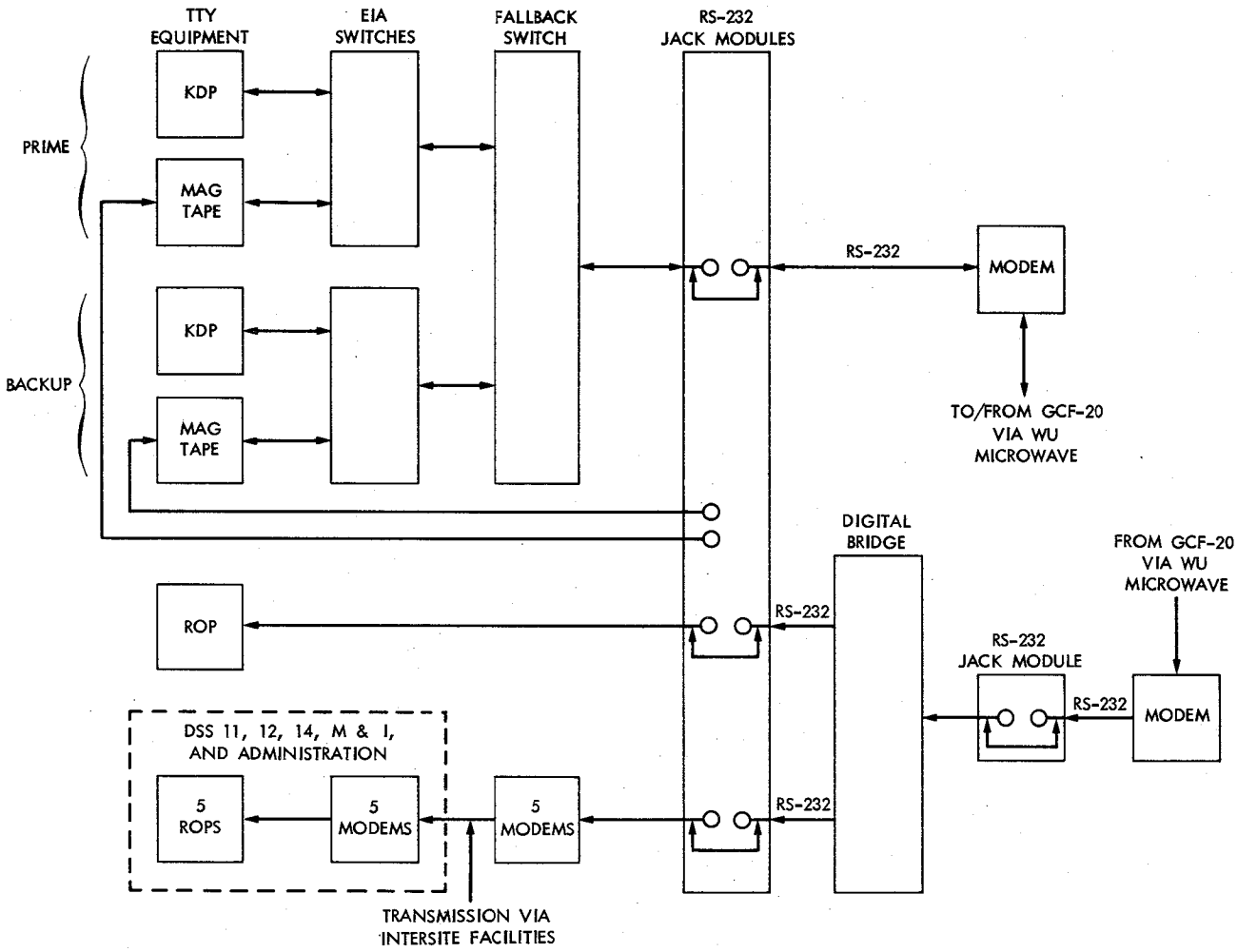

Fig. 2. Area TTY assembly (ATT), eight-level TTY configuration

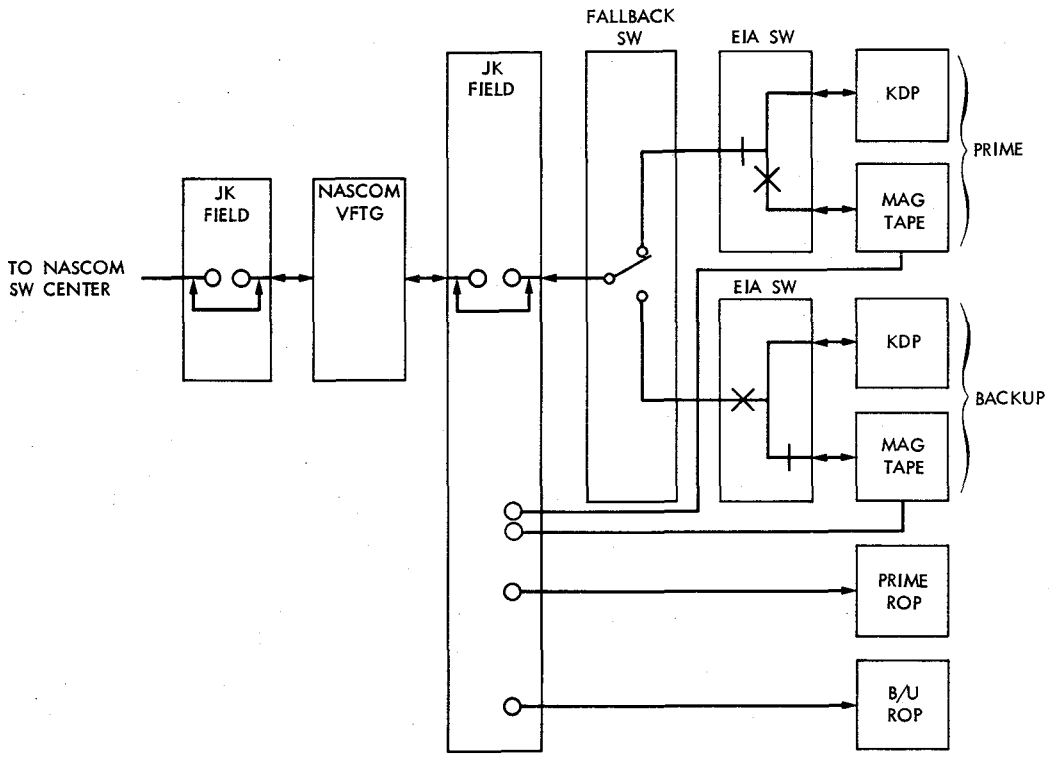

Fig. 3. Overseas stations, eight-level TTY configuration

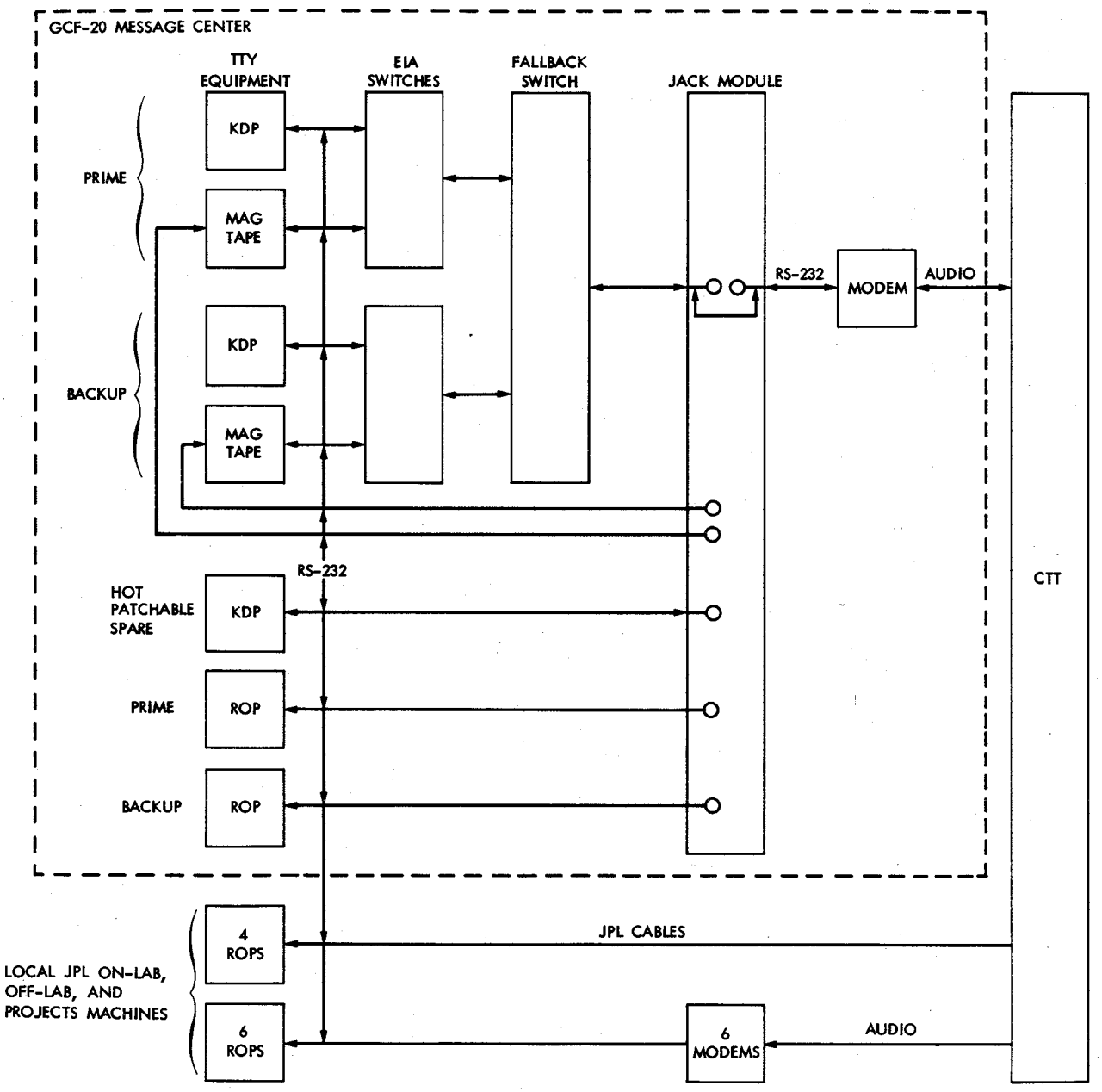

Fig. 4. External TTY distribution assembly (ETD), eight-level TTY configuration

Telemetry Degradation due to a CW RFI Induced Carrier Tracking Error for the Block IV Receiving System With Maximum Likelihood Convolutional Decoding

M. K. Sue
Telecommunications Systems Section

This article is a part of a continuing effort to develop models to characterize the behavior of the Deep-Space Network (DSN) Receiving System in the presence of a radio frequency inteference (RFI), and presents a simple method to evaluate the telemetry degradation due to the presence of a CW RFI near the carrier frequency for the DSN Block IV Receiving System using the Maximum Likelihood Convolutional Decoding Assembly (MCD). Analytical and experimental results are presented.

I. Introduction

This study is part of a continuing effort to study the adverse effects that a radio frequency interference may have on the Deep-Space Network Receiving System. Depending on the frequency and power level, an RFI can have various effects on a receiver, such as saturating receiver components, generating harmonics, and degrading the tracking loop performance. For the Block IV receiver, saturation is the dominating effect when the interference frequency is far away from the carrier frequency and degradation on the carrier tracking loop becomes a significant when the interference frequency is close. The receiver saturation and carrier loop degradation due to CW RFI have been studied and documented (Refs. 1 and 2). The purpose of this study is to evaluate the degradation on the Telemetry System due to a noisy carrier reference caused by a CW RFI with frequency close to the desired carrier frequency, say within 1 kHz.

It is well known that the Communication System employed for deep-space communication is a phase coherent system that requires phase synchronization at the receiver. Synchronization at the receiver is achieved by tracking the carrier phase with a phase-locked loop. The presence of a CW RFI will produce a phase error in the carrier tracking loop that will in turn cause an apparent reduction of the strength of the received signal and consequently an increase in bit error rate. It is the purpose of this article to evaluate this effect using an analytical model previously developed for the prediction of the carrier loop performance in the presence of a CW RFI (Ref. 2). There may be other effects such as Subcarrier Demodulation Assembly (SDA) and Symbol Synchronization Assembly (SSA) degradation, which may further degrade telemetry performance; these effects will not be discussed.

II. Analysis

It is well known that the probability of bit error of a maximum likelihood convolutional decoder with perfect carrier reference is a function of the ratio of signal energy per bit to noise spectral density (Ref. 3), i.e.,

$$P_e = f(\rho) \tag{1}$$

where ρ is the ratio of signal energy per bit to noise spectral density.

Exact analytical expression for P_e is not attainable for phase coherent demodulation and Maximum Likelihood Convolution Decoding (MCD). However, for the MCD implemented in the DSN, the probability of bit error has been approximated by the following equation (Ref. 4):

$$P_e \approx A \exp(B\rho) \tag{2}$$

where $A = 85.7501$ and $B = -5.7230$ for $K = 7$, rate ½ convolutional code with $Q = 3$. It is noted that Eq. (2) assumes perfect carrier demodulation.

When a CW RFI is present, it creates an imperfect carrier reference that will degrade the telemetry system performance. If we let $\phi(t)$ denote the phase error of the carrier tracking loop and assume that noise contribution to $\phi(t)$ is negligible, then, in the presence of a CW RFI, we have from Ref. 2:

$$\phi(t) = \lambda + m \sin(\Delta\omega t + \nu) \tag{3}$$

where λ is the static phase error (SPE), m is the modulation index, $\Delta\omega$ is the RFI offset frequency in radians per second and ν is the phase angle. Both λ and m are functions of $\Delta\omega$ and the interference-to-signal ratio (ISR) and they are related through the following set of equations (Refs. 5, 6, and 7):

$$\sin\lambda = \frac{m^2 \delta \cos\psi}{2J_0(m)} \tag{4}$$

$$\sin(\lambda - \nu) = \frac{-m^2 \delta \cos\psi}{2R_e J_1(m)} \tag{5}$$

$$R_e^2 = \left[\frac{m\delta \sin\psi + 2J_1(m)\cos\lambda}{J_0(m) - J_2(m)}\right]^2 + \left[\frac{m^2 \delta \cos\psi}{2J_1(m)}\right]^2 \tag{6}$$

$$\delta = \frac{\Delta\omega}{\alpha_L K_0 |F(j\Delta\omega)|} \tag{7}$$

where K_0 is the open loop gain, α_L is the limiter suppression factor, $F(j\omega)$ is the loop filter transfer function, ψ is the phase angle of $F(j\Delta\omega)$, $|F(j\Delta\omega)|$ is the amplitude of $F(j\Delta\omega)$, $J_i(\cdot)$ is the Bessel Function of ith order and R_e is the effective interference to signal amplitude ratio at the limiter output. Formula to compute α_L (in the presence of RFI) and R_e can be found in Ref. 2.

It is noted that $\phi(t)$ is sinusoidal with a frequency equal to the RFI offset frequency. If we assume that the RFI offset frequency is much lower than the telemetry bit rate, then $\phi(t)$ is essentially constant over the length of most decoder error. Under this condition, the conditional probability of bit error for a given phase error can be expressed as (Refs. 3 and 4):

$$P_e(\phi) = A \exp(B\rho \cos^2 \phi(t)) \tag{8}$$

Since we have assumed that $\phi(t)$ is deterministic, we can obtain an average probability of bit error by taking a time average of $P_e(\phi)$ over one period of $\phi(t)$. If we let P_R denote the average probability of bit error in the presence of RFI, then we have from Eq. (8) the following:

$$P_R = \langle P_e(\phi) \rangle = \frac{1}{T}\int_0^T A \exp(B\rho \cos^2 \phi(t))\, dt \tag{9}$$

where $T = 2\pi/\Delta\omega$ and $\langle\cdot\rangle$ denotes the time average.

It is noted that the approach taken here to derive the average probability of bit error is based on the assumption that the phase error varies slowly compared to the data rate. This approach is often referred to as the "high-rate model."

Usually, a figure of merit used to determine telemetry performance degradation due to tracking error is the equivalent loss of signal energy-to-noise ratio, which is often referred to as "radio loss." Alternatively, we can define a parameter, γ, as the ratio of the probability of bit error under the influence of a CW RFI to that with no RFI and use this ratio as a measure of the RFI effects on the Telemetry System. Recalling that the probability of bit error with no RFI is given by Eq. (2), we can obtain γ by dividing Eq.(9) by Eq. (2). After simplification, γ becomes:

$$\gamma = \frac{1}{T}\exp\left(\frac{-B\rho}{2}\right)\int_0^T \exp\left[\frac{B\rho}{2}\cos(2\lambda + 2m\sin(\Delta\omega t))\right] dt \tag{10}$$

The parameter γ is the bit error multiplication factor. For a given bit error rate in the absence of RFI, the bit error rate under the influence of a RFI is simply equal to the product of the bit error rate with no RFI and the multiplication factor.

It is noted that the foregoing analysis is based primarily on two assumptions: (1) the data rate is much higher than the RFI offset frequency, and (2) other effects such as SDA, SSA and noise contribution to the carrier tracking error are negligible. These assumptions, particularly the high-rate assumption, will probably place some restrictions on the applications of the model. It is therefore necessary to examine possible restrictions that may result from any of these assumptions. The assumption that the noise contribution to the phase error is negligible has been proven to be a satisfactory assumption with reasonably accurate results even at the recommended minimum signal level (10-dB carrier margin), as indicated in Ref. 2. Hence no restriction results from this assumption. The assumptions that the data rate is much higher than the offset frequency and that the SDA and SSA effects are negligible require that the offset frequency be much smaller than the data rate and the subcarrier frequency. This restricts the range of the offset frequency for which the model in Eq. (10) is valid. This restriction fortunately does not limit the usefulness of this model because the power level required for an RFI to produce significant degradation on the carrier loop at large offset frequency will, in general, be so strong that receiver saturation may become dominant.

It is further noted that the expression for γ given by Eq. (10) does not account for signal inversion effects caused by the phase error, $\phi(t)$. When $|\phi(t)| \leqslant \pi/2$, the effect is a reduction of the received signal strength. When $|\phi(t)|$ is larger than $\pi/2$ and less than or equal to π, the effect is a reduction in signal strength and inversion of the received signal. For the type of RFI considered, $|\phi(t)|$ does not exceed $\pi/2$ until the interference power is approximately within 1 dB of the power level required for an interference to cause the receiver to drop out of lock. For the cases considered with γ ranging from 1 to 10, $|\phi(t)|$ is always less than $\pi/2$; hence signal inversion effects can be ignored. For those who are interested in signal inversion effects, expressions are provided in Appendix A for the calculation of γ and the probability of bit error.

III. Numerical Results

The parameter γ has been evaluated using results of Eq. (2) for the DSN Block IV receiver with maximum likelihood convolutional decoding for three RFI offset frequencies, i.e., 10, 100, and 1000 Hz. The receiver is assumed to be in the typical operational configuration, i.e., 2-kHz predetection noise bandwidth, wide mode with $2BLO$ equal to 10 Hz for S-band and 30 Hz for X-band, where $2BLO$ is the threshold loop noise bandwidth. Three operating points corresponding to a bit error rate of 10^{-3}, 10^{-4}, and 10^{-5} have been chosen. The resulting bit error rate multiplication factor has been plotted as a function of interference-to-signal power ratio with RFI offset frequency as a parameter (Figs. 1 through 6). Based on these curves, it is observed that γ is relatively insensitive to the operating points.

It is noted that the phase jitter used to generate the curves for the 10-Hz case is twice the theoretical jitter obtained from Ref. 2. The factor of 2 is necessary to account for the inaccuracy of the phase-locked loop model. As it was pointed out, the predicted phase jitter is about half of the measured phase jitter for small offset frequency and small interference-to-signal ratio (Ref. 2).

IV. Experimental Verification

Experimental verification was performed in TDL using the Block IV receiver, Block III SDA, and a Viterbi decoder with $K = 7$, $R = 1/2$ and $Q = 3$. Comparison of experimental and theoretical results are shown in Figs. 4 and 5. For the cases compared, good agreement between the measured and predicted values is observed for the 10-Hz offset and the 100-Hz offset. For the 1000-Hz offset, experimental results indicate that the TDL system is 4 to 6 dB more sensitive to RFI than predicted. Judging from the simplifying assumptions made in the analysis and measurement accuracy, this discrepancy is not unexpected.

V. Conclusion

A method to evaluate the telemetry degradation due to the presence of a CW RFI near the carrier frequency has been presented for the DSN Block IV Receiving System using Maximum Likelihood Decoding. This method is based on two assumptions: (1) the data rate is much higher than the RFI offset frequency, and (2) other effects such as SSA, SDA and noise effects on the phase locked loop are negligible. These assumptions are valid for most deep-space applications with small offset frequency. As the RFI offset frequency becomes large, the accuracy of this model becomes poor. Experimental results obtained from TDL indicate that reasonably accurate prediction is obtainable even at an offset frequency of 1000 Hz for a system with a data rate of 40 kbits/s and a subcarrier frequency of 370 kHz.

Based on experimental and analytical results, it can be concluded that degradation on the Telemetry System is not as severe as that on the carrier loop for the type of RFI considered. The protection criteria proposed for the carrier loop will provide sufficient protection for the Telemetry System with a maximum increase in BER by a factor less than 2. Therefore, a separate protection criterion is not needed to protect the Telemetry System for the type of RFI considered. A curve of protection criteria proposed for the carrier loop is shown in Fig. 9 for reference.

Acknowledgment

The author would like to thank J. F. Hays and J. F. Weese for their support in TDL.

References

1. Hersey, D. R., and Sue, M. K., "Maximum CW RFI Power Levels for Linear Operation of the DSN Block IV Receiver at S-Band Frequencies," in *The Deep Space Network Progress Report 42-56*, April 15, 1980. Jet Propulsion Laboratory, Pasadena, Calif.
2. Sue, M. K., "Block IV Receiver Tracking Loop Performance in the Presence of a CW RFI," in *The Telecommunications and Data Acquisition Progress Report 42-60*, September and October 1980. Jet Propulsion Laboratory, Pasadena, Calif.
3. Heller, J. A., and Jacobs, I. M., "Viterbi Decoding for Satellite and Space Communication," *IEEE Trans. Comm. Tech.*, COM-19, No. 5, Oct 1971.
4. Webster, L., "Maximum Likelihood Convolutional Decoding (MCD) Performance Due to System Losses," in *The Deep Space Network Progress Report 42-34*, August 15, 1976. Jet Propulsion Laboratory, Pasadena, Calif.
5. Bruno, F., "Tracking Performance and Loss of Lock of a Carrier Loop Due to the Presence of a Spoofed Spread Spectrum Signal," *Proceedings of the 1973 Symposium on SSC*, Hazeltine Corp.
6. Blanchard, A., "Interference in Phase-Locked Loops," *IEEE AES-10*, No. 5, Sept. 1974.
7. Levitt, B. K., "Carrier Tracking Loop Performance in the Presence of Strong CW Interference," DSN Progress Report 42-51, March and April 1979, in *The Deep Space Network Progress Report 42-51*, March and April, 1979. Jet Propulsion Laboratory, Pasadena, Calif.

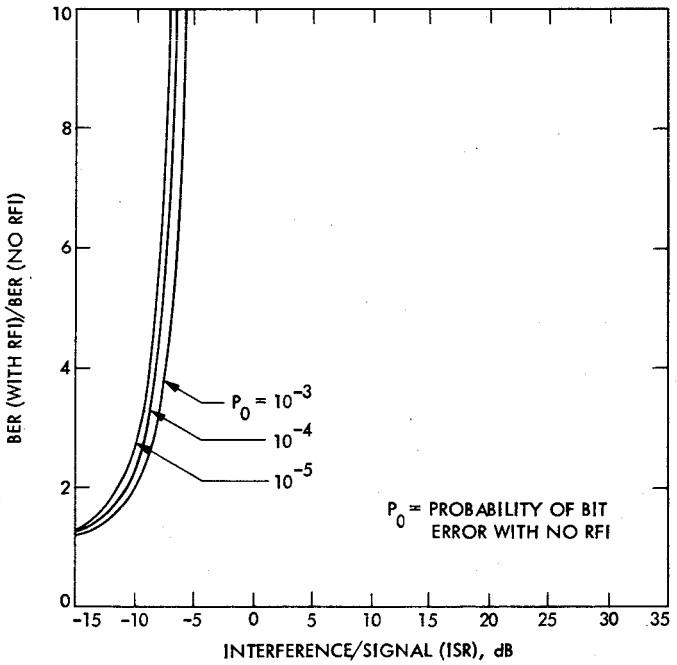

Fig. 1. TLM degradation vs ISR for 10-Hz frequency offset (wide/2 kHz/10Hz)

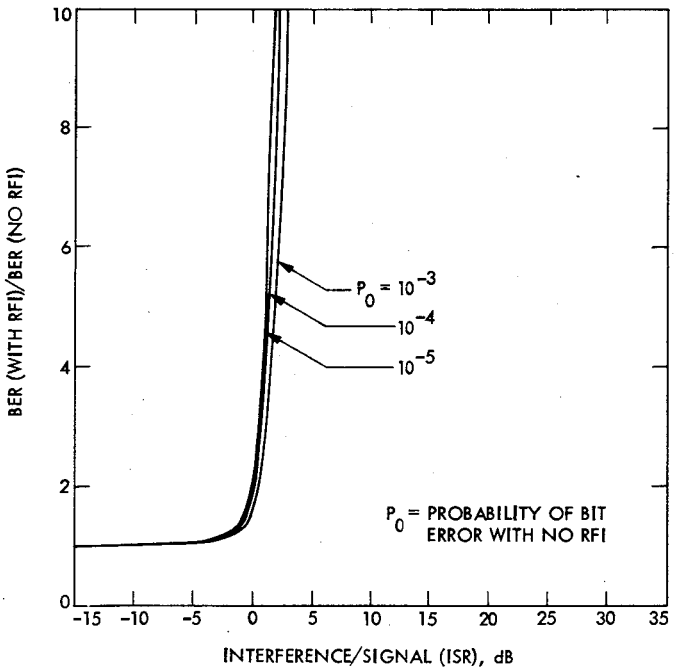

Fig. 2. TLM degradation vs ISR for 100-Hz frequency offset (wide/2 kHz/10Hz)

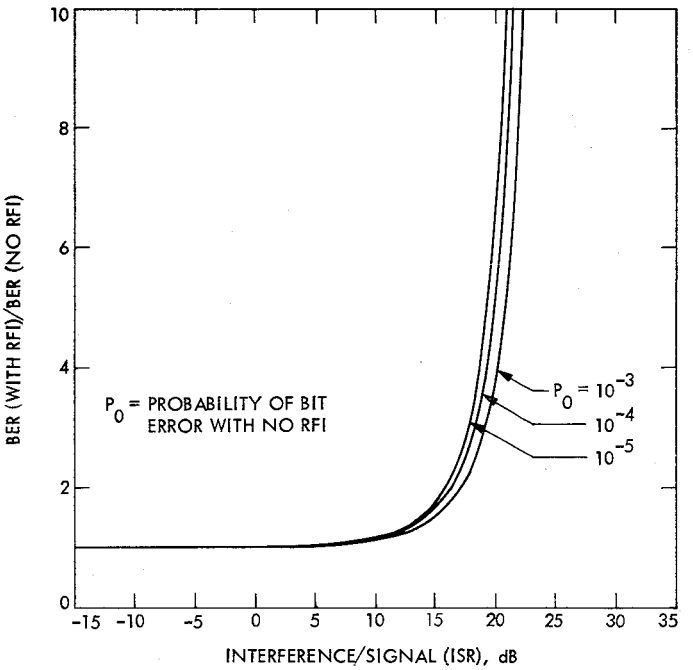

Fig. 3. TLM degradation vs ISR for 1000-Hz frequency offset (wide/2 kHz/10 Hz)

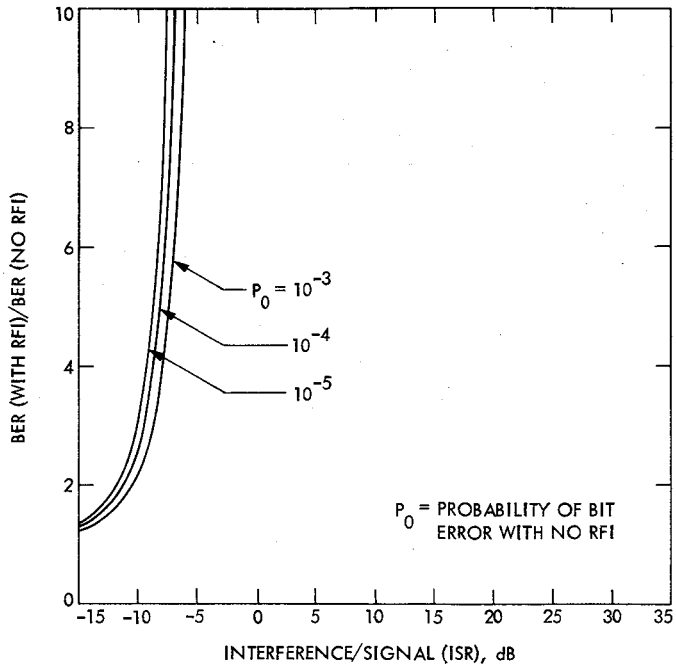

Fig. 4. TLM degradation vs ISR for 10-Hz frequency offset (wide/2 kHz/30 Hz)

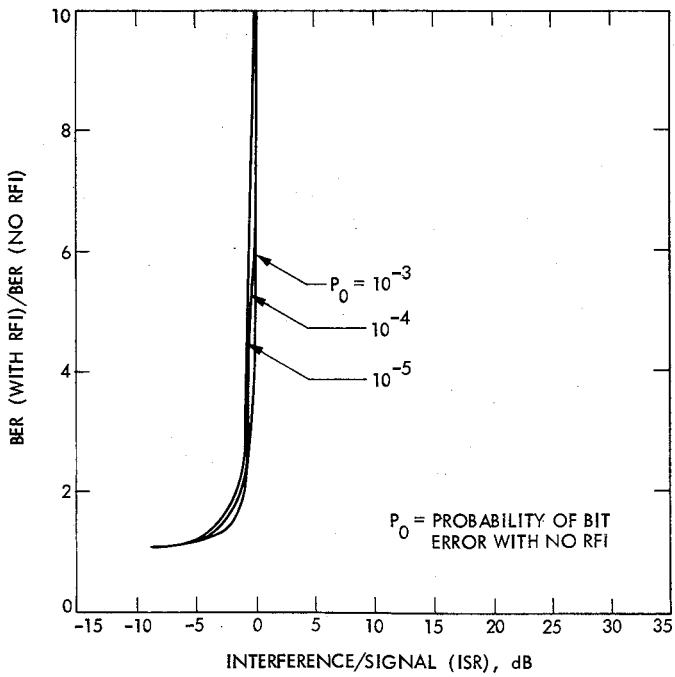

Fig. 5. TLM degradation vs ISR for 100-Hz frequency offset (wide/2 kHz/30 Hz)

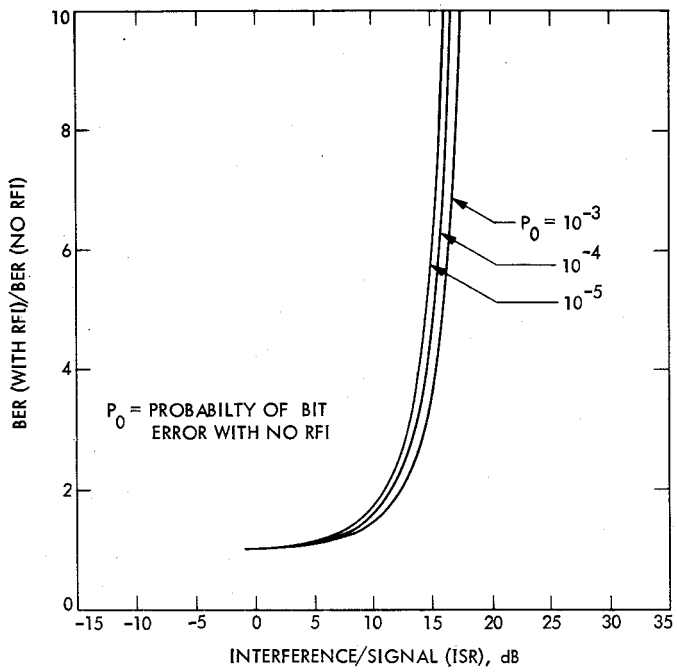

Fig. 6. TLM degradation vs ISR for 1000-Hz frequency offset (wide/2 kHz/30 Hz)

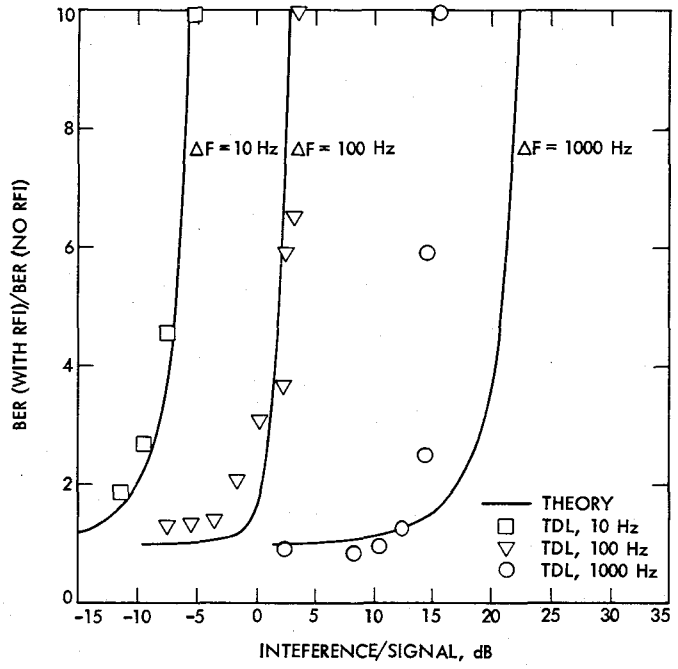

Fig. 7. Comparison of experimental and analytical results for BER (no RFI) = 10^{-3}

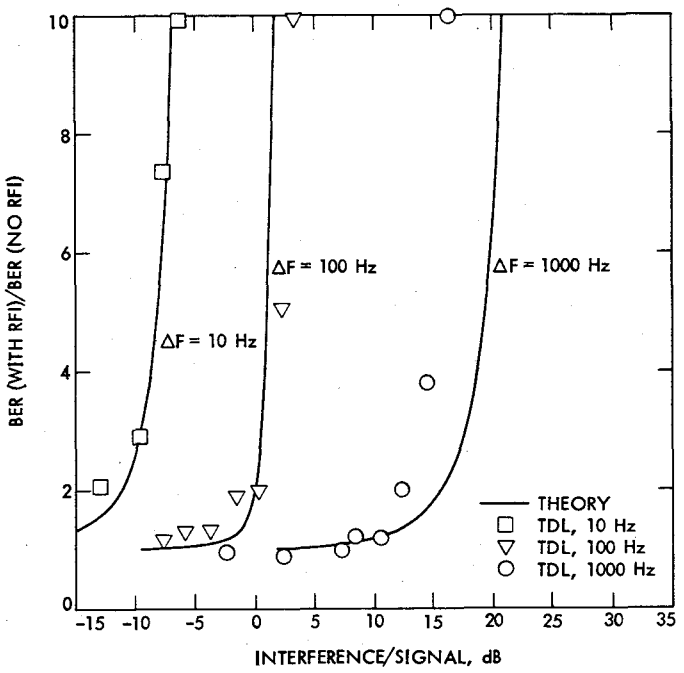

Fig. 8. Comparison of experimental and analytical results for BER (no RFI) = 10^{-5}

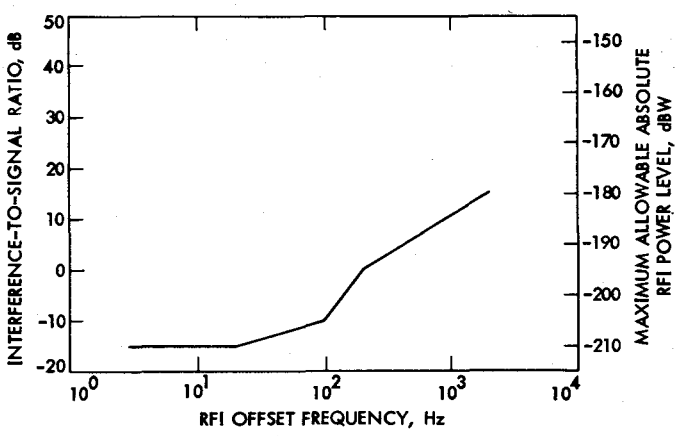

Fig. 9. Recommended protection criteria for CW RFI for Block IV Receiver (absolute power level based on 10–db carrier margin and −205 dBW noise power in a 10-Hz bandwidth) (from Ref. 2)

Appendix A
Effects of Signal Inversion

The probability of bit error for a phase coherent system with Maximum Likelihood Convolutional Decoding is a function of the signal energy per bit to noise spectral density ratio, ρ. In the presence of a phase error, $\phi(t)$, the effect is a reduction of the received signal strength when $|\phi(t)| \leq \pi/2$. When $\pi/2 < |\phi(t)| \leq \pi$, the effect is a reduction of signal strength and an inversion of the received signal. If we assume that the code is transparent and let P_1 and P_2 denote the probability of bit error for $|\phi(t)| \leq \pi/2$ and $\pi/2 < |\phi(t)| \leq \pi$ respectively, then from Eq. (2) we have

$$P_1(\phi) = A \exp(B\rho \cos^2 \phi(t)) \quad \text{for } |\phi(t)| \leq \pi/2 \tag{A-1}$$

$$P_2(\phi) = 1 - P_1(\phi) = 1 - A \exp(B\rho \cos^2 \phi(t)) \quad \text{for } \pi/2 < |\phi(t)| \leq \pi \tag{A-2}$$

and the conditional probability of bit error, $P_e(\phi)$, is

$$P_e(\phi) = \begin{cases} P_1(\phi) & |\phi(t)| \leq \pi/2 \\ P_2(\phi) & \pi/2 < |\phi(t)| \leq \pi \end{cases} \tag{A-3}$$

In the presence of a CW RFI, the phase error process under a strong signal condition can be approximated by a deterministic time function as follows:

$$\phi(t) = \lambda + m \sin(\Delta\omega t + \nu) \tag{A-4}$$

where $\Delta\omega$ is the RFI offset frequency in rad/s and ν is a phase constant. For the purpose of this analysis, ν can be assumed to be zero with no loss of generality. Since $\phi(t)$ is periodic, we can obtain the average probability of bit error, P_R, by averaging the conditional probability of bit error, $P_e(\phi)$, over one period of $\phi(t)$, i.e.,

$$P_R = \frac{1}{T}\int_0^T P_e(\phi)\, dt \tag{A-5}$$

where T is the period of $\phi(t)$, i.e., $T = 2\pi/\Delta\omega$.

To evaluate Eq. (A-5), it is necessary to determine the time periods during which $\pi/2 < |\phi(t)| \leq \pi$. Noting that the maximum value of $|\lambda|$ is $\pi/2$ and that m cannot be larger than $\pi/2$ in order for a practical receiver to remain in lock, we conclude that there is at most one such time period during which $\pi/2 < |\phi(t)| \leq \pi$. If we let t_1 and t_2 denote the end points of this time period, then from Eq. 4 we have:

$$t_1 = \left(\frac{1}{\Delta\omega}\right) \sin^{-1}\left(\frac{\frac{\pi}{2} - \lambda}{m}\right) \tag{A-6}$$

$$t_2 = \frac{\pi}{\Delta\omega} - t_1 \tag{A-7}$$

Having determined t_1 and t_2, we can now proceed to evaluate Eq. (A-5).

$$P_R = \frac{1}{T}\left[\int_0^{t_1} P_1(\phi)\, dt + \int_{t_1}^{t_2} P_2(\phi)\, dt + \int_{t_2}^{T} P_1(\phi)\, dt\right] \tag{A-8}$$

Substituting Eqs. (A-1) and (A-2) into (A-8) and rearranging terms, we have for P_R the following equation:

$$P_R = \frac{1}{T}\int_0^T A \exp[B\rho \cos^2 \phi(t)]\, dt - \frac{2}{T}\int_{t_1}^{t_2} A \exp[B\rho \cos^2 \phi(t)]\, dt + \frac{t_2 - t_1}{T} \tag{A-9}$$

where t_1 and t_2 are given by Eqs. (A-6) and (A-7). The corresponding bit error multiplication factor becomes

$$\gamma = \frac{1}{T} \exp\left[-\frac{B\rho}{2}\right] \left[\int_0^T \exp\left[\frac{B\rho}{2} \cos 2\phi(t)\right] dt - 2\int_{t_1}^{t_2} \exp\left(\frac{B\rho}{2} \cos 2\phi(t)\right) dt + \frac{t_2 - t_1}{A} \exp\left(-\frac{B\rho}{2}\right)\right] \quad \text{(A-10)}$$

Command System Output Bit Verification

C. W. Odd and S. F. Abbate
Deep Space Network Support Section

Command System bit-verification is a means of testing for errors in the command or idle bit sequences radiated from the Command Subsystem at a Deep Space Station. Errors are tested for by comparing the radiated sequences with reference sequences generated externally by the Command System Performance Test software. The test is used to determine whether or not the detected bit error rate exceeds the allowable rate specified in the Deep Space Network System Requirements document for the DSN Command System.

I. Introduction

An automatic test has been developed to test the ability of the Deep Space Station (DSS) Command Subsystem and exciter to generate and radiate, from the exciter, the correct idle bit sequence for a given flight project, or to store and radiate received command data elements and files without alteration. This test, called the Command System Output Bit Verification Test, is an extension of the Command System Performance Test (SPT) and can be selected as an SPT option.

The test compares the bit stream radiated from the DSS exciter with reference sequences generated by the SPT software program. The Command Subsystem and exciter are verified when the bit stream and reference sequences are identical. It is a key element of the acceptance testing conducted on the Command Processor Assembly (CPA) Operational Program (DMC-0584-OP-G) prior to its transfer from Development to Operations.

II. Test Configuration and Subsystem Functions

Figure 1 shows the test configuration used for bit verification testing. It is divided into two parts: a Mission Operation Center (MOC) section and a DSS section. Within the MOC section is the SPT Assembly (SPTA), which consists of the SPT software and the computer in which the program runs to simulate command functions of the MOC. The DSS section contains the following subsystems: The Communication Monitor and Formatter (CMF), the Command Subsystem which is made up of the Command Processor Assembly (CPA) and Command Modulator Assembly (CMA), the Receiver-Exciter Subsystem (exciter, test translator, receiver) and the Telemetry Subsystem which consists of the Subcarrier Demodulator Assembly (SDA), Symbol Synchronizer Assembly (SSA) and Telemetry Processor Assembly (TPA).

The SPTA simulates a MOC by generating command elements, formatting them into high-speed data (HSD) blocks and sending them to the DSS Command Subsystem. It also produces a model of the expected command bit stream radiated from the Command Subsystem. The bit verification program consists of several subprograms and overlays to the SPT program which add the capability to receive telemetry HSD blocks, reclaim the command bit stream from the telemetry blocks, generate idle sequences and compare two bit streams.

In the DSS section, the Receiver-Exciter and Telemetry Subsystems intercept the command bit stream at the output of the exciter, reformat it into telemetry HSD blocks and return it to the SPTA.

III. Software Functional Description

The ability of the bit verification test to compare command sequences in the bit stream with reference sequences is made possible by combining the capabilities of the command SPTA, with those of the Receiver-Exciter and Telemetry Subsystems. In operation it works as follows: the SPT program detects a returning telemetry block, places it in an HSD block buffer and calls a subroutine to extract its data content – whether it be an idle or a command sequence. Next, a routine is called which determines the mode of the CPA, the spacecraft for which it is configured and the presence or absence of Manchester coding. The SPT program then generates a reference sequence with which to compare the returning sequence.

When the CPA is in idle mode, the reference sequence generated is the idle sequence corresponding to the CPA project configuration. The SPT program (using the bit verification capability) compares the returned sequence with the reference sequence, one bit at a time, starting with the first bit returned. Since there is no starting point in the reference sequence, the two sequences may not be synchronized. Therefore, if the initial bits compared are not alike, the bit verification program attempts to synchronize the two sequences by shifting the output sequence one bit with respect to the reference sequence and again compares the first bit of the output sequence with the next bit of the reference sequence. This shift is repeated up to three times if no comparison is found. Finally, if this fails to find a match, a comparison is attempted with the complement of the reference sequence. If this also fails, the program will halt and display an operator message indicating an improper idle sequence. If a match is found, the program will continue to compare subsequent bit pairs until either a mismatch occurs or the SPT program sends an active mode directive to the CPA. All mismatches will cause an operator message to be displayed and identify the block containing the mismatched bit.

If an active mode directive is sent to the CPA, the idle sequence will be replaced with command data sequences in the form of contiguous command elements and files. These will be compared to reference sequence as were the idle sequences and any mismatch logged. The output and reference sequences will be synchronized with the occurrence of the active mode directive from the SPT program. However, unlike idle sequences, the reference sequences are reproductions of the actual command elements sent to the CPA. This is possible because each element generated in the SPT program is a number (or dummy command) generated by a pseudo-random number generator from an initial integer value (or seed word) saved by the SPT program. These elements are sent to the CPA in HSD blocks where they are stored by the CPA in files until ready for radiation. When they are radiated, the SPT program (which independently models these CPA functions) notes which elements are supposed to be radiated and regenerates them from the stored seed words to produce the correct reference sequence.

IV. Procedures

The bit verification option of the command SPT test procedure is a part of the DSN series 850 Standard Test Procedures.

V. Conclusion

The test was used as part of acceptance testing of the CPA software (DMC-0584-OP-G) to verify that the undetected bit error rate for data radiated from the DSS Command Subsystem did not exceed the maximum rate of one in 10^6 bits specified in the DSN System Requirements document. Four hours of error free radiation of both Helios and Voyager test commands were confirmed. This represents continuous error free radiation of approximately 115 kbits of Helios data and 230 kbits of Voyager data.

This test is incorporated in the Mark III 78 (Store-and-Forward) command program for use with the Helios, Voyager, Galileo and International Solar Polar Mission. It is useful for acceptance testing of new Command System software and software in which algorithms have been changed which affect the bit content of the Command System output. It may also be used to verify the system following Engineering Change Order implementation.

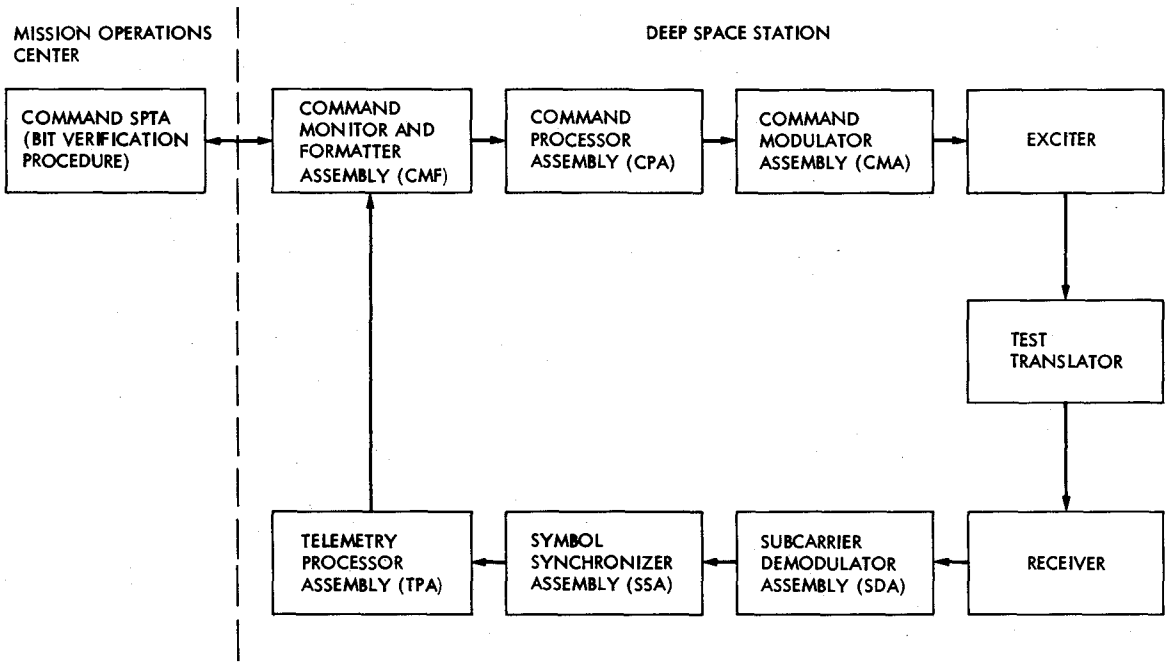

Fig. 1. Bit verification test configuration

Development of a Polymetric Grout for the Hydrostatic Bearing at DSS 14

C. E. McClung, J. L. Schwendeman, G. L. Ball III, and G. H. Jenkins
Monsanto Research Corporation

R. D. Casperson, G. P. Gale, and A. A. Riewe
DSN Engineering Section

The grout under the hydrostatic bearing runner at DSS 14 has exhibited a rapid rate of deterioration and premature failure. This report examines some of the probable causes of the deterioration. It also describes the development of a polymetric grout that is more resistive to the causes of early grout failure.

I. Introduction

A. Geometry

The hydrostatic thrust bearing of the 64-m antenna consists of a steel runner 12.7 cm thick, 24½ m outside diameter and 22½ m inside diameter, and three pads each 16258 cm^2 in area, each carrying 2.75×10^6 kg (see Figs. 1 and 2). High-pressure oil is forced between the lower surface of the pads and the top surface of the runner enabling the antenna to rotate on a thin film of oil approximately 0.25 mm thick. Because the film thickness between the bottom of the pads and the top surface of the runner is so thin, the top surface of the runner must be maintained in a very flat condition. Any degradation in the grout that supports the runner will cause the runner surface to warp into a nonflat condition with a resulting decrease in the oil-film thickness separating the bearing surfaces.

B. History

Initially the runner was precisely leveled and Embeco grout was poured between the bottom of the runner soleplate and top of the concrete pedestal. The Embeco grout contained a corrosive additive that rusted the underside of the soleplate. Soon both the Embeco and soleplate had to be replaced, this time with a thicker soleplate and a drypack grout consisting of portland cement and sand with only enough moisture to provide for bonding during placement.

However, the deterioration of the flatness of the hydrostatic bearing runner flatness, although significantly slower, persisted. It appeared to be worse in areas where bearing oil leaked from the runner joints and reservoir seals. Particles of cement and sand could be observed being flushed out of the grout with the oil leakage. Samples of oil soaked grout were subjected to compression tests and it was found that once the portland cement grout had thoroughly cured, oil did not appear to reduce the strength enough to cause the degradation we were observing.

While searching for plausible causes for the grout deterioration and for possibly a different grout material that would stand up to our rigid requirements, we contacted several

knowledgeable organizations, and finally authorized a contract to Monsanto Research Corporation, Dayton Laboratory.

This article contains much information and findings supplied by George L. Ball III, George H. Jenkins, Charles E. McClung, and James L. Schwendeman of Monsanto Research, Inc., as reported in their periodic and final reports. The work was planned for completion in two phases. Phase 1 was directed toward screening and testing five generic types of materials believed to be potentially able to meet these needs. The physical properties, strength, modulus of elasticity, and resistance to erosion and chemical attack by the oil were to be evaluated, and any unique requirements imposed by each material for mixing, placing, compacting, and cooling (where high heat of polymerization might be a factor) were to be identified. The planned objective of Phase 1 was to identify the single generic type of material best suited to replace the dry pack grout. Phase 2 consisted of developing, refining, and optimizing the selected material to achieve a high-strength, durable grout replacement.

Work in Phase 1 began in July 1978 with a visit to the Goldstone antenna site. The complete repair process—removal of the deteriorated grout, cleaning and preparation of the exposed surfaces, mixing and repacking with the dry pack, and leveling the repaired area—provided a familiarity with the service environment and the repair facilities.

II. Technical Discussion

A. Analysis of the Problem

To design a more durable antenna grout, the events and stresses leading to the early failure of the dry-pack material must be understood. Some of these factors were not identified until late in this work. However, based upon data on the track displacement during rotation, the measured physical properties of the grout, and work with the dry-pack material used to repair deteriorated sections, the early failure problem now appears to be caused by four separate, but closely interrelated factors:

(1) The flexing motion of the track as the antenna rotates is probably the initiating factor in the grout failure. With rotation, the track rises in front of each leg, collecting a pond of oil between the track and grout. As the leg passes, the track and, to some extent, the sole plates, move down, producing a high-pressure oil flushing action that penetrates and erodes the grout surface. Samples taken from the track interface at the Goldstone site show definite evidence of this erosive action.

(2) The hydration reaction of cure of a portland cement is dependent on the sustained contact of the reacting cement particles with water. When the leaking oil reaches and wets the concrete surface, further bonding and strength development is stopped. This probably happens in some areas during or very shortly after the placement of a fresh grout repair. Thereafter, the weakly bonded or nonbonded surface aggregates would be most vulnerable to erosion by the flushing oil.

(3) The materials and mix design now used produce a strong, dense, high-strength grout when the design moisture content is maintained, and when oil contact is prevented during cure. But the mix has little more than the stoichiometric amount of water needed for cure, and the grout is very vulnerable to damage by evaporative water loss during mixing and placing. Evidence of this was seen during the preparation of the control specimens when, after four days cure, the test cylinders were easily broken at the junction of each packed increment of grout. The cure-arresting effect of oil leaking into the grout would be synergistic, selectively penetrating and wetting the dry, water-poor zones. This combination of events would severly damage the grout/sole-plate surface and particularly the material at the packing increment divisions, and hasten erosion by the pumping oil.

(4) Under ideal conditions, the slow rate of cure by types 1 or 2 portland cement may not allow the grout to reach load-bearing strength within the time allotted for repairs.

B. Portland Cement Dry-Pack Grout

The preparation of dry-pack grout test specimens was included in this program to provide a basis for comparison and evaluation of the candidate replacement materials. The vulnerability of portland cement to surface coating by the leaking oil before cure was known, but its sensitivity to evaporative water loss and the extent to which this loss inhibited normal curing and accelerated damage by the oil was first noted during the preparation of the dry-pack test cylinders.

1. Water loss. Water lost from the dry-pack grout mix at two steps in the repair process may increase its vulnerability and accelerate damage done by the leaking oil. The dry-pack mix design contains adequate water for hydration. However, the 8.4% water in the mix is largely in the form of a surface coating on the particles. Because of the high surface area, the mix is very subject to evaporative drying. Some water is necessarily lost in the process of rescreening after mix to eliminate lumps. Then, with a reduced water content, the mix

is highly vulnerable to further exposure and water loss such as occurs at the surface of each increment placed and compacted. If the water content at these exposed surfaces becomes less than that needed for hydration of cement and if the overall water content has been sufficiently reduced to preclude migration from interior wetter zones, the interfaces cannot cure properly. Note: Our water content is determined by behavior of grout "as placed" not by "as mixed" performance. Thereby significantly reducing the effects of water loss.

In the laboratory environment (RH = 50%) water loss during the delumping process was found to be as high as 5% to 6% of the total water. At the site, with longer exposure times and lower humidity, the loss could be much greater. The effects of the water loss are shown in Fig. 3. Each increment packed in a 7.62-cm-diameter cylinder mold was clearly delineated, and very little bonding developed between the sections. On impact, the cylinder broke cleanly at the division, and imprints of the packing ram were clearly visible on the fracture surface. By contrast, an impact fracture within a single packing increment in this cylinder required a much greater impact force, and the fracture path was random in direction, typical of a sound concrete.

The dry, nonbonded interfaces seen in this cylinder would be readily wetted by the leaking bearing oil and thus would be subject to erosion. This condition could, in fact, be the origin of the channels (Fig. 4) observed at the grout/sole-plate interface in the deteriorated grout removed from the Goldstone site.

To determine the effect of water loss on curing rate, two batches of the dry-mix grout were prepared under identical conditions except that, with the first batch, the evaporative water loss was measured and corrected to a water-to-cement ratio (w/c) of 0.23 just before placement. The water lost from the second batch (w/c = 0.213) was not replaced. Two 16.4-cm^3 samples prepared from these mixes were tested for development of compressive strength with time over a 48-hour cure period. Three specimens were tested at each interval. The data are shown in Fig. 5.

The average compressive strengths of the two mixes were similar through the 8-hour test interval. Between 8 and 16 hours, however, the rate of strength development by the low-water mix fell off sharply. The strength of these specimens averaged about 70% of the water-corrected mix, and the disparity increased with time through the 48-hour test.

The variations from specimen to specimen seen here after identical curing times may be more significant than the average differences in strength of the two mixes. With the higher water (corrected) mix, the individual test values at all intervals were within 1.03×10^6 N/m^2 of the average, and the maximum variation occurred, as would be expected, during the periods of most rapid strength gain, between 8 and 24 hours. At other test intervals, the individual specimen values were within 6.9×10^5 N/m^2 of the average.

The data scatter observed was much greater with the low-water specimens, and reached almost 6.9×10^6 N/m^2 at 48 hours. Most significantly, this variation from sample to sample increased with cure time. The increasing scatter with time suggests a nonhomogeneous composition, some parts of which are curing normally while others (dry areas) are developing strength at a much lower rate or not at all.

The water-corrected mix gained strength rapidly, and probably became load-bearing 5.9×10^6 N/m^2 in about six hours. By contrast, the non-water-corrected specimens typically required about 8 hours, but some of these specimens at 8 hours were well below load-bearing strength. Thus movement of the antenna at such a time would have caused overloading and compressive failure in the grout.

2. Oil erosion tests. A test fixture was designed and built to simulate the erosive action of high-pressure oil flow believed to be a major contributor to the grout failure. The fixture was used to cyclically create a high-pressure oil flow across a 7.62-cm-diameter surface of the test cylinders and, at the end of each cycle, to apply a 2.07×10^7 N/m^2 compressive load. When charged with the bearing oil, the piston load is hydraulically transmitted to the sample surface. Limited to one exit port 16 mm in diameter, the compression stroke of each cycle caused a high-velocity, unidirectional oil flow over the sample surface. Oil flowing across the concrete approached a velocity of about 1000 km/h as it entered the port.

The portland cement dry-pack grout, shown in Fig. 6a after 15,500 cycles, shows only minor damage by erosion. Some minor pitting and erosion was seen near the outside rim of the specimen and mostly around the exit port area, which is the area of greatest volume movement. The pitting is shallow, and in most cases, single, small aggregate particles were lost from the outer surface. No deep channels or structural damage was seen. It is not believed that erosion to this limited extent would adversely affect the antenna operation.

Most importantly, this sample was monitored for evaporative water loss during mixing, and the water content was corrected (to w/c = 0.23) just before placement. Figures 6b and 6c show the results of placing and packing the test surface in two increments, such that a packing interface was created parallel to the direction of oil flow. Here the water lost during mixing was not replaced, and the test surface was exposed to oil after 8 hours cure. The total cure time before start of the

erosion tests was seven days, similar to other erosion test specimens.

Figure 6b shows the test surface after 5,700 cycles. Severe erosion all along the packing interface was seen and in some areas had reached depths of 5.1 mm. (Note: the halo effect on this picture is the out-of-focus oil retention sleeve, left in place for continued testing.)

Figure 6c shows the sample after 13,700 cycles. Erosion had then become so severe that testing was discontinued. The channel width had grown to 12.7 mm in places and to depths of 10 mm or more. It is interesting to note that, except for an area about 19 mm wide paralleling the channel, the erosion of the sample surface was no more severe than the surface pitting seen on the water-corrected sample.

3. Chemical reactivity with oil additives. Samples of the portland cured cement grout were immersed in saturated solutions of each of the additives used in the hydrostatic bearing oil and held at elevated (70°C) temperatures for about 200 hours to detect any deleterious action by these chemicals. While some specimens did show a small weight loss, (discussed later) no significant effect on the compressive strength of the specimens was seen. Chemical damage by the additives is not believed to be a factor in the grout failure.

The test specimens, 12.7-mm cubes cut from a grout sample obtained from the DSS 14 64-m antenna, are shown in Figs. 7 and 8. The control before (Fig. 8a) and after exposure (Fig. 8b) to the bearing oil shows virtually no change. Similarly, no effect on structure, weight or strength was observed with the Lubrizol (Fig. 7b) or PC-1244 foam suppressent samples.

The diphenylamine exposed sample (Fig. 8b) did exhibit some fractures in large aggregates at the surface. If real, this effect was probably caused by crystal growth (the samples were in a saturated solution in a water bath that cycled at ±4°C). The conditions of cycling temperature and particularly of saturation by the additive could not occur at the site and are therefore not believed to be a factor in the grout deterioration.

The sample exposed to 2,6-di-tert-butyl paracrysol (Fig. 7c) shows no evidence of concrete erosion but did lose 0.85% of its original weight during exposure. No effect on the compressive strength of the specimen was seen.

C. Polymer Concrete Grouts

The two types of polymer concrete grouts proposed—the porous, "self-draining" open network and the void-free, solid grouts—differ widely in structure and in the properties needed in the matrix resin system. For example, in the open network structure, load distribution will be largely by particle-to-particle contact. Here, the modulus of the resin will not be as critical as with the solid composite grout. But the resin mass will be less and will require greater reactivity or a higher concentration of the curing agent. Eight epoxy resins and curing agents have been identified that, as primary resin systems or as diluents and modifiers, have the properties believed necessary in each of the two grout types. The resin systems and the test results obtained are described below.

1. Epoxy resin selection. Eight epoxy resins and curing agents were selected that, on the basis of cited literature values and manufacturers' data, had the properties considered necessary either as primary resin systems or diluents and modifiers for each of the two grout designs. The resins, listed in Table 1, are reaction products of epichlorohydrin and bisphenol-A, and differ mainly in the type of reactive diluents (such as butyl glycidyl ether and phenyl glycidyl ether) used to modify the viscosity of the system. Two exceptions, Epon 812 and 815, are low molecular weight aliphatic epoxies used to blend with and modify the viscosity, reactivity, and cure rate of the selected structural resins.

Triethylenetetramine (TETA) was used to cure all the resins because it represented the midpoint of the range of curing agents thought to be suitable for this application, based on the projected rate of cure, the reaction heat generated, and the degree of crosslinking obtained.

However, it became apparent in the preparation of the test cylinders that, because the grout was highly filled and the aggregate filler was an effective heat sink, the heat of polymerization of a TETA crosslinked system was not excessive. It now seems probable that faster curing agents, such as diethylenetriamine (DETA), may be used as a component of the curing agent.

2. Compression strengths and modulus tests. Replicate 7.62-cm-diameter by 15.25-cm-long compressive test cylinders containing 11.25% and 15.5% of each of the polymers were prepared with aggregate filler to approximate the structures of an open, self-draining system and a dense, void-free grout.

The cylinders were capped with a sulful/fly ash composition to assure uniform load application, and tested for compressive strength and modulus. Data for these tests are shown in Table 2.

The cylinders, shown under test in Fig. 9, typically failed catastrophically in a 45-deg shear mode, very similar to a dense, high-strength concrete, but at much higher loadings.

The greatest strength and modulus was obtained with Epon 828, a resin containing no reactive diluents. Generally, throughout the series, reactive diluents tended to lower the physical properties in proportion to their volume content. Thus, the 8132 resin specimens were lower in strength than the 828 resin specimens and, with the Ciba resins, the 509 resin system was lower in strength than the less diluted 507 system. The significance of these data is that all the epoxy resin grouts achieved very high strengths with moduli of near or greater than 1.38×10^{10} N/m^2.

The aggregates used in these specimens were obtained from the Jet Propulsion Laboratory. They were screened to remove particles 6.4 mm in diameter and larger. For the porous grouts, particles finer than 1.5 mm were also removed to obtain the open structure and low resin content needed.

One mix was prepared to examine the properties when a more continuous size distribution was used. In this case only the fine particles smaller than 0.51 mm were removed. The resin content (15.5% Epon 828) and mixing and placement procedures were unchanged. The compressive strength obtained, 10.24×10^7 N/m^2, was the highest seen in this series, and the modulus 1.58×10^{13} N/m^2 was significantly higher than any other in the series.

It now seems likely that with the proper design of the aggregate particle size distribution, the compressive strengths can be further increased and moduli of 2.07×10^{13} N/m^2 or higher may be achieved.

3. Erosion test. The erosion test fixture previously described was also used to test the candidate polymer grouts.

The compression chamber sleeves bonded to the upper cylinder (Fig. 9) were machined to fit the piston to close tolerances (in most cases 0.05 to 0.13 mm on diameter). Within these tolerances, the oil flow between the sleeve and the piston was small compared to that flowing across the sample surface and out the exit port.

The test cycle selected was of six seconds duration (loading and unloading of the test specimen) providing a capability of 14,400 cycles per 24-hour day. The peak load setting of 2×10^9 N/m^2 represents a balance of relatively high stress (three times the actual load under the antenna legs) and short cycle times. Each piston stroke (6.35 mm) moved approximately 29.5 cm^3 of oil across the sample surface and out the 1.6-mm exhaust port in about 3 seconds, the high-pressure portion of the cycle.

The test apparatus and procedure for installing and adjusting the erosion cylinder are shown in Figs. 10 through 14. The test cylinder shown, a portland cement dry-pack specimen, is dimensionally identical to the polymer concrete cylinders.

4. Polymer concrete erosion test results. The polymer concrete grout samples, solid and porous, were exposed to severe erosion testing. No damage to either material was seen after more than 27,000 cycles (see Fig. 14). Under 10X magnification, fine machining marks transferred from the metal mold were still visible on the exposed surface.

Evidence that the porous grout would function to drain away trapped oil and eliminate the erosive effect was seen during the testing of these specimens. With the solid grout, the hydraulic pressure developed in the compression stroke was high enough that the exit port could not be closed by hand pressure. The oil flow was strong and continuous through the full downward piston stroke. By contrast, the exhaust port was easily closed by light finger pressure during testing of the porous sample. Here, a slight buildup of pressure could be felt, but the flow through the exit was readily stopped and the total volume of pumped oil moved easily through the sample.

5. Creep characteristics of epoxy polymer grouts. The creep characteristics of an epoxy polymer grout test cylinder were determined.

The test sample had the following composition:

Component	Weight, g	%
Screened JPL aggregate (< 5-mm screen)	2,704.0	84.50
Epoxy resin (DOW DER 331)	446.8	13.96
Triethylenetetramine (TETA)	49.1	1.53
Totals	3,199.9	99.99

DOW DER 331 epoxy is equivalent to Epon 828 which was used in this program. The grout test cylinder was 7.3 cm in diameter and 32.39 cm in length.

The creep for the epoxy grout was 3.5×10^{-3} mm/mm under a 1.65-N/m^2 load while the typical total creep for portland cement concretes is much greater. Moreover, the creep data for the epoxy grout appears to have reached a fairly constant value of a creep shortening strain of 3.3×10^{-3} to 4×10^{-3} mm over a period of 23 days. This may be a limiting value for the creep to be expected for epoxy polymer grouts, again less than that of typical concrete (see Fig. 15).

The preceding data for the epoxy grout should be treated with caution as it is based on a single test sample, which had ample time to develop its full strength before a constant compressive load of 1.65 N/m^2 was applied. By contrast, the concrete creep tests cited were started seven days after the specimens are made and have a lower (4.1×10^6 N/m^2) compressive load applied to them. Because of these considerations, the results of the creep test on epoxy grout are not directly comparable with those for concrete.

D. Phase II: Developing, Refining, Optimizing of Selected Material

The work was planned for completion in two phases. Phase I was directed toward selecting five generic types of materials believed to be potentially able to meet these needs. Tests of physical properties, strength, modulus, resistance to erosion, and chemical attack by the oil were evaluated, and any unique requirements imposed by each material for mixing, placing, compacting, cooling (where high heat of polymerization might be a factor) were to be identified. The planned objective of Phase I was to identify the single generic type of material best suited to replace the dry pack grout. Phase II was to consist of developing, refining, and optimizing the selected material to achieve a high-strength, durable grout replacement.

The work of Phase I pointed up two potential routes to achieve the program goal. First, polymer grouts, with significantly higher strength, shorter cure time to reach load-bearing strength, and greater resistance to damage by leaking hydraulic oil, were promising replacement materials. Secondly, three possible factors were identified (namely early exposure to hydraulic oil, and the long cure time requirement), which in combination may contribute to premature failure of the portland cement grout. These deficiencies appeared to be correctable by small changes in the placement procedure and the use of a plastic film seal to prevent oil from entering a freshly repaired zone. The development and application of such procedures may make the dry-pack grout now used a completely acceptable material.

Each of these systems offers unique advantages as well as disadvantages, some of which were discovered only during their adaptation to this application. Phase II was designed to concurrently develop, test, and evaluate both systems, looking particularly at the large volume heating (polymer exotherm), curing rate, dimensional change, and oil resistance characteristics of each.

1. Resin selection. In the work statement developed for Phase I of the program, it was proposed that several epoxy resins with various viscosities be evaluated. In a given series of diglycidylethers of bisphenol A resins, as exemplified by Epon 828, lower viscosities are usually achieved by adding reactive diluents that are generally monofunctional. As such, they detract from the maximum physical properties attainable by the cured resin. The diluents generally make mixing and handling of the resins in preparing glass fabric reinforced structural laminates easier. However, it has been found that satisfactory mixes of Epon 828, alone and with aggregate, can be made despite the high viscosity of the pure resin. Based on these considerations, it was decided not to use reactive diluents. The use of such additives was proven unnecessary.

Therefore, all work on epoxy grouts during Phase II was done using Shell Chemical Co. Epon 828 which is a light-colored epichlorohydrin/bisphenol-A type low molecular weight epoxy resin. It is widely used in surface coating, laminating, casting, and potting applications. It has the following properties:

Color 25°C (Gardner) (ASTM D1554-58T)	Viscosity 25°C, $N \cdot S/m^2$ (ASTM D445-53T)	Epoxide equivalent[a] (ASTM D1652-59T)
4 max	10 to 16	185 to 192

[a]Epoxide equivalent = grams of resin containing 1-gram equivalent of epoxide

2. Amine curing agent selection. The primary objective of this task was to balance the catalyst type and concentration for the highest possible cure rate while maintaining a limited, acceptable heat of polymerization. Temperature and dimensional change (thermal expansion) of grouts were measured as functions of the catalyst type and concentration used.

Three amine curing agents were used. They were:

Curing agent	Abbreviation	Equivalent weight, g
Ethylenediamine	(EDA)	15.0
Diethylenetriamine	(DETA)	20.6
Triethylenetetramine	(TETA)	24.3

3. Preliminary experiments. The first experiments on these materials were performed on relatively small samples (5-cm cubes and cylinders of 7-cm diameter fitted with thermocouples). The purpose of these experiments was to determine

the rate at which strength developed during cure and the temperature (exotherm) attained during cure.

The compression test samples and exotherm samples were both prepared from single batches of resin. The time between the start of loading the first compression mold in a set to the completion of loading the cylindrical mold was in excess of an hour. The results of these experiments were inconclusive, since very small exotherms were observed and strength developed slowly. Based on experience, these results were not what would have been expected from an epoxy system. Accordingly, a study was made in which the mass of the resin/aggregate was increased until more consistent results were obtained.

4. Basic curing properties of epoxy systems. The first experiments in this series were performed using neat resin (no aggregate) and resin/aggregate mixtures packed loosely in plastic beakers. The purpose of these experiments was to furnish a base set of data for comparing further experiments. These results are summarized in Table 3.

These experiments were informative. They showed that extremely high exotherms could be anticipated with neat resin. The increased evidence of thermal degradation (darker color) with DETA and TETA even at lower maximum exotherms was noteworthy. One explanation for this was that with EDA and DETA increasing amounts of the heat of reaction were used in thermally degrading the polymer (darker color than with EDA). If this is so, the total heat of reaction could have been higher than was indicated by the maximum observed temperature. A second possible explanation could be that at higher temperature the DETA and TETA oxidize more readily than does EDA. Such oxidation could account for the observed dark color.

The moderating effect of the presence of 84.5% aggregate was evident in the lower maximum temperatures reached and the increase in the time to reach the maximum exotherm.

In this work, it was observed that ethylenediamine (EDA) fumed and gave off white vapors. This would be an undesirable characteristic in a repair system. Therefore, EDA was eliminated as a possible curing agent for polymer grout.

DETA proved to be an excellent curing agent for Epon 828, but exhibited a slightly higher exotherm than does TETA. Therefore, TETA was selected as the curing agent for the polymer grout in all subsequent work.

5. Aggregate selection. The bulk of the work was done using aggregate supplied by Jet Propulsion Laboratory. This was done as such aggregate is used presently at the antenna and a great deal of testing had gone into its selection for use in portland cement grouts. It was used both as received and after the large material (> 5-mm screen) had been removed.

6. Curing studies.

a. Effect of quantity of grout on curing characteristics. This portion of the work was directed toward determining the effect of mold size (weight of grout) on the curing characteristics. The Epon 828/triethylenetetramine (TETA) system was used in the work. Three different sizes and types of molds were used for these experiments. Relevant data on these molds are summarized as follows:

Mold	Type	Weight of metal mass per unit volume of molding, g/cm^3 (g/in.^{3})	
No. 1	3-cavity brass mold	3.88	(63.6)
No. 2	Single-cavity, heavy-walled steel mold	5.02	(82.4)
No. 3	Thin-walled steel mold	0.09	(1.4)

Expansion during cure was observed with only the largest sample (4,680 g). Here the maximum expansion was 0.93% based on the 11.11-cm dimension. After cooling, the permanent expansion was 0.66%. This expansion occurred on an unrestrained grout surface.

The results of molding experiments using these molds are presented in Table 4. This work confirmed that the epoxy/grout system was sensitive to the mass and volume of the material present. As the mass of polymer increased, the rate of cure and the maximum temperature reached increased.

b. Effect of oil on curing of Epon 828. The cavities in the brass, three-cavity concrete mold (Mold 1) are 5.08 cm (2 in.) in diameter by 10.16 cm (4 in.) high [206 cm^3 (12.57 in.^{3}) or 0.002 m^3 (0.007 ft^3)]. The mold weighs 2,318 g. The three cavities are arranged side by side and three moldings were made at a time.

Cavity 1 was fitted with a thermocouple to measure the exotherm. Cavity 2 had a dial micrometer mounted over it. The foot of the micrometer was bearing on a plate positioned in the center of the top surface of the resin/sand mix.

Cavity 3 had hydraulic oil pooled on top of it to determine if oil had an adverse effect on the cure of the resin.

The presence of a pool of oil on the samples cured in the No. 1 mold did not appear to affect the surface cure of the

resin/aggregate mixture. The surfaces of samples cured with and without oil being present appeared to have the same degree of hardness (thus same degree of cure) when scratched by a steel probe.

c. Effect of varying formulation and environment conditions on large-sample properties. These samples were prepared in the thin metal molds (No. 3). The curing agent was varied (EDTA and EDA were substituted for TETA), additional TETA samples were cured with and without bottom insulation, and the proportion of resin to TETA and of aggregate to resin ratio was varied. These experiments are summarized in Table 5.

Figure 16 shows the apparatus used in these tests. A thermocouple was mounted in the approximate center of the aggregate/resin mass. The recorder monitored both the temperature at the center of the mass and the ambient air temperature. The mold was insulated on the sides with aluminum foil/glass wool insulation while the bottom was insulated (except in Run No. 4) with a 6.4-mm thick transite board. The entire assembly was set on a heavy steel plate, which was part of the support stand for a dial micrometer.

Changes in dimension along the longitudinal direction were measured using a dial micrometer. The foot of this micrometer was initially 0.013 mm from the 0.025-mm brass shim resting on the top of the aggregate/resin mass. Because of this, the micrometer's foot did not bear on the uncured surface. This prevented penetration of the foot into the grout during the early stages of the cure.

Strength development of the grout was measured using two soil test penetrometers which are normally used in measuring the bearing strength of soil.

The penetrometers could easily penetrate the mass of grout during most of the period during which the cure was taking place. However, the final stages of cure and the development of most of the strength occurred over a very brief interval of 2 to 3 minutes. For example, in Molding No. 1, the penetrometers could easily penetrate the grout mass at 65 to 67 minutes after curing agent was added to the epoxy. However, at 70 minutes the concrete penetrometer (maximum 4.83 N/m^2) would not even indent the surface under full load.

The maximum expansion occurs at the same time that sufficient strength develops to resist penetration. Both of these events precede the time at which the maximum exotherm occurs. The recorded expansions occurred on the unrestrained top surface of the grout. Subsequent work showed that the proper restraint of this surface expansion and contraction during cure ceased to be a problem.

This work indicated that mixes containing TETA cured more rapidly than those containing DETA or EDA. However, the maximum change in temperature was less with TETA. Expansion during cure was also smaller in the TETA cured grouts than in those using either DETA or EDA as curing agent.

The presence of an efficient heat sink (Molding 4) decreased the maximum temperature rise and increased the cure time, but did not appear to effect the strength properties of the final cured material.

Increasing the amount of aggregate in Run No. 5 also resulted in smaller temperature increases and slower cures. Again, the finished grout appeared to have the necessary strength properties. The results in Run No. 6 were anomalous. We would have expected an increased exotherm when the amount of aggregate was decreased (richer in resin). This did not happen. Similarly, we expected a somewhat more rapid reaction; instead it was actually slower. However, the quality of the cured grout appeared to be acceptable.

Decreasing the amount of curing agent had the expected effect of lowering the exotherm and increasing the reaction time.

Based on this work, using the Epon 828/TETA system, a useful working life of at least 65 minutes from the time amine was added to the resin could be expected. This was based on an 84.5/15.5 aggregate/resin mixture. This would indicate the possibility of increasing the working life of the grout by providing a more efficient heat sink, by adjustment of the resin/aggregate composition, or by adjustment of the ratio of epoxy resin to amine curing agent.

d. Cure of warm epoxy grout mixtures. Two experiments were made to determine the curing characteristics of epoxy grout mixtures in which all components were preheated to 38°C prior to the time they were mixed. The results were as follows:

Parameter	Test 1	Test 2
Time to maximum temperature, min.	55	52
Maximum temperature, °C	75	84
Maximum ΔT, °C		
Above temperature of grout components	38	46
Above ambient temperature	55	63
Condition of grout at time of maximum exotherm	Firm	Firm

During Test 1, the epoxy grout was probed with a penetrometer to determine the time at which the material became unworkable and developed load bearing characteristics. This occurred about 50 minutes after the grout was mixed. The probing operation disturbed the dial micrometer that was measuring expansion, so we felt these readings were unreliable. We were also surprised that the maximum temperature was not higher than 75°C. Because of these factors this test was repeated (Test 2). The peak temperature was 84°C (9°C higher than in 1), but still only 11°C higher than tests started with all ingredients at 20 to 25°C. In Test 2, the grout was not probed and the total expansion was observed to be 0.35 mm or 0.3% of the height of the sample.

e. Cure of cold epoxy grout mixtures. It was of interest to determine the curing characteristics of epoxy grout when the resin, curing agent, and aggregate were chilled to 4°C prior to mixing. One experiment was attempted to determine this property. However, when the ingredients were cooled to the desired temperature, the epoxy resin was too viscous to be mixed with the aggregate. As mixing proceeded, the first aggregate wetted with resin formed a ball of material that could not be mixed with the remaining aggregate until the mass of material had warmed to approximately 13 to 16°C (55 to 60°F).

No further work was attempted on studying the low-temperature curing characteristics of the epoxy grout system. However, if it should be necessary to perform repair work during cold weather, it would be necessary to protect the raw materials (resin, curing agent, and aggregate) from very low temperatures by keeping them in a heated 15.5°C (60°F) building.

f. Solution to the sagging properties of epoxy grout. Previous experience by the Jet Propulsion Laboratory with epoxy grouts had indicated that they sag away from the top of the mold. This is an intolerable condition for the antenna leveling application. Because of this input from JPL it became imperative to determine whether our proposed epoxy grout would sag when used and if it did whether corrective measures could be taken to make the grout nonsagging.

g. Determining the sagging characteristics of epoxy grouts. Several experiments were performed to determine whether sagging would be a problem with the developed Epon 828/amine/aggregate grout. The first such experiment was performed by packing the 84.5% aggregate, 15.5% resin grout into a rigid wooden box that was open on one end. The epoxy grout was packed into the box from the end. During the packing operation it was observed that applying a load to one part of the grout caused it to flow and deform. Packing pressure on the top or bottom position of the grout caused it to extrude from the end of the box at a point away from the stress. After packing was complete, no slumping of the angle of repose of the grout was observed at the open end. However, examination of the grout adjacent to the top of the box revealed that there was approximately a 3.2-mm gap between the top of the grout and the top of the box. Additional tamping did not correct this deficiency.

Two approaches appeared possible ways of correcting this problem. They were:

(1) Addition of a thickening agent to the presently developed epoxy grout (84.5% aggregate, 15.5% resin).

(2) Reduction of the resin content of the grout to make a drier less fluid mix.

Both of these approaches to preventing sagging were tried, both alone and in combination with each other.

As the use of thickening agents, such as finely divided silica, was more straightforward, it was tried first. The following formulation was used in our initial experiments:

Ingredient	Weight, g	%
Epon 828	273.9	13.4
Triethylenetetramine	36.1	1.8
Sand (< 5-mm screen)	1,690	82.8
Finely divided silica	40	2.0

This material was mixed and then packed into a steel mold that had a transparent (plexiglas) top. The mix appeared dry and when tamped did not have the fluid properties observed in grouts that did not contain finely divided silica.

There was no evidence of sagging when the material was viewed through the transparent top or from the open end (Fig. 7). The grout was removed from the mold after it had cured, but was still warm. The definite overhang at the top of the material and the ability of the tamped material to retain the impression of the tamper is noteworthy. Figure 8 shows the grout. The straight edge showed the sample was level across the top with no evidence of sagging.

This experiment was repeated but the epoxy grout was left in the mold until the material had cooled to room temperature. There was no visible evidence of sagging of either the warm material or after it had cooled. A piece of 0.025-mm brass shim stock could not be inserted between the top of the grout and the bottom of the plexiglas cover plate.

These initial experiments were encouraging and additional work was done on thickening agents and adjustments of the ratio of epoxy resin to aggregate.

h. Development of epoxy grouts containing antisagging additives. The initial experiments using a thickener (antisag additive) were encouraging. Thus, a series of experiments were undertaken to determine the effect of other thickeners on the sagging properties and compressive strengths of epoxy grouts.

The materials for these tests were hand mixed and packed into a steel mold fitted with a plexiglas top (Figs. 17 and 18) to determine sagging properties and a steel mold to produce 2.5-cm cubes for compression tests. The grouts were observed for evidence of sagging away from the top of the mold and compressive strength tests were made one week after the samples were prepared.

The results of this work is summarized in Table 6 and described as follows:

(1) All epoxy grouts that do not contain a thickening material sag when packed into the test mold.

(2) The strength of the grout decreases as the amount of thickening agent is increased.

(3) Between 1-1/2 and 2% thickening agent is needed to produce a nonsagging grout.

(4) Lowered resin content (< 15.5%) usually produces a grout with a lower compressive strength.

The samples made for determining compressive strength were 2.5-cm cubes and weighed an average of 36 g. The mold in which they were prepared weighed 8,123 g and contained three grout samples or 108 g of material. This gave a ratio of 75 g of metal per gram of grout material. These samples cured slowly in the presence of this large mass of metal and could be demolded in one day, at which time they were quite strong. This shows that a relatively small mass of epoxy grout will cure in the presence of a large heat sink.

i. Filling intermediate-sized cavities with epoxy grout. This work was undertaken to determine if an epoxy grout containing finely divided silica could be mixed in larger quantities and placed in a cavity without sagging.

7. Application of epoxy grout to a 0.028-m^3 cavity. This work was done using the following material:

Ingredient	Weight, g
Aggregate (< 9.5-mm screen)	17,760
Finely divided silica	320
Epoxy (Epon 828)	3,330

This formulation contained 1.5% silica thickener, which represented what was believed to be a minimum amount of thickener to prevent sagging. No curing agent was added to the epoxy. This permitted working with the grout without having to be concerned with the material curing in the mixer or while being placed in the cavity.

The cavity or mold was 45.7 cm long by 22.8 cm wide by 15.25 cm high. The mold had wooden sides, back and bottom. The front of the mold (22.8 cm × 15.25 cm) was left open and the top was closed with a plexiglas sheet that permitted observing the grout while it was being added and tamped. The mold had a volume of 15,900 cm^3.

A 141-cm^3 cement mixer was used in this experiment. The aggregate after screening out the large pebbles (> 9.5-mm screen) plus thickener was placed in the mixer and the opening was covered with a polyethylene film. These ingredients were mixed for two minutes and then the epoxy resin was added. Lumps of aggregate wetted with epoxy formed and rolled around the inner surface of the mixer. Continued mixing did not appear to be effective in breaking up these lumps. The mixer was stopped and the lumped material broken up using a large spatula. When mixing resumed, a reasonably uniform mix resulted.

This mixture was dumped out onto a plastic sheet and a portion of the "grout" was shoveled into the 22.8-cm × 45.7-cm × 15.25-cm cavity and the loose grout was tamped in place using a Skil hammer drill which delivered 3,750 blows per minute. The hammer drill was fitted with an adapter, extension arm, and a 5-cm × 5-cm foot. The mold was filled by alternate additions of loose grout and tamping. This grout was nonsagging across the 228-cm width of the cavity.

The grout was removed from the cavity and placed in the cement mixer and the necessary amount of amine (TETA) curing agent (52 g) added. The mixer was started and the amine mixed into the grout. Difficulty was once more experienced with the failure of the mixer to break up the lumps. The grout was transferred to a 9.5-liter plastic bucket and allowed to cure. A maximum exotherm of 67°C was obtained. The high exotherm probably reflected the poor heat transfer properties of the plastic bucket.

Compressive strength samples were also prepared from the grout. These samples had a very low strength value, namely 5.5 N/m^2. This low strength was attributed to the difficulty experienced in mixing.

It was concluded from this work that a cement mixer did not produce the type of mixing necessary for use in blending polymer grouts.

8. Preparation of grouts using a mortar mixer. To improve the mixing, a gasoline engine powered 0.2-m^3 mortar mixer was rented. This machine was used in all subsequent intermediate and full-scale grout tests.

The following formulation was used for this work:

Ingredient	Weight, g
Aggregate (< 9.5-mm screen)	17,760
Finely divided silica thickener	430
Epon 828/TETA (3,050 g/401 g)	3,330

The grout made from this formulation contained 2% thickener.

The aggregate and thickener were transferred to the mixer, which was closed with a polyethylene film. The dry ingredients were mixed for 5 minutes. During this time, the epoxy and amine curing agent were mixed for 2 minutes using a laboratory stirrer. This mixture was added to the aggregate and mixing continued for an additional 5 minutes.

At the end of mixing, the grout was discharged onto a plastic sheet. The grout was then transferred in small portions into an 48-cm X 48-cm X 15-cm cavity and then tamped in place using a hammer drill equipped with an extension rod and a 7.6-cm square foot. This continued until all grout from the mix was in place. Figure 10 shows the mold. Figure 20 shows the filling of this cavity, and Fig. 21 shows the partially filled cavity.

Immediately after placing the first batch, a second similar batch was made up and placed in the cavity using a similar emplacement procedure with the exception that mixing time was reduced from 5 to 2 minutes.

9. Use of epoxy grout to fill a 0.08-m^3 cavity. At the end of the Phase II program, the epoxy grout formula that was developed as a result of this work was used to fill a 0.08-m^3 cavity (see Fig. 19). The filling techniques were modeled on the methods used by JPL to emplace the present portland cement grout system, and adapted by MRC for use with epoxy grout.

A test site for the demonstration of the use of epoxy grout was built on an existing concrete slab. It is shown in Fig. 22. It provided a 46-cm X 112-cm X 15-cm cavity that approximates the size of the grout replacement section at Goldstone. One end of the cavity was closed with a 1.27-cm-thick steel plate that provided a bucking plate against which the grout could be compacted. The top was covered with 2.54-cm-thick steel plates.

Figure 13 also shows the details of the method adopted to hold down the top plates. During the emplacement and curing of the grout, it was learned that the method was not entirely satisfactory. The thermal expansion of the grout caused a very slight lifting or bowing of the angle iron. As a consequence, more deflection of the steel cover plates was observed adjacent to the hold downs than was observed along the center line of the plates.

10. Composition of epoxy grout used in filling a large cavity. Two 86.26-kg batches were used to fill the 45.7-cm X 112-cm X 15-cm cavity. Each batch had the following composition:

Ingredient	Weight, g	%	Source
Aggregate, < 9.5-mm screen	71,070	82.07	JPL
Thickener	1,720	1.99	Cabot Corp.
Epon 828	12,200	14.09	Shell Chemical
Triethylenetetramine (TETA)	1,600	1.85	Dow Chemical
Total	86,590	100.00	

The above formulation has the following composition:

Ingredient	%
Filler (aggregate + Cab-O-Sil)	84.06
Resin (epoxy + TETA)	15.94

This formulation is apparently a half percent richer in epoxy than the formulations used in the intermediate size tests. The

reason for this apparent discrepancy is that the epoxy resin and curing agent (TETA) was mixed in four separate batches, each having the composition:

Ingredient	Weight, g
Epoxy 828	3050
TETA	401

Mixing was done in four 3.785-liter paint cans. This operation is shown in Fig. 23.

When mixing was complete, the epoxy resin was poured from the can to the mortar mixer. In this operation, retention of resin in the can amounted to about 84 g/can. With this retention of about 336 g (84 g × 4 cans), the actual composition of the grout as emplaced follows:

Ingredient	Weight, g	%
JPL aggregate (< 9.5-mm screen)	71,070	82.39
Thickener	1,720	2.00
Epoxy + TETA	13,470	15.61
Total	86,260	100.00

This represents a charge of 86.26 kg that was actually mixed. The percentages are quite close to the intended composition of 84.5% aggregate and 15.5% resin. The small excess of resin would not be sufficient to significantly affect the properties of the grout.

11. Placement of epoxy grout in test cavity. The two 86.26-kg batches of epoxy grout material were mixed in a 0.2-m^3 mortar mixer driven by an 6-kW gasoline engine. The engine drove the paddles of the mixer through a V-belt. This test was done early in the day so that the test site was not heated by direct sunlight. It was felt such heating would have accelerated the cure of the grout.

Each batch was mixed separately in the mixer, and the second batch was mixed immediately after the first batch was dumped.

The log for the mixing of the grout and its emplacement and tamping in the test cavity was kept. The most notable thing about the filling of this cavity was that all the epoxy grout was mixed and tamped into place in 59 minutes from the start of the test and the last placed material had a bearing strength in excess of 4.8×10^6 N/m^2 1 hour and 32 minutes after the start of the test.

Note oil was injected into the top of the cavity to simulate the presence of oil in some regional areas at Goldstone. Special attention was given to the cure and strength of these areas to determine detrimental effects from the oil if any. See Fig. 25.

The areas of grout surrounding the holes through which oil was introduced during the placement and tamping were quite strong and did not appear to have been effected by the oil. These areas are as resistant to scratching by a steel probe as are the areas some distance from the oil.

12. Thermal effects of use of epoxy grout in a large cavity. When epoxy is cured by an amine there is a fairly large exotherm (about 25 kcal/mole of epoxy (Ref. 1). This exotherm can cause straight resins to reach quite high temperatures when they cure. However, in the grout system the large proportion of aggregate present acts as a heat sink and results in considerably lower temperatures.

An examination of the grout after the top plates were removed did not reveal any evidence of thermal stresses and cracks in the surface of the grout. There was also no evidence of thermal degradation during the cure and after removal of the top plates.

13. Dimensional stability of epoxy grout. Dimensional stability of a large mass of epoxy grout is of considerable concern. Measurements, using a depth micrometer, of dimensional change during cure and immediately thereafter, and visual observation using a straight edge of the overall levelness of the top surface, were made after the removal of the top cover plates.

The expansion and/or contraction of the grout during cure was measured using a depth micrometer to measure the distance from an aluminum angle to the top of the steel cover plates. These measurements were made across the width of the cavity and 56 cm from the back plate. The details of how these measurements were made along with the results are given in Fig. 24. Each distance from the top of the horizontal leg of the angle to the top of the steel plate represent the average of three individual measurements.

Some difficulty was experienced in making these measurements as the aluminum angle had a tendency to bend slightly over the 70-cm space, if any substantial load was placed on it. Great care was taken not to press down on the depth micrometer during the making of a measurement. It is believed they

are reliable values, in view of the care taken in making them, and they are averages of three individual readings.

All of the stations showed a slight expansion of the grout at the maximum exotherm and consequent lifting of the cover plate. These displacements generally became larger as the east side of the cavity was approached. It is believed that this increase was due to a slight lifting or rotation of the angle iron hold down. This positive displacement, along the east side of the cavity, persisted even after the grout had cooled to ambient temperature.

Some possible slight contraction of 0.025 to 0.05 mm was observed at Stations B and C after the grout had cooled. However, it is believed that these were errors in reading, as the readings at the adjacent stations (A and D) are not consistent with shrinkage having occurred. The easy removal of the cover plates also was not consistent with strong enough adhesive forces between the grout and the steel to expect that the 2.54-cm steel plates would be pulled downward.

After the removal of the cover plates, the flatness of the top of the grout was checked using a steel straight edge, as shown in Fig. 24. It was found that the grout was essentially flat when checked across the width at various positions along the 112-cm length of the cavity. When a straight edge was laid across the grout, a uniform thin band of light was observed between the straight edge and the grout surface.

When the straight edge was laid along the 112-cm axis of the grout it was found that a 381-μm shim could be slipped under the straight edge and slipped back and forth along the length of the grout, except at the ends where the ends of the straight edge were in contact with the grout. This was a disturbing observation as it appeared that the top surface of the grout was somewhat concave in the long dimension of the cavity.

However, further examination of the test site revealed that the concrete sides of the cavity had a similar contour, namely higher at the ends than in the middle of the length. A steel straight edge laid on either the grout or the concrete revealed the same clearance between the straight edge and the surface under it. Apparently, the steel cover plates were merely following the contour of the concrete side pieces.

All the data indicates that in the presence of large heat sinks and relatively heavy steel top plates, the grout upon curing does not exhibit an excessive amount of expansion or contraction and, if such displacement occur, they are highly uniform.

14. Compressive strength of epoxy grout used in prototype repair test. Samples of the grout material from both 86-kg batches were taken and used to make compressive strength (2.5 cm^3). These samples were tested for compressive strength after they had aged for one week. The results are as follows:

Batch	Compressive strength; average of 3 samples, N/m^2	Standard deviation, N/m^2
1	1.7×10^8	$\pm 4.34 \times 10^6$
2	1.57×10^8	4.9×10^6

The high compressive strengths of these samples can perhaps be attributed to the improved mixing achieved in the mortar mixer.

E. Development of Sealing Films for Uncured Portland Cement Grouts

Work was done on developing a sealing film to protect portland cement grout from attack by oil during cure.

1. Sprayed on thin-film barriers. To accomplish this, an apparatus to test the sealing properties of the candidate film materials was designed and built. The test equipment is shown schematically in Fig. 25. Hydraulic oil under nitrogen pressure (0 to 6.9×10^6 N/m^2) was supplied to ports in the sides of a concrete mold. The port on the left side of the mold was 0.25 mm in diameter and provided direct access of the pressurized oil to the back of the film. On the right side of the test fixture, two steel plates were used to simulate the junction between sole plates and the resulting elongated opening.

In use, the inside surface of the mold was coated with the film former that was being tested. The oil supply lines were filled with oil prior to the start of the test. After the film had set, the mold cavity was filled with portland cement grout. Oil pressure was applied to the film/grout after various curing times.

To establish a control for the film experiments and to work out experimental details, portland cement grouts were tested. These grouts have the following formula:

Ingredient	%
Aggregate (through 5-mm screen)	55.3
Portland cement	36.3
Water	8.4

After mixing, the grouts were packed into the mold and allowed different times to cure, as shown in the following table. After these grout cure times, oil pressure was applied to the film/grout in 3.45 X 10^5 N/m^2 increments at 5-minute intervals.

Time after addition of water to application of oil pressure, h	Results
1	Failed at 5.5 X 10^6 N/m^2 2 hours and 15 minutes after water addition. Failure evidenced by oil flowing out of top of mold.
2	No failure to 5.9 X 10^6 N/m^2. Some slight pressure drop after each increment of pressure.
4	Same as at 2 hours.

These tests indicate that after 2 hours cure the cement was sufficiently cured to withstand 5.86 X 10^6 N/m^2 pressure. Therefore, all tests on paint films and tapes were started one hour after water addition to the portland cement grout.

The film formers listed in Table 7 were tested using various methods of application and cure times for the films. Oil pressure was applied to the back side of the film one hour after water addition to the cement/aggregate mix.

Of these candidate film formers, the laboratory mixed epoxy, Sherwin-Williams Superfast Dri synthetic paint, and Dow Corning's silicone caulk did not fail below 4.14 X 10^6-N/m^2 oil pressure. This indicates they might perform satisfactorily. However, they must be cured 20 hours before use. This surpasses the 2- to 4-hour time limit allowed for repairs. This allowance is based on the permissible down time for an antenna.

2. Preformed films as seals to prevent the entrance of oil. A study was made using preformed films and tapes that have pressure sensitive adhesives on one surface. These tapes were placed over the inside surface of the test jig where leakage of oil might occur (0.025-mm hole and simulated joint between sole plates). The tape was pressed in place and the mold immediately packed with portland cement grout. This work is summarized in Table 8.

This work indicates the use of preformed films is a promising approach, but work remains to be done developing a satisfactory means of applying such film to the interior of a repair cavity.

III. Conclusions

As a result of work done during this program it can be concluded that an epoxy grout containing minor amounts of thickening agents is a feasible system for the repair of existing antenna support structures. This conclusion is based on the following:

(1) The placement of 177 kg of epoxy grout in a simulated repair cavity (0.078 m^3). The methods of placement are quite similar to the techniques currently in use for portland cement grouts.

(2) The rapid cure and consequent early development of load bearing properties by the epoxy grout. The epoxy grout becomes load bearing in approximately 2 hours after placement of a large amount of grout.

(3) The ability of epoxy grout to cure in the presence of a large heat sink (surrounding antenna support structure).

(4) Strengths considerably in excess of those realized by portland cement grouts.

(5) Good resistance during cure to hydraulic oil.

(6) Good dimensional stability when restrained by the surrounding structure.

(7) Low creep values under constant compressive loads.

(8) Readily available commercial ingredients are used to make up the grout.

(9) Safe working and handling techniques for epoxy resins are well established in industry.

In addition to the epoxy system for repairing antenna structures, a system was developed that shows promise of providing a means of protecting uncured portland cement grout from the harmful effects of hydraulic oil. This system is based on the use of preformed plastic and metal tapes that have a pressure sensitive adhesive on one face. These tapes can adhere to metal and concrete to seal openings against the entry of oil.

Reference

1. Lee, H., and Neville, K., *Handbook of Epoxy Resins*, p. 6-3. McGraw-Hill Book Co., New York, N.Y., 1967.

Table 1. Candidate epoxy resins and curing agents

Resins	Epoxide eq. wt.	Viscosity, N • S/m^2	Curing agents	Amine eq. wt.
Epon 812	188	0.4	Triethylenetetramine[a] (TETA)	24
Epon 815	185	0.6	Diethylenetriamine[a] (DETA)	21
Epon 820[a]	188	7.0	Epon V-25	163
Epon 825	175	5.0	Epon V-40	140
Epon 826[a]	182	8.0	Epon V-50[a]	130
Epon 828[a]	188	13.0	Epon V	48
Ciba 507[a]	189	0.6	Ciba 837[a]	34
Ciba 509[a]	194	0.6	Ciba 2964	(30)

[a]Primary resin and curing agent candidates.

Table 2. Compressive strengths and modulus of polymer concrete samples

Code	Polymer[a]	Polymer content, wt%	Grout type	Compression strength, N/m^2 x 10^7	MOE,[b] N/m^2 x 10^{10}
207895-1	828	11.25	Open	7.10	1.24
207895-2	828	15.5	Solid	9.62	1.38
207898-1	507	11.25	Open	6.44	1.03
207895-3	507	15.5	Solid	8.46	1.24
207895-5	509	11.25	Open	5.61	–[c]
207895-4	509	15.5	Solid	6.61	–[c]
207898-2	8132	11.25	Open	5.49	–[c]
207898-3	8132	15.5	Solid	7.58	–[c]
207898-4	826	11.25	Open	5.98	1.1
207898-5	826	15.5	Solid	9.23	1.38
1213901	828	15.5	Solid	10.24	1.59

[a]Epoxy resin designation.

[b]Modulus of elasticity.

[c]Not available.

Table 3. Basic curing data on Epon 828 resin systems

Resin	Curing agent		Aggregate[a]	Mold diameter,[b] cm (in.)	Maximum temperature, °C	Maximum ΔT, °C	Time to maximum temperature,[c] min	Comment
	Type	Amount						
200	EDA	16	–[d]	7.0 (2¾)	202	180	48	In all cases, beaker melts degradation as evidenced by color, least severe with EDA and most severe with TETA.
200	DETA	21.8	–[d]	7.0 (2¾)	196	174	46	
200	TETA	25.8	–[d]	7.0 (2¾)	190	168	49	
100	EDA	8	589	9.5 (3¾)	54	30	68	All material hard and firm when maximum exotherm is reached.
100	DETA	11	604	9.5 (3¾)	51	27	71	
100	TETA	13	615	9.5 (3¾)	45	20	72	

[a]JPL aggregate screened through 5-mm screen.
[b]Plastic beakers – 400 ml for neat resin and 1,000 ml for resin/aggregate.
[c]Maximum time was measured from time curing agent was added to resin.
[d]Not applicable.

Table 4. Effect of resin/aggregate mix volume and weight on curing characteristics

Mold No.	Type	Weight[a] of resin aggregate	Maximum temperature, °C	Maximum ΔT, °C	Time to[b] maximum ΔT, min	Comment
1	Brass 3-cavity	430 g/cavity	27.0	2.0	160	Molds uninsulated – large heat losses to surroundings. Very low exotherm – samples well set up after 160 min. No observable expansion during cure. Oil on surface did not adversely effect cure of surface.
1	Brass 3-cavity	430 g/cavity	34.5	7.5	108	Mold insulated bottom and sides – increased exotherm – samples well set up in 108 minutes. No observed expansion. Surface wet with oil well cured.
2	Thick-walled steel mold	2,850 g	46.0	20.0	99	Mold insulated top and bottom. Exotherm increases. No observable expansion.
3	Thin-walled steel mold	4,680 g	73.0	47.0	80	Mold insulated top and bottom. Increased exotherm. Total expansion 0.1 cm (0.0405 in.) at 70 minutes. Increase in length after cooling (0.07 cm) (0.029 in.).

[a]Resin/curing agent mixture 88.6/11.4, stoichiometric amounts. Aggregate/resin mix 84.5/15.5.
[b]Time from addition of curing agent to resin.

Table 5. The effect of formulation variations on the curing characteristics of 2,220-cm³ (134-in.³) aggregate/resin moldings[a]

Molding	Resin mix		Type	Resin/aggregate		Maximum temperature, °C	Maximum exotherm, °C	Time to maximum exotherm[b], min	Linear expansion		Time until penetrometer does not penetrate grout, 4.83 N/m² min	Comment
	Per cent epoxy	Per-cent amine		Per-cent resin	Percent aggregate				Maximum percent at time t, min	Residual after cooling		
1	88.6	11.4	TETA	15.5	84.5	73	47	80	0.93 at 70	0.66% when cold	70	Stoichiometric resin/curing agent mix of Epon 828 and EDTA. Insulated sides and bottom.
2	99.0	9.9	EDTA	15.5	84.5	77.5	52.5	85	1.9 at 70	1.6% when cold	70	Stoichiometric resin/curing agent mix of Epon 828 and EDTA. Insulated sides and bottom.
3	92.6	7.4	EDA	15.5	84.5	74	53	107	2.0 at 92	1.1% when cold	94	Stoichiometric resin/curing agent mix of Epon 828 and EDA. Insulated sides and bottom.
4	88.6	11.4	TETA	15.5	84.5	67	44	105	0.5 at 82	0.2% when cold	82	Stoichiometric amounts of Epon 828 and TETA. Mold insulated on sides. Bottom uninsulated, resting on heavy steel plate.
5	88.6	11.4	TETA	14.2	85.8	61	40	100	0.1 at 79		79	Stoichiometric amounts of Epon 828 and TETA. Increased aggregate content in mix. Sides and bottom insulated.
6	88.6	11.4	TETA	17	83	69	47	108	0.93 at 90	0.57% when cold	93	Stoichiometric amounts of Epon 828 and TETA. Mold insulated sides and bottom. Decreased aggregate content.
7	89.6	10.4	TETA	15.5	84.5	65	42	115	0.8 at 92	0.5% when cold	92	Less than stoichiometric amount of amine. Aggregate resin mix 84.5/15.5. Insulated sides and bottom.

[a]Moldings made in Mold No. 3.

[b]Time measured for time curing agent is added to resin.

Table 6. Characteristics of grout formulations

No.	Type	Resin[a], %	Aggregate[b]	Thickener[d]	Compression strength[c], 70.3 kgf/cm^2, (kpsi)	Characteristics
624	Portland cement	Cement 36	< 5-mm screen, 55%	–[e]	860 (12.3)	Nonsag
625	Portland cement	Cement 36	> 5-mm screen, 55%	–[e]	630 (8.9)	Slight sag
651	Epoxy	17.5	< 9.5 mm	–[e]	1,620 (23.0)	Sags
636	Epoxy	15.5	< 9.5 mm	–[e]	1,880 (26.7)	Sags
650	Epoxy	15.5	< 5-mm screen	–[e]	1,510 (21.5)	Sags
627	Epoxy	12.0	< 5-mm screen	–[e]	1,650 (23.4)	Sags
629	Epoxy	11.5	< 5-mm screen	–[e]	1,800 (25.6)	Sags
628	Epoxy	11.5	Not screened	–[e]	560 (8.0)	Sags
638	Epoxy	10.0	< 5-mm screen	–[e]	730 (10.4)	Sags
635	Epoxy	8.0	< 5-mm screen	–[e]	710 (10.1)	Sags
632	Epoxy	15.5	< 5-mm screen	2	1,470 (20.9)	Nonsag
652	Epoxy	17.5	< 9.5 mm	3%	1,330 (18.9)	Nonsag
649	Epoxy	17.5	< 9.5 mm	4%	1,370 (19.5)	Nonsag
655[d]	Epoxy	15.5	< 4.7 mm, not dried	1.0	1,620 (23.1)	Sags
654	Epoxy	15.5	< 5-mm screen	1.0	1,480 (21.1)	Slight sag
656	Epoxy	15.5	< 5-mm screen, not dried	1.5	1,500 (21.4)	Nonsag
645	Epoxy	15.5	5-mm screen, not dried	2.0	1,470 (20.9)	Nonsag
647	Epoxy	15.5		2.0	1,440 (20.5)	Nonsag
653	Epoxy	15.5	< 5-mm screen, not dried	2.0	1,410 (20.0)	Nonsag
648	Epoxy	15.5	9.5 mm	3.0	1,360 (19.4)	Nonsag
646	Epoxy	15.5	< 5-mm screen	4.0	740 (10.5)	Nonsag
642	Epoxy	10.0	< 5-mm screen	2.0	710 (10.1)	Nonsag
643	Epoxy	10.0	< 5-mm screen	4.0	530 (7.5)	Nonsag

[a] Percent resin represents combined Epon 828 and amine curing agent.
[b] All aggregates are Jet Propulsion Laboratory material obtained from San Gabriel River drainage.
[c] All tests run on 2.54-cm cubes that were individually molded. Based on one sample; other samples damaged during demolding.
[d] Cab-O-Sil M-S mode by Cabot and Co.
[e] Not applicable.

Table 7. Evaluation of film forming systems

Type	Manufacturer	Method of application	Time to cure film	Pressure at failure[a], N/m^2	Cause of failure
Epoxy	Lab mix	Spray	40 min.	6.9×10^5	Unknown.
Epoxy	Lab mix	Brush	20 h	4.1×10^6	Unknown.
Urethane (Polane)	Sherwin-Williams	Spray	20 h	–	Oil continued to seep through film.
Superfase Dri synthetic paint	Sherwin-Williams	Spray	2 h	4.8×10^6	Unknown.
Traffic paint	Sherwin-Williams	Brush	–	–	Oil seeps through film.
Automotive undercoat	Sherwin-Williams	Sprayed	20 h	6.9×10^5	Oil under pressure washed undercoat away.
Polyurethane wood varnish	Jewel Paint Co.	Spray 2X	2 h each coat plus	3.45×10^5	Poor film strength.
Floor enamel	Pratt & Lambert	Brush	4 h, plus 1 h in contact with concrete	6.9×10^5	–[b]
Floor enamel	Pratt & Lambert	Brush	4 h, plus 21 h in contact with concrete	2.75×10^6	–[b]
Hydroflex swimming pool paint	Lox System, Inc.	Brush	3 h, plus 1 h in contact with concrete	6.9×10^5	–[b]
Thickened epoxy	Lab	Brush	3 h, plus 1 h in contact with concrete	2.75×10^6	Slight leak through film.
Silicone rubber caulk	Dow Corning	Spread on with knife	20 h	5.17×10^6	Mold rusted, possibly caused by acetic acid liberated during cure.

[a]Failure is considered to have taken place when pressure drops of 3.45×10^5 N/m^2 or more occur in less than a minute.
[b]Not applicable.

Table 8. Use of preformed films as oil barriers

Type	Manufacturer	Pressure applied N/m^2	Failure	Comment
Brown plastic tape 6487DK02-4	Borden	5.86×10^6	Yes	Film damaged by tamping tool.
Aluminum foil	–[a]	5.86×10^6	No	–[a]
Electrical aluminum tape	3M	5.86×10^6	No	–[a]
Trifoil type 603	Oak Materials Group, Tripoint Division	5.86×10^6	No	–[a]
Teflon tape	3M	5.86×10^6	Yes	Film damaged by tamping tool.
Lamotape 980 (aluminum on Mylar)	Lamotite	5.86×10^6	No	–[a]

[a]Not applicable.

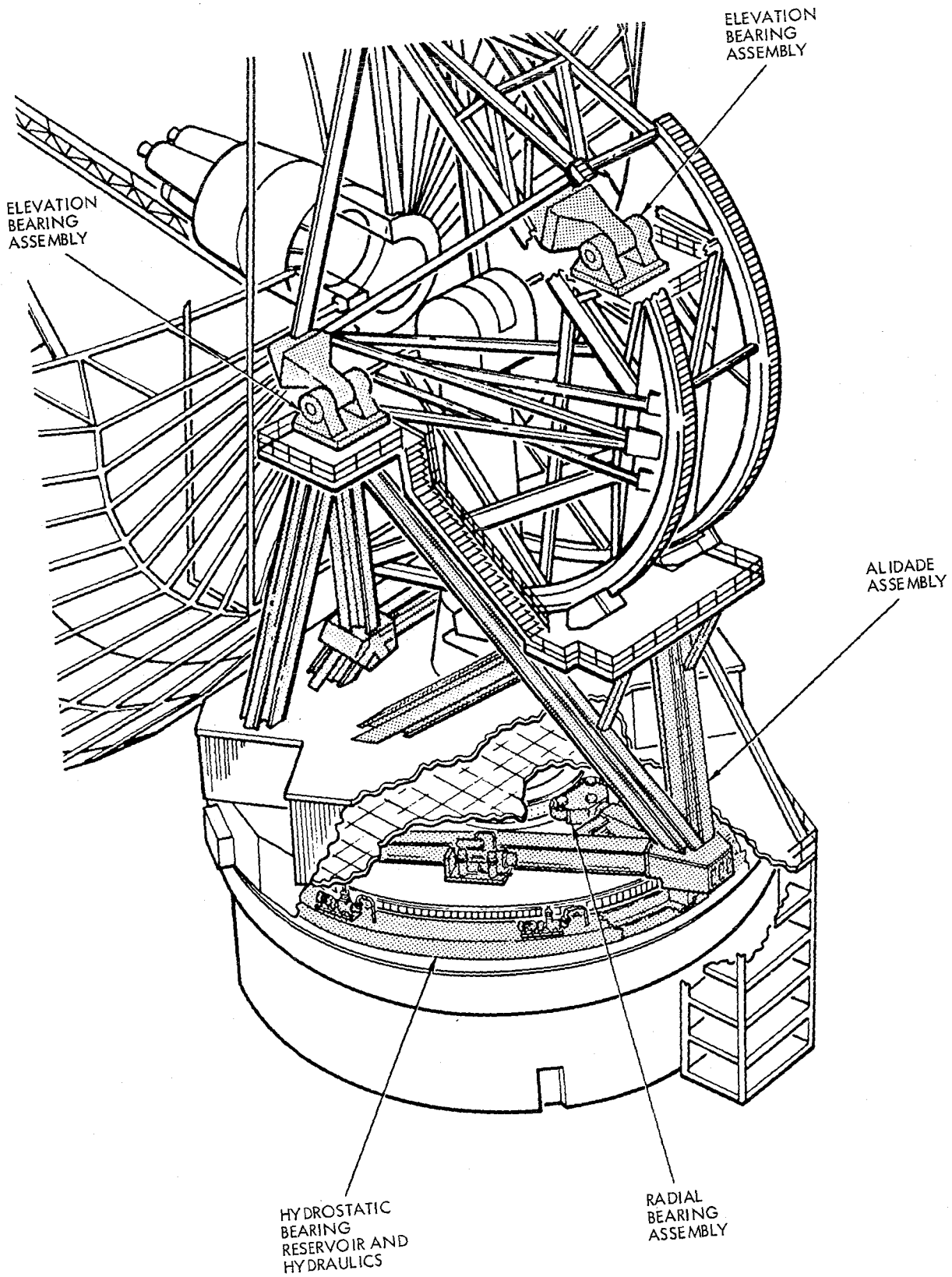

Fig. 1. Antenna mount

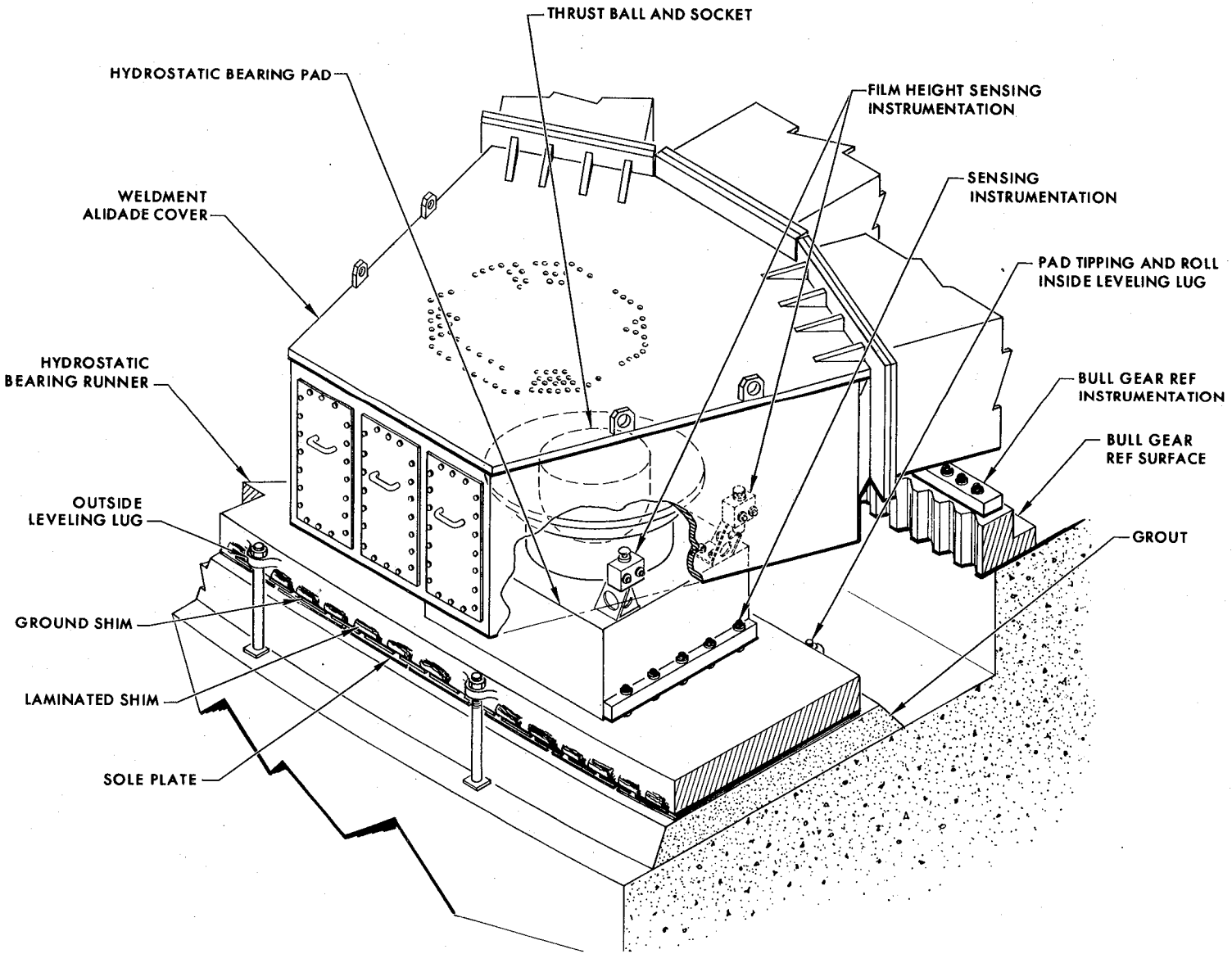

Fig. 2. Hydrostatic bearing cross section

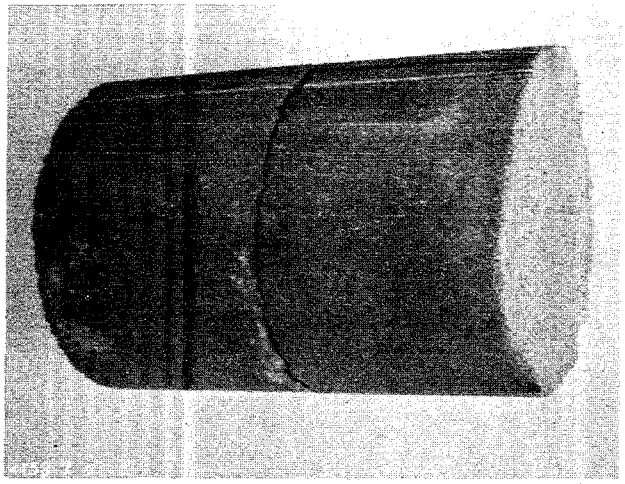

(a) FRACTURES CONSISTENTLY OCCURRED ACROSS THE PACKING INTERFACE.

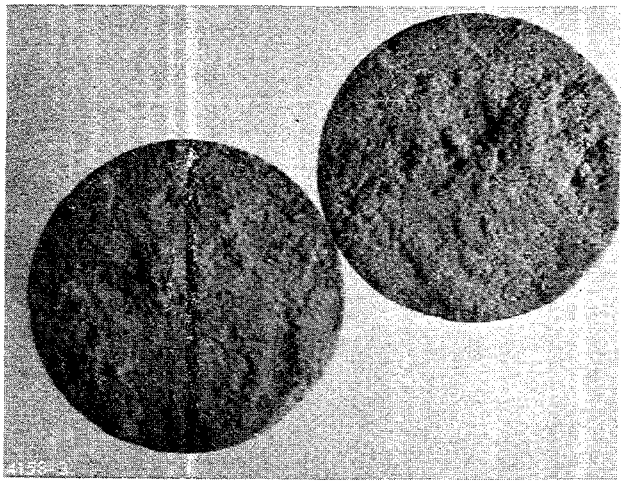

(b) PACKING RAM IMPRINTS ON THE FRACTURE SURFACE SHOW THE CYLINDER PARTED AT THE PACKING INTERFACE.

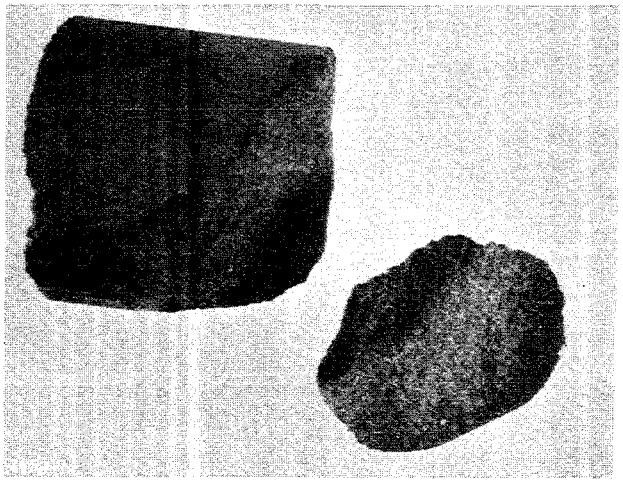

(c) AN IMPACT FRACTURE WITHIN A SINGLE PACKING INCREMENT FOLLOWS THE RANDOM PATH OF A SOUND CONCRETE.

Fig. 3. The effects of water loss. The loss of 5% to 6% of the mix water caused dry, weakly bonded packing interfaces, but material within a single packing increment underwent normal cure

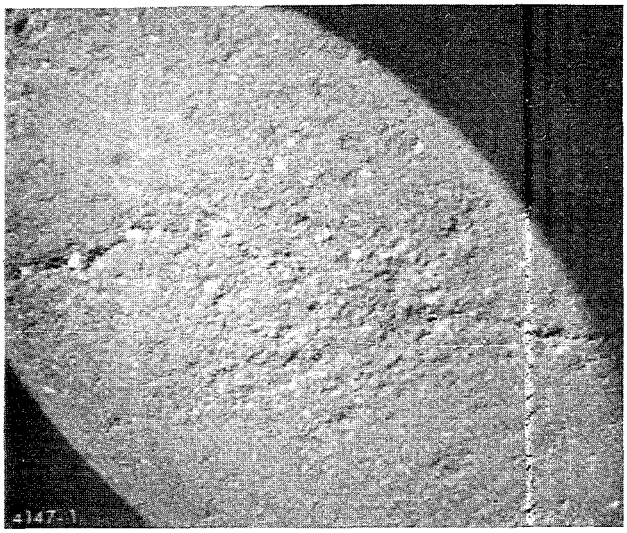

(a) BROAD, SHALLOW EROSION AREAS ARE CONNECTED BY DEEPER CHANNELS.

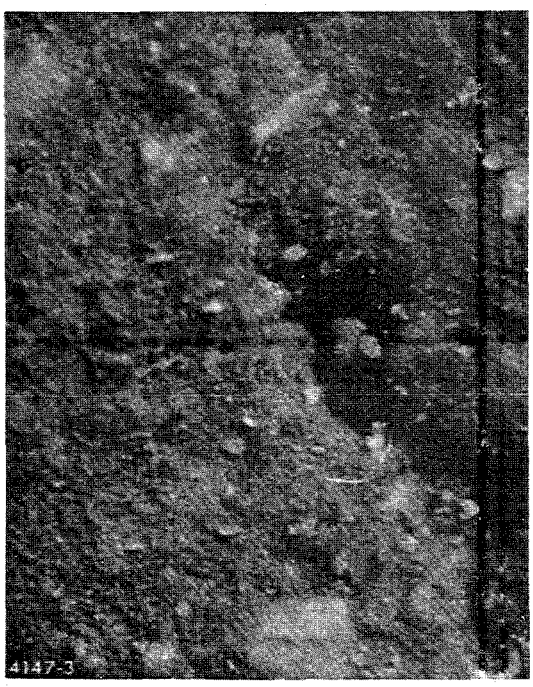

(b) THE CHANNELS FORM A CONTINUOUS NETWORK OVER THE GROUT SURFACE.

Fig. 4. The eroded areas and channels in a grout sample removed from the Goldstone site

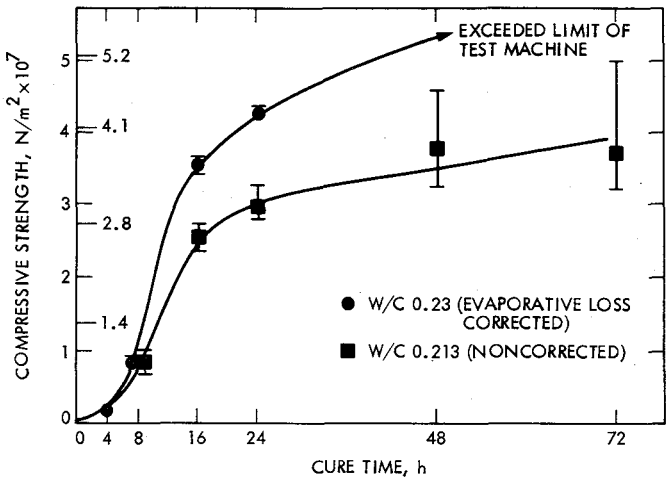

Fig. 5. Effect of evaporated water loss on the rate of compressive strength development by the dry-pack portland cement grout

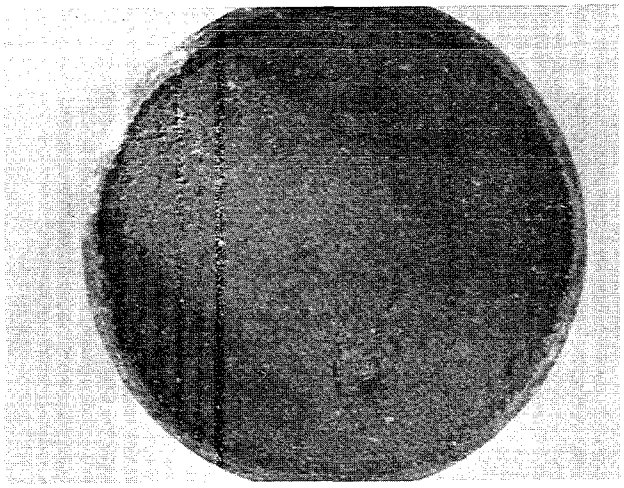

(a) A WATER-CORRECTED DRY-PACK GROUT SURFACE AFTER 15,500 CYCLES SHOWS ONLY MINOR SURFACE PITTING. THE DAMAGED AREAS APPEAR TO BE SUPERFICIAL AND ISOLATED WITH NO EROSION CHANNELS.

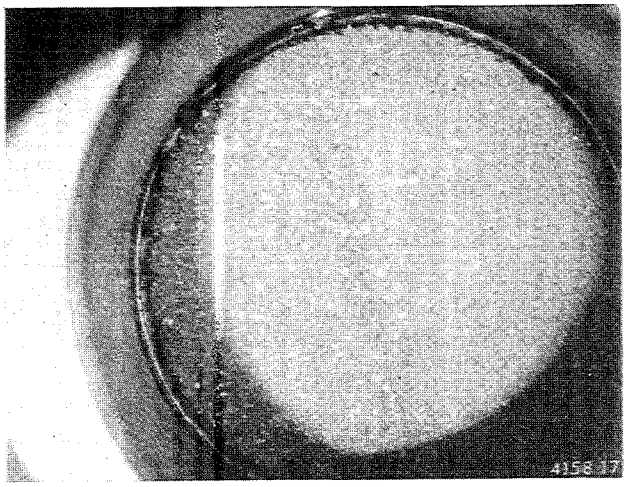

(b) THE DRY-PACK GROUT WITH PACKING INTERFACE, NOW WATER-CORRECTED AND EXPOSED TO OIL AFTER 8 h, SIMULATING PROBABLE REAL CONDITIONS, SHOWS SEVERE EROSION DAMAGE AFTER 5,700 CYCLES.

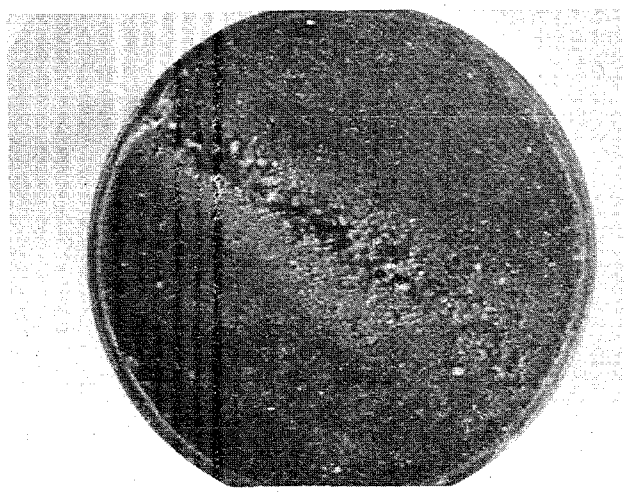

(c) AFTER 13,700 CYCLES, THE DRY PACKING INTERFACE IS 12.7 mm OR DEEPER AND THE CHANNEL WIDTH HAS UNDERGONE SIMILAR WIDENING. OTHER AREAS OF THE SURFACE HOWEVER, ARE NOT SERIOUSLY DAMAGED.

Fig. 6. While water-corrected grout appears highly durable to erosive effects, its vulnerability to water loss is clearly seen

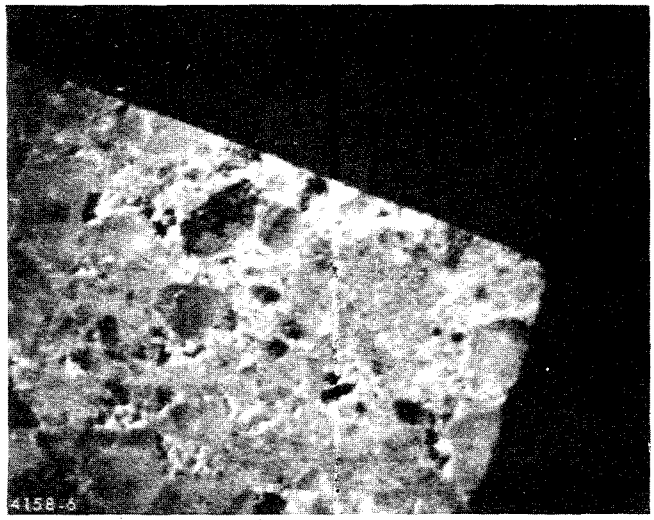

(a) CONTROL SPECIMEN BEFORE EXPOSURE.

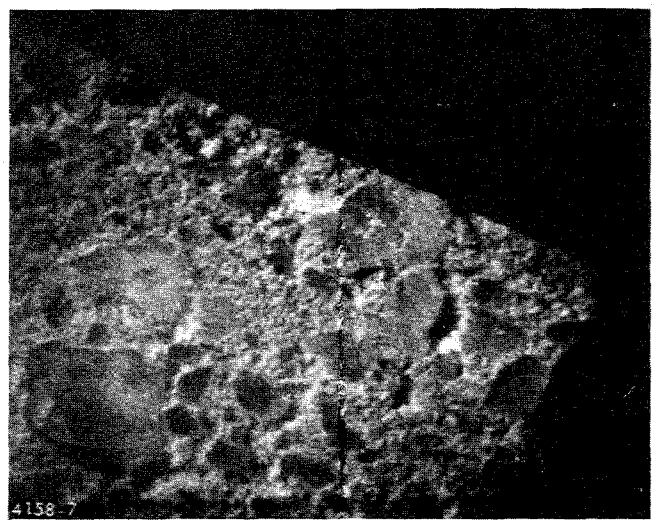

(b) LUBRIZOL EXPOSED SAMPLE SHOWS NO EVIDENCE OF EROSION OR WEIGHT LOSS.

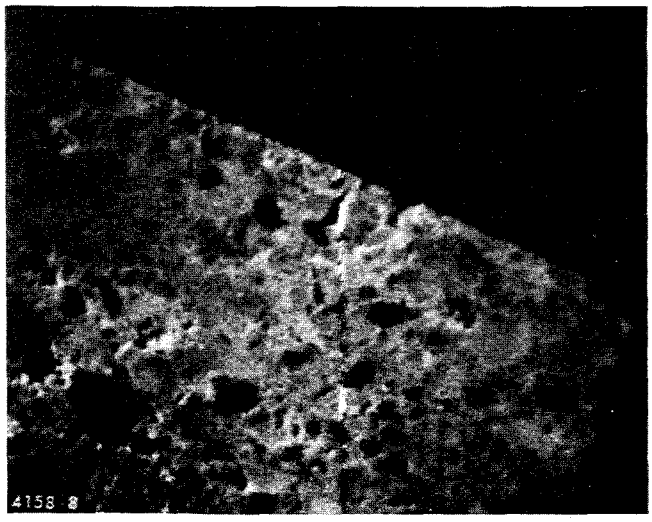

(c) 2, 6-DI-TERT-BUTYL PARACREYSOL SAMPLE, NO EROSION BUT SHOWS WEIGHT LOSS OF 0.85%.

Fig. 7. Effect of oil additives, I

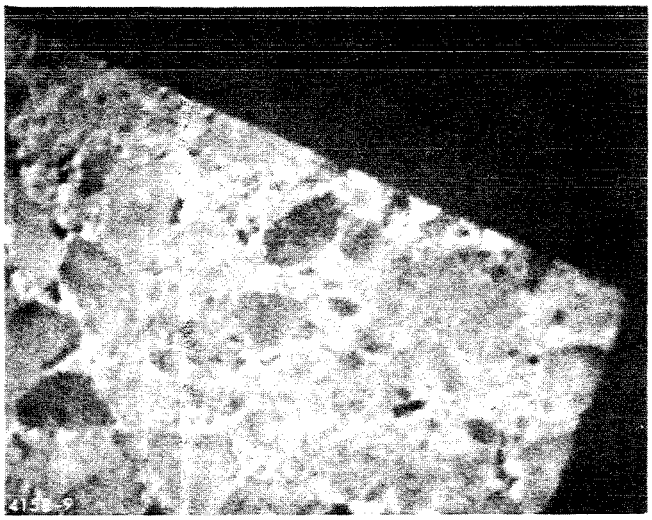

(a) CONTROL AFTER EXPOSURE TO THE BEARING OIL. NO WEIGHT LOSS, NO EVIDENCE OF CHEMICAL EROSION.

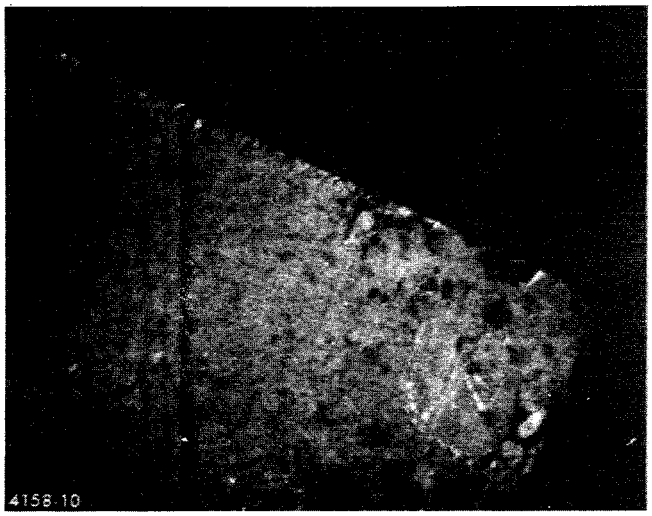

(b) DIPHENYLAMINE - EXPOSURE SAMPLE SHOWS NO WEIGHT LOSS BUT POSSIBLE EVIDENCE OF FRACTURING (CRYSTAL GROWTH) OF THE LARGE AGGREGATES.

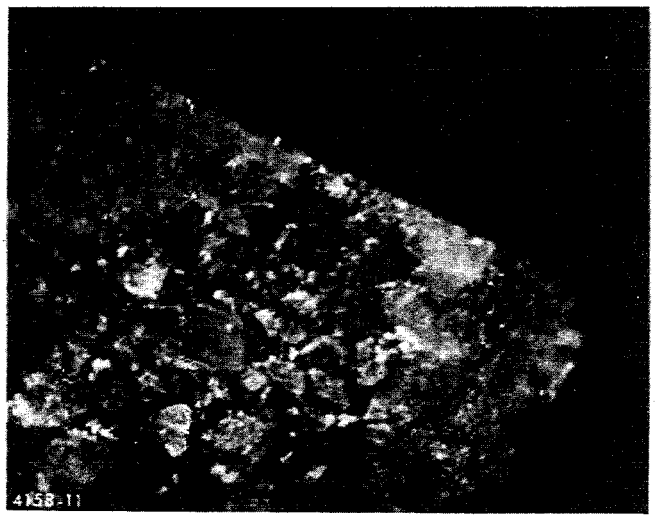

(c) PC 1244 POLYMERIC FOAM SUPPRESSANT EXPOSED SAMPLE SHOWS NO EVIDENCE OF DAMAGE.

Fig. 8. Effect of oil additives, II

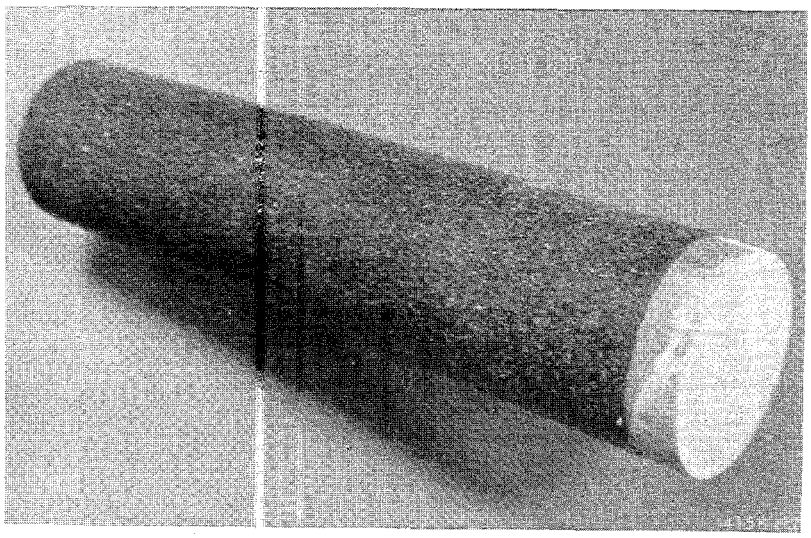

(a) A TYPICAL EPOXY POLYMER CONCRETE CYLINDER IN THE COMPRESSION TEST APPARATUS. THE 7.62-cm × 15.25-cm CYLINDERS WERE GAGED TO MEASURE CHANGES IN THE SPECIMEN LENGTH AND DIAMETER UNDER LOAD.

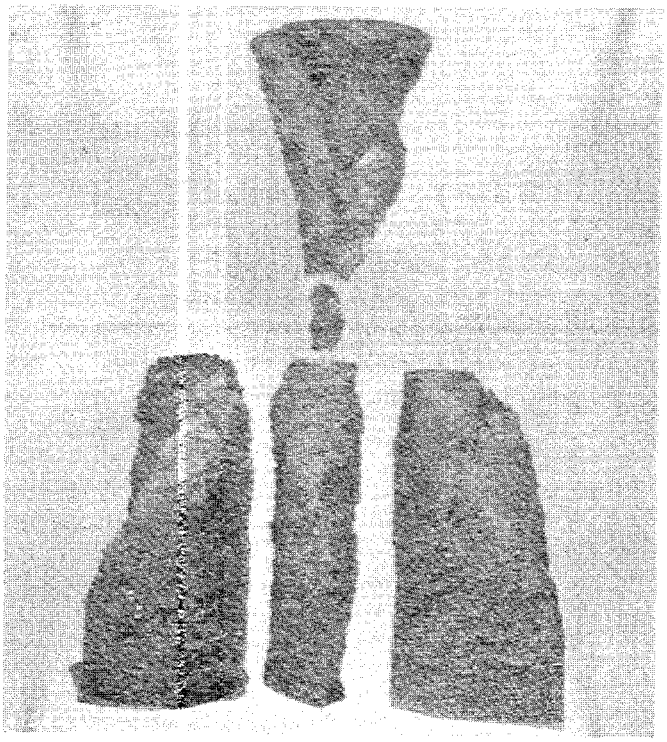

(b) THE SPECIMENS FAILED CATASTROPHICALLY AND SHOW THE 45° SHEAR FAILURE CHARACTERISTICS TYPICAL OF A HIGH-STRENGTH CONCRETE.

Fig. 9. The epoxy resin test cylinders show high compressive strength and modulus characteristics

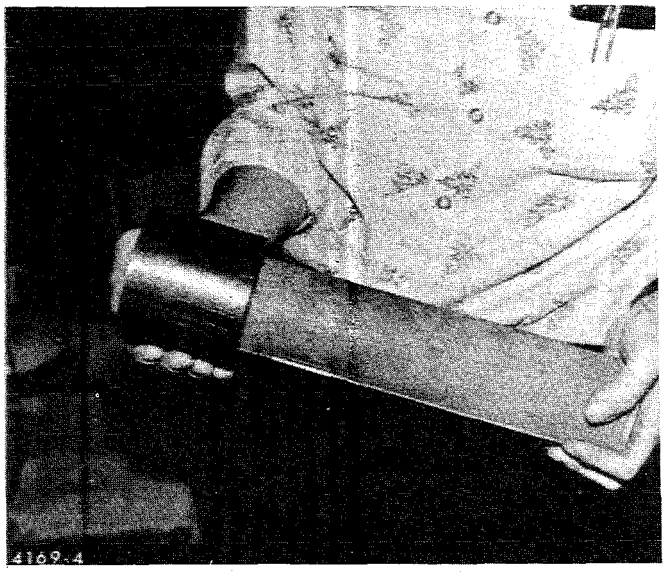

Fig. 10. An erosion test cylinder (dry-pack) with the oil chamber sleeve bonded in place

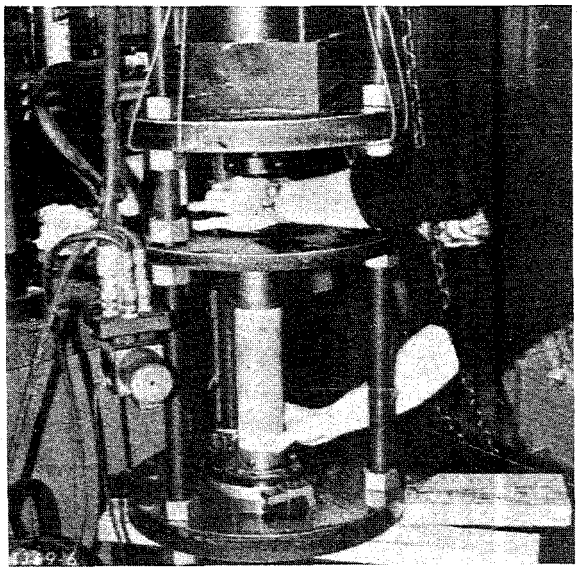

Fig. 12. The piston and sleeve are carefully aligned and the stroke length set so that the piston contacts and exerts full pressure on the cylinder surface in each cycle

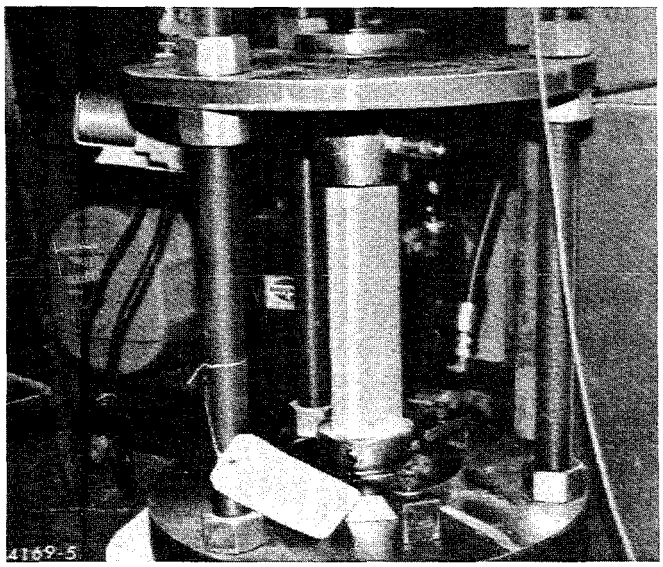

Fig. 11. After inserting the piston into the oil chamber sleeve, the assembly is locked in position by retaining rings top and bottom

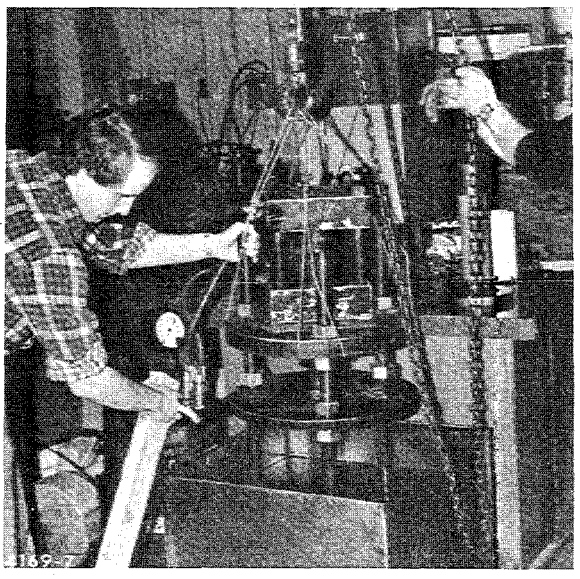

Fig. 13. After final checks, the apparatus is lowered into the oil reservoir

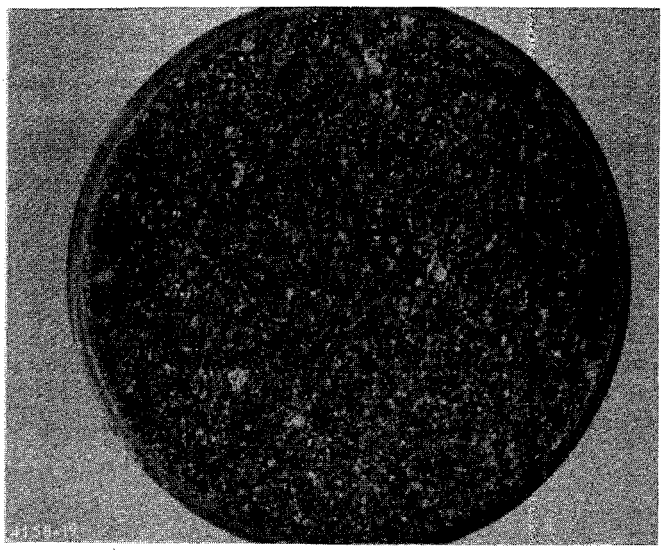

(a) EROSION SURFACE OF THE SOLID DESIGN POLYMER CONCRETE SAMPLE AFTER 28,300 CYCLES.

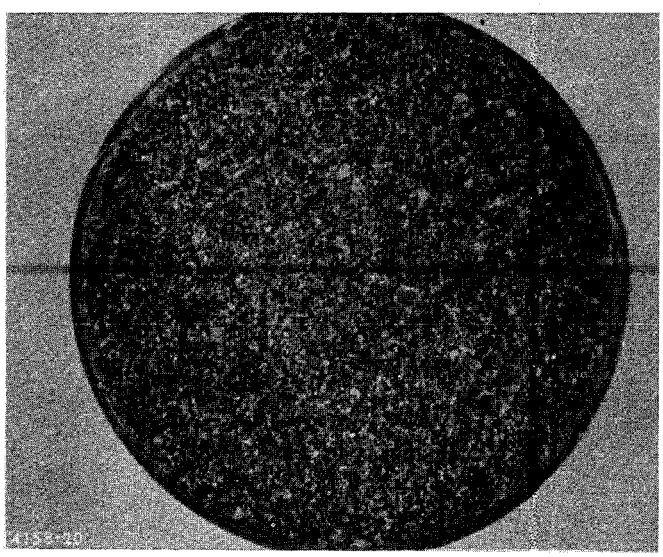

(b) EROSION SURFACE OF THE POROUS POLYMER CONCRETE AFTER 27,500 CYCLES.

Fig. 14. Polymer concretes showed virtually no sign of erosion or compression damage after more than 27,000 cycles

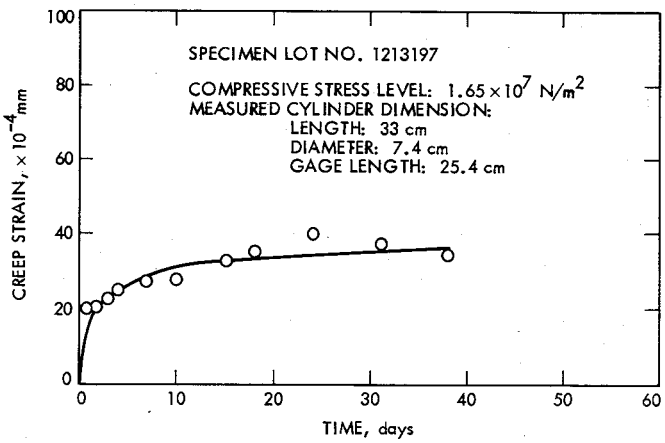

Fig. 15. Creep of polymer concrete cylinder

Fig. 16. Apparatus for testing the curing characteristics of aggregate/resin grouts

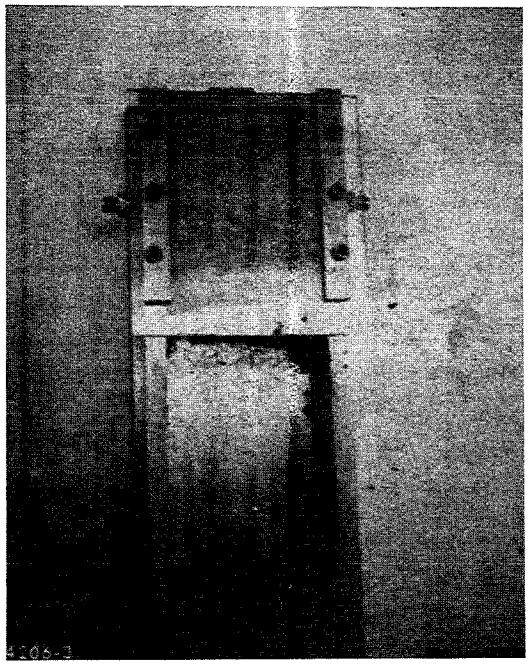

Fig. 17. Epoxy grout containing finely divided silica packed into mold; no evidence of sagging observed

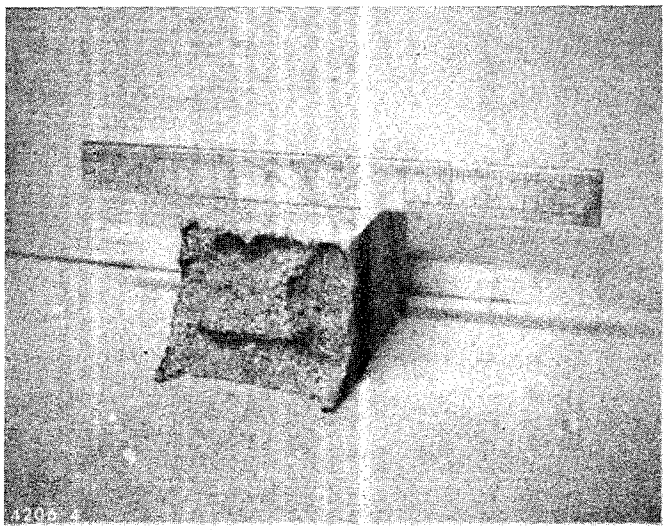

Fig. 18. Epoxy grout after removal from the mold indicating little sag and retention of impressions from tamping

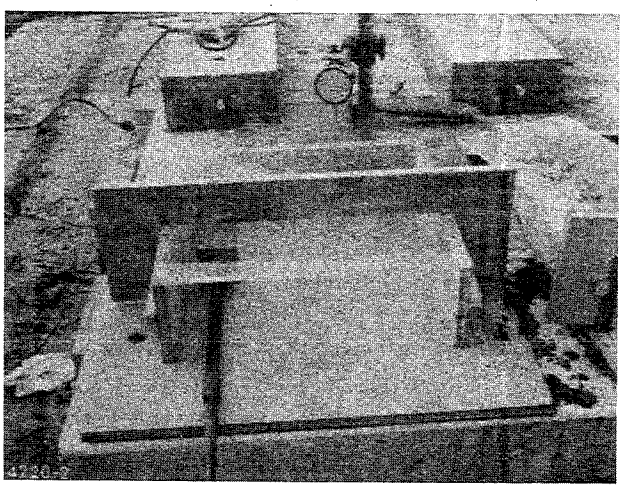

Fig. 19. Test cavity (48 cm × 48 cm × 15 cm) before filling; cavity has wooden sides, bottom, and back, and a plexiglass top; front end is open to permit loading of grout

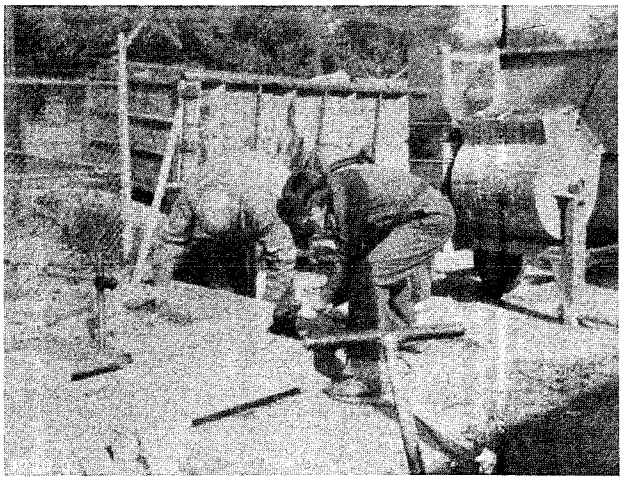

Fig. 20. Loading 48-cm × 48-cm × 15-cm cavity with epoxy grout

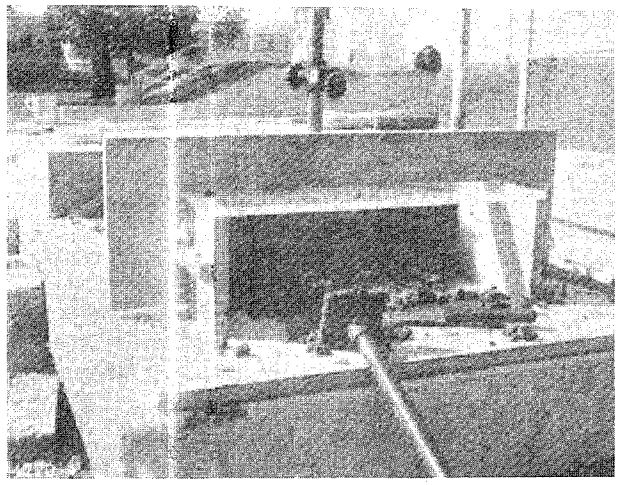

Fig. 21. Partially filled 48-cm × 48-cm × 15-cm cavity; foot of tamper is visible in foreground

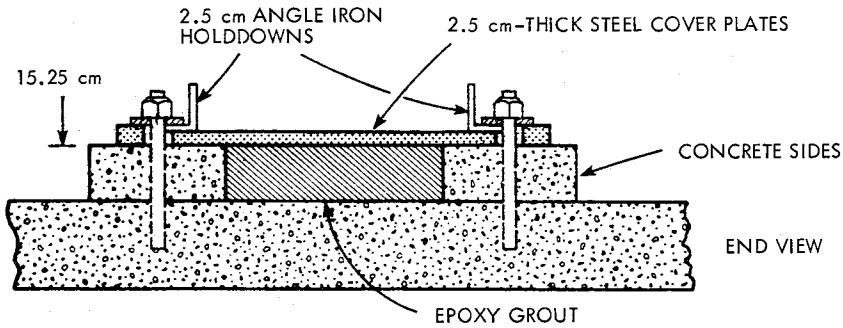

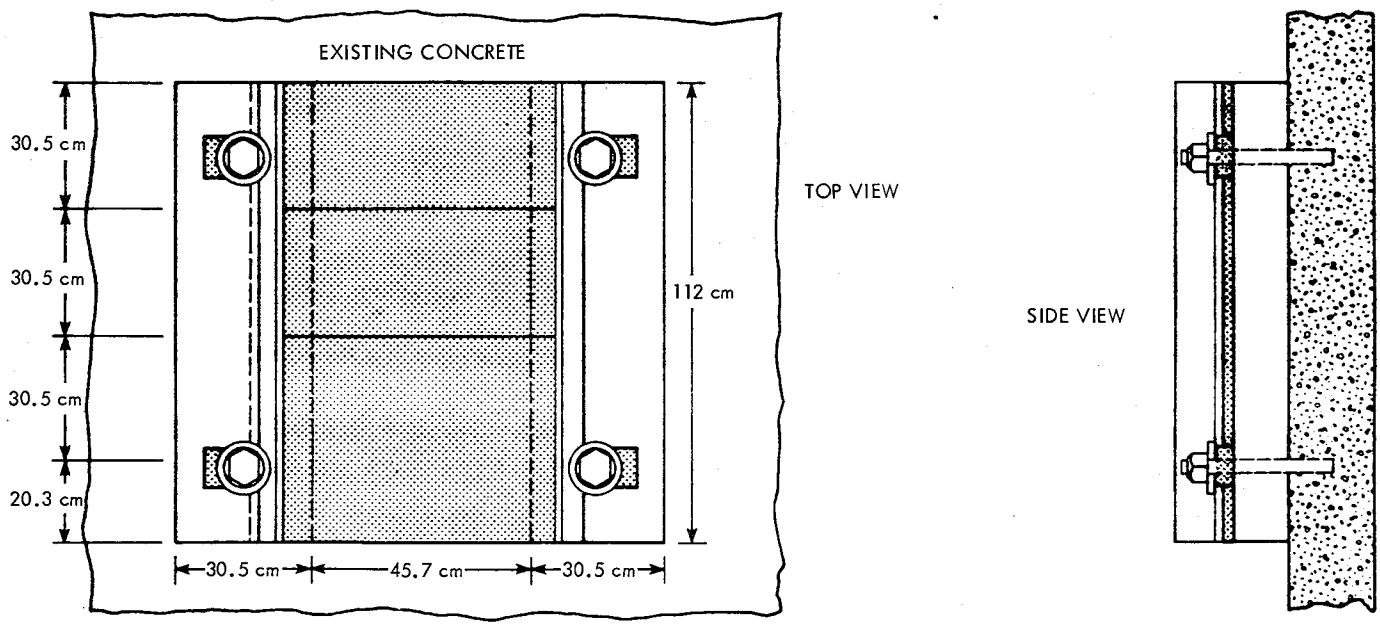

Fig. 22. Test device for demonstration of epoxy grout

Fig. 23. Hand mixing of epoxy-TETA resin in 3.785-liter cans

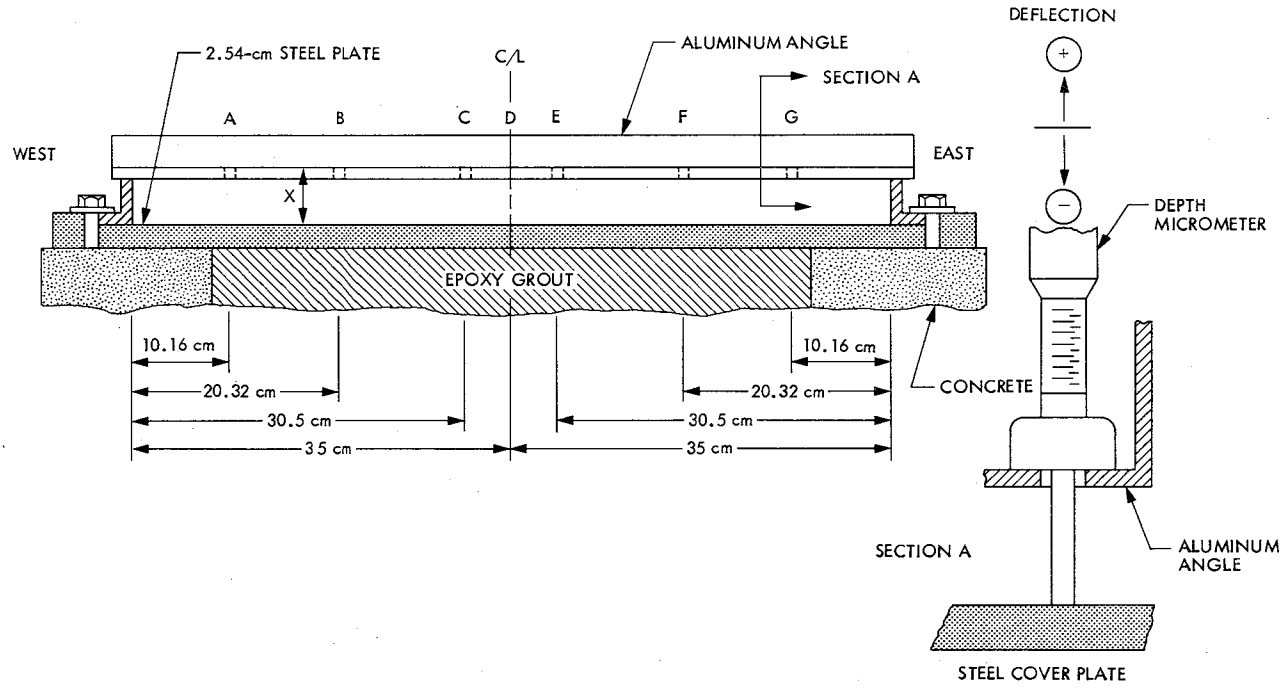

		A	B	C	D	E	F	G
BEFORE TEST	(X)	2.934	2.913	2.908	2.901	2.908	2.908	2.913
AT MAXIMUM EXOTHERM	(X)	2.931	2.911	2.898	2.893	2.896	2.898	2.896
Δ		+0.003	+0.002	+0.010	+0.008	+0.012	+0.010	-0.017
4-1/2 hours AFTER PLACEMENT	(X)	2.921	2.913	2.908	2.901	2.903	2.898	2.903
Δ		+0.013	+0.000	+0.000	+0.000	+0.005	+0.010	+0.010
24 hours - COLD	(X)	2.931	2.916	2.913	2.901	2.903	2.901	2.901
Δ		+0.003	-0.003	-0.005	0.000	+0.005	+0.007	+0.012

DISTANCE X MEASURED WITH DEPTH MICROMETER; DIMENSIONS IN cm

Fig. 24. Apparatus for measuring expansion and contraction of the grout

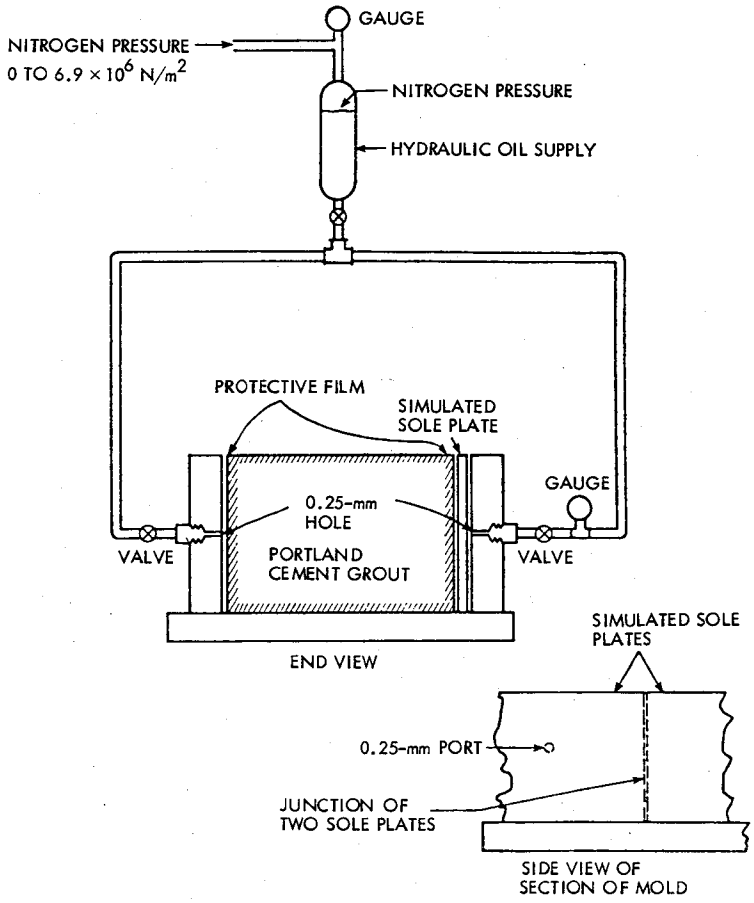

Fig. 25. Schematic drawing of test rig for evaluation of oil sealing films

Wind Loads for Bar-Truss Structures

M. S. Katow
DSN Engineering Section

When a computer model of a bar-truss structure exists for analysis by the NASTRAN or IDEAS computing programs, it can also be used to calculate the wind loadings. By using the cross-flow principles and vector analysis, a software was generated for computing the wind loads on the nodes or joints of the computer model. Detailed descriptions of the algorithms used and probable accuracy of the solution are included.

I. Introduction

The subreflector of the 64-meter antenna is supported by a quadripod using a truss-type structure (Fig. 1) for the legs and apex. With the multiplicity of square tubes in the wind stream at odd angles to the wind direction, a simple method of calculating the wind drag of a truss structure should enhance the wind loading analysis for stresses and deflections.

In the analysis method to be described, the existing structural analyzing NASTRAN or IDEAS model consisting of the CBAR element and the GRID coordinate cards defining the locations of the joints of the truss structures are used as inputs to the wind forces calculating software. Presently, the truss is assumed to use round bars that are an approximation to the actual square tubes used for the 64-meter quadripod.

The algorithms used to calculate the drag and lift of single cylindrical bars at angles to the wind direction axis are described (Ref. 1) with data showing excellent confirmations of the predicted values by experimental results.

For the nominal wind velocities, the viscous pressure drag caused by boundary-layer separation resulting in varied distribution of forces normal to the body surface is the dominating effect. The skin friction effects are low (approximately 2 or 3 percent).

The drag ($\mathbf{C}_D$) and lift ($\mathbf{C}_L$) coefficients of a cylindrical bar as defined in Ref. 1 by the cross-flow principle are:

$$\mathbf{C}_D = \mathbf{C}_D\text{-Basic } (\sin^3 \alpha)$$

$$\mathbf{C}_L = \mathbf{C}_D\text{-Basic } (\sin^2 \alpha \cos \alpha)$$

Using angle α as defined in Fig. 2, $\mathbf{C}_D$-Basic is the drag coefficient value with the axis of the cylindrical bar normal to the wind direction. It follows that vectors $\mathbf{C}_D$ and $\mathbf{C}_L$ will lie in the same plane defined by the axis of the bar and the wind direction vector even if the bar is at any angle to the basic coordinate system.

Thus the wind force vectors at the end nodes of the cylindrical bar (Fig. 2) are:

$$\text{lift}/2 = \mathbf{C_L} \cdot \text{diameter} \cdot \text{length} \cdot q \quad (1)$$

$$\text{drag}/2 = \mathbf{C_D} \cdot \text{diameter} \cdot \text{length} \cdot q \quad (2)$$

$$q = \frac{PV^2}{Z} = \text{dynamic pressure}$$

p = air density

v = wind velocity

II. Solution Description

The coordinate system defining the structural model will be used as the basic system since the wind-load vectors must be compatible to it.

Defining a bar **OA** by the basic coordinate system in the second quadrant (Fig. 3) and the wind vector **OB** to lie in the fourth quadrant (quadrants defined in plane *XOZ*), the angle α between the bar vector and the wind vector is calculated by the dot or scalar product as:

$$|\mathbf{OA}| \cdot |\mathbf{OB}| \cos\alpha = \mathbf{OA} \cdot \mathbf{OB}$$

where

$$|\mathbf{OA}| = \sqrt{a_1^2 + a_2^2 + a_3^2}$$

$$|\mathbf{OB}| = \sqrt{b_1^2 + b_2^2 + b_3^2}$$

$$\mathbf{OA} \cdot \mathbf{OB} = a_1 b_1 + a_2 b_2 + a_3 b_3$$

$\mathbf{a}_i$ = components of **OA**

$\mathbf{b}_i$ = components of **OB**

The drag vector for a bar will always be in the same direction as the wind vector; however, the lift vector **OC** will be normal to the drag vector and also lie in the plane defined by the bar vector and the wind vector.

Thus the drag value for each end of the bar can be calculated using Eq. (2) and its unit vectors are the same as for the wind direction.

The lift vector can be calculated using the vector triple product (Ref. 2)

$$\mathbf{OB} \times (\mathbf{OB} \times \mathbf{OA})$$

The vector product $\mathbf{OB} \times \mathbf{OA}$ defines a vector **OD** (not shown in Fig. 3), which is perpendicular to both **OB** and **OA**. Then the vector product $\mathbf{OB} \times \mathbf{OD}$ defines a vector **OC**, which is perpendicular to both the wind vector **OB** and **OD**. Thus the life vector **OC** lies in the plane determined by the bar vector **OA** and the wind vector **OB**.

In vector analysis terms, the components of the vector product $\mathbf{OB} \times \mathbf{OA}$ are:

$$d_x = a_y b_z - a_z b_y$$

$$d_y = a_z b_x - a_x b_z$$

$$d_z = a_x b_y - a_y b_x$$

Then the components of the cross product $\mathbf{OB}\,(\mathbf{OB} \times \mathbf{OA})$ are:

$$c_x = a_y d_z - a_z d_z$$

$$c_y = a_z d_x - a_x d_z$$

$$c_z = a_x d_y - a_y d_x$$

III. Conclusions

(1) The circular cylinder was used in the solution algorithm because of its insensitivity to the axis rotation. The basic drag coefficients for a circular cylinder from Ref. 1 is shown in Fig. 4. For the wind velocities of normal interest, the curve is flat at approximately 1.2 $\mathbf{C_D}$.

Figure 5 illustrates the drag coefficients for a standard square tubing (Ref. 1); as there is a drag rise for the orientation shown as (b), an average value used for computing the wind load should result in an accuracy within 10 percent.

(2) The circular and square tubings used in truss structures are normally assembled by welding, using close fitting joints. This results in smooth joints so that the actual lengths between the centerline intersections can be used for the drag and lift calculations.

(3) There will be interference effects resulting from turbulence created by air passing by the joints and bars before striking the next rows of joints and bars. This action should reduce slightly the drags and lifts of the trailing structure because of the sparseness of the normal trusses.

IV. Software Description

The program was coded for the 1100-81 computer to read the free-field columns integer used for NASTRAN or IDEAS structural model data; these data consist of GRID and CBAR information. Since the CBAR cards define a PBAR card (bar property data), an equivalent card was read in to input the diameter and the basic drag coefficient.

After checking for duplicate GRID and no match between the grid nodes in the CBAR card and the GRID listings, the drag and lift components are computed using the algorithms previously described. For each GRID node, the three-component drag and lift values for all bars connected to a grid joint are listed, followed by the wind loading as vector sum.

The wind loading values in three components are output as standard NASTRAN or IDEAS force cards in file 10 and also listed in the output. These force cards can be directly input into the structural analyzing program.

References

1. Hoerner, S. F., *Fluid-Dynamic Drag*, University Microfilm International, Ann Arbor, Michigan, 1958.
2. Wylie, C. R., Jr., *Advanced Engineering Mathematics*, McGraw-Hill Book Co., Inc., 1960.

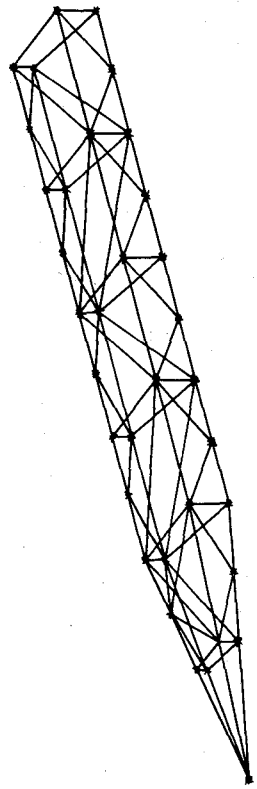

Fig. 1. Isometric view of bottom part of 64-m quadripod leg

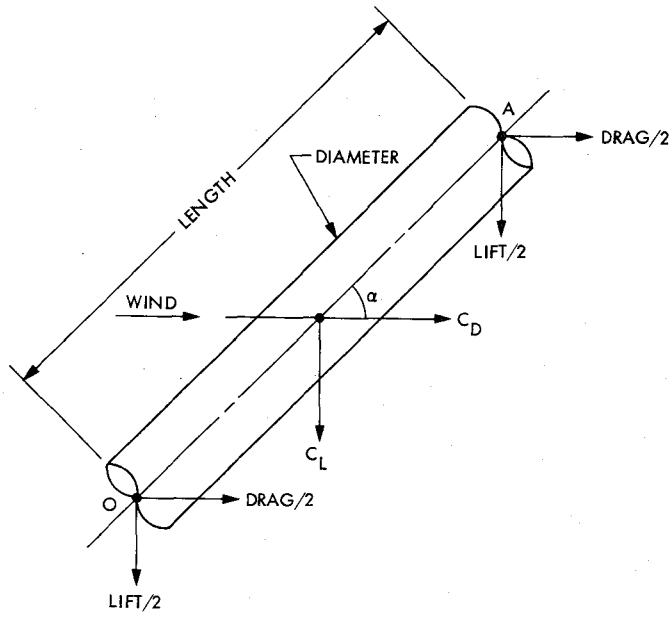

Fig. 2. Cross-flow notations

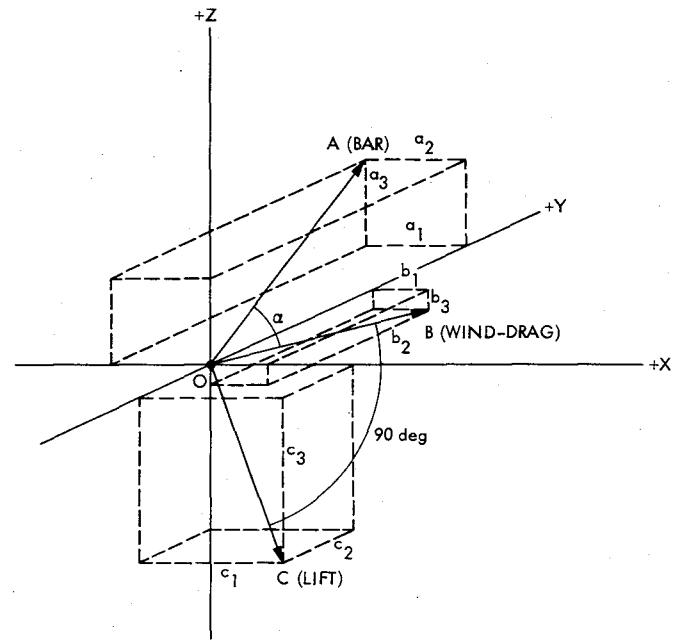

Fig. 3. Bar-wind vectors

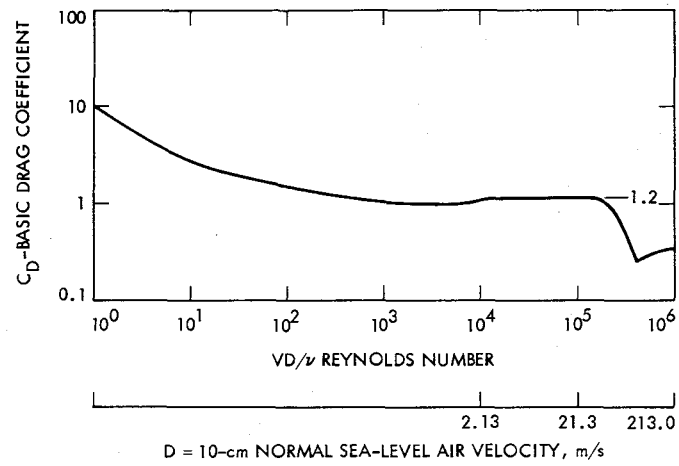

Fig. 4. Basic drag coefficient of circular cylinder (between walls)

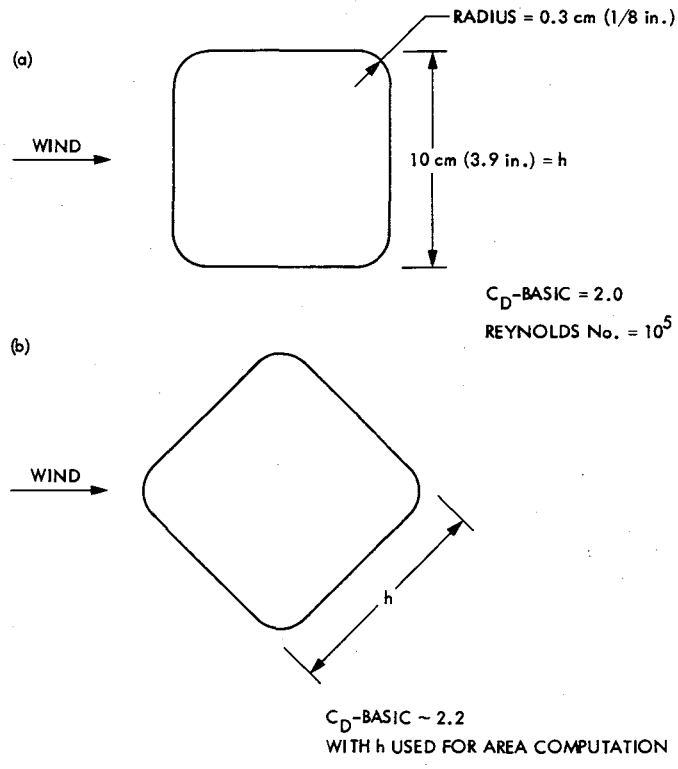

Fig. 5. Basic drag coefficient-square tubing

Fuel Cells Feasibility Status Report

D. Schonfeld and T. Charng
DSN Engineering Section

Fuel cells are electrochemical devices that promise a more efficient use of fossil fuels. The present feasibility study describes the operation of fuel cells and shows their potential benefits to the DSN. The authors describe the current research effort in this field and point out the major technical problems which still remain. Because of these major problems and because of DOE funding uncertainties, the authors conclude that fuel cells will probably not become commercially viable until the early 1990s.

I. Introduction

As part of the Master Plan of the Energy Conservation Project for the Deep Space Network, fuel cells are forecast to play an important role in future power generation subsystems. A management directive was given to review the technical and economic status of fuel cells as of 1980 and provide an up-to-date account of where the fuel cell technology is and where it will be 5 to 10 years hence. Furthermore, preliminary answers are sought for the very practical question of whether fuel cells can be used economically at the DSN Goldstone Deep Space Communications Complex to take part of, or eventually replace, the electrical load now being generated by diesel engines.

This article summarizes the efforts and results of the fuel cell task which have been carried out by members of the technical staff at the Advanced Engineering and Energy Conservation Group of the DSN Engineering Section. The article is divided into five parts. Following the introduction, the second part begins with a short review of what a fuel cell is, how it operates, and what its outputs are. The technical problems of each of the components are analyzed next. The fourth part concentrates on the economics of fuel cell use, with emphasis on fuel costs. The last part of the article details the conclusions that have been drawn from the review and makes some predictions for the future of fuel cells.

Fuel cells can be classified by electrolyte, by temperature of operation, by oxidant, and by fuel types. Possible combinations of these factors are limited due to the constraints the electrolyte imposes on the other factors and vice versa. For various technical reasons, most of the industry's efforts have been concentrated into the development of phosphoric acid fuel cells (PAFC) so named after the electrolyte in them. These cells have reached a relatively high level of technological maturity and they will probably be the first to be commercially available.

The second generation of cells will probably be that of molten carbonate fuel cells (MCFC). Their technological development is about 5 years behind that of PAFC.

The conclusions presented at the end of this article are based on literature sources as well as on numerous personal communication with members of the fuel cell community. These conclusions can change if DOE funding will modify its direction and magnitude.

II. Technology of Fuel Cells

A. Fuel Cell Operation

The fuel cell is a device that converts chemical energy of fuels into an electric energy by electrochemical reactions. As shown in Fig. 1, a single fuel cell unit can be considered as two electrodes separated by electrolyte. The electrolyte is either a liquid or solid substance and allows free passage of ions, but not electrons. The two electrodes are connected by an external path for an electric current to occur. Fuel is supplied to the anode and oxygen or air to the cathode. The electrochemical oxidation of the fuel at the anode produces electrons. The electrons flow through the external circuit to the cathode on which oxygen is reduced. The ionic and neutral species that participate in the electrochemical reactions are different for the various types of fuel cells.

In the case of acid cells, the electrolyte is typically an aqueous solution of phosphoric acid stored in a matrix structure. The electrodes are thin, porous carbon structures catalyzed with a noble metal such as platinum. At the anode, hydrogen molecules in the fuel gas are dissociated into hydrogen ions, releasing electrons:

$$H_2 \rightarrow 2H^+ + 2e^- \quad (1)$$

At the cathode, oxygen from the air is reduced by reaction with the hydrogen ions passing through the electrolyte and electrons flowing from the external circuit to produce water vapor:

$$\frac{1}{2} O_2 + 2H^+ + 2e^- \rightarrow H_2O \quad (2)$$

The overall cell reaction, combining Eqs. (1) and (2), is the oxidation of hydrogen to water, producing electricity and some waste heat:

$$H_2 + \frac{1}{2} O_2 \rightarrow H_2O + \text{Heat} + \text{Electricity} \quad (3)$$

The mechanism of creating the ions and electrons at the anode using catalysts has been described elsewhere (Ref. 1). Molecular hydrogen can be dissociated into hydrogen ions when passed over a catalyst. The most often used catalyst is platinum (Pt) and the reaction also produces free electrons ($2e^-$). Typical of catalytic reactions, the electron yield will increase if the surface area of interstices over which the reaction takes place is increased. Thus, increasing the surface area of the anode will increase the efficiency of the cell. This is achieved by using porous electrodes which result in a very large contact area between the gaseous fuel and electrode interstices. Classically, the production of electrons will be speeded up as the amount of catalyst is increased. In practice, one cannot increase the catalyst loading indefinitely, otherwise polarization of the electrode will occur, which results in a loss of cell efficiency. Thus, catalyst loading represents a compromise between reaction kinetics and diffusion rates.

The choice of electrolyte is based on its tolerance to fuel gas impurities. The most widely used fuel cell electrolyte today is phosphoric acid. This limits the temperature operating range of the cell to between 150 and 200° C. Below the 150° C limit, the phosphoric acid electrolyte has a poor ionic conductivity. Above the 200° C limit, the electrode materials tend to become unstable (Ref. 2). The choice of electrolyte not only depends on the operating temperature, but also on the way that ions migrate between the electrodes. In the phosphoric acid cell, the electrolyte is an acid and the H^+ ions move from the anode section to the cathode section. In other types of fuel cells, such as the molten carbonate, the electrolyte is a carbonate salt and the ions ($CO_3^=$) migrate from the cathode to the anode.

B. Types of Fuel Cell

A number of fuel cell types offering reduced heat rate and capital costs are: molten carbonate cell, solid oxide cell, phosphoric acid cell, and alkaline cell. The electrochemical reactions for those cells are given in Table 1.

The first two fuel cells, molten carbonate and solid oxide, operate at high temperature and offer high power density at about 7913 kJ/kWh_e (7500 Btu/kWh_e) heat rate (46 percent overall efficiency). Because carbon monoxide (CO) is shifted in molten carbonate fuel cells, a separate water-gas shift converter is not required as part of the fuel processor. Higher operating temperatures facilitate waste heat rejection and integration with other power plant functions. The development efforts for the molten carbonate cell are focused on improving cell endurance and performance and on establishing the initial scaleup needed in practice. Solid oxide cells operating at 980° to 1090° C have been under investigation. Because this temperature range imposes severe material and design requirements, the solid oxide cell development effort is focused on establishing a cell concept which operates satisfactorily at a temperature range similar to the molten carbonate cell (650° C).

The two low-temperature cells are the phosphoric acid and the alkaline cells. Alkaline cells offer higher performance than phosphoric acid cells. However, carbon oxides present in fuel and in air streams fed to the cell cause a rapid conversion of hydroxide to carbonates and loss of performance. The phosphoric acid cell performance is promising for the near-term applications. The material costs are acceptable, but the cell components require relatively expensive manufacturing processes. Development efforts are focused on both the reduction of manufacturing costs and the increase of the tolerance of the phosphoric acid cell to sulfur and other impurities in the fuel gas stream.

Fuel cells with sulfuric acid, sulfonic acid, or solid polymers as the electrolyte are limited by the vapor pressure of the water in the electrolyte. If air is used as the oxidant, these fuel cells must be operated at temperatures below 100° C. Otherwise, the electrolyte becomes unstable due to water evaporation and the associated venting of nitrogen. At temperatures below 100° C, however, high efficiency cannot be achieved. These electrolytes are, therefore, not receiving much attention for nonspace applications.

C. Fuel Cell Powerplant System

The schematic of a fuel cell power plant system is shown in Fig. 2. The full system is composed of three elements: the fuel processor, the power section, and the inverter. The fuels for the fuel cell powerplant can be of various types such as natural gas, coal-derived gases and liquids, alcohols, naphtha, and other hydrocarbon-based fuels. The fuel processor is used to break up the raw fuel into a gas rich in hydrogen (H_2).

The power section converts processed fuel and air into direct current power. At present technology levels, a single fuel cell unit generates roughly 100 to 200 watts of direct current (dc) electricity for each square foot (0.093 m^2) of electrode area at a potential on the order of 1 volt. In a fuel cell power section, a number of single cells are connected in series to permit generating hundreds of volts in a stack. Connecting a number of stacks in parallel permits power levels from kilowatts to multimegawatts.

The power conditioner (inverter) converts the direct electric current into alternating current to meet the customer requirements. Two basic types of inverter systems were considered for dispersed generation application of fuel cell powerplants; they are line-commutated inverters and self-commutated inverters. In line-commutated inverters, the kVA required to turn off the power thyristors is supplied by the ac system; in self-commutated inverters, it is supplied by energy stored within the inverter itself.

D. Operational Advantages

Direct energy conversion by fuel cells promises to be a highly efficient process. Since fuel cells do not have Carnot cycle limitations (Ref. 3), their thermodynamic efficiency is of the order of 95 percent. In contrast, a Carnot cycle operating between 150° and 200° C, the PAFC temperature limits, has an efficiency of only 11 percent. However, the efficiency η of the fuel cell stack is made up of voltage and current efficiencies in addition to the thermodynamic one (Ref. 4):

$$\eta_{stack} = \eta_{thermo} \times \eta_{current} \times \eta_{voltage} \tag{4}$$

With voltage and current efficiencies of the order of 75 percent, the stack efficiency is of the order of 42 percent for PAFC and 48 percent for MCFC.

The total fuel cell system includes the power sections, the power conditioner and the fuel processor. This system's efficiency is expressed as

$$\eta_{system} = \eta_{stack} \times \eta^{1}_{\substack{power \\ converter}} \times \eta^{2}_{\substack{fuel \\ processor}} \tag{5}$$

If the stack efficiency is taken as 42 percent, the fuel processor efficiency 85 percent, and the power conditioner efficiency 95 percent, the system efficiency is about 34 percent. This number does not take into account possible heat recovery. A comparison of the total fuel cell system efficiency with other power plants (Ref. 5) is given in Fig. 3. Figure 3 also indicates that fuel cells have a relatively constant heat rate (efficiency) versus load characteristics. Therefore, the fuel cell power plant offers greater economies than conventional power generation when utilized for load following or spinning reserve applications.

Other operational advantages of fuel cell systems include their nonpolluting quality and their dispersibility. The pollution levels from experimental fuel cell power plants are very low. Typically, nitrogen oxide emissions are of the order of 3 ppm, hydrocarbons 4 ppm, sulfur dioxide 0.1 ppm, as sketched in Fig. 4 (Refs. 6 and 7). In addition, fuel cells are noise and vibration free and require no auxiliary machinery except fuel pumps and cooling fans. Fuel cells do not offer economy of scale. Thus, one could build modular units which can be installed at distributed users' locations. This is in

[1] Defined as the ratio of ac power/dc power since the fuel cell produces a dc voltage.

[2] Defined as the heating value of processed gaseous fuel/heating value of raw fuel.

contrast to conventional large power plants which require a central station together with electrical transmission lines. It is estimated that savings in transmission line losses are in the order of 5 to 9 percent.

III. Technical Problems of Fuel Cell Systems

The history of fuel cells dates back to 1842. Grove (Ref. 8) wrote of experiments with fuel cells in 1842, and practical devices were already sought in the 1880s (Ref. 9). Despite this early interest, and the more recent impetus given by the Apollo space program and by the increase in fossil fuel costs, fuel cells are still mostly in a "demonstration" stage. It appears that most of the work is being done by three companies: (1) United Technologies Corporation (UTC), Power Systems Division, South Windsor, Connecticut, (2) a consortium between Westinghouse Electric Corporation in Pittsburgh and Energy Research Corporation (ERC) in Danbury, Connecticut, and (3) Engelhard Minerals and Chemicals Corporation – Engelhard Industries Division in Menlo Park, New Jersey. Most of our discussion will reflect the opinions and experiences of these companies.

A. Fuels and Fuel Processing

The near-term technology of fuel processing in fuel cell systems uses petroleum-based fuels as the raw fuels to produce hydrogen-rich gas. The far-term technology will use coal or some sort of renewable resource such as biomass for H_2 generation. A schematic of the paths leading from raw fuels to processed fuels is shown in Fig. 5 (Ref. 10). Of the fuels shown in Fig. 5, the following types are discussed:

1. Gaseous fuels. The basic technology for steam-reforming of gaseous fuels, such as methane, is relatively mature. In the future, the important factor will be the design of fuel processors to use the stack-generated heat. For gaseous fuels, commercial catalysts (e.g., Pt) are readily available. ERC is doing exploratory studies of fuel processors for Molten Carbonate fuel cells. UTC and Westinghouse/ERC are working on the engineering development of fuel processors. The first application of UTC's fuel processor is likely to be at a 4.8 MW_e demonstrator plant being built for ConEd in New York City. A similar plant is also being built in Tokyo. Westinghouse/ERC is working on processors for dispersed systems, the so-called OS/IES (On-Site Integrated Energy System).

2. Alcohol fuels. The basic technology for processing alcohol-based fuels, such as methanol, is not as advanced as that for gaseous fuels. Between methanol and ethanol, it is likely that methanol processors will be built first. ERC plans to have methanol-fueled 2- to 10-kW power plants by 1982 (Ref. 11). Engelhard is also working in methanol processors initially for a 5-kW unit (Ref. 12). They base their work on the projected availability of methanol from coal by 1990.

3. Hydrocarbon liquid fuels. Mid-distillates and heavier hydrocarbon liquid fuels hold a promise mainly because of the availability of coal in the United States. Unfortunately, the technology for processing these liquids is not very well developed. The major problems associated with the processing of these fuels are thermal efficiency and prevention of carbon formation in the processor. Several processing schemes are being investigated at the bench scale level with support from DOE and EPRI.

Adiabatic steam reforming technology is being developed at UTC to process No. 2 fuel oil (a heavy liquid) and other coal-derived liquids (Ref. 13). In this reformer, air is added to the fuel and steam to provide, by combustion, the endothermic heat for reforming in the catalyst bed. The combustion of additional air is also necessary to raise the reactor to high temperature to compensate for deactivation of the catalyst by sulfur in the feed.

Similar reformers for processing heavy liquid fuels are being studied at Engelhard (Ref. 14). They have developed noble metal catalysts (Pt/Rh) which allow partial oxidation of the feed stock and its conversion to lower molecular weight hydrocarbons.

A high-temperature steam reforming called THR Process combined with autothermal reforming (ATR) step has been identified as one of the most promising technologies for processing of distillate fuels. The THR process is now under pilot plant development by Toyo Engineering Corporation, Japan. The ATR step, as part of the reformer train, is used to complete the reforming conversion of the fuel and, therefore, it is a key to achieving the high thermal efficiency. The processing of light hydrocarbon liquids, such as naphtha, are being developed by UTC, but limited, by their questionable availability. It is possible, however, that naptha will be tried at the 4.8 MW ConEd pilot plant.[3]

The conclusion for hydrocarbon liquids seems to be that by 1982, a decision will have to be reached whether to build a commercial demonstrator for the processing of these liquids (Ref. 10). If such a plant is going to be built, the completion or production date is envisioned to be around 1990. Until that time, natural gas based fuels, and possibly methanol, will be the feedstock of choice.

[3]The cost of naphtha may be getting too high to run tests with it at the ConEd plant. Also, fire department mandated safety tests are making naphtha an expensive trial feedstock.

B. The Fuel Cell Power Section

1. The electrodes and the catalyst. Fuel cell electrodes are basically flat plates of some material throughout which catalyst crystals are dispersed. The electrode material is usually carbon, and the catalyst is usually platinum (Pt) in acid fuel cells. The role of the electrodes is to conduct and at the same time provide a solid support for the catalyst. Cathode corrosion has been, and still is, one of the operational problems. Corrosion of the catalyst support as well as recrystallization and dissolution of the high-surface-area platinum catalyst downgrade fuel cell performance. Electric Power Research Institute (EPRI) is funding contracts (the EPRI RP 1200 series) to develop new technology for better catalyst support (Ref. 15). Under one of these contracts, Stonehart Associates, Danbury, Connecticut, has found (Ref. 16) that the degree of corrosion can be correlated with lattice parameters and with the degree of graphitization. Acetylene Black, Shawinigan, and fluorinated phosphonated Vulcan show promise for good corrosion performance and manufacturability. There are very few published results that indicate the lifetime of electrodes in hours (Fig. 6) and it is difficult, therefore, to predict when commercial use electrodes will become available.

Catalyst performance depends on the dispersion and activity of the catalyst. It is desirable to have the catalyst crystallites dispersed at a certain distance from each other as this will maintain a high catalyst surface area. Furthermore, one must take into account that platinum has a certain solubility in acids depending on the electric potential and the operating temperature. Stonehart Associates (Ref. 16) has shown that catalyst crystallites initially at 100 m^2/g degrade to 20 m^2/g after 40,000 hours in phosphoric acid at 200° C and 0.7 volts. Note that the desired end-of-life surface area is taken to be 80 m^2/g.

It seems that Pt area loss depends upon initial Pt surface area and is unrelated to the surface energy of the crystallite. Tests at Engelhard (Ref. 12) show that a new catalyst (No. 11099-39) has little surface area decay after 2000 hours.[4] However, in general, attempts at solving crystallite migration in the phosphoric acid fuel cell environment have been only marginally successful (Ref. 17).

The activity of the catalyst in fuel cells is reduced by catalyst poisoning. At the anode, catalyst poisoning is due to the presence of carbon monoxide and sulfur traces in the fuel. Work at Lawrence Berkeley Laboratory indicates that Pt-V alloys have increased the activity and durability of the cathode. Similar claims for the Pt-Rh catalysts have been put forward at Engelhard (Ref. 14).

2. The electrolyte. Electrolyte problems are of two kinds. The electrolyte must be physically and chemically stable at the high temperatures used in fuel cells. Second, the electrolyte must not be lost during the cell's lifetime through flooding of the electrodes.

New and better electrolytes are continuously sought. In this area, ECO, Inc., Buzzards Bay, Massachusetts, has found two new very promising electrolytes: difluoromethanediphosphonic acid $[CF_2(PO_3H_2)_2]$ and difluoromethanedisulfonic acid $[DF_2(SO_3H)_2]$. Both appear to be very stable at high temperatures. The United States Army (MERADCOM, Ft. Belvoir, Virginia) is also sponsoring ERC research in aqueous solutions of trifluoromethanesulfonic acid as an electrolyte. Solid electrolyte research is being conducted at Westinghouse (Ref. 18), and at some national laboratories such as Brookhaven National Laboratory (Ref. 19) and the National Bureau of Standards (Ref. 20). All of these projects are in the early experimental stages.

Molten Carbonate fuel cells have been tested for a number of years and they appear promising as second generation fuel cells. An active research program in Molten Carbonate fuel cells is being pursued nationally with DOE funding (currently at about $12 million per year). The tasks of this program are to:

(1) Develop a reference coal-fueled power plant design.

(2) Develop fuel cell stack components and verify 10,000 hour life of single cells.

(3) Initiate development of full-scale stack testing capability.

(4) Determine tolerance to contaminates in coal-derived gas.

The bulk of this work is concentrated in two major long-term contracts with United Technologies Corporation (UTC) and General Electric Company (GE).

EPRI funding (currently at $3.5 million per year) is focused on power plant technology development at UTC (20 KW breadboard) and on advanced concepts at GE, ERC, UTC, and Institute of Gas Technology (IGT). The Gas Research Institute (GRI) funding (at $1 million per year) is directed at systems studies and experimental work in the area of cogeneration applications at UTC, IGT, and ERC. Niagara Mohawk (in New York state), ERDA, and the Tennessee Valley Authority (TVA) are supporting power plant technology development.

[4] At the present time, about 10 percent Pt at 0.5 mg Pt/cm^2 represents the most desirable configuration.

If projected funding levels are maintained, mid-1982 appears to be a branch-point for the Molten Carbonate Fuel Cell Program. At that time, the major technology development contracts will be coming to a close. If the objectives have been accomplished and readiness to proceed with engineering development has been established, funding levels must be increased to support the more demanding tasks of full-scale stack testing and system integration. If the objectives of the current contracts are not met, the nature of the problems must then be determined and the program reevaluated and restructured as appropriate.

3. Fuel cell stack performance. The typical phosphoric acid fuel cell unit produces between 0.6 and 0.85 volts dc. A fuel cell stack consists of a number of unit cells arranged in series. For example, the 4.8 MW plant being built for ConEd in New York uses 20 stacks, in parallel, of about 500 cells each. The output power of such stacks is simply the sum of the outputs of the individuals. Therefore, overall stack performance can be established by looking at a single cell's performance characteristics.[5]

There are a number of indexes that show how well a cell performs. One of these indexes is a plot of cell voltage versus time. Such a graph totals all the losses that the cell suffers over a length of time. The losses appear as a decay in the cell's voltage. Figure 7 indicates the performance of cells from various manufacturers. Two observations can be drawn from this figure. First, some cells undergo a voltage decay after 5000 hours from the beginning of the test. Some published results indicate that progress is being made in limiting this voltage decay. As an example, for some UTC phosphoric acid cells the rate has been decreased from 60 mV per 1000 hours to approximately 12 mV per 1000 hours (Ref. 24). The second observation from Fig. 7 is the limited amount of time that these tests represent and the small number of cells that form the stacks. A notable exception is the ERC data where cell voltage shows practically no decay after almost 2 years of running. This improved performance is due to a new electrolyte matrix with better retention of the electrolyte. It is also possible that better data exists as manufacturers proprietary information.

An alternate way of looking at cell performance is to plot voltage versus current density. (Current density is a function of Pt loading, Ref. 25.) Such a plot gives an idea of the power that can be obtained per cell unit area. Figure 8 shows such a graph, representing tests from various manufacturers.

Cell performance can be improved by increases in both temperature and pressure. In both cases, this is due to an increased reaction rate. It is typical of the engineering problems of fuel cells that an attempt to optimize one parameter may cause an adverse effect in another. For example, while a temperature increase will improve the reaction rate, it will also cause an increase in the decay rates. Furthermore, "from the overall power plant standpoint, the optimum pressure and temperature depend not only on stack technology and development, but also on the cost and performance implications upon the balance of the system (turbocompressors, heat exchangers, piping, etc.)" (Ref. 24).

Molten Carbonate fuel cell development at ERC (Ref. 26) has focused on improving cell and stack technology in the areas of component stability, material compatibility, fabrication techniques, operating power density, sulfur tolerance, and lightweight stack design. Test results have showed no performance loss for a fuel gas containing up to 15 ppm H_2S for a total test duration of 400 hours. A significant advance has been made in stack design and performance during the past 2 years. The latest stack, assembled with four 300 cm^2 cells, was successfully operated for 1000 hours including a thermal cycle. The improvements made in the stack design are due to different stack components such as gas manifolds, seals, and bipolar plates. The stack was operated for 1000 hours with stable performance. A theoretical open circuit voltage of 1.03 volts per cell was attained, indicating no crossleaks. Efficiencies of 94 to 96 percent were achieved for anode and cathode gases, respectively; average cell potential of 0.75 volt per cell at 100 mA/cm^2 was obtained. The stack operation also included a thermal cycle at about 400 hours.

At IGT (Ref. 27), bench-scale cell testing was conducted to evaluate new materials and components for performance and endurance at 1 to 10 atm operating pressure. Performance testing at pressures about 1 atm continues to show gains twice as large as those predicted by Nernst.[6] One of the reasons for the larger gains is that the effective cell resistance decreases with increasing pressure. Two bench-scale cells attained 10,000 hours of continuous operation, the last 2,300 hours on a low-Btu coal gasification fuel. Decay rates were approximately 9 to 10 mV/1000 hours, 60 percent due to increase in measured internal resistance.

Electrolyte powders containing alkali carbonates and $LiAlO_2$ support particles are prepared by the potassium-free

[5] This point is illustrated in Ref. 2 where a simple formula is given for the efficiency of the overall power plant (from fuel processor to AC current). This formula is $N_p = 59\ V_c$ "where N_p is the efficiency of the plant, as a percent, and V_c is the voltage of a single cell. This relation is accurate to within 5 percent and illustrates the importance of single-cell voltage in establishing the overall efficiency of a plant."

[6] The Nernst potential relates the equilibrium cell voltage to the partial pressures of the gases.

aqueous slurry process. The K_2CO_3 required in the final electrolyte composition is added after the carbonation step. The final characteristics of the $LiAlO_2$ support are established in the firing step (600° to 700°C). Electrolyte tiles hot-pressed from such powders yield high cell performance levels. Decay rates of 9 to 10 mV/1000 hours observed in bench-scale cells operated for 8,000 to 10,000 hours without carbonate additions are influenced significantly by loss of surface area and phase change in $LiAlO_2$ and electrolyte loss. Progress in tile thermal cycling response has been achieved by improving tile mechanical properties, reduction of tile thermal expansion coefficients, and fabrication and cell design modifications.

Promising results were obtained on the processing of powders by spray drying. Development of this process is continuing. The advantages of spray drying include easier and more efficient processing, high production rate, and more homogeneous powder product. Tiles fabricated from spray-dried powders have more uniform microstructures and higher strength. Preparation of $LiAlO_2$ without carbonates, adaptable to alternative tile fabrication techniques, has also been demonstrated by spray drying.

The stack tests at UTC (Ref. 28) have been with cells of 1 square foot (0.093 m^2) total area containing 8 to 20 cells per stack. The primary feature of the stack was a temperature cyclible tile configuration that had proven successful in bench-scale size cells. During the initial 2000-hour time period, the stack was subjected to five thermal cycles. The reactant gas leakage was acceptable and remained essentially unchanged through the thermal cycles. The 20-cell stack was subsequently rebuilt into a 16-cell stack, which accumulated an additional 650 hours of testing. The rebuild was undertaken to determine whether Molten Carbonate stacks could be refurbished after removing poorer performing cells. This is considered to be a significant advantage in reducing cost and minimizing time in a fuel cell stack development program. The leakage was unchanged. However, all of the cell internal resistance increased; those of the replacement cells being the highest. It was concluded that the increased IR was caused during the rebuilding by disruption of the cathode current collector contact area with the separator plate which resulted in high contact losses. Planned changes to component design may alleviate this problem.

IV. System Economics

The fuel cell powerplant system is still in the research and development stage. Many of the characteristics such as capital cost, operation and maintenance (O & M) requirements and costs, availability, etc., have not been established. A reliable economic analysis cannot be done until the power plant technology has been further demonstrated. Installed costs for the fuel cell power plant including manufacture, supplied equipment, and site ancilliaries in a range of $350 to $750 kW in 1978 dollars were suggested by DOE. Costs of annual O & M have ranges of 1.8 to 4.0 mills/kWh and 4.4 to 10.0 mills/kWh with the capacities of 88.1 and 30 percent, respectively, as estimated by UTC (Ref. 29).

To make the fuel cell power plants commercially attractive depends in a large part on the financial support that either the manufacturer and/or the government are willing to give the user. This support can take the form of either the government underwriting the cost of the initial units and/or the manufacturer taking the "risk of underwriting the learning curve" from present day prices to the target figure. Among the various uncertainties of the national fuel cell program, what stands out clearly is a price of $1500/$kW_e$ in 1980 dollars that a potential user must be willing to spend *today* for a fuel cell power plant (Ref. 30).

Spurred by the current shortage in petroleum-based fuels, the fuel costs in the future is unpredictable. Figure 9 (Ref. 31) represents these costs in a somewhat conservative projection. Fuel cell systems available in the near future, most likely, are natural gas-fueled phosphoric acid cells. Hence, a 40 kWh_e[7] plant with a heat rate of 9918 kJ/kWh_e will consume about 255 cubic meters per day of natural gas. For an isolated site such as the Goldstone complex, the transportation and the storage of natural gas could be more complicated than that of diesel fuels.

Similarly, it is extremely difficult to establish the cost benefits of cogeneration. Most of the analyses in the literature refer to the 4.8 MW UTC-designed unit. This is similar to the one to be used by ConEd in New York City and it is to be noted that this unit was not designed with cogeneration in mind.[8] We limit ourselves to quoting from Criner and Steitz (Ref. 32):

> "Faced with a variety of uncertainties in the input parameters, an economic study must examine the sensitivity of results over the range of reasonable uncertainty in the variables. However, beyond the range of such sensitivity results, it usually is not possible to make definite conclusions regarding the economic viability of

[7] A 40 kW unit is chosen as an example partly because there exists a national program to install demonstrator 40 kW units at different facilities throughout the country.

[8] Two types of thermal energy could be generated by such a unit: "High quality" meaning saturated steam at 241 kPa and "low quality" meaning heated water at 34° C. With natural gas as a fuel, this unit can produce 9.28 GJ/h "high-quality" heat and 110 GJ/h "low quality" heat (Ref. 29).

fuel cell cogeneration (or other types of advanced cogeneration).

It appears, then, that the ultimate question of economic viability must be resolved through installation of a significant number of cogeneration fuel cells to establish actual costs and performance. With such experience, advanced fuel cell designs potentially could achieve significant commercial penetration for industrial cogeneration applications in the pulp and paper industry."

V. Conclusions

One of the objectives of this study is to find what can be predicted about the future commercialization of fuel cells. In the literature on fuel cells, there is a considerable optimism regarding their future. This optimism emanates from manufacturers, from utility groups, and from contract monitoring agencies.[9] DOE has a "Phosphoric Acid National Fuel Cell Plan" which is currently being coordinated by other funding agencies such as EPRI, GRI, TVA, etc. This plan is as follows (Ref. 33):

Electric Utility Power Plants	Year
First power plant delivery	1984 (UTC), 1986 (W/ERC)
Design phase concluded	1984-1985
Field testing	1986-1987
OS/IES Systems	
Breadboard testing	1982 (UTC)
Field testing	1985

Figure 10 presents the "history" of predictions for fuel cell plants under this plan. The basic conclusion, from this figure, is that past predictions have been too optimistic. For example, in 1975, UTC predicted that the first commercial electrical utility plants will be delivered in 1977 to 1978. In 1980, the prediction is that these units will appear in 1987 to 1988.

Furthermore, the delay between the time of prediction and the predicted event has grown. Thus, in 1975, the event was predicted for 2 to 3 years from that time (1977 to 1978); by 1980 the delay had grown to 7 to 8 years, with predicted dates of 1987 to 1988. A similar history exists for OS/IES systems and for the 4.8 MW_e demonstrator plant of ConEd.[10]

In the previous sections we have discussed the progress being made in solving the technological problems of fuel cells. We wish to stress that all these results refer to laboratory devices only. At the present time, no demonstrator models are in operation. The first such demonstrator devices (i.e., fuel cell systems working in a real life environment) will be the ConEd and Tokyo plants. The testing programs for these demonstrators are expected to last between 4 and 5 years.

It is unlikely that industry will move into commercial production of fuel cells until the demonstrator units are proven. Furthermore, the industry is still waiting for market acceptability of fuel cells. It is at this point that the relationship among government, manufacturers, and utilities becomes a rather complicated one. Both manufacturers and DOE agree on the need for government support for the demonstrator plants; the disagreement is on the amount of this support.

Partly because of this disagreement the schedule for the demonstrator plants keeps slipping. For example, the latest schedule for the ConEd plant is a checkout of the reformer in late spring of 1981, with the plant scheduled to be operational in July 1981. For the Tokyo plant, the schedule is for the equipment to arrive in Japan before September 1981 and for the operational start to occur in February 1982 (Ref. 43).

Similar funding problems exist in the 40 kW_e demonstration program (Ref. 44). This program provides that about fifty 40 kW_e UTC units will be distributed at various sites around the country in order to monitor and better understand the performance of these units. Sites have already been selected, most of them belonging to the utilities. However, no units for this program have been built yet. This still awaits funding negotiations between DOE, GRI, and UTC.

From the open literature cited and from personal communications held with members of the fuel cell community, we estimate that commercial fuel cell systems will not be available before 1990, with a probable range 1985 to 1992. This conclusion is based on funding difficulties, on lack of market support and, last but not least, on remaining technological difficulties. We wish to stress again that at the present time no commercial or demonstrator systems are operational. All present cost estimates, e.g. $350 to $400 (1978)/kW (Ref. 45), are based on the future commercial availability of ConEd type systems.

[9]NASA Lewis is the lead center for the DOE fuel cell program. The Marshall Space Center is monitoring the 40-kW program.

[10]In July 1980, the predictions for the start up of the ConEd plant were for April 1981. By September 1980, the predictions had been postponed to July 1981.

We were not able to obtain any costs per installed kW for the smaller OS/IES systems.

We close this article by suggesting the following topics for further study:

(1) Size and obtain specifications for a 40 kW system to be installed at Goldstone. This phase should include not only the design of the fuel cell stack, but also include detailed information regarding the fuel availability at Goldstone, the fuel processor, and the inverter. Potential cogeneration should also be studied.

(2) Obtain from the manufacturers 1982 cost estimates for a system such as that described above.

Both the 40 kW size and the 1982 time frame are arbitrarily set. Regardless, it would be very useful to have a thorough preliminary design and cost estimate for potential use at Goldstone.

References

1. Gregg, D. C., *Principles of Chemistry*, 2nd ed., Allyn and Bacon, Boston, 1973.
2. Fickett, A. P., "Fuel Cell Power Plants," *Scientific American*, Vol. 239, No. 6, pp. 70-76, Dec. 1978.
3. Lay, J. E., *Thermodynamics*, C. E. Merrill, Columbus, Ohio, 1963.
4. Benjamin, T. C., Camara, E. H., and Selman, J. R., "Fuel Cell Efficiency," Paper 799117, 14th Intersociety Energy Engineering Conference (IEEC), Vol. I, p. 579, Aug. 1979.
5. Blurton, K. F., "The Fuel Cell Option," *Conference on National Energy Economics II*, Tulsa, Okla., Sept. 1, 1978.
6. Tantram, A. D. S., "Fuel Cells: Past, Present and Future," *Energy Policy*, pp. 56-64, Mar. 1974.
7. Martin, K. F., "Apollo Spurred Commercial Fuel Cell," *Aviat. Week and Space Tech.*, Vol. 98, No. 1, pp. 56-59, Jan. 1973.
8. Grove, W. R., "On Gaseous Voltaic Battery," *Phil. Mag.*, Vol. 21, pp. 417 ff, 1842.
9. Mond, L., and Langer, C., *Proc. Roy. Soc.*, Vol. 46, pp. 296 ff, 1889.
10. Young, J. E., "National Fuel Cell Processing Overview," *5th National Fuel Cell Seminar* (*5th NFCS*), San Diego, Calif., July 14-16, 1980.
11. Personal Communication with H. C. Maru, Energy Research Corporation, Danbury, Conn., June 1980.
12. Kaufman, A., "Phosphoric Acid Fuel Cell Stack and System Development," *5th NFCS*, July 1980.
13. Bett, J. A. S., et al., "Development of the Adiabatic Reformer to Process No. 2, Fuel Oil and Coal Derived Liquids," *5th NFCS*, July 1980.
14. Yarrington, R. M., et al., "The Evaluation of Steam Reforming Catalysts for Use in the Autothermal Reforming Hydrocarbon Feedstocks," *5th NFCS*, July 1980.
15. Appleby, A. J., "A Summary of Phosphoric Acid Technology Status," *5th NFCS*, July 1980.

16. Stonehart, P., et al., "Development of Electrocatalysts and Conductive Substrates for Cathodes in Phosphoric Acid Fuel Cells," *5th NFCS*, July 1980.

17. Burton, K. F., et al., paper submitted for publication in *Electrochim. Acta.*

18. Personal Communication with D. Hoover, Westinghouse Electric Corporation, Pittsburgh, Penn., June 1980.

19. Issacs, H., "Solid Electrolyte Fuel Cells: Air and Fuel Electrode Kinetics," *5th NFCS*, July 1980.

20. Franklin, A., "Transport Properties by Impedance Measurements for Solid Electrolyte Kinetics," *5th NFCS*, July 1980.

21. Baker, B., et al., "Progress in Phosphoric Acid Technology," *5th NFCS*, July 1980.

22. George, M., "Scale-Up of Aqueous TFMSA Fuel Cell Technology," *5th NFCS*, July 1980.

23. Camara, E., and Claar, T., "Molten Carbonate Fuel Cell Technology Development," *5th NFCS*, July 1980.

24. Prokopius, P. R., et al., "Commercial Phosphoric Acid Fuel Cell System Technology Development," Paper 799109, *14th IEEC*, Aug. 1979.

25. Fickett, A. P., "Fuel Cell Electrocatalysis: Where Have We Failed?", *Proc. of Symp. on Electr. Mater. and Proc. Energy Conversion and Storage*, p. 547 ff, 1977.

26. Dharia, D., Maru, H. C., and Patel, P. S., "Sulfur Tolerance and Stack Testing for Molten Carbonate Fuel Cells," *5th NFCS*, July 1980.

27. Camara, E., and Claar, T., "Molten Carbonate Fuel Cell Technology Development," *5th NFCS*, July 1980.

28. Reiser, C. A., and Schrool, C. R., "Molten Carbonate Fuel Cell Stack Testing," *5th NFCS*, July 1980.

29. Criner, D. E., et al., "Feasibility of Cogeneration Application of a 4.8 MW Fuel Cell Power Plant at a Santa Clara, Calif., Paper Mill," Burns & McDonnell Report, July 1979.

30. Personal Communication with Mr. Hayman, ConEd, N.Y., June 1980.

31. Darrow, Jr., K., "National Fuels Outlook," *5th NFCS*, July 1980.

32. Criner, D. E.,, and Steitz, P., "Fuel Cell Cogeneration in a Paperboard Mill," *5th NFCS*, 1980.

33. Personal Communication with Mr. M. Warshay, NASA Lewis Research Center, Cleveland, Ohio, July 1980.

34. Kunz, H. Z., "The State-Of-The-Art of Hydrogen-Air Phosphoric Acid Electrolyte Fuel Cells," *Proc. of Symp. on Electr. Mater, and Proc. Energy Conversion and Storage,* p. 607 ff, 1977.

35. United Technologies Corporation Memo from C. C. Morrill to R. Baugh, DSN Engineering, June 1975.

36. Handley, L. M., et al., "4.8-Megawatt Fuel Cell Module Demonstrator," Paper No. 779057, *12 IECEC*, 1977.

37. Sperberg, R. T., and Fiore, V. B., "The Reality of On-Site Fuel Cells," GRI, NTIS Paper A80-11973.

38. Glasser, K., "4.8 MW Fuel Cell Demonstrator Program – A Progress Report," *5th NFCS*, July 1980.

39. Kalhammer, F., "R & D Status Report, Energy Management and Utilization Division – First-Generation Fuel Cells," *EPRI J.*, p. 62, June 1980.

40. "Fuel Cell Energy System," *Mechanical Engineering*, p. 22, March 1980.

41. "Commercial Prototype Program for Phosphoric Acid Fuel Cell Plate," Westinghouse Electric Corporation, Pittsburg, Penn., 1979.

42. "Phosphoric Acid Fuel Cell; On-Site Integrated Energy System (OS/IES)," Westinghouse Electric Corporation, 1979.

43. Personal Communication with C. Cannon, Asst. Director Energy Programs, United Technologies Corporation, Wash., D.C., Sept. 1980.

44. Personal Communication with B. Podolny, United Technologies Corporation, South Windsor, Conn., Sept. 1980.

45. Gillis, E. A., "Process Equipment Requirements for Electric Utility Fuel Cells," *88th National Meeting and 2nd Chemical Plant Equipment Exposition*, AICHE, Philadelphia, Penn., June 8-12, 1980.

Table 1. Electrochemical reaction of some fuel cells

	Molten carbonate cell	Solid oxide cell	Phosphoric acid cell	Alkaline cell
Anode	$H_2 + CO_3^{=} \rightarrow H_2O + CO_2 + 2e^-$	$H_2 + O^{=} \rightarrow H_2O + 2e^-$	$H_2 \rightarrow 2H^+ + 2e^-$	$H_2 + 2OH^- \rightarrow 2H_2O + 2e^-$
Cathode	$\frac{1}{2} O_2 + CO_2 + 2e^- \rightarrow CO_3^{=}$	$\frac{1}{2} O_2 + 2e^- \rightarrow O^{=}$	$\frac{1}{2} O_2 + 2H^- + 2e^- \rightarrow H_2O$	$\frac{1}{2} O_2 + H_2O + 2e^- \rightarrow 2OH^-$
Overall	$H_2 + \frac{1}{2} O_2 \rightarrow H_2O$ + Heat + Electricity	$H_2 + \frac{1}{2} O_2 \rightarrow H_2O$ + Heat + Electricity	$H_2 + \frac{1}{2} O_2 \rightarrow H_2O$ + Heat + Electricity	$H_2 + \frac{1}{2} O_2 \rightarrow H_2O$ + Heat + Electricity

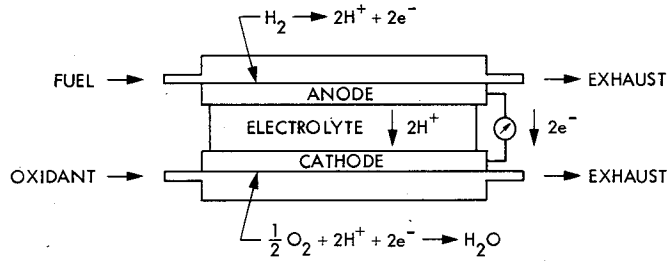

Fig. 1. Operation of acid fuel cell

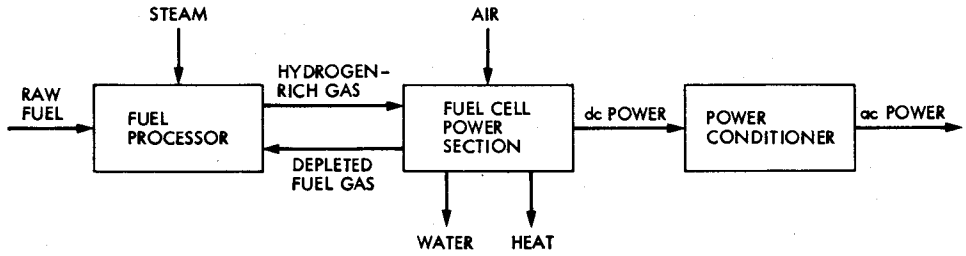

Fig. 2. Fuel cell power plant elements

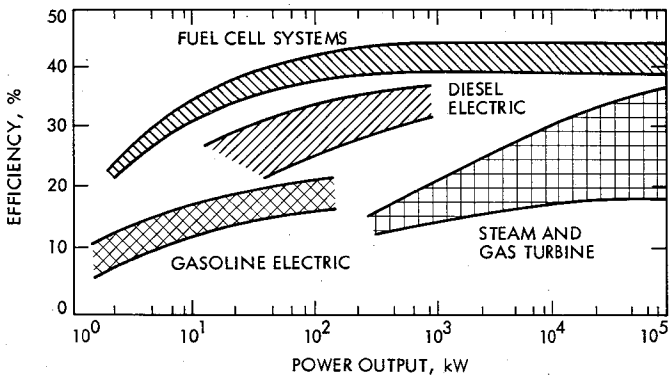

Fig. 3. Efficiency of power generation systems

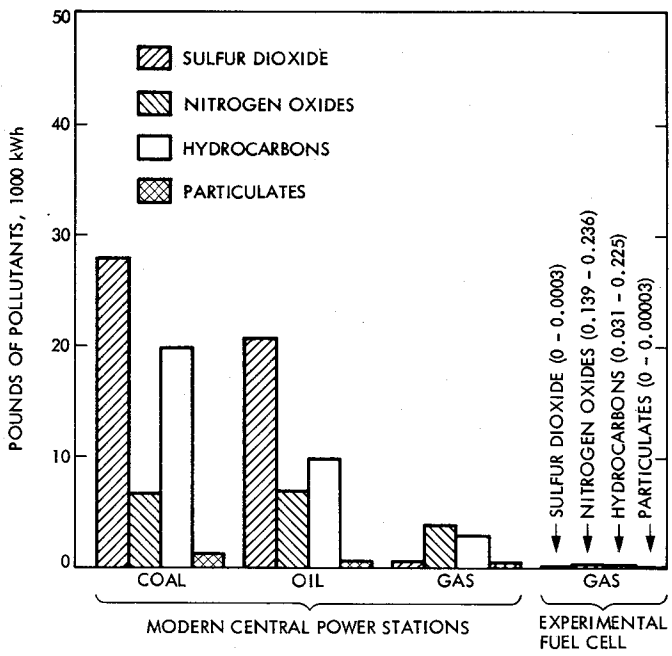

Fig. 4. Pollutants from power generation systems

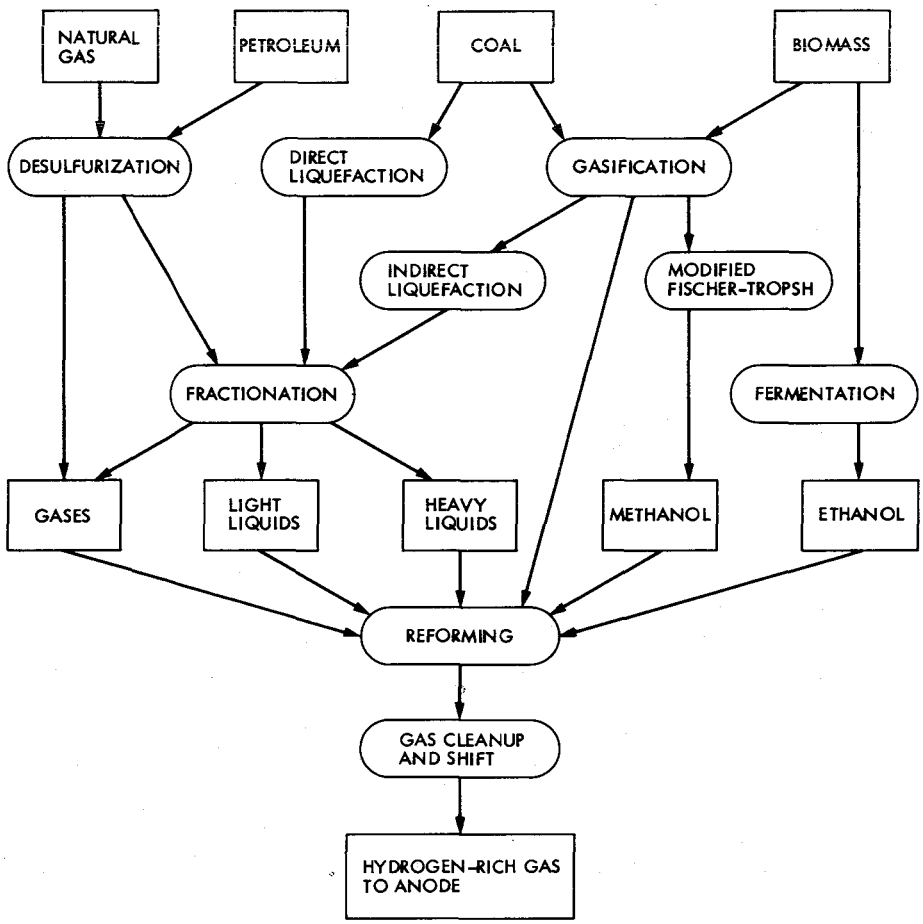

Fig. 5. Raw fuels for fuel cell application

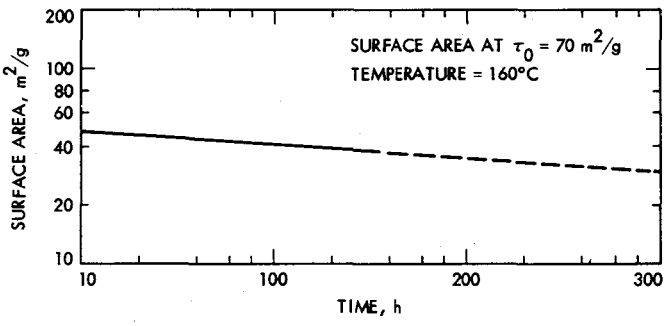

Fig. 6. Platinum surface area reduction on carbon substrate

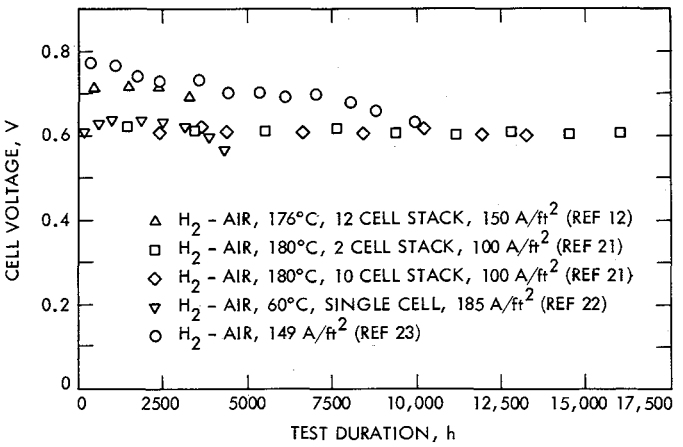

Fig. 7. Fuel cell stack endurance

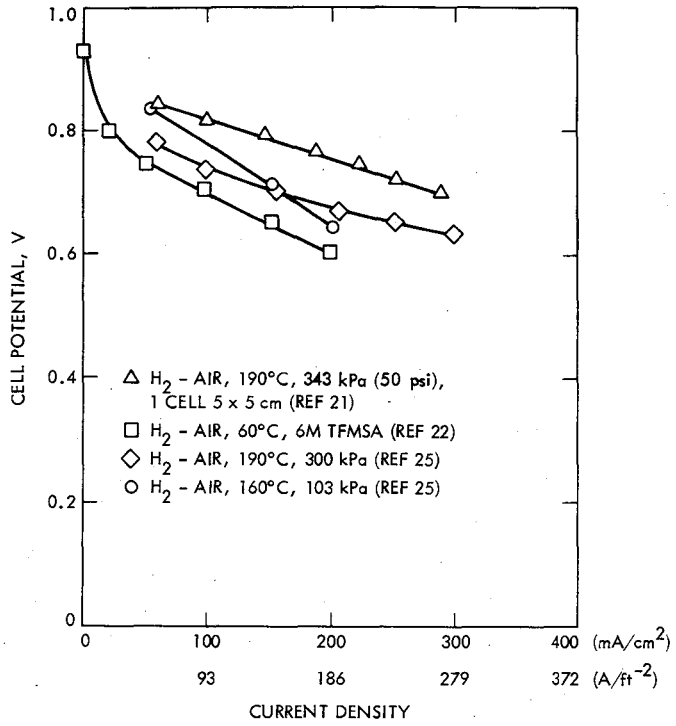

Fig. 8. Fuel cell performance

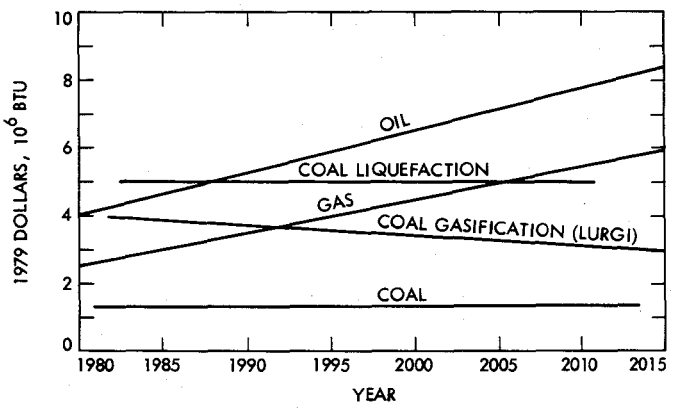

Fig. 9. Fuel costs projection

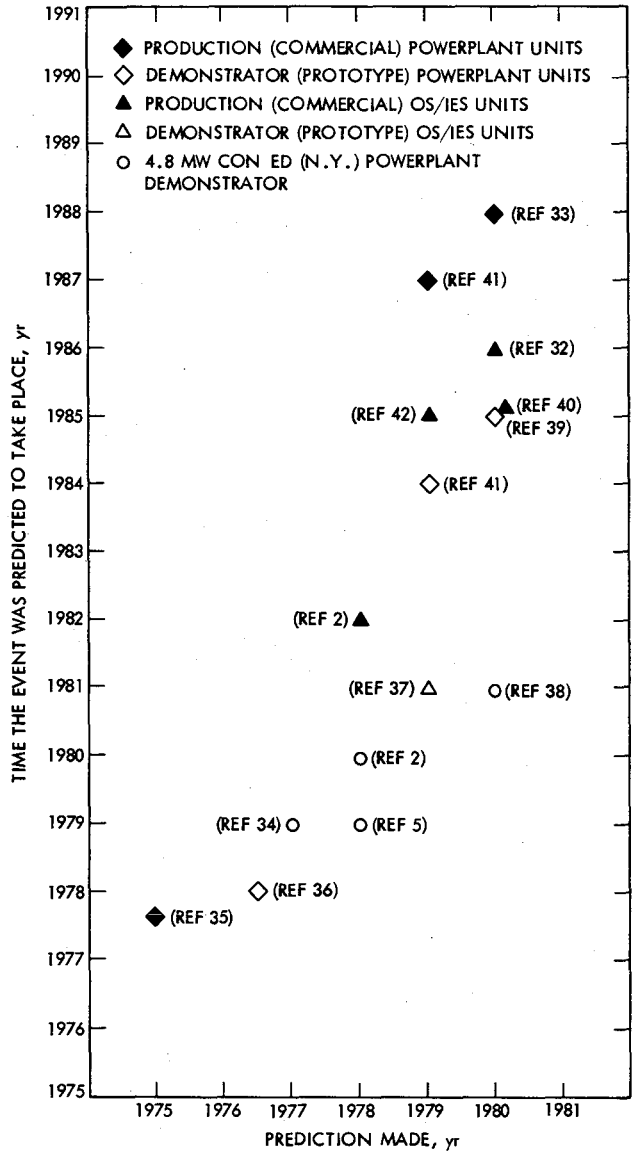

Fig. 10. Fuel cell development prediction history

Bibliography

Ananda, M. P., "Lunar Gravity: A Mass Point Model," *J. Geophys. Res.*, Vol. 82, No. 20, pp. 3049-3064, July 10, 1977.

Anderson, J. D., et al., "Experimental Test of General Relativity Using Time-Delay Data From Mariner 6 and Mariner 7," *Astrophys. J.*, Vol. 200, No. 1, pp. 221-233, Aug. 15, 1975.

Anderson, J. D., et al., "Tests of General Relativity Using Astrometric and Radio Metric Observations of the Planets," *Acta Astronautica*, Vol. 5, No. 1-2, pp. 43-61, Jan.-Feb. 1978.

Barton, W. R., and Miller, R. B., *Tracking and Data System Support for the Pioneer Project: Pioneer 11–Prelaunch Planning Through Second Trajectory Correction: to May 1, 1973*, Technical Memorandum 33-584, Vol. II, Jet Propulsion Laboratory, Pasadena, Calif., Mar. 15, 1975.

Bartos, K. P., et al., *Implementation of the 64-Meter-Diameter Antennas at the Deep Space Stations in Australia and Spain*, Technical Memorandum 33-692, Jet Propulsion Laboratory, Pasadena, Calif., Jan. 15, 1975.

Bathker, D. A., Brown, D. W., and Petty, S. M., *Single- and Dual-Carrier Microwave Noise Abatement in the Deep Space Network*, Technical Memorandum 33-733, Jet Propulsion Laboratory, Pasadena, Calif., Aug. 1, 1975.

Bathker, D. A., *Microwave Performance Characterization of Large Space Antennas*, JPL Publication 77-21, Jet Propulsion Laboratory, Pasadena, Calif., May 15, 1977.

Beatty, R. W., and Otoshi, T. Y., "Effect of Discontinuities on the Group Delay of a Microwave Transmission Line," *IEEE Trans. Microwave Theor. Techniq.*, Vol. MTT-23, No. 11, pp. 919-923, Nov. 1975.

Benjauthrit, B., and Reed, I. S., "Galois Switching Functions and Their Applications," *IEEE Trans. Comput.*, Vol. C-25, No. 1, pp. 78-86, Jan. 1976.

Benjauthrit, B., and Reed, I. S., "On the Fundamental Structure of Galois Switching Functions," *IEEE Trans. Comput.*, Vol. C-27, No. 8, pp. 757-762, Aug. 1978.

Berlekamp, E. R., et al., "On the Inherent Intractability of Certain Coding Problems," *IEEE Trans. Inform. Theor.*, Vol. IT-24, No. 3, pp. 384-386, May 1978.

Berman, A. L., and Ramos, R., "Pioneer Venus Occultation Radio Science Data Generation," *IEEE Trans. Geosci. and Remote Sensing*, Vol. GE-18, No. 1, pp. 11-14, Jan. 1980.

Berman, A. L., and Rockwell, S. T., *New Optical and Radio Frequency Angular Tropospheric Refraction Models for Deep Space Applications*, Technical Report 32-1601, Jet Propulsion Laboratory, Pasadena, Calif., Nov. 1, 1975.

Berman, A. L., *The Prediction of Zenith Range Refraction From Surface Measurements of Meteorological Parameters*, Technical Report 32-1602, Jet Propulsion Laboratory, Pasadena, Calif., July 15, 1976.

Born, G. H., and Mohan, S. N., "Orbit Determination for Mariner 9 Using Radio and Optical Data," *J. Spacecraft Rockets*, Vol. 12, No. 7, pp. 439-441, July 1975.

Butman, S. A., "Linear Feedback Rate Bounds for Regressive Channels," *IEEE Trans. Inform. Theor.*, Vol. IT-22, No. 3, pp. 363-366, May 1976.

Butman, S. A., et al., "Design Criteria for Noncoherent Gaussian Channels With MFSK Signaling and Coding," *IEEE Trans. Commun.*, Vol. COM-24, No. 10, pp. 1078-1088, Oct. 1976.

Butman, S. A., and Lesh, J. R., "The Effects of Bandpass Limiters on *n*-Phase Tracking Systems," *IEEE Trans. Commun.*, Vol. COM-25, No. 6, pp. 569-576, June 1977.

Chao, C.-C., "Interstation Frequency Offset Determination Using Differenced 2-Way/3-Way Doppler Data," paper presented at the 1978 Spring Meeting of the American Geophysical Union, Miami, Florida, Apr. 17-20, 1978.

Christensen, C. S., and Reinold, S. J., "Navigation of the Mariner 10 Spacecraft to Venus and Mercury," *J. Spacecraft Rockets*, Vol. 12, No. 5, pp. 280-286, May 1975.

Christensen, C. S., et al., "On Achieving Sufficient Dual Station Range Accuracy for Deep Space Navigation at Zero Declination," paper presented at AAS/AIAA Astrodynamics Specialist Conference, Jackson Hole, Wyo., Sept. 7-9, 1977.

Christensen, E. J., et al., "The Mass of Phobos from Viking Flybys," *Geophys. Res. Lett.*, Vol. 4, No. 12, pp. 555-557, Dec. 1977.

Clauss, R., Flesner, L. D., and Schultz, S., "Simple Waveguide Reflection Maser with Broad Tunability," *Rev. Sci. Instrum.*, Vol. 48, No. 8, pp. 1104-1105, Aug. 1977.

A Collection of Articles on S/X-Band Experiment Zero Delay Ranging Tests, Technical Memorandum 33-747, Vol. I, Jet Propulsion Laboratory, Pasadena, Calif., Nov. 1, 1975.

Curkendall, D. W., "Algorithms for Isolating Worst Case Systematic Data Errors," *J. Guidance Contr.*, Vol. 1, No. 1, pp. 56-62, Jan.-Feb. 1978.

Dickinson, R. M., "The Beamed Power Microwave Transmitting Antenna," *IEEE Trans. Microwave Theor. Tech.*, Vol. MTT-26, No. 5, pp. 335-340, May 1978.

Duxbury, T. C., Johnson, T. V., and Matson, D. L., "Galilean Satellite Mutual Occultation Data Processing," *Icarus*, Vol. 25, No. 4, pp. 569-584, Aug. 1975.

Edelson, R. E., "An Observational Program to Search for Radio Signals From Extraterrestrial Intelligence Through the Use of Existing Facilities," Preprint IAF-A-76-033, Int. Astronaut. Fed. XXVII Congress, Anaheim, Calif., Oct. 10-16, 1976.

Edelson, R. E., and Levy, G. S., "The Search for Extraterrestrial Intelligence: Telecommunications Technology," *Proceedings of the 1976 National Telecommunications Conference,* Vol. I, Dallas, Tex., Nov. 29-Dec. 1, 1976.

Edelson, R. E., "An Experimental Protocol for a Search for Radio Signals of Extraterrestrial Intelligent Origin in the Presence of Man-Made Radio Frequency Sources," paper presented at the XXVIIIth International Astronautical Congress, Prague, Czechoslovakia, Sept. 25-Oct. 1, 1977.

Estabrook, F. B., and Wahlquist, H. D., "Response of Doppler Spacecraft Tracking to Gravitational Radiation," *Gen. Relat. Grav.*, Vol. 6, No. 5, pp. 439-447, Oct. 1975.

Estacion Espacial de Madrid: Madrid Space Station, Special Publication 43-26, Jet Propulsion Laboratory, Pasadena, Calif., Aug. 31, 1975.

Ferrari, A. J., and Ananda, M. P., "Lunar Gravity: A Long-Term Keplerian Rate Method," *J. Geophys. Res.*, Vol. 82, No. 20, pp. 3085-3097, July 10, 1977.

Fjeldbo, G., et al., "Viking Radio Occultation Measurements of the Martian Atmosphere and Topography: Primary Mission Coverage," *J. Geophys. Res.*, Vol. 82, No. 28, pp. 4317-4324, Sept. 30, 1977.

Fortenberry, J. W., Freeland, R. E., and Moore, D. M., *Five-Meter-Diameter Conical Furlable Antenna*, Technical Report 32-1604, Jet Propulsion Laboratory, Pasadena, Calif., July 15, 1976.

Freiley, A. J., Batelaan, P. D., and Bathker, D. A., *Absolute Flux Density Calibrations of Radio Sources: 2.3 GHz*, Technical Memorandum 33-806, Jet Propulsion Laboratory, Pasadena, Calif., Dec. 1, 1977.

Goldstein, R. M., and Morris, G. A., "Ganymede: Observations by Radar," *Science*, Vol. 188, No. 4194, pp. 1211-1212, June 20, 1975.

Goldstein, R. M., Green, R. R., and Rumsey, H., Jr., "Venus Radar Images," *J. Geophys. Res.*, Vol. 81, No. 26, pp. 4807-4817, Sept. 10, 1976.

Goodwin, P. S., et al., *Tracking and Data Systems Support for the Helios Project: Project Development Through End of Mission Phase II*, Technical Memorandum 33-752, Vol. I, Jet Propulsion Laboratory, Pasadena, Calif., July 1, 1976.

Goodwin, P. S., et al., *Tracking and Data Systems Support for the Helios Project: DSN Support of Project Helios April 1975 Through May 1976*, Technical Memorandum 33-752, Vol. II, Jet Propulsion Laboratory, Pasadena, Calif., Jan. 15, 1977.

Goodwin, P. S., Jensen, W. N., and Flanagan, F. M., *Tracking and Data Systems Support for the Helios Project: DSN Support of Project Helios May 1976 Through June 1977*, Technical Memorandum 33-752, Vol. III, Jet Propulsion Laboratory, Pasadena, Calif., Mar. 1, 1979.

Gulkis, S., et al., "An All-Sky Search for Narrow-Band Radiation in the Frequency Range 1-25 GHz," paper presented at the 1976 U.S. National Commission, International Union of Radio Science, Amherst, Mass., Oct. 10-15, 1976.

Harris, A. W., et al., "2290-MHz Flux Densities of 52 High-Declination Radio Sources," *Astron. J.*, Vol. 81, No. 4, pp. 222-224, Apr. 1976.

Higa, W. H., "Spurious Signals Generated by Electron Tunneling on Large Reflector Antennas," *Proc. IEEE*, Vol. 63, No. 2, pp. 306-313, Feb. 1975.

Higa, W. H., *The Superconducting Cavity-Stabilized Maser Oscillator*, Technical Memorandum 33-805, Jet Propulsion Laboratory, Pasadena, Calif., Dec. 15, 1976.

Hunter, J. A., "Orbiting Deep Space Relay Station, A Study Report," paper presented at AIAA Conference on Large Space Platforms, Future Needs and Capabilities, Los Angeles, Calif., Sept. 27-29, 1978.

Jacobson, R. A., McDanell, J. P., and Rinker, G. C., "Use of Ballistics Arcs in Low Thrust Navigation," *J. Spacecraft Rockets*, Vol. 12, No. 3, pp. 138-145, Mar. 1975.

Jurgens, R. F., and Goldstein, R. M., "Radar Observations at 3.5 and 12.6 cm Wavelength of Asteroid 433 Eros," *Icarus*, Vol. 28, No. 1, pp. 1-15, May 1976.

Jurgens, R. F., and Bender, D. F., "Radar Detectability of Asteroids," *Icarus*, Vol. 31, No. 4, pp. 483-497, Aug. 1977.

Katow, M. S., "Evaluating Computed Distortions of Parabolic Reflectors," *Record of IEEE 1977 Mechanical Engineering in Radar Symposium, Arlington, Virginia, Nov. 8-10, 1977*, IEEE Publication 77CH 1250-0 AES, pp. 91-93.

Kliore, A. J., Woiceshyn, P. M., and Hubbard, W. P., "Pioneer 10 and 11 Radio Occultations by Jupiter," *COSPAR Space Research*, Vol. XVII, pp. 703-710, Pergamon Press Ltd., Oxford, 1978.

Kliore, A., et al., "The Polar Ionosphere of Venus Near the Terminator From Early Pioneer Venus Orbiter Radio Occultation," *Science*, Vol. 203, No. 4382, pp. 765-768, Feb. 23, 1979.

Kuiper, T. B. H., and Morris, M., "Searching for Extraterrestrial Civilizations," *Science*, Vol. 196, pp. 616-621, May 6, 1977.

Lesh, J. R., "Sequential Decoding in the Presence of a Noisy Carrier Reference," *IEEE Trans. Commun.*, Vol. COM-23, No. 11, pp. 1292-1297, Nov. 1975.

Levitt, B. K., "Long Frame Sync Words for Binary PSK Telemetry," *IEEE Trans. Commun.*, COM-23, No. 11, pp. 1365-1367, Nov. 1975.

Levy, G. S., et al., "Helios-1 Faraday Rotation Experiment: Results and Interpretations of the Solar Occultations in 1975," *J. Geophys.*, Vol. 42, No. 6, pp. 659-672, 1977.

Levy, R., "Computer-Aided Design of Antenna Structures and Components," *Comput. Struc.*, Vol. 6, Nos. 4/5, pp. 419-428, Aug./Oct. 1976.

Levy, R., and McGinness, H., *Wind Power Prediction Models*, Technical Memorandum 33-802, Jet Propulsion Laboratory, Pasadena, Calif., Nov. 15, 1976.

Levy, R., and Katow, M. S., "Implementation of Wind Performance Studies for Large Antenna Structures," *Record of IEEE 1977 Mechanical Engineering in Radar Symposium, Arlington, Virginia, Nov. 8-10, 1977*, IEEE Publication 77CH 1250-0 AES, pp. 27-33.

Levy, R., "Antenna Bias Rigging for Performance Objective," *Record of IEEE 1977 Mechanical Engineering in Radar Symposium, Arlington, Virginia, Nov. 8-10, 1977*, IEEE Publication 77CH 1250-0 AES, pp. 94-97.

Liu, A. S., and Pease, G. E., "Spacecraft Ranging From a Ground Digitally Controlled Oscillator," *J. Spacecraft Rockets*, Vol. 12, No. 9, pp. 528-532, Sept. 1975.

Martin, W. L., and Zygielbaum, A. I., *Mu-II Ranging*, Technical Memorandum 33-768, Jet Propulsion Laboratory, Pasadena, Calif., May 15, 1977.

Melbourne, W. G., "Navigation between the Planets," *Sci. Amer.*, Vol. 234, No. 6, pp. 58-74, June 1976.

Miller, R. B., *Tracking and Data System Support for the Pioneer Project: Pioneer 10–From April 1, 1972, Through the Jupiter Encounter Period, January 1974*, Technical Memorandum 33-584, Vol. III, Jet Propulsion Laboratory, Pasadena, Calif., June 15, 1975.

Miller, R. B., et al., *Tracking and Data System Support for the Pioneer Project: Pioneer 10–From January 1974 to January 1975; Pioneer 11–From May 1, 1973 Through Jupiter Encounter Period, January 1975*, Technical Memorandum 33-584, Vol. IV, Jet Propulsion Laboratory, Pasadena, Calif., Dec. 1, 1975.

Mudgway, D. J., *Tracking and Data System Support for the Viking 1975 Mission to Mars: Prelaunch Planning, Implementation, and Testing*, Technical Memorandum 33-783, Vol. I, Jet Propulsion Laboratory, Pasadena, Calif., Jan. 15, 1977.

Mudgway, D. J., and Traxler, M. R., *Tracking and Data System Support for the Viking 1975 Mission to Mars: Launch Through Landing of Viking 1*, Technical Memorandum 33-783, Vol. II, Jet Propulsion Laboratory, Pasadena, Calif., Mar. 15, 1977.

Mudgway, D. J., *Tracking and Data System Support for the Viking 1975 Mission to Mars: Planetary Operations*, Technical Memorandum 33-783, Vol. III, Jet Propulsion Laboratory, Pasadena, Calif., Sept. 1, 1977.

Mudgway, D. J., *Tracking and Data System Support for the Viking 1975 Mission to Mars: Extended Mission Operations December 1976 to May 1978,* Technical Memorandum 33-783, Vol. IV, Jet Propulsion Laboratory, Pasadena, Calif., Dec. 15, 1978.

Muhleman, D. O., Esposito, P. B., and Anderson, J. D., "The Electron Density Profile of the Outer Corona and the Interplanetary Medium From Mariner-6 and Mariner-7 Time-Delay Measurements," *Astrophys. J.,* No. 211, No. 3, Part 1, pp. 943-957, Feb. 1, 1977.

Murray, B. C., Gulkis, S., and Edelson, R. E., "Extraterrestrial Intelligence: An Observational Approach," *Science,* Vol. 199, No. 4328, pp. 485-492, Feb. 3, 1978.

Ohlson, J. E., "Polarization Tracking of a Partially Coherent Signal Using a Double Loop," *IEEE Trans. Commun.,* Vol. COM-23, No. 9, pp. 859-866, Sept. 1975.

Ohlson, J. E., and Reid, M. S., *Conical-Scan Tracking With the 64-m-diameter Antenna at Goldstone,* Technical Report 32-1605, Jet Propulsion Laboratory, Pasadena, Calif., Oct. 1, 1976.

Ong., K. M., et al., "A Demonstration of a Transportable Radio Interferometric Surveying System With 3-cm Accuracy on a 307-m Base Line," *J. Geophys. Res.,* Vol. 81, No. 20, pp. 3587-3593, July 10, 1976.

Otoshi, T. Y., and Stelzried, C. T., "Cosmic Background Noise Temperature Measurement at 13-cm Wavelength," *IEEE Trans. Instr. Meas.,* Vol. IM-24, No. 2, pp. 174-179, June 1975.

Phillips, R. J., et al., "Simulation Gravity Modeling to Spacecraft-Tracking Data: Analysis and Application," *J. Geophys. Res.,* Vol. 83, No. B11, pp. 5455-5464, Nov. 10, 1978.

Posner, E. C., "Random Coding Strategies for Minimum Entropy," *IEEE Trans. Inform. Theor.,* Vol. IT-21, No. 4, pp. 388-391, July 1975.

Posner, E. C., "Life Cycle Costing with a Discount Rate," *Utilitas Mathematica,* Vol. 13, pp. 157-188, 1978.

Powell, R. V., and Hibbs, A. R., "An Entree for Large Space Antennas," *Astronaut. Aeronaut.,* Vol. 15, No. 12, pp. 58-64, Dec. 1977.

Reed, I. S., Truong, T. K., and Benjauthrit, B., "On Decoding of Reed-Solomon Codes over GF(32) and GF(64) Using the Transform Techniques of Winograd," *Conference Record, 1978 National Telecommunications Conference*, Vol. 2, Birmingham, Alabama, Dec. 3-6, 1978.

Simon, M. K., "A Generalization of Minimum-Shift-Keying (MSK) Type Signaling Based Upon Input Data Symbol Pulse Shaping," *IEEE Trans. Commun.,* Vol. COM-24, No. 8, pp. 845-856, Aug. 1976.

Simon, M. K., "An MSK Approach to Offset QASK," *IEEE Trans. Commun.,* Vol. COM-24, No. 8, pp. 921-923, Aug. 1976.

Simon, M. K., "The False Lock Performance of Costas Loops with Hard-Limited In-Phase Channel," *IEEE Trans. Commun.,* Vol. COM-26, No. 1, pp. 23-34, Jan. 1978.

Simon, M. K., "On the Calculation of Squaring Loss in Costas Loops with Arbitrary Arm Filters," *IEEE Trans. Commun.*, Vol. COM-26, No. 1, pp. 179-184, Jan. 1978.

Simon, M. K., "Tracking Performance of Costas Loops With Hard-Limited In-Phase Channel," *IEEE Trans. Commun.*, Vol. COM-26, No. 4, pp. 420-432, Apr. 1978.

Sjogren, W. L., et al., "Gravity Fields," *IEEE Trans. Geosci. Electron.*, Vol. GE-14, No. 3, pp. 172-183, July 1976.

Slade, M. A., et al., "Alsep-Quasar Differential VLBI," *The Moon*, Vol. 17, pp. 133-147, 1977.

Tausworthe, R. C., *Standard Classifications of Software Documentation*, Technical Memorandum 33-756, Jet Propulsion Laboratory, Pasadena, Calif., Jan. 15, 1976.

Thomas, J. B., et al., "A Demonstration of an Independent-Station Radio Interferometry System With 4-cm Precision on a 16-km Base Line," *J. Geophys. Res.*, Vol. 81, No. 5, pp. 995-1005, Feb. 10, 1976.

Toukdarian, R. Z., *Final Engineering Report for Goldstone Operations Support Radar,* Technical Memorandum 33-800, Jet Propulsion Laboratory, Pasadena, Calif., Nov. 1, 1976.

Truong, T. K., and Reed, I. S., "Convolutions Over Residue Classes of Quadratic Integers," *IEEE Trans. Inform. Theor.*, Vol. IT-22, No. 4, pp. 468-475, July 1976.

Truong, T. K., and Reed, I. S., "Convolutions over Quartic Integer Residue Classes," *Proceedings of the International Conference on Information Sciences and Systems,* Patras, Greece, Aug. 19-24, 1976.

Truong, T. K., Liu, K. Y., and Reed, I. S., "Fast Number-Theoretic Transforms for Digital Filtering," *Electron, Lett.*, Vol. 12, No. 24, Nov. 1976.

Truong, T. K., et al., "X-Ray Reconstruction by Finite Field Transforms," *IEEE Trans. Nucl. Sci.*, Vol. NS-24, No. 1, pp. 843-849, Feb. 1977.

Truong, T. K., Golomb, S. W., and Reed, I. S., "Integer Convolutions Over the Finite Field $GF(3 \cdot 2^n + 1)$," *SIAM J. Appl. Math.*, Vol. 32, No. 2, pp. 356-365, Mar. 1977.

Truong, T. K., Reed, I. S., and Liu, K. Y., "Fast Algorithm for Computing Complex Number-Theoretic Transforms," *Electron. Lett.*, Vol. 13, No. 10, pp. 278-280, May 12, 1977.

Weber, W. J., III, "Performance of Phase-Locked Loops in the Presence of Fading Communication Channels," *IEEE Trans. Commun.*, Vol. COM-24, No. 5, pp. 487-499, May 1976.

Weber, W. J., III, Ackerknecht, W. E., and Kollar, F. J., *Viking X-Band Telemetry Experiment Final Report,* Technical Memorandum 33-794, Jet Propulsion Laboratory, Pasadena, California, Sept. 1, 1976.

Wong, J. S. L., et al., *Review of Finite Fields: Applications to Discrete Fourier Transforms and Reed-Solomon Coding,* JPL Publication 77-23, Jet Propulsion Laboratory, Pasadena, Calif., July 15, 1977.

Woo, R., "Measurements of the Solar Wind Using Spacecraft Radio Scattering Observations," in *Study of Traveling Inter-Planetary Phenomena,* pp. 81-100, D. Reidel Publishing Co., Dordrecht, Holland/Boston, 1977.

Woo, R., "Radial Dependence of Solar Wind Properties Deduced from Helios 1/2 and Pioneer 10/11 Radio Scattering Observations," *Astrophys. J.*, Vol. 219, No. 2, Part 1, pp. 727-739, Jan. 15, 1978.

Woo, R. T., "Observations of Turbulence in the Atmosphere of Venus Using Mariner 10 Radio Occultation Measurements," *J. Atmos. Sci.*, Vol. 32, No. 6, pp. 1084-1090, June 1975.

Yuen, J. H., *A Practical Statistical Model for Telecommunications Performance Uncertainty*, Technical Memorandum 33-732, Jet Propulsion Laboratory, Pasadena, Calif., June 15, 1975.

NASA—JPL—Coml., L.A., Calif.

End of Document